MODELING THE EVOLUTION OF TRACE SPECIES IN THE POST-COMBUSTOR FLOW PATH OF GAS TURBINE ENGINES

by

ANTHONY T. CHOBOT III

B.S. Mechanical Engineering
University of Illinois at Urbana-Champaign, 1995

Submitted to the Department of Mechanical Engineering
in partial fulfillment of the requirements for the degree of

MASTER OF SCIENCE IN MECHANICAL ENGINEERING

at the

MASSACHUSETTS INSTITUTE OF TECHNOLOGY

September 2000

Author: _____
Anthony T. Chobot III
Department of Mechanical Engineering
August 18, 2000

Certified by: _____
Professor Ian A. Waitz
Associate Professor of Aeronautics and Astronautics
Thesis Supervisor

Certified by: _____
Professor Ahmed F. Ghoniem
Professor of Mechanical Engineering
Thesis Reader

Accepted by: _____
Professor Ain A. Sonin
Professor of Mechanical Engineering
Chairman, Departmental Graduate Committee

MODELING THE EVOLUTION OF TRACE SPECIES IN THE POST-COMBUSTOR FLOW PATH OF GAS TURBINE ENGINES

by

Anthony T. Chobot III

Submitted to the Department of Mechanical Engineering
on August 18, 2000 in Partial Fulfillment of the
Requirements for the Degree of Master of Science in
Mechanical Engineering

ABSTRACT

A consensus among scientists has formed that human activities have an influence on the atmosphere and are contributing to global warming. Recently, aviation has garnered a significant amount of attention since it is the fastest growing sector of transportation and it is thought to be an important component of such impacts. Trace species emitted by aircraft directly into the upper atmosphere are believed to have an enhanced influence relative to other common emissions generated by human activity near the surface of the earth. Prior work has concluded that trace species can change significantly in the engine post-combustor gas path. Research efforts to understand the role of aircraft gas turbine engine emissions in global climate change and the mechanisms by which their emissions are produced have been intensified.

A modeling methodology was developed which can be used to predict the evolution of trace species in the post-combustor flow path of gas turbine engines. The modeling methodology incorporates various levels of detail to accurately and efficiently predict levels of intra-engine trace species by considering the key parameters affecting their evolution, specifically temperature, pressure, residence time, and species concentration. The core of the model is a computer code which performs a numerical solution to the fluid mechanics and chemical kinetics problems. The model is intended to improve the overall understanding of the fundamental physical processes that effect trace species evolution and to serve as a predictive design tool which can direct the development of new engine technologies which reduce undesirable aviation emissions.

The development effort consisted of several refinements aimed at increasing the accuracy and usability of the model. The improvements included an improved species initial condition specification procedure, improved grid generation, capability for multiple inlet/exit planes, addition of parallel chemistry subroutines, revision of chemistry convergence criteria, addition of circumferentially-varying unsteady inlet conditions, and incorporation of a new chemical mechanism.

Several validation exercises were performed which benchmark the capabilities of the model and test the added features. Past simulations of a duct and rotor were used as a baseline to verify several of the improvements. These simulations were used to improve the chemistry convergence criteria, perform a comparative study of several chemical mechanisms, and verify the periodic boundary conditions. The Princeton University Variable Pressure Flow Reactor was also simulated as a validation exercise in an attempt to evaluate the overall effectiveness of the model in predicting the flow field, mixing, and species concentrations in a well known and controlled environment.

The model was used to perform the first complete post-combustor engine simulation in support of an engine measurement campaign. The results provided guidance for test parameters and measurement strategies. This simulation was further used to assess the effects of flow non-uniformity on the evolution of trace species in a typical aircraft engine and to refine the current modeling practice. Engine operating conditions, multi-dimensional non-uniformities, and the unsteady interaction of non-uniformities with subsequent blade rows were all found to influence trace species evolution.

Thesis Supervisor: Professor Ian A. Waitz
Title: Associate Professor of Aeronautics and Astronautics

ACKNOWLEDGEMENTS

I would first like to thank my thesis advisor, Professor Ian Waitz, for his leadership, guidance, support, and encouragement throughout my academic career which was invaluable to my learning experience. I would also like to thank Steve Lukachko for his constant advice and assistance during my work on this project. I am also grateful to the remainder of the research team at Aerodyne Research Inc., Dr. Richard Miake-Lye, Dr. Robert Brown, and Dr. John Zhang who also provided substantial guidance and advice throughout this work. Thanks to Chowen Wey and Nan-Suey Liu at NASA for their support in our research endeavors.

Thanks to Professor Dawes, Caleb Dhanasekeran, Albert Demarnge, and the staff at the Whittle Laboratory at Cambridge University for their cooperation, generous hospitality during my visits, and assistance with my research questions. I am also indebted to Chris Wilson, Michel Whiteman, and Andrew Clague at DERA for answering numerous requests for data and providing considerable advice. I also owe thanks to Professor Fred Dryer and Mark Mueller at Princeton University for contributing data and being supportive during the course of this work. Of course, thanks to the staff of the Gas Turbine Laboratory, especially Paul Warren and Lori Martinez.

I appreciate the time and consideration offered by my thesis reader, Professor Ahmed Ghoniem. Also, thanks to Leslie Regan for her support and who has been especially helpful throughout my stay as a graduate student.

I am very grateful to Electro-Motive Division of General Motors, especially Ed Cryer, Kelly Jones, Jim Korenchan, Paula McGhee, Tom Savage, John Zagone, and the people I have worked with in the Turbocharger Design Group and Mechanical and Analytical Group for the support and encouragement they have given me. I would especially like to thank Jim Heilenbach for being a mentor throughout my studies.

The friends I have made during my stay in Boston will never be forgotten. I would like to thank all my friends at the GTL, including Dongwon Choi, Taek-Jin Choi, Keith Dalbey, Rick Francis, Jeff Freedman, Yifang Gong, Joe Lee, Shengfang Liao, Hyung-Soo Moon, Nick Savoulides, Brian Schuler, Patrick Shum, Bobby Sirakov, Chris Spadaccini, Zolti Spakovszky, Jessica Townsend, Yang Tzeng, Bret Van Poppel, Sanith Wijesinghe, and Duc Vo. It has been great working and having fun with all of you. Special thanks to Dan Kirk, Jin-Wook Lee, Sumita, Jon Protz, Chris Protz, and Chris Spadaccini for all the great times we have had together.

Also, thanks to all the other friends I have made in Boston, especially Sylwia Daniszewska, Leonard Dvorson, Randal Guendel, Olivier Kahwati, Alexandra Porter, and Nora Sasz.

Also, thanks to all my close friends from home, especially Ed Cortez, Steve Gibbs, Ted Glaser, Susan Loo, Beth McCauley, Michele Rickerson, and Vince Rimkunas. The tremendous support and encouragement I have received from all my friends has helped me immensely.

Thanks to Joe Contrada and the staff and patrons of the Muddy Charles Pub for all the great times I had there. Thanks to Trudy Moris and the Edgerton desk staff, it was a pleasure working with you all.

Finally, most of all I would like to thank my family. My grandparents Anthony and Betty Chobot and Lucille Bekavac. My close relatives in the Blaszynski, Karhoff, Nieckula, Bekavac, Smyth, Jurcev, Merigold, Diehl, and Byrne families.

My sister and brother-in-law Anne and Edson and my nephew Edson Jr. My brother Andrew and my sister Aimee. They have given me so much love and support throughout my lifetime, I owe many of my accomplishments to them.

This thesis is dedicated to my mother and father, Anthony and Angela.

This work was supported by NASA under grant number NAG3-2179 and was a joint project between the MIT Aero-Environmental Research Laboratory and Aerodyne Research, Inc.

TABLE OF CONTENTS

LIST OF TABLES

LIST OF FIGURES

NOMENCLATURE

ACRONYMS:

AEAP	Atmospheric Effects on Aviation Project
AR	Area Ratio
ASE	Advanced Subsonic Engine
ATOL	Absolute Tolerance
CAD	Computer Aided Design
CIAP	Climatic Impact Assessment Program
CFD	Computational Fluid Dynamics
DERA	Defence Evaluation and Research Agency
DOT	Department of Transportation
EI	Emissions Index
HPT1	High Pressure Turbine – Stage 1
HPT2	High Pressure Turbine - Stage 2
HSCT	High Speed Civil Transport
hv	photoelectric energy
in-situ	in-flight
IPCC	Intergovernmental Panel on Climate Change
L/D	Length to Diameter Ratio
LPT1	Low Pressure Turbine – Stage 1
LPT2	Low Pressure Turbine – Stage 2
MIT/ARI	MIT and Aerodyne Research Inc. team
NASA	National Aeronautics and Space Administration
NGV	Nozzle Guide Vanes
ODE	Ordinary Differential Equation
R-K	Runge-Kutta
RMS	Root Mean Square
RTOL	Relative Tolerance
SST	Supersonic Transport
TE	Trailing Edge
UARP	Upper Atmosphere Research Program
UMR	University of Missouri – Raleigh Team
VPFR	Variable Pressure Flow Reactor

ROMAN:

c	Chord
c_p	Specific heat at constant pressure
D	Diameter
ds	Differential length along curve
L	Length
M	Mach number
$\dot{m}$	Mass flow rate

P	Pressure
R	Universal Gas Constant
r	Radius
s	Spacing
T	Temperature
t	Time
V	Velocity
u	Time average x component of velocity

PARAMETERS:

Da	Damköhler Number
$\Delta S(VI)$	Severity Parameter for sulfur six
Re	Reynolds Number, $\rho uA/\mu$
σ	Solidity parameter (c/s)
δ_t	Deviation

GREEK:

β	Flow Angle
Δ	Change in a quantity
ϕ	Equivalence Ratio
γ	Ratio of specific heats
η	Combustion Efficiency
η_{poly}	Polytropic Efficiency
μ	Coefficient of thermal viscosity
π	Pressure Ratio
ρ	Density
τ	Characteristic time scale, or Temperature Ratio
ωr	Tangential velocity of rotor

SUBSCRIPTS:

a	Axial
c	Centerline
e	Exit
d	diameter
max	Maximum
min	Minimum
o	Stagnation
r	Radial
T	Total
t	Throat, or tangential
x	In x-direction
y	In y-direction
z	In z-direction

1 INTRODUCTION

Aviation is currently the fastest growing transportation sector. Trace species emitted by aircraft directly into the upper atmosphere are believed to have an enhanced influence relative to other common emissions generated by human activity near the surface of the earth. Therefore, research efforts to understand the role of aircraft gas turbine engine emissions in global climate change and the mechanisms by which these emissions are produced have been amplified. Of particular interest are trace chemical constituents, which are understood to be particularly influential in affecting local air quality and the global atmosphere. The Atmospheric Effects of Aviation Project (AEAP), created by NASA to study the influence of aviation on the global atmosphere, initiated the effort to develop a model to predict the evolution of trace species in the post-combustor flow path of gas turbine engines. The work contained in this thesis is part of an ongoing research effort aimed at gaining accurate and informative data on these trace chemical species. Ultimately, a modeling methodology was developed and applied to a research engine in support of an engine test program being conducted for the project. A computational model which can predict the evolution of trace species within gas turbine engines is an essential tool which can be used to help understand intra-engine trace species evolution. The model can be used to investigate how the operating parameters and design characteristics of gas turbine engines affect their emissions. It can also help provide a physical understanding of trace species evolution and could be used to direct the development of new engine technologies that reduce aviation emissions.

1.1 CHAPTER OVERVIEW

The purpose of this chapter is to give a short introduction to aircraft emissions and their potential impacts on the local and global atmosphere. A brief history of the research on atmospheric effects of aviation is described. The composition of aircraft exhaust emissions is explained, the origins of a few trace species are presented, and a description of the exhaust deposition process is given. A few climatic and ozone effects are highlighted, with further details for subsonic and supersonic aircraft given. An overview of prior work to characterize trace species emissions is presented, including work done in near field plume and wake modeling and turbine and exhaust nozzle modeling. The importance of trace species modeling in the turbine and exhaust nozzle is established by several previous studies, which gives motivation for the current research. This chapter also lists the overall objectives and contributions of the current research effort which serves as a thesis roadmap.

In summary, the following are the main points of the chapter:

- Aircraft emissions can impact the environment both locally and globally and future growth in aircraft fleets is expected to increase these effects, thus it is desirable to obtain an understanding of aircraft emissions and effects of these emissions on the atmosphere. See the IPCC report [2], "Aviation And The Global Atmosphere," for detailed background information related to this thesis topic.

- Two main environmental effects of aviation emissions are changes in radiative forcing and ozone depletion, which can occur directly or indirectly. A few examples are: changes in ozone concentrations due to photochemical processing of emissions, changes in local radiative forcing due to NO_x and SO_x emissions, or formation of persistent contrails and clouds due to soot and sulfate particle emissions. Trace species from engine exhaust are important to characterize since they are involved in chemical reactions that affect the environment.

- The region of the atmosphere where emissions are deposited determines their effects on the atmosphere. A decrease in the ozone concentration in the upper and middle stratosphere leads to global warming whereas a decrease in ozone in the upper troposphere/lower stratosphere leads to global cooling. Overall, subsonic and supersonic aircraft emit species which causes formation and destruction of ozone that impacts the earth-atmosphere system in the direction of global warming.

- Prior work has involved modeling and measuring trace species in the near field plume and wake of an aircraft and computational fluid-chemical modeling in the intra-engine environment. Results suggest that most trace species chemistry occurs early, thus there is a need for better characterization of trace species in the intra-engine environment. See the thesis by Lukachko [1], "Research on the Science And Politics of the Atmospheric Effects of Aviation Debate," for more background and preliminary work on intra-engine modeling.

- Computational modeling is an efficient means to acquire detailed information about intra-engine trace species chemistry since experimental techniques are complicated, time consuming, and expensive.

- The contributions of this thesis include:

    - Continued development the post-combustor trace species modeling methodology
    - Improvements to modeling tools
    - Continued validation of the model and improvements to the modeling tools
    - Performed the first complete post-combustor engine simulation to support an engine test campaign
    - Investigation of a few physical phenomena which influence trace species evolution

    They are aimed at further characterization of aircraft emissions, in particular modeling the evolution of trace species in the post-combustor flow path of gas turbine engines.

Section 1.2 gives an overview of aircraft exhaust emissions, where these emissions are deposited, and the effects of both subsonic and supersonic aircraft exhaust emissions on the environment. Section 1.3 reviews some prior work on emissions characterization, speciffically near field plume and wake modeling and turbine and exhaust nozzle modeling. Section 1.4 discusses the motivation for the work and lists the contributions of this thesis. Section 1.5 is the chapter summary.

1.2 ATMOSPHERIC EFFECTS OF AVIATION

Aircraft emissions can impact the environment both locally and globally. The aviation industry is becoming a more significant part the world economy, in terms of both commercial and military activity, and it contributes to these atmospheric effects primarily via the emissions released from gas turbine engines. Future growth in aircraft fleets is expected to increase these effects [3]. Therefore, a complete understanding of aircraft emissions and effects of these emissions on the atmosphere is necessary in assessing the current and possible future effects of aircraft. The need to characterize trace species evolution has been heightened because trace species concentrations are known to change through the post-combustor gas path of the engine (turbine and exhaust nozzle), exhaust plume, and aircraft wake prior to deposition in the atmosphere. These processes collectively govern the impact of engine exhaust which can affect the global climate. Although there is still uncertainty surrounding the effects of emissions impacts on the global climate, a number of scientific and technological investigations have helped clarify the issue. The following sections discuss the reasons for focusing on aviation emissions, provide a brief overview of potentially influential aircraft emissions, describe atmospheric deposition, and highlight impacts of both subsonic and supersonic aircraft on the atmosphere.

The history of research on this issue dates back to the 1972, when the US Department of Transportation commissioned the Climatic Impact Assessment Program (CIAP) to record all the scientific research on the effects of aviation on the atmosphere up to that date. After CIAP was completed in 1975, NASA became the primary agent for atmospheric research and its Upper Atmosphere Research Program has been active ever since. NASA's research has also been incorporated into reports of the Intergovernmental Panel on Climate Change (IPCC) [2]. In 1988, the AEAP was established to comprehensively predict the atmospheric impacts of future aircraft. The program is a collaborative effort between several government agencies, academic institutions, and industry which was created to study the influence of aviation on the global atmosphere.

The IPCC report [2], entitled "Aviation And The Global Atmosphere," is the most comprehensive source of detailed background information related to this thesis topic. This chapter highlights a few of the relevant topics, refer to the original report for more information.

1.2.1 AIRCRAFT EXHAUST EMISSIONS

Understanding the effects of aircraft emissions upon the atmosphere requires knowledge of the chemical species emitted from aircraft engines and the region of the atmosphere in which they are emitted. Nitrogen (N_2), carbon dioxide, (CO_2), water vapor (H_2O), and unconsumed oxygen (O_2) (for fuel-lean reactions) constitute the primary exhaust constituents. The trace components consists of nitrogen oxides (NO_y), carbon monoxide (CO), hydrocarbons (HC), sulfur oxides (SO_x), soot, and radical species such as atomic oxygen (O) and hydroxyl (OH) to name a few. Engine operating conditions and the effects of flow-chemistry interactions in the combustion process impact many of these species. For example, combustion efficiency is never 100% and other products form as a result of finite-rate kinetic reactions. Significant amounts of NO_y can result from high temperature combustion in air. Concentrations of CO, HC, and soot are greater than at their equilibrium because of inadequate oxidation before leaving the combustor. Hydrocarbon fuels typically contain some sulfur, which is where the trace exhaust constituents in SO_x family originate. Figure 1.1 shows a summary of typical combustion products and Table 1.1 gives typical emissions indices for gas turbine engines.

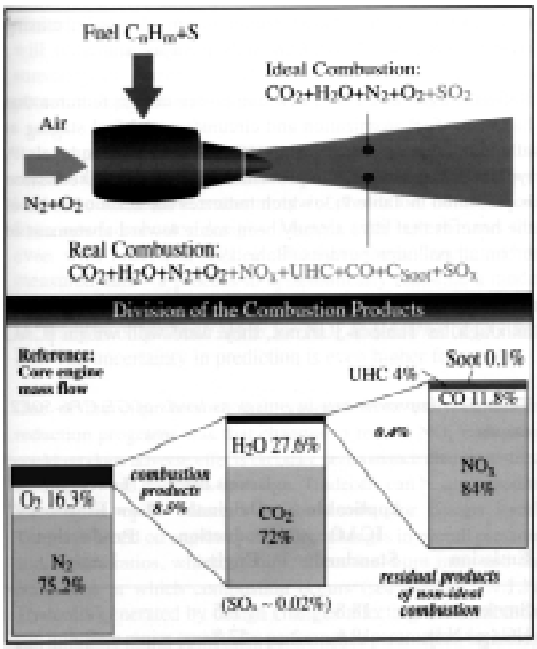

Figure 1.1 Summary of combustion products [3]

	Operating Condition		
Species	**Idle**	**Take-Off**	**Cruise**
CO_2	3160	3160	3160
H_2O	1230	1230	1230
CO	25 (10-65)	< 1	1-3.5
HC (as CH_4)	4 (0-12)	< 0.5	0.2-1.3
NO_x (as NO_2)	3-6	10-65	7.9-15.4
SO_x (as SO_2)	1	1	1

Table 1.1 Typical emission index levels (g/kg fuel) [3]

The exact concentrations of the species emitted from the engine are difficult to determine since each combustor behaves differently, and an efficient scheme for collecting accurate data is yet to be established. The levels of the trace species NO_y and SO_x emitted at the engine exit plane are kinetically determined by the amount of time spent in each section of the flow path and the time variability of the temperature and pressure histories realized through the engine (from combustor to the exhaust nozzle). Therefore, the engine specifications and thermodynamic cycle have a direct effect on the emissions. For example, higher temperatures result in greater radical concentrations at the engine exit [1].

1.2.2 ALTITUDE DEPOSITION PROCESS

The area of the atmosphere in which emissions are deposited determines the effects they have upon the atmosphere. Aircraft emissions are released at altitudes ranging from the lower troposphere into the middle stratosphere. The troposphere is the region of the atmosphere located between the ground and about 10 to 15 km (thinner in polar regions and thicker of the equator), the stratosphere is located between the altitudes of 10 to 15 km to about 50 km, and the tropopause is the area dividing these regions. Typical subsonic aircraft operate primarily in the upper troposphere and the lower stratosphere, while supersonic aircraft, such as the Concorde or military aircraft, fly in the middle stratosphere, the exact height being a function of the design Mach number.

When exhaust first exits an aircraft engine, it enters a region termed the near-field plume region, where the engine plume and the aircraft wake do not interact. The initial, turbulent shear induced dispersion of the exhaust jet is more important than any aerodynamic perturbation from the aircraft. Eventually, as the momentum of the exhaust plume is diffused, the vorticity shed from the aircraft wings begins to influence the jet plume. In this wake vortex region, the plumes are entrained and confined in the two counter-rotating tip vortices formed by the self-induced vortex sheet roll-up of the aircraft wake. This structure, at cruise altitude, sinks about 100 m for subsonic aircraft and several hundred meters for supersonic aircraft through a self-induced downwash. After a certain amount of time, the structure begins to deteriorate and break up due to

hydrodynamic instabilities. A residual turbulent atmospheric perturbation is left over after dissipation and the exhaust is free to mix with the atmosphere [1].

1.2.3 CLIMATIC AND OZONE EFFECTS

The two main effects of aircraft emissions deposited at altitude are changes in radiative forcing and ozone depletion, which can occur directly, when the emitted compound is the species that can modify the climate, or indirectly, where the climate altering species is a byproduct of atmospheric reactions involving the emitted species. Aircraft emissions are concentrated mostly in regions where heavy airplane traffic ensues, namely North America, over the North Atlantic, and Europe. Table 1.2 summarizes the effects of aircraft emissions that are important to the atmosphere. The impact of these emissions depends on the relative change they induce in the background atmosphere and on their role in atmospheric photochemical, dynamical, and radiative processes. Photochemical processing of these emissions can affect ozone and other important species. Climate change may result from changes in concentrations of radiatively important species, formation of contrails, or changes in clouds caused by aircraft emissions.

Emitted Species	Region of Atmosphere	Major Effect at Earth's Surface
CO_2	Troposphere	Direct radiative forcing ⇒ global warming
	Stratosphere	
H_2O	Troposphere	Direct radiative forcing ⇒ warming Increased contrail formation ⇒ radiative forcing ⇒ warming
	Stratosphere	Direct radiative forcing ⇒ warming Enhanced PSC formation ⇒ O3 depletion ⇒ enhanced UV-B Modifies O3 chemistry ⇒ O3 depletion ⇒ enhanced UV-B
NO_x	Troposphere	O3 formation in upper troposphere ⇒ radiative forcing ⇒ warming ⇒ reduced UV-B Decrease in CH-4 ⇒ less radiative forcing ⇒ cooling
	Stratosphere	O3 formation below 18-20km ⇒ reduced UV-B O3 formation above 18-20km ⇒ enhanced UV-B Enhanced PSC formation ⇒ O3 depletion ⇒ enhanced UV-B
SO_x and H_2SO_4	Troposphere	Enhanced sulfate aerosol concentrations Direct radiative forcing ⇒ cooling Contrail formation ⇒ radiative forcing ⇒ warming Increased cirrus cloud cover ⇒ radiative forcing ⇒ warming Modifies O3 chemistry
	Stratosphere	Modifies O3 chemistry
Soot	Troposphere	Direct radiative forcing ⇒ global warming Contrail formation ⇒ radiative forcing ⇒ warming Increased cirrus cloud cover ⇒ radiative forcing ⇒ warming Modifies O3 chemistry
	Stratosphere	Modifies O3 chemistry

Table 1.2 Effects of species contributing to climate change [2]

The exact impact of these emissions on the climate is hard to attribute to a particular source, but they can be compared to each other and to climate effects from other sectors by using the concept of radiative forcing.

Radiative forcing is a measure of the importance of a potential climate change mechanism. It expresses the perturbation or change to the energy balance of the earth-atmosphere system in watts per square meter (W/m^2). Positive values of radiative forcing imply a net warming, while negative values imply cooling. Figure 1.2 shows the radiative forcing from different aircraft emissions in 1992 and a projection for 2050.

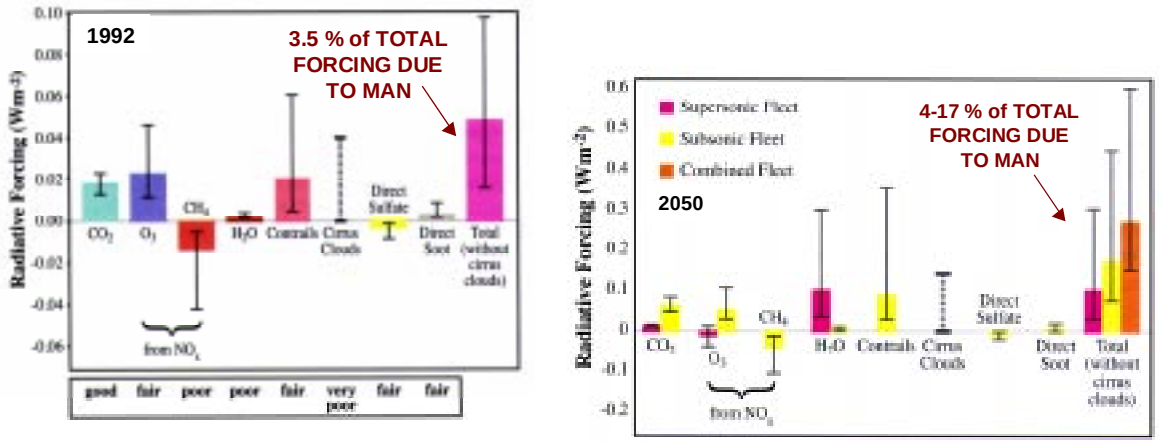

Figure 1.2 Radiative forcing of various trace species [2]

The impacts of CO_2 are well known due to its long atmospheric residence time (~100 years). It becomes well mixed throughout the atmosphere and thus the effects of its emission from aircraft are impossible to differentiate from the same quantity of carbon dioxide emitted by any other source [3]. Emissions such as NO_x, SO_x, and water vapor have shorter residence times and remain concentrated near the aircraft. Thus they lead to changes in radiative forcing localized near the flight route as opposed to emissions that are globally mixed.

Increases in particles emitted from aircraft have mixed effects: soot tends to warm the earth's surface, while sulfate particles tend to cool it. While direct effects of these particles are believed to be small, increases in their emissions by jet aircraft may potentially influence the formation of clouds and contrails, thin white-line clouds seen behind jet aircraft in the upper atmosphere, which may contribute to future climate change [4].

It is difficult to discern the impact of aircraft emissions upon changes in ozone concentration since a decrease in the ozone in the upper and middle stratosphere lead to global warming whereas decreases in ozone in the upper troposphere/lower stratosphere lead to global cooling. In addition, supersonic aircraft, flying in the middle stratosphere, emit species that lead to the destruction of ozone whereas subsonic aircraft, flying in the upper troposphere/lower stratosphere, emit species that lead to the formation of ozone. This formation and destruction of ozone along with emission of species such as CO_2 and H_2O impact the radiative balance of the earth-atmosphere system in the direction of global warming [1].

1.2.3.1 SUBSONIC AIRCRAFT EFFECTS

Subsonic aircraft emissions are emitted mainly in the troposphere region, and affect chemical and radiative processes that determine the concentration of tropospheric ozone. Precise effects are difficult to determine because the troposphere region is not well understood and accurate data is difficult to obtain. However, estimates indicate that present subsonic aircraft operations may have increased NO_x concentrations at upper tropospheric altitudes in the North Atlantic flight corridor by about 10 to 100%, water vapor concentrations by about 0.1% or less, SO_x by about 10% or less, and soot by about 10% compared with the atmosphere in the absence of aircraft and assuming all aircraft are flying below the tropopause [5].

There is much imprecision in the data gathered about NO_x. The uncertainty in NO_x emissions is related to the relative magnitude of the aircraft source compared to lightning, rapid vertical conversion of surface NO_x from other human activities such as industrial sources and vehicular traffic, and other sources of tropospheric NO_x. However, it is known that NO_x is more damaging in the troposphere relative to the ground. There is 20 times more ozone created per unit NO_x in the troposphere and the radiative forcing is 30 times more sensitive relative to the ground [1]. Ozone is created in the troposphere when there is an abundance of NO_x and increases in NO_x also affect this region of the atmosphere in a photochemically-induced catalytic chemical cycle which is calculated to increase the concentration of hydroxyl (OH) radicals by a few percent throughout the Northern Hemisphere. This OH change results in a decrease in the concentration of methane and because this chemical process is part of the same chemical processes that increases ozone, calculated CH_4 and ozone effects are correlated. Other potentially impacting trace species in the SO_x family have effects in the lower stratosphere through direct cooling associated with enhanced sulfate aerosols. In the troposphere, aerosol enhancement can lead to the formation of persistent contrails and can enhance or initiate cirrus cloud formation, which both have direct implications for radiative forcing and for atmospheric photochemistry.

In the lower stratosphere, water vapor emissions can build up and lead to higher concentrations which can enhance the formation of contrails that are expected to warm the earth's surface. In addition, extensive cirrus clouds have been observed to develop after the formation of persistent contrails. The increases in cirrus cloud cover have been positively correlated with aircraft emissions in a limited number of studies. On average, an increase in cirrus cloud cover also tends to warm the earth's surface [4].

Aircraft emissions such as CO_2 and NO_x in the troposphere have potential to influence climate changes. Current emissions of carbon dioxide from aircraft are 2.5% of the total emissions from fossil fuel use. Over the last 30 years, aircraft have contributed about 1.5% of the industrial increase in atmospheric carbon dioxide, or approximately 0.5 ppmv (parts per million by volume). In equilibrium this would lead to a calculated surface air temperature change of approximately 0.007 °C [6]. NO_x emissions are estimated to have the same effect as that of CO_2, and as NO_x and carbon dioxide increase in the future the climate response will increase as well.

Global warming due to ozone and water vapor in the upper troposphere/lower stratosphere altitudes is greater than at the surface due to low background concentrations, longer residence times, and large radiative efficiency near the tropopause as compared to the surface.

1.2.3.2 SUPERSONIC AIRCRAFT EFFECTS

Supersonic aircraft fly in the middle stratosphere, near the peak concentration of atmospheric ozone, the exact height being a function of the design Mach number. Figure 1.3 shows the variation of ozone concentration with altitude. The peak ozone range of Mach 2.4 to 4 is where the most recently proposed US high speed-speed civil transport (HSCT) designs operate.

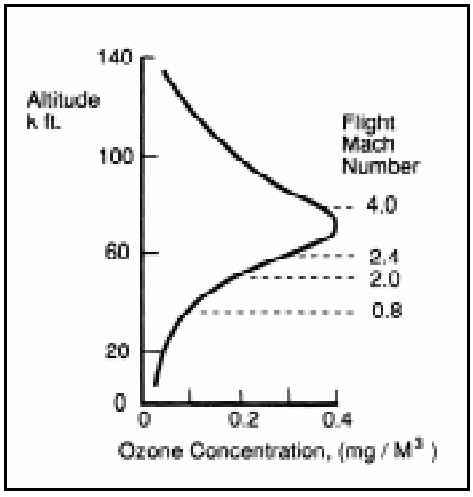

Figure 1.3 Variation of ozone concentration with altitude [7]

NOx is the trace species that is the most significant contributor to the reduction of ozone, by the following catalytic cycle [7]:

$$NO + O_3 \rightarrow NO_2 + O_2$$

$$NO_2 + h\nu \rightarrow NO + O_2$$

and

$$NO_2 + O \rightarrow NO + O_2$$

In this cycle, no NO is destroyed, but O_3 is combined with O to form O_2. This problem was first publicized in 1971, when Johnston (1971) calculated that emissions of oxides of nitrogen from a fleet of five hundred supersonic transport aircraft flying at an altitude of 20 kilometers could reduce stratospheric ozone by a global average of 10 to 20 percent [8].

The abundance of NO_x is also determined by reactions on sulfate aerosols composed of sulfuric acid (H_2SO_4) and water (H_2O). Observations show that the concentration of NO_x falls in response to increases in aerosol surface area. Because increases in sulfur, water vapor, and soot from HSCT emissions will change the surface area, composition, and number of particles in the lower stratosphere, the emissions indirectly influence ozone loss rates. In low-temperature regions near the poles, both liquid and frozen aerosols form that contain nitric acid (HNO_3) in addition to H_2O and H_2SO_4 [9]. Sulfate aerosol (SO_x) may considerably alter chemical and physical processes in the stratosphere, by possibly increasing ozone destruction and perhaps leading to direct and indirect radiative effects associated with increases in background aerosol, the formation of persistent contrails, and the enhancement of cirrus clouds. SO_x, soot, and water all contribute to changes in atmospheric aerosol characteristics, thus having the effect of increasing heterogeneous chemical activity and of altering the probability of polar stratospheric cloud formation.

Climate changes in the stratosphere are very hard to predict given the complexity of the global atmosphere. For a fleet of HSCT aircraft, climate can be affected by changes in the abundance of water vapor, soot, or sulfate in the stratosphere. Climate can also be affected by changes in cirrus cloud properties or by the radiative consequences of changes in ozone and its vertical distribution.

1.3 PRIOR WORK

Before discussing the specific contributions of this thesis, prior contributions to the assessment of trace species emissions are discussed. A brief account of trace emissions characterization through experiments and modeling is presented.

1.3.1 GENERAL TRACE EMISSIONS CHARACTERIZATION

Trace species are important because SO_x and NO_y families have acids and radicals that play a role in aerosol formation and oxidation processes leading to acid formation. The short-lived nature of several chemical processes involving trace species emphasizes the importance for understanding the near-field region of the aircraft where concentrations of trace species are determined primarily by atmospheric perturbations caused by the aircraft. Modeling is important because detailed experimental tests within the engine necessary for understanding trace species evolution are difficult and limited in informational content. In addition to understanding the evolution of exhaust and trace species within the engine, knowledge of the downstream fate of trace emission constituents in the aircraft plume and wake also provides a reference for modeling upstream within the engine, particularly in choosing appropriate chemical models and in focusing on the evolution of certain important species.

The chemistry that occurs during the deposition process in the plume and wake regions occurs at higher temperatures (500 to 600 K) than atmospheric (200 to 300 K), but lower than the temperatures encountered during the combustion process. At these temperatures, the inclusion of heterogeneous chemistry and dynamics for aerosol formation within the overall processing mechanism is necessary. Primary pollutant and trace species are highly active in the atmosphere, involving both gas-phase and heterogeneous chemistry. The hydroxyl (OH) radical, emitted either with the exhaust stream or formed by photochemical breakdown of atmospheric or exhaust constituents (O_3, H_2O) initiates and propagates several reactions including gas phase conversions of NO_x to NO_y which occur in general though the reactions:

$$NO + OH + M \leftrightarrow HNO_2 + M$$

$$NO_2 + OH + M \leftrightarrow HNO_3 + M$$

$$NO_2 + O \leftrightarrow NO_3 : NO_2 + NO_3 + M \leftrightarrow N_2O_5$$

Water vapor also has an important role. The primary SO_2 gas phase oxidation reactions are:

$$SO_2 + O + M \leftrightarrow SO_3 + M$$

$$SO_2 + OH + M \leftrightarrow HSO_3 + M : HSO_3 + O_2 \leftrightarrow SO_2 + SO_3$$

$$SO_3 + H_2O \leftrightarrow H_2SO_4$$

Competition for the O and OH radical also occurs with the conversion of CO to CO_2 via the reactions:

$$CO + OH \leftrightarrow CO_2 + H$$

$$CO + O + M \leftrightarrow CO_2 + M$$

The gas phase chemistry consists of other conversion processes, most notably the inevitable conversion of NO to NO_2. Oxidation with the HO_x family can occur in many different ways including reactions with O and H.

Oxidation of SO_2 to SO_3 and H_2SO_4 is of greater interest to modeling and exhaust sampling now since studies have shown that increases in SO_3 concentration lead to higher total aerosol surface area, and greater activation of soot particles. The enhancement of aerosols, as mentioned before, can have important consequences for ozone and climatic impacts. Gas phase species such as N_2O_5 and NO_3 and SO_3 are readily converted in the presence of water containing aerosols to form aqueous HNO_3 and H_2SO_4.

1.3.2 NEAR FIELD PLUME AND WAKE MODELING

Most in-situ and stationary measurements have been done for subsonic aircraft. These efforts concentrated on chemical activity occurring outside the engine, while only a limited understanding could be gained about the

chemical processes occurring in the plume and wake regions. These tests indicated that some important chemistry occurred within the engine, specifically in the post-combustor regime. Fluid-chemical computational models also supports the importance of intra-engine modeling in the assessment of aircraft engine emissions.

Most computational modeling efforts concentrated on chemical-flow interactions outside the engine in the near-field plume and wake vortex regions, since it is difficult to take experimental samples using in-situ measurements. The modeling helped determine local atmospheric effects, exhaust dispersion in the atmosphere, and more recently important factors in the formation of aerosols [12], [13], [14],[15], and [16].

The first fluid-chemical flow models were presented by Quackenbush et al. [17] for the high-speed civil transport aircraft. Quackenbush used an 18 species and 12-reaction mechanism for SO_x oxidation to show that fluid mechanical effects are important to the chemical evolution of trace species. Miake-Lye et al. [13] also computed the post-engine fluid-chemical evolution by incorporating a simple one dimensional computation to simulate changes that occur within the post-combustion sections of the engine in an attempt to establish more appropriate initial conditions at the engine exit plane. Brown et al. [14] provided a more detailed study of the near-field plume region, modeling both gas phase chemistry and aerosol dynamics to understand the nucleation process in the exhaust plume and these studies, as well as others [18],[19] are based on several assumptions about exhaust composition within the engine. Also, many times the turbine and exhaust nozzle are neglected or are treated through simple, 1D, averaged, passive chemistry calculations based on specified flow parameters [12].

The results from these models described above suggest that most trace species chemistry occurs early, and is less affected by the atmosphere or fluid mechanical perturbations in the plume and wake than which occur in the engine. The conclusions also indicate the need for better characterization of the trace species, especially in the intra-engine environment.

1.3.3 TURBINE AND EXHAUST NOZZLE MODELING

Most efforts to understand chemical evolution in the post-combustor flow path, namely the turbine and exhaust nozzle, have been performed by Lukachko [1]. However, previously some work was done that suggested the importance of intra-engine modeling. One study [13] compared equilibrium and non-equilibrium evolutions from the combustor exit to show the kinetic effects that occur downstream of the combustor are important. In this study OH levels were found to be about twelve orders of magnitude higher than an equilibrium calculations at the nozzle exit. Also, other studies have considered the potential impact of intra-engine heterogeneous chemistry (soot, internal engine surfaces) on trace species chemistry [14] and the evolution of chemiions through the turbine and exhaust nozzle [12]. The results from these post-combustor characterization efforts point towards the need for additional study.

The research by Lukachko [1], entitled "Research on the Science And Politics of the Atmospheric Effects of Aviation Debate," is a primary source of work on turbine and exhaust nozzle modeling. The research performed in this thesis is an extension of the work by Lukachko. Lukachko also presents a more detailed summary of other prior work on intra-engine modeling. Refer to the original document for more information related to this section.

1.4 MOTIVATION

As discussed in Section 1.2, important chemical reactions occur in the post combustor flow path which potentially alter the trace species concentration at the nozzle exit plane. Trace species play an important role in the problem of emissions characterization because SO_x and NO_y families have acids and radicals that influence aerosol formation and oxidation processes, which effect the processes that occur outside the aircraft and on a global scale.

The two principal components in the efforts to characterize aircraft emission are physical tests and analytical modeling. Combustor emissions data is gathered using uninstalled combustor-only and full-scale engine tests. Full-scale engine tests at altitude conditions are the most relevant, so some tests have been performed in-flight (in situ). However, in-flight experiments are limited in accuracy due to the distances that must remain between the two aircraft. From combustor-only tests and full-scale engine tests, useful data can be gathered to determine the products that travel though the turbine and exhaust nozzle. There has been few stationary tests preformed to measure NO_x, CO and HC [10], [11]. Corrections such as those for humidity and other ambient conditions must be applied to make the test results comparable to each other.

All the above approaches are valid, but there are even more complexities within a combustor. A diversity of both reactants and products of combustion are involved in hundreds of simultaneous reactions. So while the aforementioned species are the majority of the resulting compounds, there are many minor constituents that exist in very small, trace amounts. These species form because of the non-equilibrium chemical state of the exhaust gas and include the hydroxy family (HO_x), nitrogen compounds (NO_y), and the sulfur oxide family (SO_x). These species are emitted at the engine exit plane in levels that are kinetically determined, governed by the time variability of temperature and pressure histories realized within the combustor and through the turbine and exhaust nozzle of the engine as well as the amount of time spent in any particular section of flow path. Therefore, the thermodynamic cycle on which a particular engine is based will have a direct effect on these emissions. Higher temperatures generally result in greater radical speciations and less oxidation progress at the engine exit.

Due to lack of suitable test opportunities and adequate instrumentation only limited data has been acquired. Since experimental testing is expensive and time consuming, computer modeling is an efficient method for trace

emissions characterization. Due to the complexities of taking measurements within the engine, computational modeling in the turbine and exhaust nozzle flow path is especially useful. Using computer modeling several engine design iterations can be analyzed quickly and cost effectively to find the most effective engine geometry to reduce potentially dangerous emissions.

1.4.1 OBJECTIVES AND CONTRIBUTIONS

This thesis continues the efforts towards emissions characterization and understanding the processes which influence emissions initiated in [1], [2], [12], [28], and [58] by extending the computational modeling techniques and performing relevant simulations which can give insight into parameters which affect gas turbine engine emissions.

There are five main areas of contribution, (1) further development of the post-combustor trace species modeling methodology, (2) improvements to the modeling tools, (3) continued validation of the model and the improvements to the modeling tools, (4) to perform the first complete post-combustor engine simulation, specifically in application to an engine test to be conducted as a collaboration effort between NASA and DERA, and (5) to investigate some physical phenomena which can influence trace species evolution.

1.4.2 THESIS OVERVIEW

The following sections serve as a outline for the remainder of this thesis. Section 2 describes the modeling methodology developed to simulate intra-engine trace chemistry. A few modeling elements are listed and the modeling procedure is discussed. This section gives the details of a time scale analysis and the chemistry initial conditions procedure. Section 3 describes the modeling tools and some improvements made to them during the current research period. Section 4 discusses several validation exercises. A simulation of Princeton University's variable pressure flow reactor was attempted to benchmark the accuracy and test some new features of the modeling tools. A simulation of the Cambridge No 2 turbine rotor was used for a comparative study of several reaction mechanisms. Also, a study was performed on the chemistry convergence criteria and the periodic boundary conditions. Section 5 applies the modeling methodology to an engine test for a first of its kind analysis. The simulation of the NASA/DERA engine provides some insight into the effects of several flow phenomena on the evolution of trace species in the post-combustor flow path of the engine. The thesis concludes with an overall summary in Section 6. The appendix contains the detailed analysis of the Princeton flow reactor simulation, the chemical mechanism recommended for future turbine chemistry work, an analysis used to extract fluid boundary conditions for high fidelity modeling of the engine test, a complete set of results and input files for one condition modeled for the engine test, and a index for a CD containing additional results from this research.

1.4.2.1 MODELING METHODOLOGY

A modeling methodology was developed to simulate trace species evolution in the post-combustor flow path of a gas turbine engine. The methodology involves a fundamental time scale analysis which can help guide the overall modeling strategy and provide insight into the mechanisms influencing trace species evolution. The methodology includes specifying chemical initial conditions, fluid boundary conditions, and performing numerical solutions to the fluid mechanics and chemical kinetics problems at various levels of detail using either high fidelity, low fidelity, or a combination of modeling techniques. Key parameters affecting levels of intra-engine trace species were identified and incorporated into the model thereby improving the accuracy and increasing the efficiency of the model.

1.4.2.2 MODELING TOOLS

Usability and modeling accuracy improvements to the existing modeling tools were made, which included:

- incorporating a 3D fully unstructured grid generation tool which allows simulations of complex arbitrary geometries
- adding multiple inlet/exit capability which allows simulation of mixing flows
- adding parallel chemistry routines to improve execution time
- refining circumferentially varying unsteady inlet conditions to improve modeling accuracy and further investigate the effects of flow non-uniformity on chemistry
- improving chemistry initial condition specification procedure
- adopting improved chemistry convergence criteria
- selecting a new chemical mechanism which incorporates new kinetic data for sulfur chemistry provided by Princeton University

1.4.2.3 VALIDATION

Some model limitations were established through a validation exercise that attempted to model the Princeton University Variable Pressure Flow Reactor. The new grid generator and multiple inlet/exit modifications were demonstrated, but the fluid, mixing, and chemistry modeling could not be validated due to compressibility limits of the code, as well as, the possible unsteady flow regime of the reactor.

Further validation efforts were performed on a representative 1D engine cycle and 2D turbine geometry. They included evaluation of various chemical mechanisms, species convergence criteria, periodic boundary conditions, and the parallel code modifications.

1.4.2.4 MODELING THE NASA/DERA ENGINE TEST

The modeling methodology was applied to an engine to perform the first complete post-combustor engine simulation. Trace species concentrations were predicted at the nozzle exit for several test cases based on an

experimental engine to be tested in a joint effort between NASA and DERA. The results of the simulation provided guidance for setting test parameters and planning measurement strategies. The effects of flow non-uniformity, operating conditions, unsteadiness, and some modeling practices on species evolution were assessed.

1.5 CHAPTER SUMMARY

The purpose of this chapter was to give a short introduction to aircraft emissions and their potential impacts on the local and global atmosphere. A brief history of the research on atmospheric effects of aviation was described. The composition of aircraft exhaust emissions was explained, the origins of a few trace species were presented, and a description of the exhaust deposition process was given. A few climatic and ozone effects were highlighted, with further details for subsonic and supersonic aircraft given. An overview of prior work to characterize trace species emissions was presented, including work done in near field plume and wake modeling and turbine and exhaust nozzle modeling. The importance of trace species modeling in the turbine and exhaust nozzle was established by several previous studies, which gave motivation for the current research. This chapter also listed the overall objectives and contributions of the current research effort which serves as a thesis roadmap.

In summary, the following is a list of all relevant points presented in this chapter:

- Aircraft emissions can impact the environment both locally and globally and future growth in aircraft fleets is expected to increase these effects, thus it is desirable to obtain an understanding of aircraft emissions and effects of these emissions on the atmosphere.

- See the IPCC report [2], "Aviation And The Global Atmosphere," for detailed background information related to this thesis topic.

- N_2, CO_2, H_2O, and O_2 constitute the primary exhaust products while NO_y, CO, HC, SO_x, O and OH are a few important trace constituents. The SO_x and NO_y families have acids and radicals that are important in aerosol formation and oxidation processes leading to acid formation.

- Two main environmental effects of aviation emissions are changes in radiative forcing and ozone depletion, which can occur directly or indirectly. A few examples are: changes in ozone concentrations due to photochemical processing of emissions, changes in local radiative forcing due to NO_x and SO_x emissions, or formation of persistent contrails and clouds due to soot and sulfate particle emissions. Trace species from engine exhaust are important to characterize since they are involved in chemical reactions that affect the environment.

- The region of the atmosphere where emissions are deposited determines their effects on the atmosphere. A decrease in the ozone concentration in the upper and middle stratosphere leads to global warming whereas a decrease in ozone in the upper troposphere/lower stratosphere leads to global cooling. Overall, this formation and destruction of ozone impact the earth-atmosphere system in the direction of global warming.

    - Subsonic aircraft affect chemical and radiative processes mainly through emission of NO_x, but also H_2O, SO_x, and soot. These emissions lead to the formation of ozone in the upper troposphere/lower stratosphere.
    - Supersonic aircraft fly in the middle stratosphere near the peak concentration of atmospheric ozone. Through NO_x emissions they lead to the destruction of ozone

- Prior work has involved modeling and measuring trace species in the near field plume and wake of an aircraft and computational fluid-chemical modeling in the intra-engine environment. Results suggest that most trace species chemistry occurs early, thus there is a need for better characterization of trace species in the intra-engine environment.

- See the thesis by Lukachko [1], "Research on the Science And Politics of the Atmospheric Effects of Aviation Debate," for more background and preliminary work on intra-engine modeling.

- Computational modeling is an efficient means to acquire detailed information about intra-engine trace species chemistry since experimental techniques are complicated, time consuming, and expensive.

- The contributions of this thesis include:

    - Continued development the post-combustor trace species modeling methodology
    - Improvements to modeling tools
    - Continued validation of the model and improvements to the modeling tools
    - Performed the first complete post-combustor engine simulation to support an engine test campaign
    - Investigation of a few physical phenomena which influence trace species evolution

    They are aimed at further characterization of aircraft emissions, in particular modeling the evolution of trace species in the post-combustor flow path of gas turbine engines.

2 MODELING METHODOLOGY

The outcomes of this work are several tools which can be used to evaluate and improve the design of gas turbine engines with respect to trace species emissions as well as investigate the effects of various fluid or chemical parameters on the evolution of trace species. Section 1.4 detailed the motivation and advantages of modeling the evolution of species in the post-combustor flow path. In many cases, the numerical tools can be used as a fast and inexpensive means to evaluate potential designs or to probe specific research questions. The procedure developed is adaptable to several levels of modeling detail (or accuracy) and its capability can easily be extended beyond its current state. Many aspects of the models have been previously validated. The flow solver itself is a well-established turbomachinery code [51]. Validation exercises done by Lukachko [1] verified proper calculation of kinetics as specified in the chemical mechanism, species convection, species diffusion, mixing, influence of heat transfer or boundary layers, and some numerical issues on the chemistry solution. The validation efforts are ongoing, with several code improvements verified through test cases in this thesis (see Section 4) and the ensuing effort to benchmark the code against actual engine test data in the NASA/DERA engine test simulation. The modeling methodology is a collaboration of work from many researchers [3], in particular it is a continuation of work by Lukachko [1].

2.1 CHAPTER OVERVIEW

The purpose of this chapter is to provide an overview of the intra-engine species evolution modeling methodology presented in this thesis. Various physical processes that can be incorporated into the models, as well as their potential effects, are listed. The basic procedure for a time scale analysis is defined. The relevance and advantages of performing a preliminary time scale analysis are presented, using several examples to demonstrate the utility of the time scale analysis. This chapter also discusses some of the details associated with the specification of the initial chemical conditions at the combustor exit plane. Finally, a broad overview of both the low and high fidelity modeling techniques is presented.

In summary, the following are the main points of the chapter:

- There are many complex flow features associated with gas turbine engines which can influence trace species evolution in the post-combustor flow path. Temperature, pressure, residence time, species concentration, and scale are key parameters that can affect intra-engine chemistry.

- The intra-engine trace chemistry modeling methodology involves a time scale analysis, specifying chemistry initial conditions, and a detailed simulation using high or low fidelity models.

- Time scale analyses are useful in formulating a overall modeling strategy by indicating the critical areas of the engine flow path to investigate with higher fidelity modeling.

- Time scale analyses can also be used to provide insight into the physical phenomena influencing trace species evolution. For example, a time scale analysis can be applied to assess of the impact of engine operating condition, blade cooling, or chemistry on SO_3 evolution.

Section 2.2 gives examples of various modeling elements or physical processes which can be important to intra-engine chemistry modeling. Section 2.3 describes the modeling methodology developed for studying trace species evolution in the post-combustor flow path of gas turbine engines. Section 2.4 is the chapter summary.

2.2 MODELING ELEMENTS

Thermodynamic, fluid mechanic, and chemical kinetic interactions in a gas turbine engine can potentially affect trace species evolution. An important aspect of the modeling effort is to identify the features of the engine which are important to model and to determine the level of modeling detail required. Currently, the knowledge base for intra-engine chemistry is quite limited. However, using prior modeling and experimental work, along with fundamental knowledge of fluids and chemistry, hypotheses can be formulated to help select features or flow phenomena typical of gas turbine engines to investigate. Table 2.1 lists some possible modeling elements and physical processes and their potential influence on intra-engine species evolution.

Modeling Element Or Physical Process	Potential Effects On Species Evolution
Chemical mechanism	Important to capture appropriate reactions for accuracy [Section 4.3]
Boundary layers and wakes	Changes residence time and thermodynamic state
Engine operating condition	Higher combustor exit temperatures enhance SO_3 conversion [3], [Section 5.6.1]
Combustor temperature non-uniformities	Induces large scale non-uniformity [Section 5.6.2]
Downstream persistence of non-uniformities	Various implications [Section 5.6.3]
Blade cooling (thermal)	Enhances SO_3 conversion [1], [Section 5.6.2]
Heat release or secondary reactions	Can be important locally, details unknown [65]
Chemiions	Negligible effect [58]
Heterogeneous chemistry	Negligible effect [58]
Blade cooling (mass addition)	Unknown
Turbulence	Unknown

Table 2.1 Some possible modeling elements influencing intra-engine chemistry

Table 2.1 is not meant to be a comprehensive list of all physical processes and modeling elements which can impact intra-engine chemistry and their effects, but rather a list of a few items which were brought out in the course of this research. It is important to note that the effects of many of the modeling elements or physical processes are often inter-related and may not be important in all situations. Hence, the term "potential effects" meaning that the effect was observed for a given set of conditions modeled, however, is not necessarily always the case nor the only possible effect. The modeling methodology and tools developed in this thesis incorporate many of the elements listed in Table 2.1 or can be readily adapted to include them. The modeling exercises in Section 4, Validation, and Section 5, Modeling the NASA/DERA Engine Test, explore the impacts of several these modeling elements and physical processes. The exercises were used to investigate the magnitude of the impacts and develop appropriate models that can be used to simulate the relevant processes.

The main effects typically derive from the interaction of fluid mechanics and chemistry. The fluid mechanical phenomena can alter the chemistry through parameters involved in the Law of Mass Action or Arrhenius Equation, specifically through the temperature, pressure, residence time, or chemical composition which will be discussed in more detail in Section 3. The scale (i.e. size) of the fluid mechanical phenomena can have an impact on the magnitude of the effects.

2.3 PROCEDURE

The steps outlined in Sections 2.3.1 through 2.3.3 constitute the modeling methodology for studying the trace species evolution in the post-combustor flow path of gas turbine engines. Figure 2.1 is a graphical depiction of the procedure.

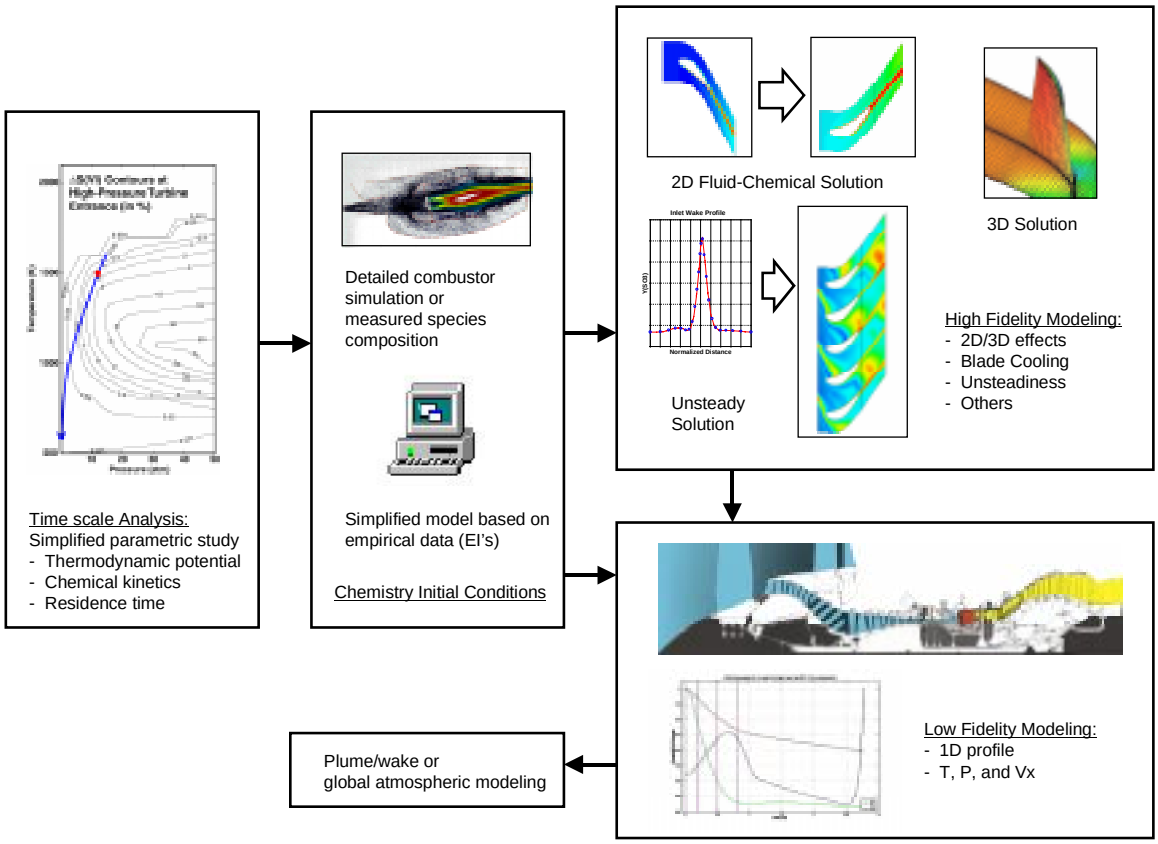

Figure 2.1 Intra-engine trace chemistry modeling methodology

A time scale analysis is first done in order to indicate which regions of the engine require higher fidelity modeling. This is accomplished by identifying regions which are most chemically active at a particular set of conditions. An overall modeling strategy is then developed. Once the strategy is in hand, an initial chemical composition for the gas at the combustor exit is determined. Finally, high fidelity, low fidelity, or a combination of modeling techniques is used to simulate the evolution of trace species in the engine or study physical phenomena influencing trace species evolution.

2.3.1 TIME SCALE ANALYSIS

The objective of a time scale analysis is to guide the modeling effort by providing preliminary estimates for species evolution and insight into the regions of the engine which are most chemically active which is used to help develop the overall modeling strategy. Thus, the first step of the modeling methodology is to perform a time scale analysis for the species (or set of species) of interest. A time scale analysis is essentially a simplified chemical kinetics solution. The time scale analysis can be used to quickly identify conditions impacting chemical evolution, thereby indicating locations within the engine or operating conditions for which detailed

analysis is benificial. Furthermore, the time scale analysis can be used to assess the impact of detailed flow processes and influence of various chemistries. The time scale analysis includes three fundamental controls on chemical evolution; thermodynamic potential, chemical kinetics, and residence time.

The concept and method of the time scale analysis were developed by Lukachko [31] and are further detailed in unpublished internal research documentation. An endeavor to formally publish the work is planned in the near future.

2.3.1.1 BASIC PROCEDURE

The thermodynamic potential is the difference between a given composition and the equilibrium composition. This potential change in a given species and the chemical time scale required for the change can be mapped out over a large temperature and pressure parameter space using only the key reactions of interest. Figure 2.2 shows a typical plot of the thermodynamic potential, expressed as % SO_3/SO_x at equilibrium, over a parameter space relevant to gas turbine engines. Several additional simplifying assumptions about the chemistry can be made in this preliminary analysis. In this case, SO_3 chemistry is being investigated using only the O and OH pathways from [28], using only forward reactions, and assuming equilibrium radical levels.

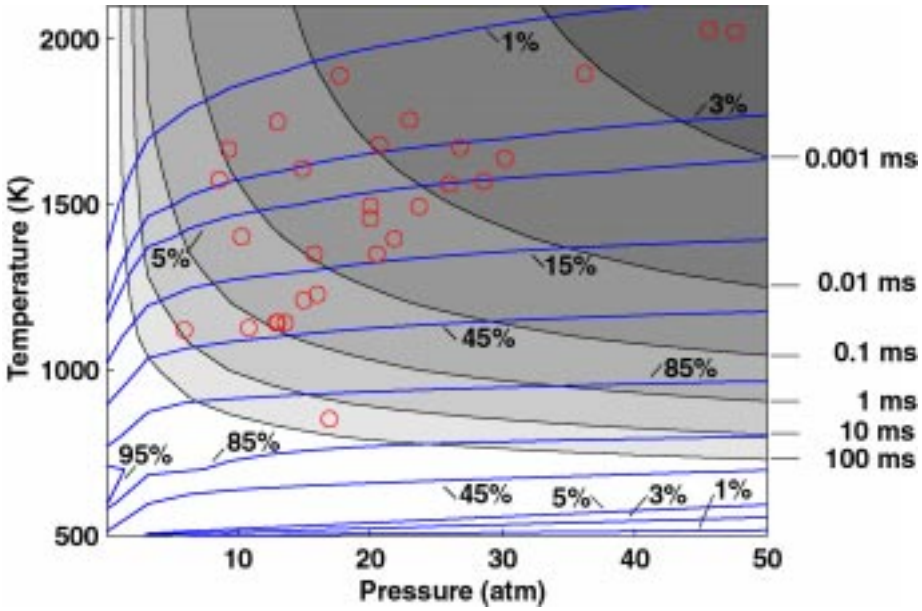

GREY = contours of τ_{SO3}
BLUE = lines of constant % $SO_3/SO_x|_{eq}$
RED = combustor exit conditions for various engines

Figure 2.2 Typical thermodynamic potential and chemical time scale plot underlying a time scale analysis for S O_3 (courtesy of Stephen Lukachko)

From Figure 2.2 it is also evident that combustor exit conditions from different engines at various operating points span a large range of the temperature and pressure parameter space. The flow-through times for a single blade row and the entire post-combustor flow path are on the order of 0.1 ms and 1 to 10 ms, respectively. The gray regions labeled on the right of the figure represent the characteristic chemical time required to reach equilibrium at the underlying temperature and pressure. From the figure it is also evident that certain engines and operating points are more favorable to SO_3 emissions.

Next, by incorporating a residence time for a given engine section the three fundamental controls can be recast in terms of a severity parameter which is the basis of the time scale plot. The severity parameter is defined as follows (using SO_3 as an example):

$$\Delta S(VI) = Da_{SO_x}\left(\left[\frac{SO_3}{SO_x}\right]_{equil} - \left[\frac{SO_3}{SO_x}\right]_{current}\right) \tag{2-1}$$

The current value in equation (2-1) represents the SO_3/SO_x ratio at the state for which the time scale plot was generated (labeled with a red symbol in the examples given in Section 2.3.1.2). And the Damköhler number, Da, is defined as the ratio of the flow time to the chemical time:

$$Da_{SO_x} = \frac{\tau_{flow}}{\tau_{SO_3}} \tag{2-2}$$

Figure 2.3 shows the resulting plot of severity parameter for SO_3 at the high and low pressure turbine entrance (red symbols) from a typical time scale analysis. The flow time scale of (2-2) used in the figure is the blade row convection time. The potential for additional species conversion can be read directly from the severity parameter plot.

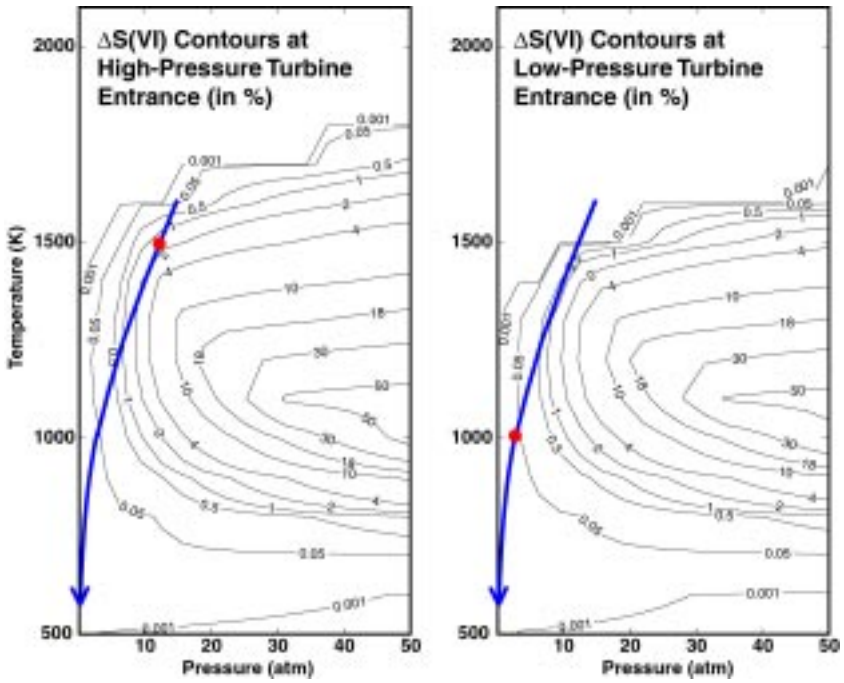

Figure 2.3 Severity parameter for SO_3 from typical time scale analysis at two engine stations (courtesy of Stephen Lukachko)

A curve representing the post-combustor flow path can be plotted on the map. The example in Figure 2.3 shows a curve (blue) for a representative engine at cruise. The severity parameter plot can be used to point out several aspects of the selected chemistry. First, notice that the contours of constant ΔS(VI) shift as one traverses through the engine. The shift is due to the amount of conversion which previously occurred, the new thermodynamic state, and to a lesser extent the change in residence time at the specific engine station. Second, the contours indicate a zone of maximum SO_3 formation. In this case, there is more than 10% conversion for temperatures of 1,000-1,300K and pressures over 20 atm. Finally, the severity parameter plot at the low pressure turbine entrance indicates that there is a negligible amount of further conversion possible (i.e. the active chemistry has completed in the high pressure turbine). This would suggest that the need for higher fidelity modeling should be concentrated in the high pressure turbine region.

Finally, by integrating along the path shown in the figure preliminary estimates can be made for the evolution of the species. The simplifying assumptions inherent in the time scale analysis must be considered when making quantitative estimates. Thus, the time scale analyses are primarily used as a guide for further modeling.

2.3.1.2 FURTHER EXAMPLES OF THE UTILITY OF TIME SCALE ANALYSES

Time scale analyses can also be used to assess the impact of detailed flow processes and the influence of various chemistries. Some examples of these uses are presented in Figure 2.4, Figure 2.5, and Figure 2.6. An understanding of the influence of blade surface cooling on sulfur conversion can be deduced from the severity parameter plot in Figure 2.4. Static temperature for a cooled blade is plotted on the right. The solid red point on the severity parameter plot represents the nominal temperature at the high pressure turbine entrance and the red cross hatched region shows a range of temperatures which occur in the stator due to the blade surface cooling. Given the location on the plot, blade cooling will increase the amount of sulfur conversion over the blade row since the cross hatched region extends into regions of greater potential conversion. However, also notice that only a small portion of the fluid is cooled by the blade and that the scale of the non-uniformity is important in determining the overall effect.

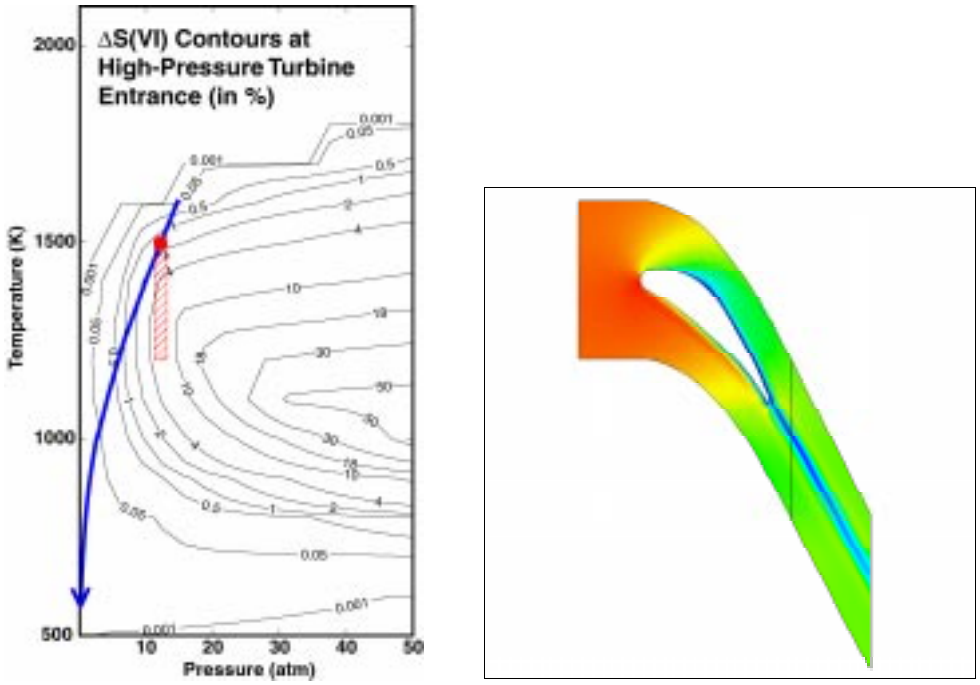

Figure 2.4 Investigating the impact of blade cooling on SO_3 chemistry using time scale analysis (courtesy of Stephen Lukachko)

Another example of how a time scale analysis can help to elucidate a flow process is depicted in Figure 2.5. In this plot a cruise condition operating line (solid blue) is compared to a hypothetical line for take-off conditions (dashed blue). The plot indicates that the take-off conditions would have a greater sulfur conversion. In general, higher temperatures and pressures associated with new technology engines are expected to enhance sulfur conversion in the post-combustor flow path.

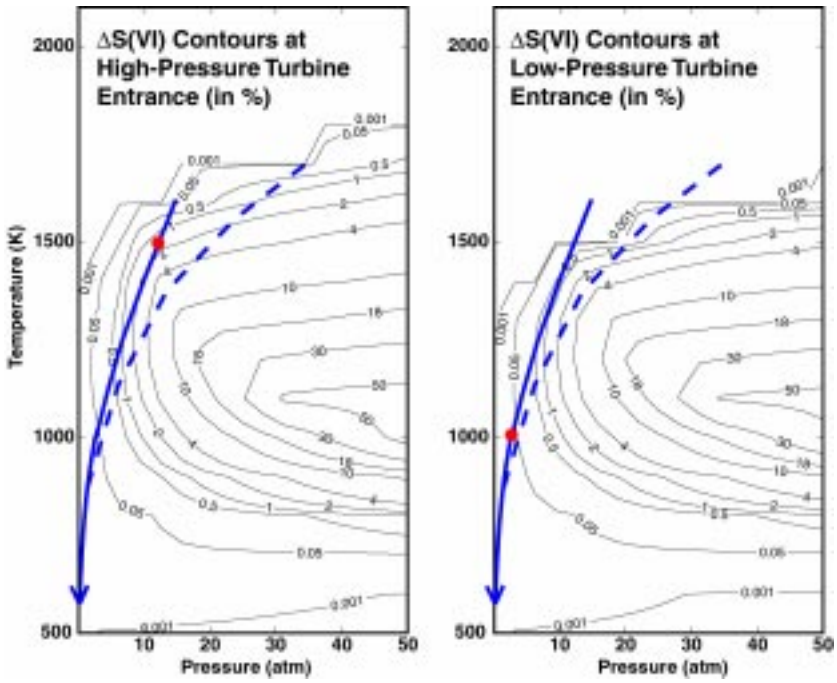

Figure 2.5 Investing the effects of operating condition on chemistry using time scale analysis (courtesy of Stephen Lukachko)

As a final example of the utility of the time scale analysis, the influences of different chemistries can be assessed. Figure 2.6 shows a comparison of two time scale analyses, one using only the SO_2 + O pathway for SO_3 formation, and the second using both SO_2 + O and SO_2 + OH pathways. In this situation, which assumes an equilibrium level of OH/O of about 10 , it is evident that the OH route is more active than the O route. Thus, the time scale analysis can give insight as to which chemical pathways are most important for the species subset being studied.

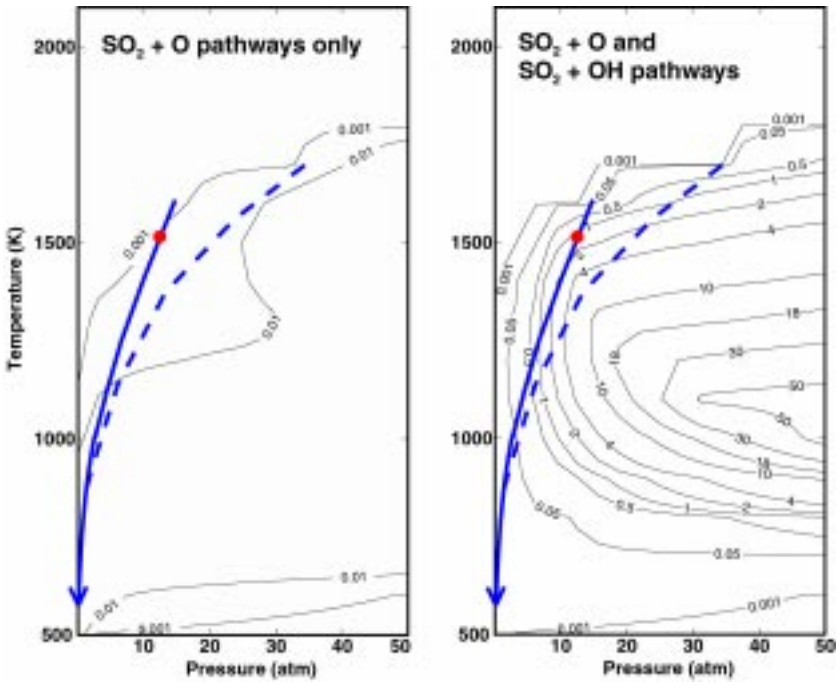

Figure 2.6 Investing the effects of various chemistry using time scale analysis (courtesy of Stephen Lukachko)

In summary, the preliminary time scale analysis is used to focus the overall modeling effort by indicating the regions of the engine where higher fidelity modeling may be beneficial. Using information derived from the time scale analysis and the desired level of accuracy, the overall modeling strategy can be formed with low fidelity, high fidelity, or a combination of the modeling techniques to be discussed in the following sections. Also, the time scale analyses are useful to help develop an intuitive understanding for the physical phenomena influencing chemistry. Also, they can be used to provide first order comparative studies to the magnitude of these effects.

2.3.2 CHEMISTRY INITIAL CONDITIONS

Once the time scale analysis is completed it is necessary to formulate the initial chemical composition for the gas at the combustor exit. The details of the combustion process are complex, and thus, the gas leaving the combustor is at a non-equilibrium state containing multiple trace species. The accuracy of the initial condition is essential to a successful post-combustor simulation because the final outcome of the simulation is based on the initial condition. Therefore, it would be preferable to begin with species composition data from a measurement at the combustor exit plane or from a detailed combustion simulation. However, since this data is not readily available, a code was developed to provide a quick and reasonable estimate of the composition [31].

Some minor improvements to the code were made to address the rapid initial shift in some species found in past simulations. A overview of the initial conditions code procedure is given in Figure 2.7.

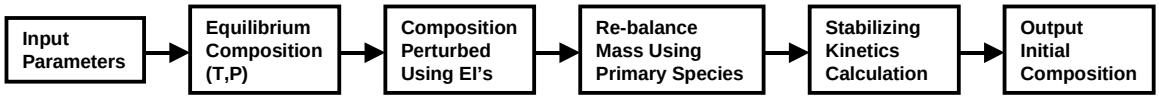

Figure 2.7 Overview of chemistry initial condition specification

The code starts with the equilibrium composition at the combustor exit conditions. The composition is then perturbed using specified emissions indices or species ratios. The addition of the trace species is balanced by adjusting the levels of the primary combustion products. Finally, a constant temperature and pressure kinetics calculation is run for a very short time to reach a stable non-equilibrium composition. Table 2.2 lists the input parameters for the code.

Initial Conditions Code Input Parameters
Temperature (K)
Pressure (atm)
ϕ (equivalence ratio)
η (combustion effeciency)
CO/H_2/HC ratio
EI(NO_x) (g/kg fuel)
NO/NO_x ratio
EI(S) (g/kg fuel)
SO_3/SO_x ratio
EI(CO) (g/kg fuel)

Table 2.2 Input parameters to initial conditions code

The improvements to the technique in [1] were made by changing some of the input parameters used to perturb the equilibrium composition and also in performing the kinetics calculation to stabilize the composition, see Section 2.3.2 for more details. The non-equilibrium solution initially output from the code is inherently unstable. Although some attempt is made to redistribute the mixture to a "stable non-equilibrium state" when applying the EI's, the entire set of reactions in the mechanism can not be considered easily. Running the kinetics calculation for a short time allows the species to make the initial rapid re-adjustment to a "stable non-equilibrium state" with a negligible change to the overall composition. The duration of the kinetics calculation was chosen by plotting each species versus time for the constant temperature and pressure calculation and then moving back to the point where each species was deemed to be outside of the "initial shift region." Figure 2.8 and Figure 2.9 show the mole fraction of a few species and several of the EI's versus time during the stabilizing kinetics calculation. The left column of graphs show the result of the entire calculation, which was chosen as 5 ms to exceed a typical blade passage flow-through time. The green lines indicate 0.30 ms, and the graphs on the right column are an enlarged detail of the 0 to 0.3 ms region. For this case, the red line at 0.02 ms was

chosen as the point where the species initial conditions was deemed stable and it is the composition at that point that is output for use in the detailed modeling.

This technique is justified since the EI's, major species, and specified trace species do not change significantly. Mainly the radical species and unspecified trace species shift considerably, however, this is as expected and bring the composition to a reasonable and stable non-equilibrium state. The end result is a non-equilibrium initial gas composition which is well characterized by the parameters specified, yet none of the species concentrations are grossly out of line with the equilibrium composition for the given pressure and temperature.

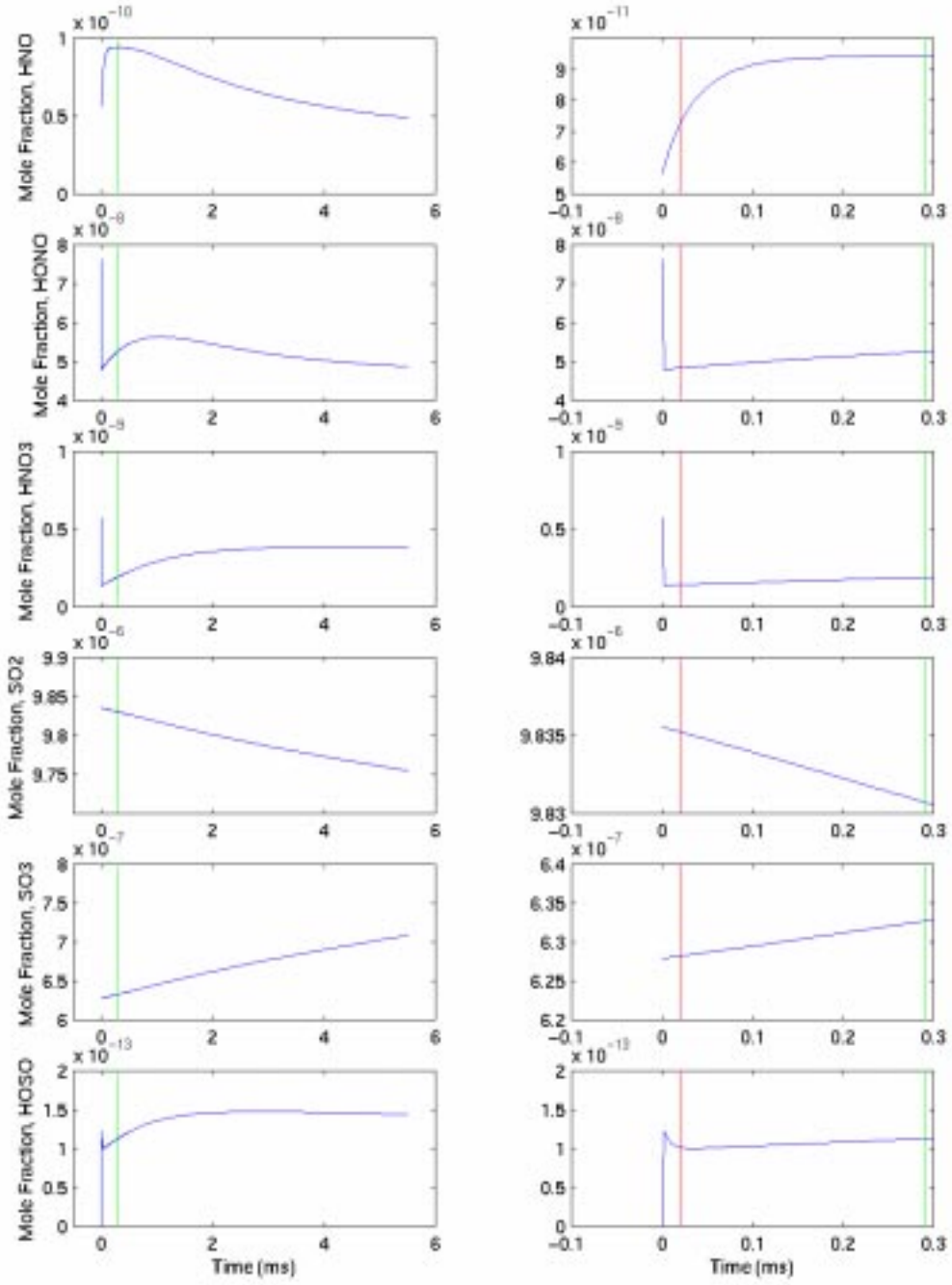

Figure 2.8 Representative constant temperature and pressure kinetics calculations for selected species for initial conditions formulation

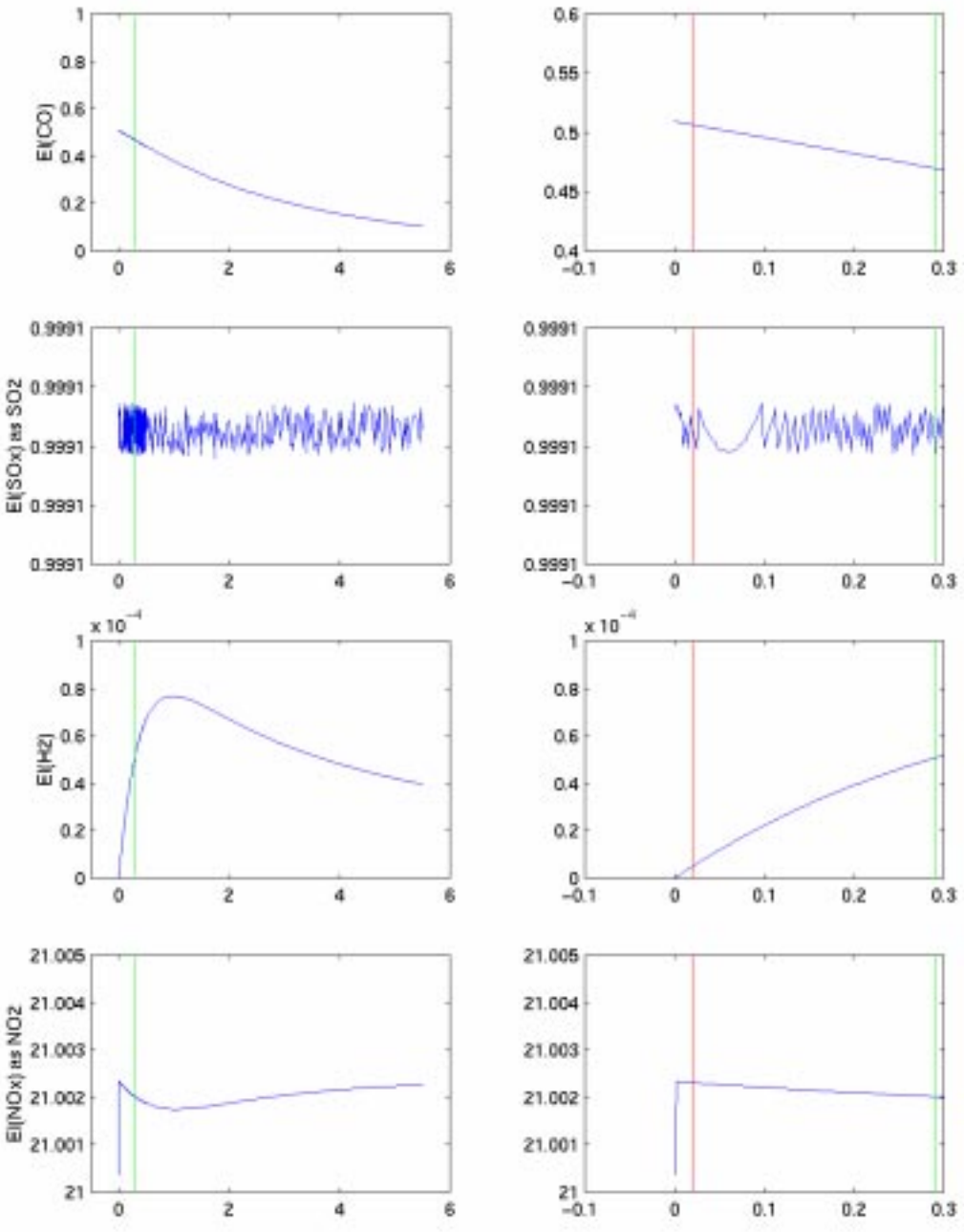

Figure 2.9 Change in selected EI's during kinetics calculation for initial conditions formulation

2.3.3 HIGH AND LOW FIDELITY MODELING

The modeling techniques are divided up into two categories, high fidelity and low fidelity. The word fidelity can mean accuracy in details or exactness, and high or low fidelity represents the degree to which a reproduction is faithful to the original. In the sense of the modeling methodology being described here, a low fidelity model is a simple 1D simulation which can in general only track average quantities. A high fidelity model is any model which can directly simulate more detailed multi-dimensional flow features and thus account for chemical or flow non-uniformities. The high fidelity model, containing more details of the actual system being modeled is expected to be more accurate, although, the accuracy of the high fidelity model is also based on its ability to accurately represent the details being simulated.

In contrast to a simplified time scale analysis which is based on chemical kinetics alone, the low and high fidelity models are based on integrating the equations of mass, momentum, and energy over a discrete domain (see Section 3.2) coupled with the chemical kinetics solution. For a low fidelity model the integration occurs over a 1D profile and for a high fidelity model it occurs over a 2D or 3D grid.

A time scale analysis can be used as a guide to map out the modeling strategy. It is desirable to concentrate modeling resources on areas of the engine which have a high degree of chemical activity for the species of interest. A 2D or 3D reacting fluid-chemical simulation can be done on the regions of the engine flow path targeted for higher fidelity models. A suite of numerical tools to be discussed in more detail in Section 3 was further developed in the context of this thesis. It consists of a grid generator, fluid and chemical kinetic solvers, and flow visualization codes which can be used to do such higher order modeling. The higher order modeling can include the effects of many physical phenomena typically encountered in a turbomachinery environment such as complex geometries, viscous walls, cooled surfaces, and unsteadiness (see Section 2.2). These phenomena can cause local temperature, pressure, or species gradients, which can influence the subsequent evolution of chemical species. Higher fidelity modeling requires more user effort to set up and post-process and is more computationally intensive. These simulations take roughly 10 to 100 times an investment in resources compared to a low fidelity model. A typical high fidelity simulation may take several days to weeks to setup and run whereas a low fidelity simulation can be completed in a matter of hours or days (see Section 3.3.3 for more details). However, the high fidelity models can increase the predictive capability of the modeling methodology and help provide insight into the mechanisms responsible for altering chemical evolution if applied in regions where chemistry is suspected to be more reactive.

The complete details of the procedure needed to perform a higher fidelity simulation are numerous and highly dependent on the particular modeling situation. Many of these details are discussed further elsewhere in this thesis (especially Section 3) or in several external references such as [1], [48], and [49]. The basic process

involves generating a 2D or 3D grid, formulating the fluid and chemical boundary conditions, solving the reacting flow problem, and post-processing the result. Several examples of high fidelity modeling are given in Section 5, Modeling the NASA/DERA Engine Test.

On the other hand, the time scale analysis may suggest using low fidelity models for some or all of the simulation. A 1D analysis can be used for situations where the species of interest are not highly reactive for the given operating condition or when a high degree of accuracy is not required. A simple 1D profile of temperature, pressure, and velocity is used along with geometric data to track species evolution through the post-combustor flow path of the engine.

Again, further details of the procedure to perform a low order simulation are give in Section 3 and [48]. Also, example results from a typical low order simulation are given in Section 5, Modeling the NASA/DERA Engine Test.

2.4 CHAPTER SUMMARY

The purpose of this chapter was to provide an overview of the intra-engine species evolution modeling methodology presented in this thesis. Various physical processes that can be incorporated into the models, as well as their potential effects, were listed. The basic procedure for a time scale analysis was defined. The relevance and advantages of performing a preliminary time scale analysis were presented, using several examples to demonstrate the utility of the time scale analysis. This chapter also discussed some of the details associated with the specification of the initial chemical conditions at the combustor exit plane. Finally a broad overview of both the low and high fidelity modeling techniques was presented.

In summary, the following is a list of all relevant points presented in this chapter:

- A outcome of this research is a modeling methodology and modeling tools which can be used to simulate intra-engine chemistry. Many aspects of the model have been validated and there is an ongoing effort to continue its validation.

- There are many complex flow features associated with gas turbine engines which can influence trace species evolution in the post-combustor flow path. Temperature, pressure, residence time, species concentration, and scale are the key parameters that can affect intra-engine chemistry.

- The intra-engine trace chemistry modeling methodology involves a time scale analysis, specifying chemistry initial conditions, and a detailed simulation using high or low fidelity models.

- Time scale analyses are useful in formulating a overall modeling strategy by indicating the critical areas of the engine flow path to investigate with higher fidelity modeling.

- A time scale analysis is a simple parametric study which incorporates thermodynamic potential, chemical kinetics, and residence time. The output is a plot of severity parameter for a given species of interest, although, a preliminary estimate of species evolution can be obtained.

- Time scale analyses can also be used to provide insight into the physical phenomena influencing trace species evolution. A few example time scale analyses were used to show:

    - Blade cooling can enhance sulfur conversion.
    - Engine operating condition can influence sulfur conversion, take-off conditions can have higher sulfur conversion than cruise conditions.
    - The OH pathway to SO_3 can be more active than the O pathway.

- A simple method for specifying chemistry initial conditions involves perturbing an equilibrium composition , re-balancing the species based on mass, and doing a stabilizing kinetics calculation.

- High and low fidelity models involve integrating the equations of mass, momentum, and energy over a discrete domain coupled with chemical kinetics to simulate intra-engine chemistry. A high fidelity model can incorporate many multi-dimensional effects (i.e. non-uniformities) while a low fidelity model uses average quantities.

3 MODELING TOOLS

Underlying the modeling methodology presented in Section 2 are several computer codes which are used to generate grids, specify initial conditions, numerically solve the fluid mechanics and chemical kinetics problems, and visualize the results for geometries of interest to intra-engine chemistry.

3.1 CHAPTER OVERVIEW

The purpose of this chapter is to present a brief overview of the modeling tools and discuss the improvements made to these tools during the course of this research. The existing modeling tools consist of the PRE grid generation code, PROCESS grid pre-conditioner code, POST grid post-processor code, CNEWT and CALCHEM flow-chemistry solvers, and CNEWTVS6 flow visualization code. The improvements made to the existing tools allow for more complicated geometries, multiple inlet and exits, improved execution time for solutions with chemistry, and a specification of a pressure, temperature, and species concentration deficits associated with a wake of an upstream blade or blade row.

In summary, the following are the main points of the chapter:

- CNEWT and CALCHEM are useful modeling tools for studying intra-engine trace species flow-chemistry problems. Other supporting codes necessary for turbine chemistry modeling are PRE, PROCESS, POST, and CNEWTVS6.

- For more details on the structure and numerical mechanics of the codes, refer to "Research on the Science And Politics of the Atmospheric Effects of Aviation Debate" by Lukachko [1] as the primary source of information.

- In order to provide further insight into trace species characterization, improvements were made to existing modeling tools which include:

    - Obtaining a new grid generator
    - Adding multiple inlet/exit capability
    - Parallelizing chemistry subroutines
    - Implementing a wake model boundary condition

The improvements were validated using test cases to ensure they worked properly.

Section 3.2 is an overview of the existing tools, with references to detailed information. Section 3.3 describes the improvements made to these tools during the course of this research. Section 3.4 is the chapter summary.

3.2 OVERVIEW OF EXISTING MODELING TOOLS

The two primary modeling tools that have been used to investigate research questions for the assessment effort of intra-engine trace species are CNEWT and CALCHEM. These codes were designed to allow for several levels of physical approximation, to incorporate chemical models containing any extent of reactions or species, to calculate robust solutions for complex systems, and for the ease of implementing improvements [1].

CNEWT was built on the NEWT turbomachinery CFD code [51] which employs a vertex-centered, finite-volume solution method incorporating a Runge-Kutta time discretization scheme to solve the full Reynolds-averaged Navier-Stokes, conservation of mass and conservation of energy equations for three-dimensional geometries. CHEMKIN II is a set of subroutines for the calculation of gas phase chemical kinetics [68]. CNEWT combines well-established computational fluid dynamics and chemical kinetics solution mechanisms within a structure currently capable of calculating passively reacting internal flows. Any chemical mechanism can be represented using a system of ODE's which are solved via the VODE solver [61]. To accomplish the fluid-chemical integrations under the passive chemistry approximation in CNEWT, an explicit, operator-splitting algorithm, where flow and chemistry are decoupled and calculated essentially separately was chosen. CALCHEM is a 1D version of CNEWT, allowing for simple solutions based on 1D pressure, temperature, and velocity profiles rather than a multi-diminsional 2D or 3D domain. Thus, the CALCHEM code is used for low fidelity modeling and the CNEWT code is used for high fidelity modeling.

Several other supporting codes are used along with CNEWT. PRE is a grid generator specifically suited for meshing turbomachinery blade geometries. A tool called POST can be used to refine the grids (see the Princeton VPFR in Appendix A for an example). PROCESS adds the chemistry variables to the NEWT grids to create CNEWT grids. CNEWTVS6 is a flow visualization code for the fluid-chemistry solutions which is based on VISUAL3 [71].

For more details on the structure, numerical mechanics, and use of the codes, refer to "Research on the Science And Politics of the Atmospheric Effects of Aviation Debate" by Lukachko [1] as the primary source of information, as well as [28], [48], [49], [50], [51], [52], [62], [68], and [71].

3.3 IMPROVEMENTS

Several improvements to the modeling tools were made during the course of this research aimed at extending the capability and improving the accuracy of the modeling tools. A few extensions are discussed elsewhere in this thesis; first, the procedure for specifying chemistry initial conditions was improved and as detailed in Section 2.3.2, next, a new chemical mechanism for turbine chemistry modeling was adopted as described in Section 4.3, finally, the chemistry convergence criteria were refined as discussed in Section 4.4. This section describes several additional improvements to the modeling tools. In particular, a new grid generator was obtained, a option for multiple inlets/exits was added, the chemistry subroutines were parallelized, and a wake model boundary condition was implemented into the codes.

3.3.1 CAD BASED FULLY UNSTRUCTURED GRID GENERATION

Grid construction is important since it determines the resolution (i.e. accuracy) of the flow solution and impacts the computational time, therefore an accurate and efficient grid construction is desired. The grid generator used for previous investigations, called PRE, is best suited to turbomachinery blade passages. The grids typically had four sides, with a blade form either entirely within the domain (block 5 input format) or on the side boundaries (block 3 input format). The grids are initiated as a structured mesh composed of hexahedral cells and are transformed into tetrahedral grids simply by dividing the hexahedrons. Hence they were "pseudo-unstructured," since although being tetrahedral, the cells were still in an orderly arrangement based on the initial hexahedral grid. By piecing together several blocks, a more complicated grid can be obtained, such as a blade with tip clearance.

The structured or "pseudo-unstructured" grid is less flexible in the types of geometry it can mesh and it may cause some numerical issues. In previous work, of validation runs using a PRE meshed geometries, the temperature and velocity exit plane contour plots showed an undesirable result of hotter, slower flow in the corners perpendicular to the mesh diagonal and grid scale oscillations in solution variables which could be linked to the structure of the grid [1].

New grid generation tools developed at Cambridge University were implemented to overcome these potential problems and extend the codes to more complex arbitrary geometries [35] and [66]. This set of grid tools requires an initial CAD-generated geometry, which can be created with typical commercial solid modeling software. Thus, virtually any arbitrary geometry can be created and meshed. There are essentially three main aspects that comprise the new grid generation tools; the solid model, the surface mesh, and the volume mesh. Figure 3.1 shows the difference between a pseudo-unstructured grid made with PRE and fully unstructured grid made with the new grid generator.

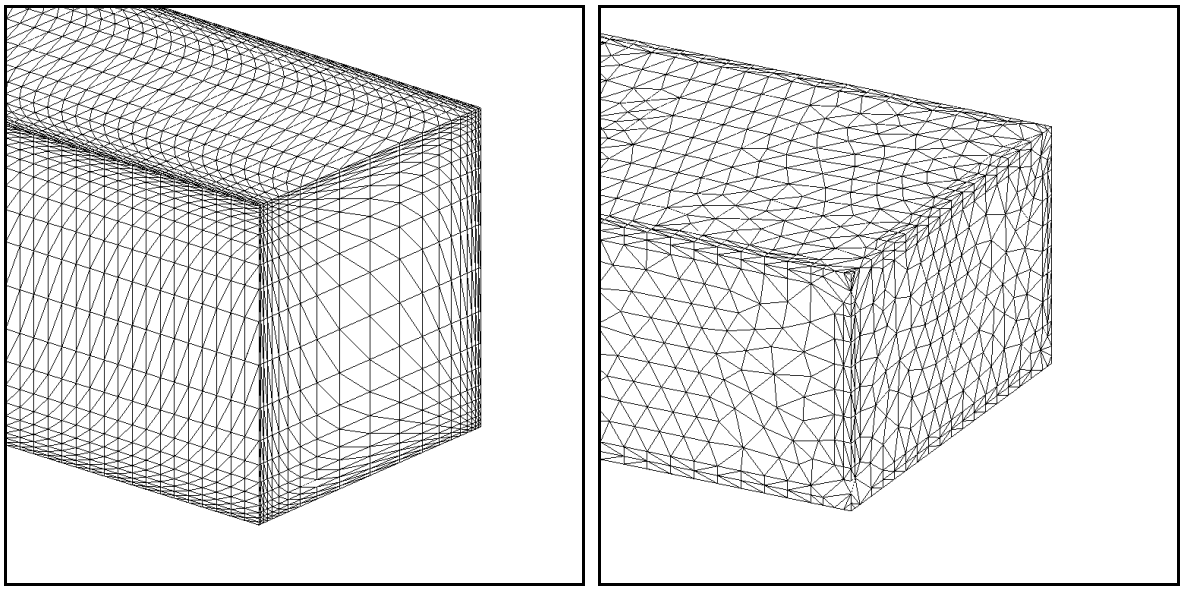

Figure 3.1 Examples of a pseudo-unstructured (left) and fully unstructured (right) grid

Solid Model

A CAD based solid model can be exported in IGES format and a program called "3D_GEO" can be used to convert the geometry to a generic CAD file format (.geo) suitable for use with the new grid generation tools. The code can also be used to display vertices, edges, surfaces of geometry in 3D which aids in repairing the translated geometry.

Surface Mesh

The generic CAD file is used by the surface meshing routine to create a unstructured mesh on the surfaces of the solid model. All grid controls are applied in the surface meshing step. A boundary condition file (.bcf) ties the CAD entities to names and boundary conditions, as well as allowing some general grid control. A source term file (.src) allows finer grid controls through specification of point, line, or triangle sources which dictate grid point spacing. The surface meshing program performs the following basic steps:

- CAD edge division based on grid controls
- 2D Delauney triangularization on surfaces based on criteria from the grid controls by:
  - inserting a node on a surface
  - edge swapping the triangles on that surface
  - repeat until grid quality criteria are met

The output of the surface mesh are a front file (.fro) and a .m2d file which contain the surface grid in text and binary format, respectively.

Volume Mesh

The volume meshing routine uses the binary surface mesh file to create the final 3D grid. There are no grid controls which can be applied during volume meshing, except for specification of viscous layers. Rather, the volume grid generator attempts to make an isotropic mesh with cells that are a uniform size. There are three stages involved in the volume meshing which perform the following basic steps:

Stage 1:
- creates 8 construction nodes encompassing the surface mesh
- starts with the initial construction cell and connects surface nodes into tetrahedrons using 3D Delauney triangularization by marching across domain, grabbing, and constraining each surface node

Stage 2:
- generates viscous layers by extruding nodes near walls flagged as viscous
- moving front

Stage 3:
- in-fills domain by inserting new nodes into cells that fail quality measures
- locates tetrahedral cell that the new node is in, then divides into many new tetrahedral cells
- edge swapping based on 3D Delauney to improve local mesh quality

Figure 3.2 shows a mesh after a stage 1 dump and two meshes, one without viscous layers and one with viscous layers, after a stage 3 dump.

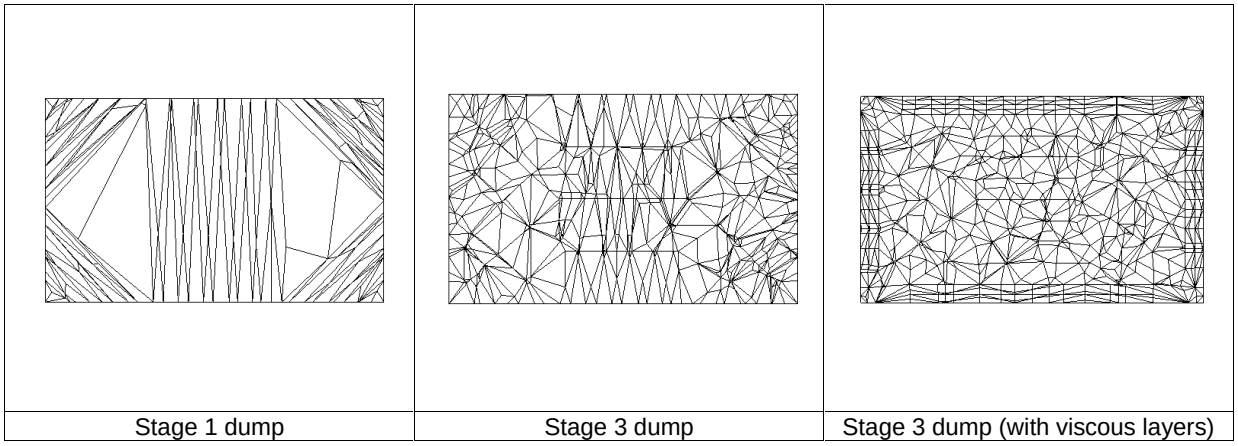

Figure 3.2 Volume mesh stage dumps

Note that the cells in the cross-section may not look uniform, because the cutting plane intersects some cells near a vertex (giving the appearance of a very small cell), some cells near an edge (giving the appearance of a sliver shaped cell), as well as some near the center of the cell. The volume mesh routine outputs a mesh connectivity variable file (.mcv) which contains the 3D mesh in NEWT format. More details of the new grid generation tools can be found in [66].

During the period of work on this thesis, the new grid generation tools were in a developmental stage. They worked well for simpler geometries, however, some difficulties were encountered for more complex

geometries. The translation step from the CAD solid model to the generic CAD file was troublesome. Frequently, the generic CAD file (.geo) had extraneous entities, missing entities, or entities which were not geometrically exact. In particular, the edge between two intersecting surfaces was not always coincident. Thus, it was necessary to manually edit the file, which could get quite large and cumbersome for complex geometries, to correct the errors. Also, in the volume meshing process, when nodes are inserted in stage 3, the routine calculates several geometric distances (which can be quite small) to determine which cell contains the node. The code uses double precision variables help resolve the small distances, however, occasionally it can not accomplish the task and crashes. The meshing procedure must then be re-started using a new surface mesh to seed the volume mesh routine, making volume meshing somewhat of a hit or miss iteration procedure. The key to achieving a 3D grid it to start with a good quality surface mesh (i.e. cells which are have a reasonable aspect ratio and a grid which has smooth transition between cells of different sizes).

The Princeton VPFR (see Appendix A) and multiple inlet/exit test (see Section 3.3.2) geometries were successfully meshed using the new grid generator. The CAD translation and numerical issues in volume meshing made it very difficult to obtain a valid grid for the Princeton VPFR. The VPFR has a fairly complicated shape and an extreme aspect ratio. The generic CAD file (.geo) for the Princeton VPFR had nearly 8,000 lines for 28 faces, 85 edges, and 56 vertices. Manually editing this file to repair the geometry was very complicated and tedious. Furthermore, the geometry had to be scaled to reduce the aspect ratio then the resultant mesh was re-scaled to obtain the final mesh to overcome the numerical problems in the volume mesher.

3.3.2 MULTIPLE INLETS/EXITS

The advent of the new fully unstructured grid generator described in Section 3.3.1 leads to the possibility of analyzing more complicated flow situations. A natural extension to this was the capability to have more than one inlet and/or exit boundary, which, for example can be used to model mixing flows such as film cooling on a turbine blade. This feature was required to model the injection in the Princeton VPFR validation exercise (see Section 4.2). This new feature was implemented into NEWT at the Cambridge University Whittle Laboratory [35], and the CNEWT code was updated by incorporating similar code modifications. Currently, the domain can have one main inlet with either a wake model (see Section 3.3.4) or a radially varying static profile for the variables on the inlet plane and several secondary inlets with the inlet plane variables specified as constant. The domain can have many exit boundaries with the exit plan variables specified as constants.

A duct with two inlets, two exits, and a rectangular hole was made as a learning exercise for the new grid generator and to test the multiple inlet/exit code additions. Figure 3.3 shows a result from the test case computation, which was used only to make a qualitative assessment of the multiple inlet exit additions. The

case demonstrated that the multiple inlet/exit code additions to CNEWT work properly, however, further validation should be pursued.

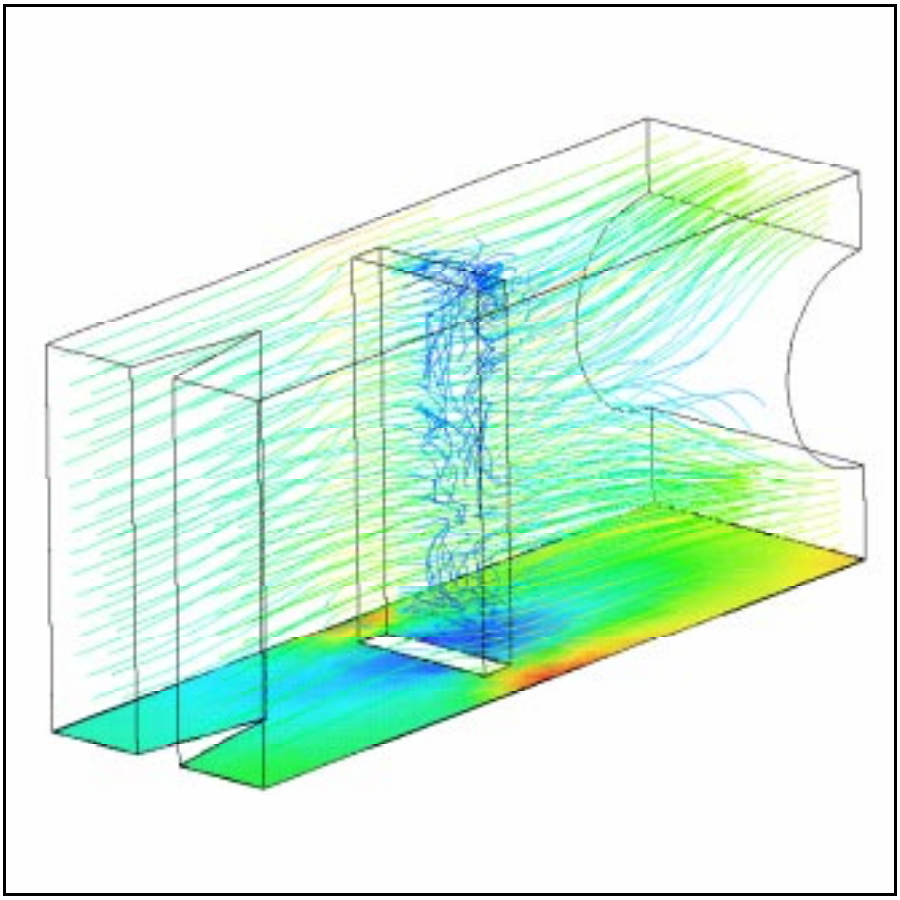

Figure 3.3 Multiple inlet/exit test case, X direction velocity on streamlines

Another implementation of the multiple inlet/exit feature is the Princeton VPFR validation exercise presented in Section 4.2 where flow reactor injector inlets are shown in Figure A.18.

3.3.3 PARALLEL CHEMISTRY SUBROUTINES

A high fidelity model of a coupled fluid and chemistry problem can require a large amount of computational resources. For a typical problem, the chemistry solution requires about 90% of the computational time. The desire to improve accuracy by resolving geometries with more detailed grids and through the use of broader chemical mechanisms, as well as, the desire to increase the turn-around time for high fidelity models prompted the exploration of methods to improve execution time. The structure of the CNEWT code, with the explicit operator-splitting algorithm in which the fluid and chemistry solutions are decoupled lends itself to a

straightforward implementation of parallel computing on the chemistry problem. In the chemistry subroutine, a set of chemical kinetic ordinary differential equations is solved at each node of the grid with respect to time using the averaged fluid properties and the species mass fraction results from the previous iteration as the initial condition. Thus, each nodal calculation is independent and can be computed in parallel.

The CNEWT code was modified to capitalize on this potential to compute the chemical kinetics equations in parallel. The components necessary to build a network of workstations, or cluster, can purchased relatively cheaply. Furthermore, a cluster of personal computers is easily scalable and the system is simple to maintain. Therefore, the strategy was to adapt the code to run on a networked cluster of personal computers using a standard message passing library. Further background information on parallel computing can be found in [45], [46], and [47]. The parallel modifications to the CNEWT code were implemented with the assistance of John Zhang at Aerodyne Research, Inc. The code was modified to run in parallel by simply dividing the domain into equal subsets of grid points based on the number of compute nodes. Each compute node solves for a subset of the chemical kinetics equations and the solved subsets are exchanged between nodes to obtain a complete solution. The CNEWT code was designed to run in parallel on a cluster of 2, 3, 4, 5, 6 or 12 nodes running the Linux operating system on an Intel based personal computer architecture using MPICH, a freely available implementation of the MPI (message passing interface) standard [46].

The Cambridge No 2 turbine rotor was used as a test case for the parallel code modifications. The test case was run on a 400Mhz Pentium II cluster with a fast 100Mbps ethernet. The run time statistics for 100 iterations on the test case are given in Table 3.1.

# of CPU's	Run time (hrs)	fluid (sec)	chemistry (sec)	User time/iteration (sec)
1	16.05	57.3	534.9	577.8
6	4.73	57.4	113.7	170.4
12	3.28	57.9	60.1	118.2

Table 3.1 Run time stastics for parallel code test case

These results show that the CNEWT code is about 3.4 times faster on 6 nodes and 4.9 times faster on 12 nodes for the test case. For 6 nodes the time for the chemistry solution is about twice that for the fluid solution and for 12 nodes they are about equal, thus a 6 node cluster was a fairly optimal configuration for solving problems typical of the ones presented in this thesis. A similar result was obtained by John Zhang on the Aerodyne Research Inc. cluster, which consisted of 300 MHz personal computers networked at 100 Mbps, as shown in Figure 3.4.

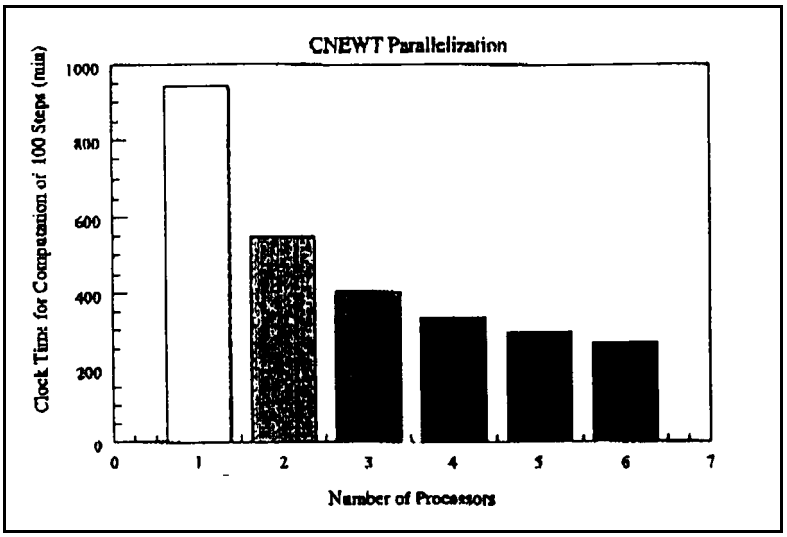

Figure 3.4 Run time stastics for parallel CNEWT

The solutions were also checked for accuracy by comparing a few maximum and minimum flow and species variables for the original code and the parallel version across several nodes. The fluid solutions for the original and parallel version (any number of processors) of the code were identical. The difference between the original and parallel version of the code with regard to the chemistry solution was found to be less than 0.2% in all of the species quantities checked. Also, the chemistry solutions from the parallel code were identical when the number of nodes was varied. Further instructions on how to compile and run the parallel version of the code are given in the README.TXT file included with the CNEWT code.

3.3.4 SPECIES AND TEMPERATURE WAKE MODEL

The original CNEWT code employs a wake model which allowed the specification of a rotating, circumferentially varying inlet profile for total pressure. The main purpose of this wake model was to allow the specification of a pressure deficit associated with the wake(s) of an upstream blade or blade row without the need to do a full unsteady calculation with both blade rows using, for example, a sliding plane technique. Thus the code could be run in unsteady mode, with a fixed timestep, and the unsteady effects of the wakes could be captured using a single blade row.

This wake model was extended to include total temperature and chemical species mass fractions. With these modifications, the capability of the code was increased by allowing a more accurate specification of the inlet conditions and enabling the investigation of the unsteady interaction of chemical and temperature non-uniformities with downstream blade rows.

The wake model requires additional data added to the CNEWT run file: the beginning and ending circumferential location of the domain in radians, the rotation of the wakes (in rpm) referenced to the relative frame, and a set of profiles for the wakes (i.e. a circumferential location versus magnitude of each parameter). See the file "HPT1 rotor - Max power - Unsteady wake model" in Appendix D for a sample run file using the wake model.

A simple test was conducted to determine that the wake model was functioning properly after the addition of the new variables. An arbitrary wake profile was specified for each variable and a 6 degree single pitch turbine blade grid was run for a few thousand iterations. The expected rotation of the wake profile at the inlet is:

$$\theta = \theta_{ref} + \omega \cdot \tau \cdot N_{iter} \cdot \left(\frac{1\text{min}}{60\,\text{sec}}\right) \cdot \left(\frac{2 \cdot \pi\ \text{rad}}{1\,\text{rev}}\right) \cdot \left(\frac{180^\circ}{\pi\ \text{rad}}\right) \qquad (3.1)$$

Which equates to $\theta = 0.959^\circ$ for a θ_{ref}, the initial reference angle, of 0, a ω, the rotational speed, of 800 rpm, a τ, the timestep size, of 0.3331E-6 seconds, and a N_{iter}, the number of iterations, of 600. Figure 3.5 shows the result of the wake model test case over 600 iterations:

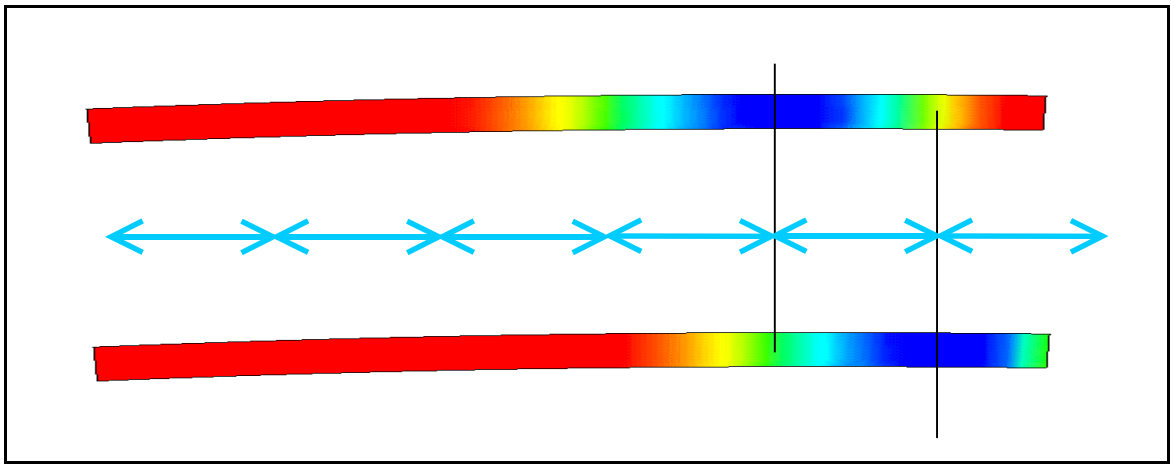

Figure 3.5 Wake model validation case, total temperature change over 600 iterations

The figure shows that the total temperature at the inlet had the specified profile and rotated the amount expected (roughly 1/6th of the domain). The wake model case was also checked for each variable and demonstrated to be working properly. More examples of the wake model can be found in Figure 5.22, the plots in Appendix D entitled "Time series of SO_3 mass fraction for one blade passing cycle", and the animations in Appendix F (Figure F.6 through Figure F.10).

3.4 CHAPTER SUMMARY

The purpose of this chapter was to present a brief overview of the modeling tools and discuss the improvements made to these tools during the course of this research. The existing modeling tools consist of the PRE grid generation code, PROCESS grid pre-conditioner code, POST grid post-processor code, CNEWT and CALCHEM flow-chemistry solvers, and CNEWTVS6 flow visualization code. The improvements made to the existing tools allow for more complicated geometries, multiple inlet and exits, improved execution time for solutions with chemistry, and a specification of a pressure, temperature, and species concentration deficits associated with a wake of an upstream blade or blade row.

In summary, the following is a list of all relevant points presented in this chapter:

- CNEWT and CALCHEM have been useful modeling tools for studying intra-engine trace species flow-chemistry problems. CNEWT is a code created by Lukachko [1] which was built upon the NEWT turbomachinery CFD code from Dawes [51]. CALCHEM is a simple, 1D version of CNEWT.

- Other supporting codes necessary for turbine chemistry modeling are PRE, PROCESS, POST, and CNEWTVS6.

- For more details on the structure and numerical mechanics of the codes, refer to "Research on the Science And Politics of the Atmospheric Effects of Aviation Debate" by Lukachko [1] as the primary source of information.

- In order to provide further insight into trace species characterization, improvements were made to existing modeling tools which include:

    - A new CAD solid model based grid generator which allows for the simulation of more complicated, arbitrary geometries. The output is a truly unstructured grid. The tools were in a developmental stage and a few difficulties were encountered with the translation step and numerical issues in the volume mesher. The VPFR was successfully meshed with the new grid generator.
    - Addition of multiple inlet/exit capability which allows for simulation of mixing flows. A test case and the Princeton VPFR were used to validate the multiple inlet/exit code modifications.
    - Addition of parallel chemistry subroutines. A test case showed a factor of 3.4 improvement in time on 6 compute nodes. The accuracy of the parallel chemistry modifications was verified.
    - Implemented and tested a wake model boundary condition for temperature and chemical species which allows for the investigation of unsteady effects including flow-chemistry interactions.

4 VALIDATION

Validation of the modeling tools is essential to provide confidence in the results obtained using the modeling methodology and verify new features or modifications. A validation exercise using the Princeton Variable Pressure Flow Reactor (VPFR) was pursued in order to prove the accuracy of the analysis tools and modeling methodology, in particular the new grid generator and multiple inlet/exit modifications. The chemical mechanism is a fundamental element underlying the intra-engine chemistry model. Thus the selection of an appropriate chemical mechanism for intra-engine chemistry modeling must also be justified. The convergence criteria and periodic boundary conditions are also important aspects of the model that must be proved accurate. All of the validation exercise presented help add to the knowledge base available to improve the modeling of intra-engine post-combustor chemistry.

4.1 CHAPTER OVERVIEW

The purpose of this chapter is to describe the validation exercises performed during the current research period. An attempt to benchmark the modeling tools through simulation of a flow reactor experiment is presented. Although it was not completely successful, it provided the opportunity to test several code improvements, investigate the limitations of the modeling tools, and analyze flow features of the reactor. A chemical mechanism study which investigated the effects of the chemical mechanism on intra-engine chemistry modeling and selected a mechanism for use in the NASA/DERA engine test modeling is detailed. This chapter also discusses a convergence criteria study which resulted in improved chemistry convergence indicators. Finally, a periodic boundary condition study is presented.

In summary, the following is a list of the main points of the chapter:

- An attempt was made to model a VPFR experiment to benchmark the accuracy of the modeling tools, however, a limitation to the flow solver prevented this ultimate objective. The flow features from the simulation did not match those expected from experimental data and empirical correlations.
- The VPFR validation exercise proved useful in validating some improvements to the modeling tools, namely the new fully unstructured grid generator and the multiple inlet/exit improvement.

- The modeling tools are limited to simulations of compressible flow.

- The Princeton VPFR may operate with large scale unsteady stall.

- A comparative study was performed on four chemical mechanisms by repeating a 1D and 2D computation from prior work. The selection of chemical mechanism does impact intra-engine chemistry modeling, however, accurately representing key reactions in the mechanism produces reasonable results.

    - The species concentration trends were the same for all mechanisms studied.
    - Prior work using Lukachko et al. (1998) was supported.
    - The Mueller et al. (2000)-truncated mechanism was selected for future intra-engine modeling.

- The original chemistry convergence criteria did not represent convergence of trace species well. They were improved by using the RMS average of individual species residuals for the species of interest to determine solution convergence.

- Periodic boundary conditions did not introduce any significant error into the computation, selected fluid and species variables at the boundary were within 1.6% of their corresponding value with no boundary present.

Section 4.2 is a overview of the Princeton Flow reactor modeling, further details are given in Appendix A. Section 4.3 describes a study into chemical mechanisms relevant to intra-engine chemistry modeling. Section 4.4 investigates the convergence criteria use for the modeling tools. Section 4.5 details a study of the periodic boundary conditions. Section 4.6 is the chapter summary.

4.2 PRINCETON FLOW REACTOR MODELING

The Princeton University's VPFR is an experimental apparatus specifically designed to measure chemical kinetic data at the high temperatures and pressures typical of energy conversion systems. The VPFR has an operating range for pressure from 0.3 to 20 atm and for temperature from 290 K to 1200 K. Design and operating characteristics of the VPFR are discussed in [25], [27] and [26]. The general concept behind the flow reactor is to flow a premixed reactive mixture of gaseous species through a cylindrical tube under highly controlled conditions to allow for convenient measurement of fluid and species quantities.

The VPFR is used extensively to help develop chemical mechanisms. In particular, the chemical mechanism used in the NASA/DERA engine test simulation was partially developed using the Princeton VPFR (see Section 4.3, Section 5, [23], or [24]). Therefore, there is an abundant set of detailed experimental data available, which can be used as a basis of comparison in benchmarking the modeling tools. In light of the fact that there is little validation data for actual engines available, modeling a VPFR experiment is a attractive alternative.

This validation effort was conducted in collaboration with Princeton University. Professor Fred Dryer and Mark Mueller made important contributions to the work presented in this section.

4.2.1 OBJECTIVES

The VPFR is ideally suited to evaluate the capability of the modeling tools to represent many flow features of interest , mixing, and passively reacting flow. The specific objectives of the VPFR modeling effort were to:

- Model a VPFR reacting flow experiment in order to benchmark the accuracy of the modeling tools
- Identify the capabilities and limitations of the analysis tools, specifically with regard to characterizing the flow features, mixing, and chemistry
- Help expand the modeling techniques by evaluating several new code features, in particular, the new grid generator, multiple inlet and exit planes, and parallel chemistry subroutines
- Help establish the modeling methodology applicable to studying intra-engine trace chemistry
- Provide an analysis that can identify potential improvements to the flow reactor facilities or experimental protocol

The approach was to model a published flow reactor experiment and compare the simulation data to the experimental data. The plan was to first simulate the flow-only, then flow with inert species, and finally passively reacting flow. In the end, the objectives of the flow reactor were reduced due to the restriction of the code to simulation of compressible flows.

4.2.2 SUMMARY OF RESULTS

Limitations of the flow solver hampered the ultimate objective of validating the modeling tools through a successful reacting flow simulation of the Princeton VPFR. Although the validation exercise was not completed, many code improvements were tested, a considerable amount was learned about the limitations of the tools, and some potential issues with the flow reactor design were identified.

The new fully unstructured CAD based grid generator was successfully used to mesh the complex VPFR geometry. At the time of the work in this thesis, the new grid generation tools were in a developmental state. A significant amount of geometry repair was required to obtain a surface mesh and the volume mesh routine had trouble with large aspect ratio geometries. The multiple inlet/exit improvement was qualitatively validated. It was found that the VPFR grid had to be initialized to a zero initial guess for the velocity to achieve a solution due to the complicated geometry.

Several experimental conditions were considered when applying the modeling tools. The assumptions for passively reacting flow, steady or unsteady flow, and compressible or incompressible flow need to be addressed prior to embarking on a modeling effort. Two cases were presented to illustrate the major findings of the VPFR validation efforts, a low Re case (Run 1) and a high Re case (Run 12). The results were evaluated by

comparison to experimentally and empirically derived diffuser pressure recovery coefficients and velocity profiles. The VPFR is designed to operate with fully developed turbulent flow in the test section, thus a typical "top hat" velocity profile was expected. An experimentally derived diffuser flow regime map indicated that the diffuser of the VPFR may operate in the regime of fully developed two dimensional stall.

In both cases presented, the velocity profiles were not similar to the "top hat" profiles expected in fully developed turbulent flow. They were peaked and had an inflected shape, which supported the notion that the flow reactor may operate with large scale unsteady stall and the experimental profiles could potentially be time-averages of unsteady flow. The point of first separation in the diffuser was anticipated based on the diffuser flow regime map. In an attempt to better resolve the velocity profile in the boundary layer region the grid was refined near the walls of the test section, however, the results did not improve. Also, the pressure recovery coefficients computed from the simulations did not match up well with the experimental data.

Finally, to further investigate the possible unsteadiness of the VPFR, Run 12 was extended by continuing the solution with a uniform timestep to give a proper unsteady solution. The shape of the velocity profiles was similar to the steady cases. Furthermore, negative velocity near the outer wall of the test section indicated separated, reversed flow. The unsteady computation exhibited a vortex shedding frequency which was close to one computed by an acoustic resonance calculation.

The modeling tools were developed for turbomachinery applications and are thus intended for compressible flow. Large errors in mass flow and the poor correlation of the experimental and empirical flow features in the VPFR simulations to those expected was attributed to the codes inability to compute incompressible flow. The Mach number in the test section of the flow reactor was on the order of 0.01 for the typical experimental conditions. The modeling tools are currently restricted to situations which the bulk of the flow field is above a Mach number of 0.2, an estimate for the compressibility limit for the code. Modifications to the modeling tools aimed at simulating incompressible flows were outside of the context of the research agenda, however, a similarity approach using non-dimensional analysis was considered to improve the solution quality.

Performing a solution using a similarity approach proved to be very difficult due to the large number of non-dimensional parameters required to match the flow features, mixing, and chemical kinetics. For example, dealing with the shock in the diffuser, matching the momentum ratio of the injection jet and the opposing primary flow, and scaling the flow reactor geometry to model a higher velocity flow would be difficult.

Overall, a complete reacting flow solution was never achieved for the VPFR. However, the validation exercise was a valuable learning experience in the development process since many code improvements were tested and the limitations of the tools were explored. A detailed account of the Princeton VPFR validation modeling can be found in Appendix A.

4.3 CHEMICAL MECHANISM STUDY

An important element of the modeling methodology is the chemical mechanism, which describes the reactions among the species set. Previous work [1] on intra-engine chemistry modeling used a chemical mechanism that was published in [28] and was developed by Aerodyne Research, Inc. [67]. The mechanism was created by doing a survey of the chemical kinetic literature and piecing together various reactions and sub mechanisms which were of interest to intra-engine trace species chemistry. The main species of interest to intra-engine modeling are HNO_2, HNO_3, SO_2, SO_3, H_2SO_4, OH, H_2O_2, HO_2, O, and NO_x [67]. However, the task of assembling literature data into a mechanism is not easy since much of the chemical kinetics data available is not applicable to the ranges of pressure and temperature experienced in gas turbine engines. As the current research was being conducted, a new chemical mechanism was developed at Princeton University based on flow reactor experimental data. This section contains a study of chemical mechanisms which was conducted to validate the prior intra-engine chemistry work [1] and possibly improve the chemical mechanism used in the modeling methodology.

4.3.1 OBJECTIVES

The main objective of this study is to investigate the sensitivity of the modeling methodology to the selection of chemical mechanism. In essence, the effects of chemical kinetics on trace species evolution were studied. The results of this study were used to validate prior work and to select the chemical mechanism for the NASA/DERA engine test modeling. The selected mechanism is also recommended for future intra-engine trace chemistry modeling.

4.3.2 APPROACH

The approach was to repeat prior calculations done by Lukachko [1] using variations of a mechanism which was based on recent experimental data. A comparative study was done on the following four turbine chemistry mechanisms:

- Lukachko et al. (1998) [28] (26 species and 74 reactions)
- Glarborg et al. (1996) [24] (56 species and 169 reactions)
- Mueller et al. (2000) – full [23] (56 species and 169 reactions)
- Mueller et al. (2000) – truncated [23] (29 species and 73 reactions)

The Glarborg et al. (1996) and Mueller et al. (2000) mechanisms were based on experimental data and contain similar species subsets as Lukachko et al. (1998). The Mueller et al. (2000) mechanism is based on the Glarborg et al. (1996) mechanism with modifications in the SO_x chemistry at higher pressures. The Mueller et al. (2000) mechanism is split into a full and truncated version. The full mechanism contains the complete set of

reactions as published in [23]. The truncated mechanism was made by eliminating reactions thought to have minimal effect on the trace species of interest in the full mechanism, and was created in hopes of reducing the computational burden in the high fidelity modeling.

The 1D ASE engine calculations and the Cambridge No 2 turbine rotor cases which were presented in [1] were selected as the baseline for comparison.

4.3.3 1D ASE ENGINE CYCLE

A 1D analysis was performed using profile data for the ASE engine, which is repeated in Figure 4.1 for reference.

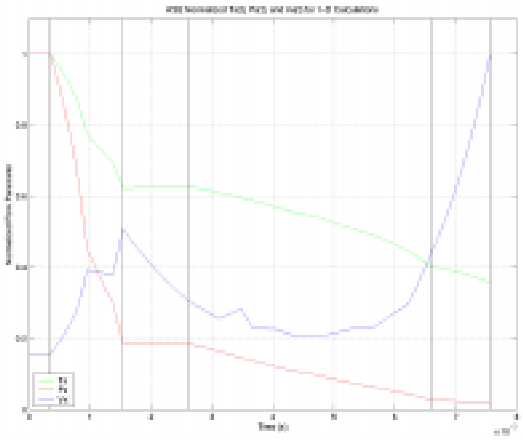

Figure 4.1 1D profile data for ASE engine [1]

Four of the cases presented in [1] were selected as the basis of comparison. The cases were: Case 1, the baseline case with non-equilibrium initial conditions and mass addition, Case 2, an equilibrium combustor exit condition, Case 8, a lower temperature case, and Case 15, a case with no mass addition. The results of these simulations is given in Figure 4.2, Figure 4.3, Figure 4.4, Figure 4.5, respectively. A summary of the results is given in Table 4.1, Table 4.2, Table 4.3, and Table 4.4, respectively. In these figures and tables the Mueller et al. mechanisms are labeled “Princeton.”

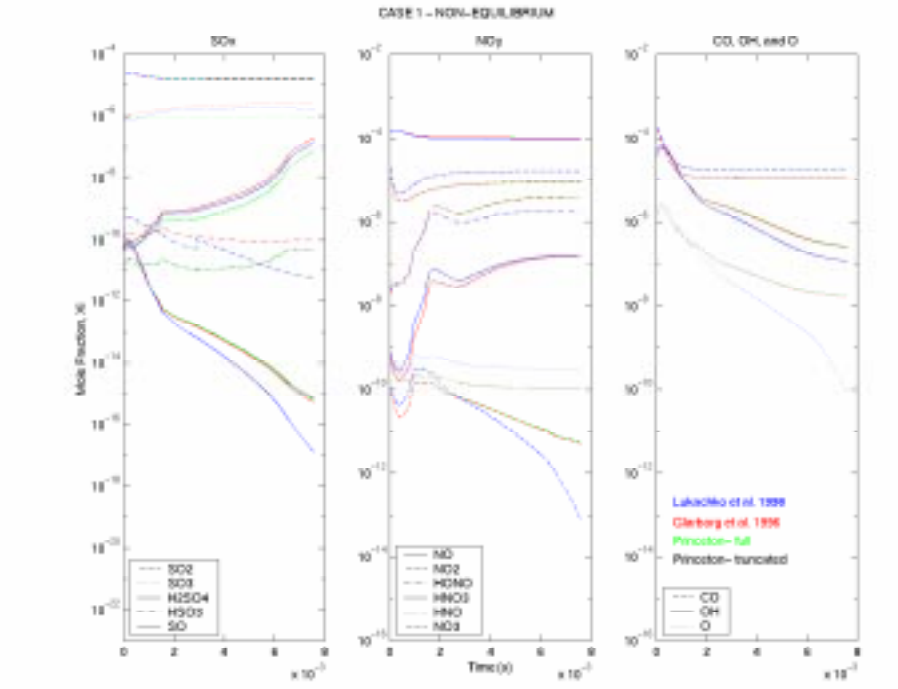

Figure 4.2 Chemical mechanism study for Case 1

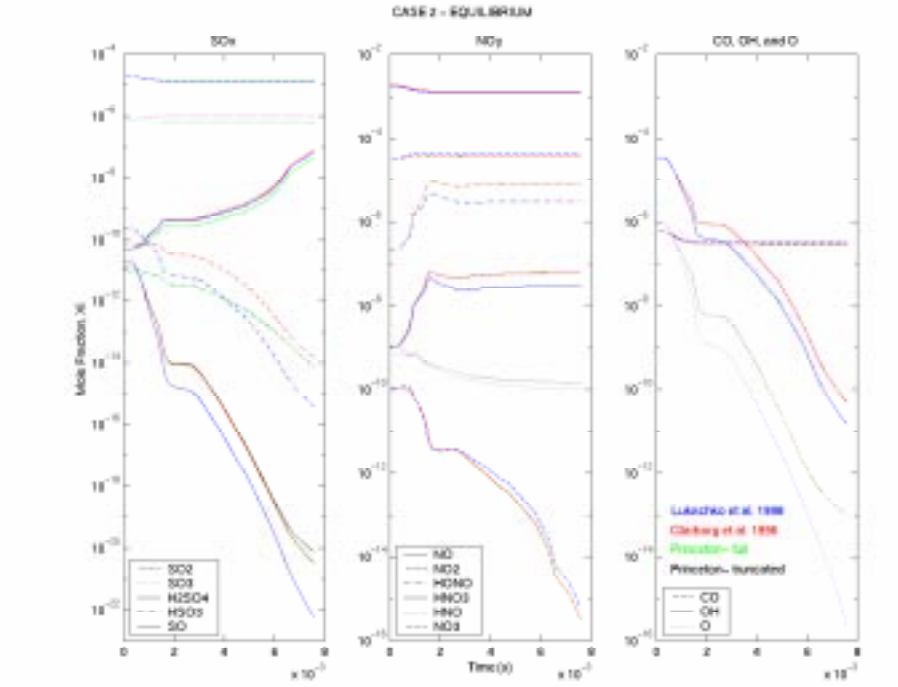

Figure 4.3 Chemical mechanism study for Case 2

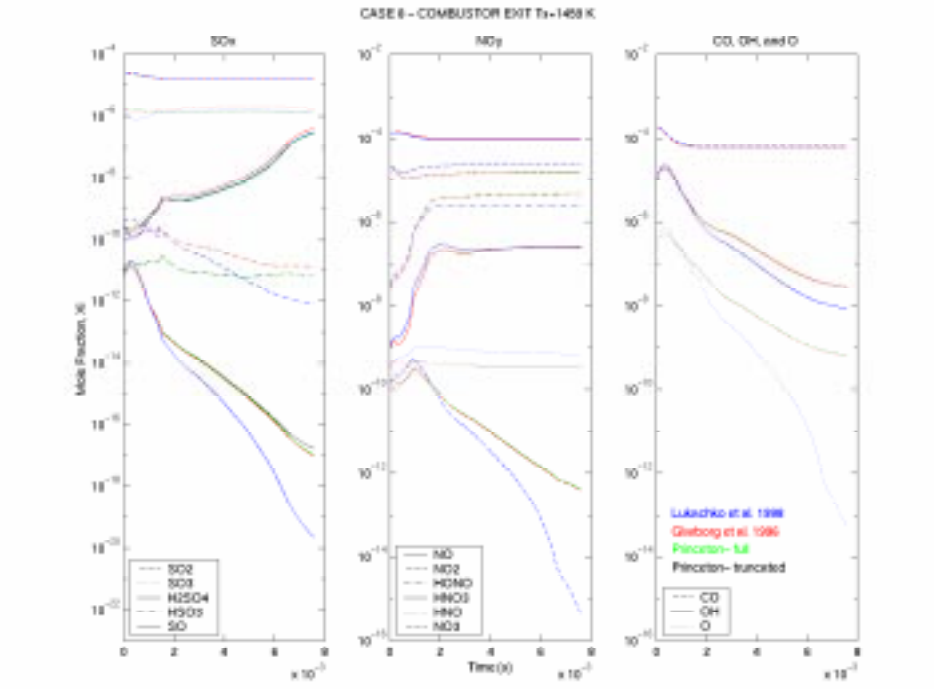

Figure 4.4 Chemical mechanism study for case 8

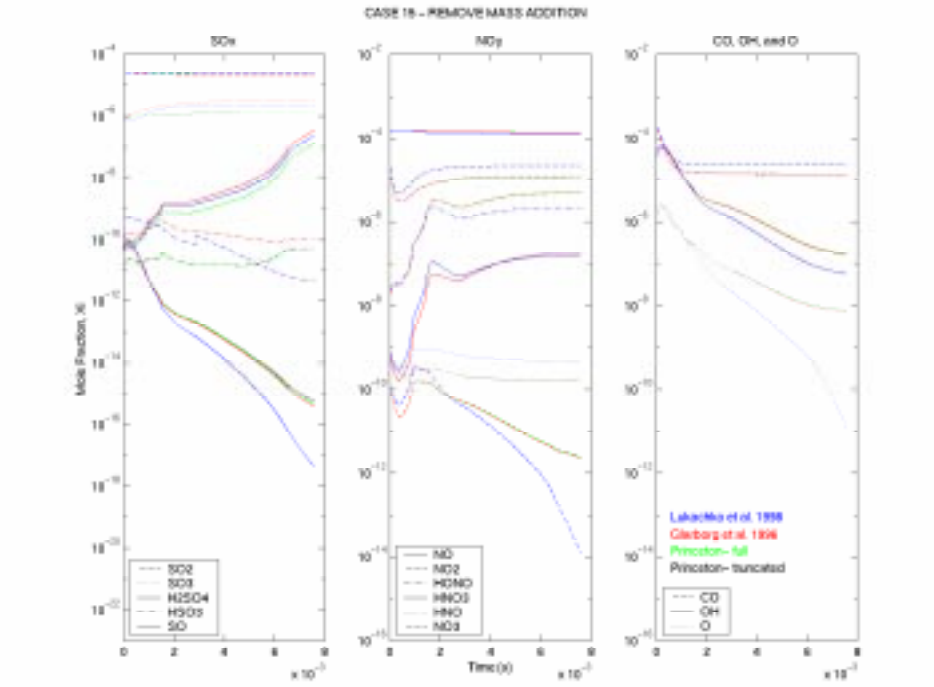

Figure 4.5 Chemical mechanism study for case 15

	Nozzle Exit (ppmv) - Case 1: Non-Equlibrium IC's														
	JGR paper			Lukachko			Glarborg			Princeton - full			Princeton - truncated		
	comb exit	nozzle exit	noz/comb	comb exit	nozzle exit	noz/comb	comb exit	nozzle exit	noz/comb	comb exit	nozzle exit	noz/comb	comb exit	nozzle exit	noz/comb
NO	130	95.6	0.74	129.68	95.58	0.74	129.68	98.92	0.76	129.68	99.03	0.76	129.68	99.03	0.76
NO2	14.5	10.4	0.72	14.47	10.38	0.72	14.47	5.79	0.40	14.47	5.63	0.39	14.47	5.63	0.39
HNO	0.012			0.011989	0.000284	0.024	0.011989	0.000098	0.008	0.011989	0.000099	0.008	0.011989	0.000099	0.008
HNO2	0.14	1.21	8.64	0.140	1.207	8.60	0.140	2.451	17.45	0.140	2.503	17.82	0.140	2.501	17.81
HNO3	0.000471	0.0737	156.48	0.0004712	0.0737322	156.49	0.0004712	0.0717786	152.34	0.0004712	0.0720466	152.91	0.0004712	0.0720058	152.83
NO3	0.0000432			4.319E-05	3.847E-08	0.00089	4.319E-05	2.384E-06	0.05521	4.319E-05	2.492E-06	0.05770	4.319E-05	2.489E-06	0.05764
OH	60	0.196	0.0033	59.9970	0.1959	0.0033	59.9970	0.4364	0.0073	59.9970	0.4488	0.0075	59.9970	0.4486	0.0075
O	1.47	0.000157	0.00011	1.4737146	0.0001573	0.00011	1.4737146	0.0292526	0.01985	1.4737146	0.0314803	0.02136	1.4737146	0.0314410	0.02133
SO	0.0000136			1.355E-05	8.226E-12	6.070E-07	1.355E-05	3.274E-10	2.416E-05	1.355E-05	3.815E-10	2.814E-05	1.355E-05	4.446E-10	3.280E-05
SO2	10.6	7.46	0.70	10.619	7.461	0.70	10.619	7.176	0.68	10.619	7.768	0.73	10.619	7.767	0.73
SO3	0.332	0.635	1.91	0.3316	0.6346	1.91	0.3316	0.9020	2.72	0.3316	0.3467	1.05	0.3316	0.3470	1.05
HSO3	0.0000985			9.849E-05	2.151E-06	0.022	9.849E-05	3.695E-05	0.375	9.849E-05	1.818E-05	0.185	9.849E-05	1.818E-05	0.185
H2SO4	0.0000209	0.0416	1990.43	0.0000209	0.0415417	1988.02	0.0000209	0.0583012	2790.06	0.0000209	0.0223709	1070.58	0.0000209	0.0223870	1071.35
CO	201			200.67	18.14	0.090	200.67	11.53	0.057	200.67	11.49	0.057	200.67	11.47	0.057
CO2	50300			50300.71	37507.40	0.75	50300.71	37514.09	0.75	50300.71	37514.11	0.75	50300.71	37514.13	0.75
NOy	144.65	107.28	0.74	144.31	107.23	0.74	144.31	107.23	0.74	144.31	107.23	0.74	144.31	107.23	0.74
SOx	10.93	8.14	0.74	10.95	8.14	0.74	10.95	8.14	0.74	10.95	8.14	0.74	10.95	8.14	0.74
COx	50501			50501.38	37525.54	0.74	50501.38	37525.62	0.74	50501.38	37525.60	0.74	50501.38	37525.60	0.74
(SO3+H2SO4)/SOx	3.04%	8.32%		3.03%	8.31%		3.03%	11.80%		3.03%	4.54%		3.03%	4.54%	
(HNO2+HNO3)/NOy	0.10%	1.20%		0.10%	1.19%		0.10%	2.35%		0.10%	2.40%		0.10%	2.40%	
CO/COx	0.40%			0.40%	0.05%		0.40%	0.03%		0.40%	0.03%		0.40%	0.03%	

Table 4.1 Summary of results from chemical mechanism study case 1

	Nozzle Exit (ppmv) - Case 2: Equlibrium IC's														
	JGR paper			Lukachko			Glarborg			Princeton - full			Princeton - truncated		
	comb exit	nozzle exit	noz/comb	comb exit	nozzle exit	noz/comb	comb exit	nozzle exit	noz/comb	comb exit	nozzle exit	noz/comb	comb exit	nozzle exit	noz/comb
NO	1670	1230	0.74	1655.80	1215.82	0.73	1765.51	1302.51	0.74	1765.51	1302.61	0.74	1765.51	1299.06	0.74
NO2	19	28.6	1.51	20.94	28.45	1.36	21.05	23.78	1.13	21.05	23.67	1.12	21.05	23.62	1.12
HNO				0.000650	0.000099	0.152	0.001140	0.000140	0.123	0.001140	0.000140	0.123	0.001140	0.000139	0.122
HNO2	0.141	1.95	13.83	0.141	1.922	13.65	0.141	5.103	36.27	0.141	5.111	36.33	0.141	5.103	36.27
HNO3	0.000471	0.0131	27.81	0.0004951	0.0129257	26.11	0.0004948	0.0275126	55.60	0.0004948	0.0274213	55.41	0.0004948	0.0274091	55.39
NO3				5.034E-05	2.952E-10	0.00001	5.031E-05	1.617E-10	0.00000	5.031E-05	1.602E-10	0.00000	5.031E-05	1.602E-10	0.00000
OH	60	0.0000244	0.0000	57.2072	0.0000	0.0000	57.2022	0.0001	0.0000	57.2022	0.0001	0.0000	57.2022	0.0001	0.0000
O	1.47	0	0.00000	1.5547043	0.0000000	0.00000	1.5544046	0.0000002	0.00000	1.5544046	0.0000002	0.00000	1.5544052	0.0000002	0.00000
SO				1.075E-05	3.662E-17	3.408E-12	1.059E-05	2.027E-15	1.915E-10	1.059E-05	2.132E-15	2.014E-10	1.059E-05	4.658E-15	4.399E-10
SO2	10.6	7.71	0.73	8.713	6.324	0.73	8.712	6.275	0.72	8.712	6.464	0.74	8.712	6.445	0.74
SO3	0.332	0.402	1.21	0.2853	0.3440	1.21	0.2858	0.4072	1.42	0.2858	0.2283	0.80	0.2858	0.2290	0.80
HSO3				7.659E-05	1.458E-10	0.000	2.790E-05	5.698E-09	0.000	2.790E-05	2.745E-09	0.000	4.177E-06	2.740E-09	0.001
H2SO4	0.0000209	0.0263	1258.37	0.0000153	0.0193242	1261.53	0.0000152	0.0227225	1496.97	0.0000152	0.0127387	839.23	0.0000152	0.0127421	839.45
CO				0.62	0.35	0.575	0.62	0.32	0.521	0.62	0.32	0.521	0.62	0.32	0.519
CO2				41134.12	30569.60	0.74	41134.12	30652.69	0.75	41134.12	30652.68	0.75	41134.14	30569.64	0.74
NOy	1689.14	1260.56	0.75	1676.89	1246.21	0.74	1786.69	1331.42	0.75	1786.69	1331.42	0.75	1786.69	1327.81	0.74
SOx	10.93	8.14	0.74	9.00	6.69	0.74	9.00	6.71	0.75	9.00	6.71	0.75	9.00	6.69	0.74
COx				41134.73	30569.95	0.74	41134.74	30653.01	0.75	41134.74	30653.00	0.75	41134.76	30569.96	0.74
(SO3+H2SO4)/SOx	3.04%	5.26%		3.17%	5.43%		3.18%	6.41%		3.18%	3.59%		3.18%	3.61%	
(HNO2+HNO3)/NOy	0.01%	0.16%		0.01%	0.16%		0.01%	0.39%		0.01%	0.39%		0.01%	0.39%	
CO/COx				0.00%	0.00%		0.00%	0.00%		0.00%	0.00%		0.00%	0.00%	

Table 4.2 Summary of results from chemical mechanism study case 2

	Nozzle Exit (ppmv) - Case 8: Combustor Exit Ts=1459K														
	JGR paper (BASELINE-Case 1)			Lukachko			Glarborg			Princeton - full			Princeton - truncated		
	comb exit	nozzle exit	noz/comb	comb exit	nozzle exit	noz/comb	comb exit	nozzle exit	noz/comb	comb exit	nozzle exit	noz/comb	comb exit	nozzle exit	noz/comb
NO	130	95.6	0.74	129.69	90.76	0.70	129.69	94.55	0.73	129.69	94.63	0.73	129.69	94.63	0.73
NO2	14.5	10.4	0.72	14.47	14.80	1.02	14.47	9.65	0.67	14.47	9.53	0.66	14.47	9.53	0.66
HNO	0.012			0.000220	0.000664	3.013	0.000220	0.000312	1.419	0.000220	0.000314	1.424	0.000220	0.000313	1.421
HNO2	0.14	1.21	8.64	0.097	1.518	15.67	0.097	2.867	29.59	0.097	2.906	30.00	0.097	2.907	30.00
HNO3	0.000471	0.0737	156.48	0.0004941	0.1152097	233.19	0.0004941	0.1202412	243.37	0.0004941	0.1211621	245.24	0.0004941	0.1210178	244.95
NO3	0.0000432			2.408E-05	2.226E-10	0.00001	2.408E-05	1.858E-07	0.00772	2.408E-05	1.957E-07	0.00813	2.408E-05	1.953E-07	0.00811
OH	60	0.196	0.0033	17.4575	0.0147	0.0008	17.4575	0.0465	0.0027	17.4575	0.0467	0.0027	17.4575	0.0467	0.0027
O	1.47	0.000157	0.00011	0.2125991	0.0000001	0.00000	0.2125991	0.0011160	0.00525	0.2125991	0.0011912	0.00560	0.2125991	0.0011892	0.00559
SO	0.0000136			1.313E-06	1.431E-14	1.090E-08	1.313E-06	5.944E-12	4.526E-06	1.313E-06	6.550E-12	4.987E-06	1.313E-06	1.043E-11	7.944E-06
SO2	10.6	7.46	0.70	10.259	7.562	0.74	10.259	7.367	0.72	10.259	7.585	0.74	10.259	7.594	0.74
SO3	0.332	0.635	1.91	0.6661	0.4658	0.70	0.6661	0.6303	0.95	0.6661	0.4473	0.67	0.6661	0.4403	0.66
HSO3	0.0000985			5.618E-05	2.931E-07	0.005	5.618E-05	5.067E-06	0.090	5.618E-05	2.378E-06	0.042	5.618E-05	2.378E-06	0.042
H2SO4	0.0000209	0.0416	1990.43	0.0000779	0.0897012	1151.70	0.0000779	0.1203958	1545.79	0.0000779	0.0854637	1097.29	0.0000779	0.0841302	1080.17
CO	201			200.68	68.34	0.341	200.68	61.89	0.308	200.68	61.89	0.308	200.68	61.82	0.308
CO2	50300			50302.96	37457.52	0.74	50302.96	37464.05	0.74	50302.96	37464.04	0.74	50302.96	37464.11	0.74
NOy	144.65	107.28	0.74	144.26	107.19	0.74	144.26	107.19	0.74	144.26	107.19	0.74	144.26	107.19	0.74
SOx	10.93	8.14	0.74	10.93	8.12	0.74	10.93	8.12	0.74	10.93	8.12	0.74	10.93	8.12	0.74
COx				50503.63	37525.87	0.74	50503.63	37525.94	0.74	50503.63	37525.93	0.74	50503.63	37525.93	0.74
(SO3+H2SO4)/SOx	3.04%	8.32%		6.10%	6.84%		6.10%	9.25%		6.10%	6.56%		6.10%	6.46%	
(HNO2+HNO3)/NOy	0.10%	1.20%		0.07%	1.52%		0.07%	2.79%		0.07%	2.82%		0.07%	2.82%	
CO/COx				0.40%	0.18%		0.40%	0.16%		0.40%	0.16%		0.40%	0.16%	

Table 4.3 Summary of results from chemical mechanism study case 8

	Nozzle Exit (ppmv) - Case 15: Remove Mass Addition														
	JGR paper (BASELINE-Case 1)			Lukachko			Glarborg			Princeton - full			Princeton - truncated		
	comb exit	nozzle exit	noz/comb	comb exit	nozzle exit	noz/comb	comb exit	nozzle exit	noz/comb	comb exit	nozzle exit	noz/comb	comb exit	nozzle exit	noz/comb
NO	130	95.6	0.74	129.68	128.87	0.99	129.68	133.36	1.03	129.68	133.52	1.03	129.68	133.52	1.03
NO2	14.5	10.4	0.72	14.47	14.02	0.97	14.47	7.84	0.54	14.47	7.62	0.53	14.47	7.62	0.53
HNO	0.012			0.011989	0.000445	0.037	0.011989	0.000151	0.013	0.011989	0.000152	0.013	0.011989	0.000151	0.013
HNO2	0.14	1.21	8.64	0.140	1.370	9.76	0.140	3.043	21.67	0.140	3.105	22.12	0.140	3.104	22.11
HNO3	0.000471	0.0737	156.48	0.0004712	0.0737527	156.53	0.0004712	0.0844899	179.32	0.0004712	0.0846823	179.73	0.0004712	0.0846364	179.63
NO3	0.0000432			4.319E-05	5.987E-09	0.00014	4.319E-05	1.055E-06	0.02442	4.319E-05	1.110E-06	0.02569	4.319E-05	1.108E-06	0.02566
OH	60	0.196	0.0033	59.9970	0.0982	0.0016	59.9970	0.2819	0.0047	59.9970	0.2886	0.0048	59.9970	0.2884	0.0048
O	1.47	0.000157	0.00011	1.4737146	0.0000231	0.00002	1.4737146	0.0129632	0.00880	1.4737146	0.0140452	0.00953	1.4737146	0.0140270	0.00952
SO	0.0000136			1.355E-05	2.950E-12	2.177E-07	1.355E-05	2.418E-10	1.784E-05	1.355E-05	2.836E-10	2.092E-05	1.355E-05	3.623E-10	2.673E-05
SO2	10.6	7.46	0.70	10.619	10.124	0.95	10.619	9.711	0.91	10.619	10.471	0.99	10.619	10.471	0.99
SO3	0.332	0.635	1.91	0.3316	0.7602	2.29	0.3316	1.1410	3.44	0.3316	0.4415	1.33	0.3316	0.4416	1.33
HSO3	0.0000985			9.849E-05	1.574E-06	0.016	9.849E-05	3.723E-05	0.378	9.849E-05	1.876E-05	0.191	9.849E-05	1.877E-05	0.191
H2SO4	0.0000209	0.0416	1990.43	0.0000209	0.0674211	3226.50	0.0000209	0.0999795	4784.62	0.0000209	0.0386312	1848.73	0.0000209	0.0386399	1849.15
CO	201			200.67	23.49	0.117	200.67	14.70	0.073	200.67	14.66	0.073	200.67	14.63	0.073
CO2	50300			50300.71	50483.23	1.00	50300.71	50492.15	1.00	50300.71	50492.16	1.00	50300.71	50492.19	1.00
NOy	144.65	107.28	0.74	144.31	144.33	1.00	144.31	144.33	1.00	144.31	144.33	1.00	144.31	144.33	1.00
SOx	10.93	8.14	0.74	10.95	10.95	1.00	10.95	10.95	1.00	10.95	10.95	1.00	10.95	10.95	1.00
COx				50501.38	50506.72	1.00	50501.38	50506.85	1.00	50501.38	50506.82	1.00	50501.38	50506.82	1.00
(SO3+H2SO4)/SOx	3.04%	8.32%		3.03%	7.56%		3.03%	11.33%		3.03%	4.38%		3.03%	4.38%	
(HNO2+HNO3)/NOy	0.10%	1.20%		0.10%	1.00%		0.10%	2.17%		0.10%	2.21%		0.10%	2.21%	
CO/COx				0.40%	0.05%		0.40%	0.03%		0.40%	0.03%		0.40%	0.03%	

Table 4.4 Summary of results from chemical mechanism study case 15

The results show that the species concentration evolution trends are the same for all the mechanisms at the conditions considered. The Mueller et al. (2000) mechanism is based on the Glarborg et al. (1996) mechanism except for modifications in the SO_x chemistry and, as can be expected, the species concentration profiles are similar for the two except for SO_x species. In all cases, the SO_x conversion was less than 12% for all mechanisms analyzed. There was a notable difference in the exit plane species concentrations for the Lukachko et al. (1998), Glarborg et al. (1998), and Mueller et al. (2000)-full mechanisms. Specifically the SO_x conversion from the combustor exit to the nozzle exit for Case 1 was 8.3%, 11.8%, and 4.5% for those mechanisms, respectively. And the SOx conversion for Case 8 was 6.8%, 9.3%, and 6.6%, respectively. This would suggest that the new kinetic data incorporated into the Mueller et al. (2000) mechanisms suppresses SO_x oxidation, especially at higher temperatures and pressures relative to the Glarborg et al. (1996) mechanism. In general the Lukachko et al. (1998) mechanism was in between the Glarborg et al (1996) and Mueller et al (2000) mechanisms. It was also found that the Mueller et al. (2000)-truncated mechanism produced results that were within 1% of the Mueller et al. (2000)-full mechanism in each 1D case.

4.3.4 2D CAMBRIDGE NO 2 TURBINE ROTOR BLADE ROW

The 2D high fidelity model for the Cambridge No 2 turbine rotor was also re-run using the Lukachko et al. (1998) and Mueller et al. (2000)-truncated mechanisms. An example result for the Lukachko et al. (1998) mechanism case is given in Figure 4.6. The species contours for both mechanisms looked similar, and the species gradients were largely driven by local temperature gradients. The mass averaged SO_x conversion across the blade row for the Lukachko et al (1998) and Mueller et al. (2000)-truncated cases were 2.928% and 2.964%, respectively.

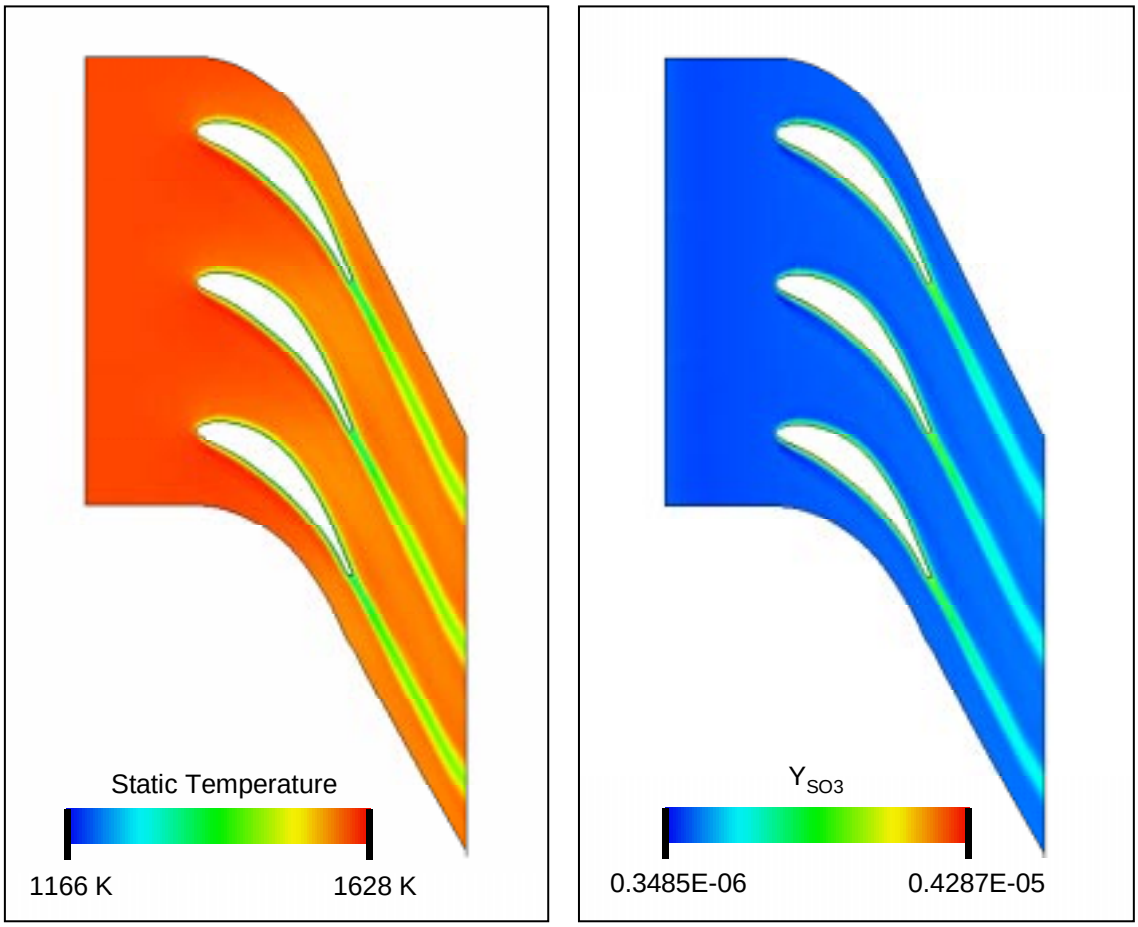

Figure 4.6 Example result of 2D calculation on Cambridge No 2 turbine rotor with Lukachko et al (1998) mechanism

4.3.5 CONCLUSIONS

Overall, the 1D ASE engine cycle and 2D Cambridge No 2 turbine rotor blade row calculations both show that the species concentration trends are the same and in particular the range of SO_x conversion for a given case was 2.7% to 7.3% for all the mechanisms. This result would imply that the chemical mechanism does have some impact on the results of the modeling effort. However, as long as the key reactions are included in the mechanism the results are in fairly good agreement. Therefore, the prior calculations [1] were substantiated by new experimentally-derived kinetic data.

The modifications to the SO_x chemistry at high pressures in the Mueller et al. (2000) mechanisms were based on experimental data and are considered an improvement with respect to the turbine chemistry mechanism previously employed. Therefore, the Mueller et al. (2000)-truncated mechanism was selected as the best option

for the current turbine chemistry studies since it requires less computational expense and is nearly as accurate as the Mueller et al. (2000)-full mechanism which was based on recent experimental data.

4.4 CONVERGENCE CRITERIA STUDY

The initial implementation of CNEWT used the fluid convergence indicators from the NEWT code [49] along with two very simple convergence indicators on chemistry. Due to the small quantities involved in research on trace chemical species it is essential that the chemistry solution is fully converged to ensure the accuracy of the results. A study of the chemistry convergence indicators was conducted using the Cambridge No. 2 turbine rotor and the Lukachko et al. (1998) chemical mechanism.

4.4.1 OBJECTIVES

The objectives of the convergence criteria study were to:

- Assess the capability of the original convergence indicators
- Propose potential improvements to the chemistry convergence criteria
- Investigate the effectiveness of the newly proposed convergence indicators

4.4.2 BACKGROUND

Convergence criteria originally used in the CNEWT code consisted of a timestep-normalized RMS average of all species residuals combined (i.e. the average of the sum of species residuals in each cell) and an overall maximum nodal species residual. These original convergence indicators are plotted in Figure 4.7 for the Cambridge No 2 turbine rotor test case.

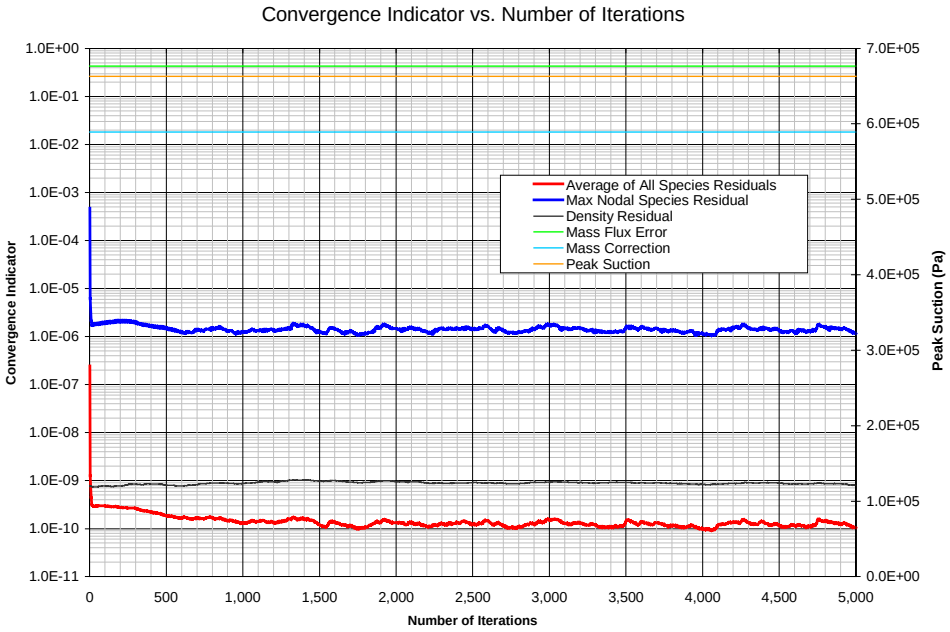

Figure 4.7 Original CNEWT fluid and chemistry convergence indicators

From the figure, it appears that the maximum nodal species residual converged by 600 iterations and the combined average converged by 1,000 iterations for the test case. The fluid solution was already converged at the start of this solution. It was suspected that the trace species could still be changing after the average and maximum criteria had converged since the trace species would play a minor roll in the average calculation and would not necessarily be the maximum residual. In other words, the average and maximum quantities could mask the actual changes in the chemistry solution since large portions of the domain could be converged while small portions could be changing significantly. Several potentially improved convergence criteria were proposed, including monitoring the maximum nodal mass fraction for individual species of interest, the RMS average for individual species of interest, or the maximum nodal residual divided by that species mass fraction.

4.4.3 RESULTS

First, a straightforward visual approach was employed to determine the actual convergence for a few trace species of interest. The chemical variables were re-initialized for the test case and it was set-up to re-run with a solution file dumped every 100 iterations. Time history plots for the species evolution of O, OH, and SO_3 mass fraction were generated for 5,000 iterations. As an example, the mass fraction of O is plotted at several points during the solution in Figure 4.8. Also, animations for all three species are included in Appendix F.

A visual inspection of all the time evolution results, suggests that solution has converged by about 3,000-3,500 iterations. Therefore, monitoring the overall maximum or combined average convergence quantities can be misleading.

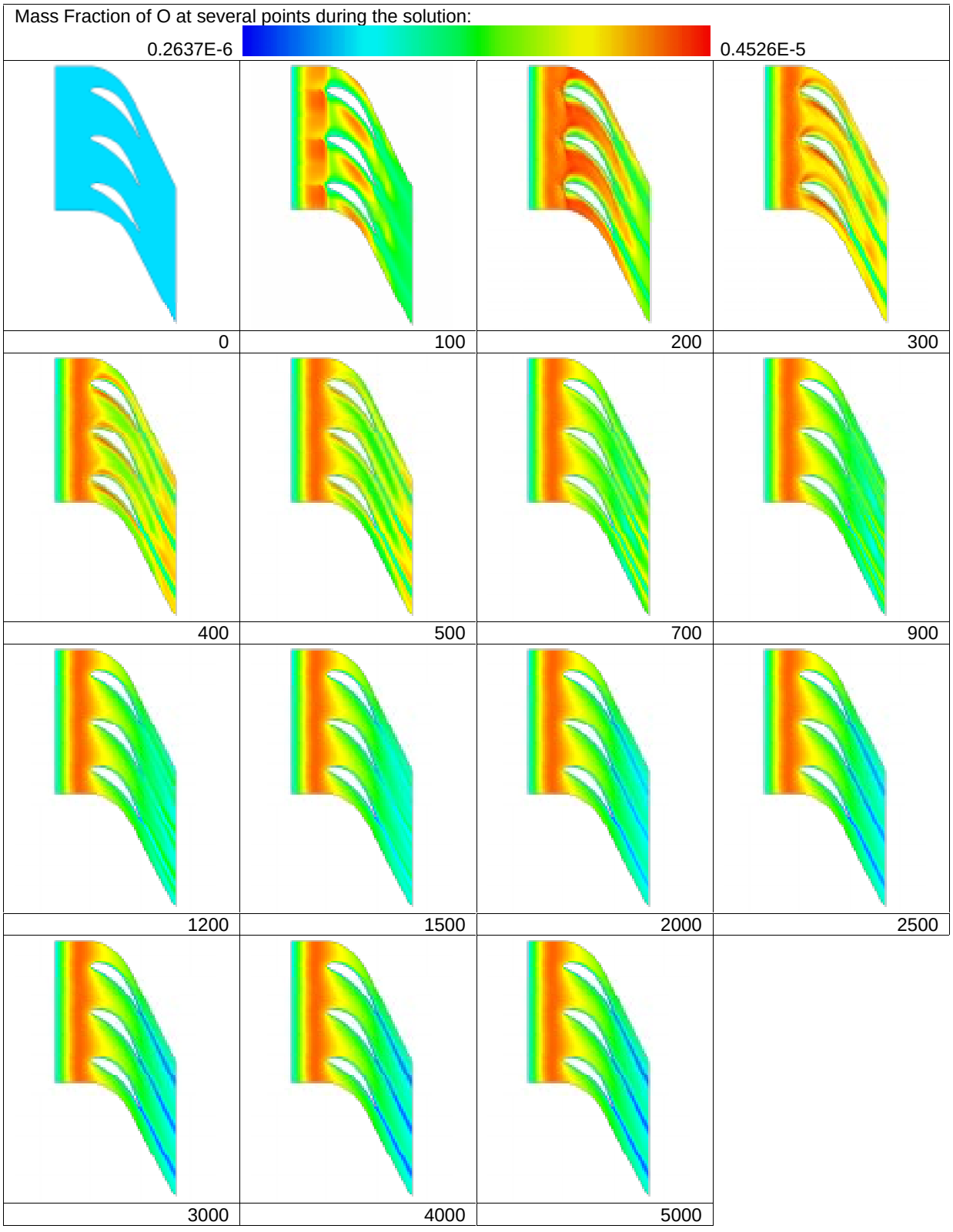

Figure 4.8 Convergence of O mass fraction by visual time evolution

As a first attempt at improving the chemical convergence criteria, monitoring the maximum species mass fraction within the entire domain for individual species of interest was tried since the data was easily obtainable. Figure 4.9 plots the maximum and minimum species mass fraction for O, OH, and SO_3.

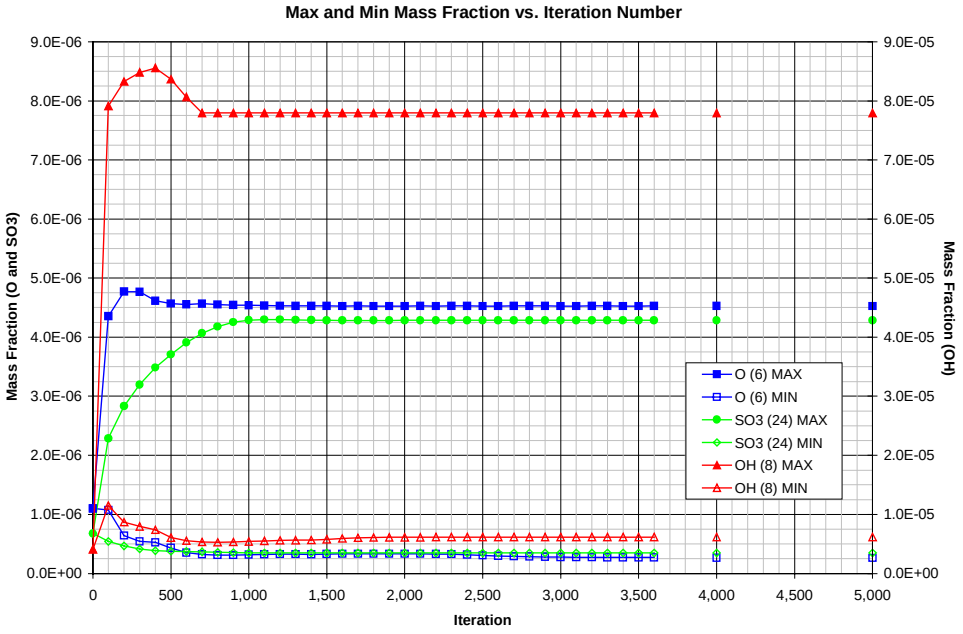

Figure 4.9 Maximum and minimum species mass fraction versus iteration

The solution appears to have converged by about 1,000 iterations for the three species selected. Although this technique appears better than monitoring the overall maximum nodal species residual, it is still susceptible to the problem of not capturing the changes throughout the entire domain.

Next, the code was modified to output the timestep-normalized RMS average of each species residual separately. Figure 4.10 shows a comparison of the original convergence indicators and these individual species averages. In the figure it is evident that the major species, in particular N_2 in this case, have an overwhelming impact on the original convergence indicators. Furthermore, many of the trace species residuals are still decreasing after the maximum and combined average have converged. On the other hand, all of the individual species residuals appear converged by about 4,000 iterations which is in line with the visual time evolution result. However, it is important to note that some computational overhead is required to calculate the extra convergence indicators. Overall, the results presented in this section suggest that it is best to monitor the RMS average for individual species of interest to determine solution convergence. This technique was employed for the NASA/DERA engine test simulations using O, OH, SO_2, SO_3, NO, NO_2, and NO_3 (see Appendix B).

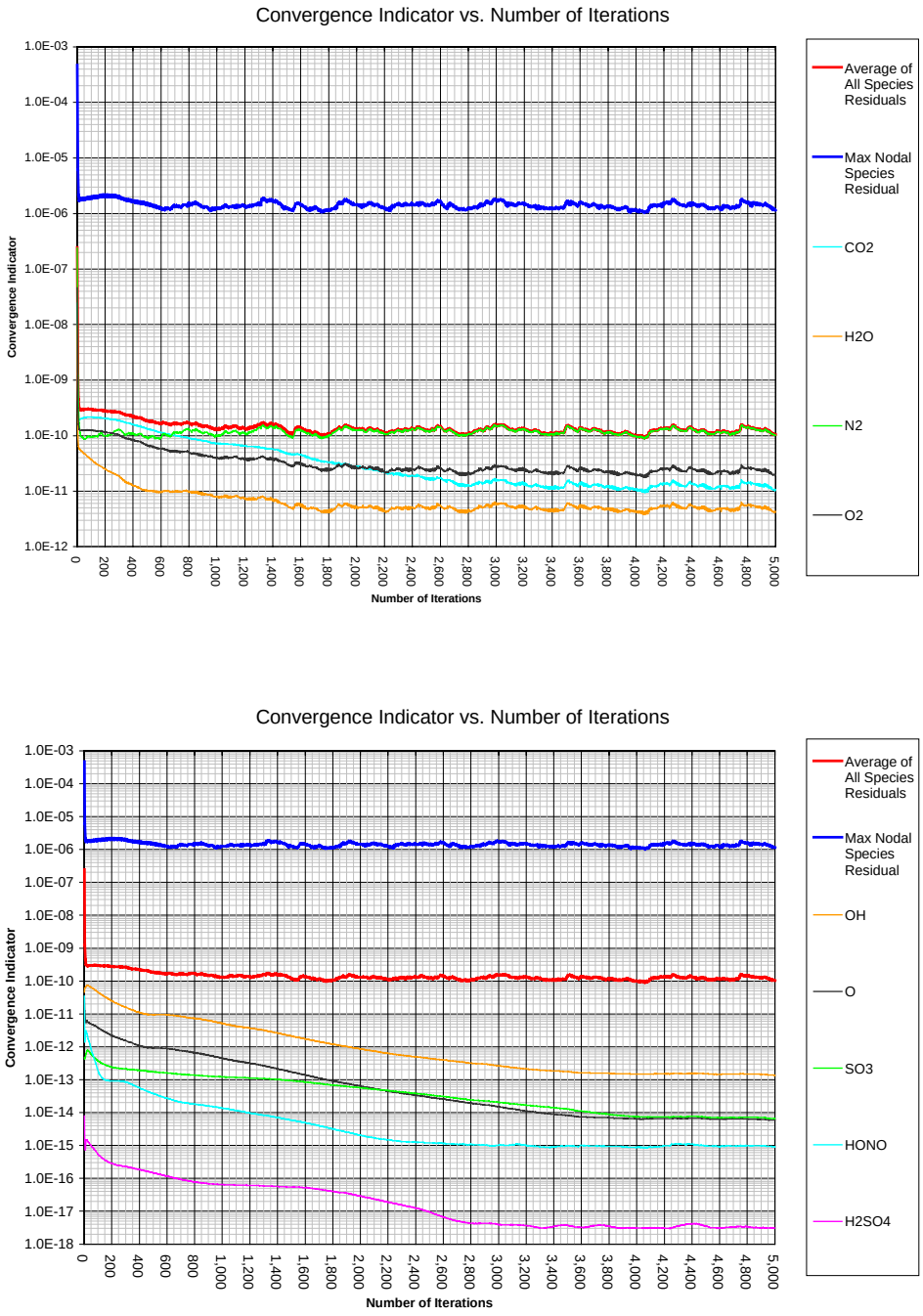

Figure 4.10 Comparison of original and new chemistry convergence indicators for major species (top) and trace species (bottom)

4.5 PERIODIC BOUNDARY CONDITION STUDY

Previous turbomachinery blade row computations using CNEWT were performed on a three pitch grid [1]. This approach helped ensure that the central blade pitch was unaffected by the periodic boundary conditions applied on the circumferential boundaries of the domain at the expense of a significant computational burden. The results from the three pitch solutions in [1] showed no apparent errors that could be attributed to the periodic boundary conditions. Therefore, a specific study of the periodic boundary conditions was conducted using the Cambridge No. 2 turbine rotor and the Lukachko et al. (1998) chemical mechanism.

4.5.1 OBJECTIVE AND BACKGROUND

The objective of this study was to validate the accuracy of the periodic boundary conditions. A converged solution of the Cambridge No. 2 turbine rotor on the three pitch grid was interrogated to determine the effects of the periodic boundary conditions on the solution variables. Seven axial stations were chosen for comparison; one near the inlet, one near the exit, one just before the blade, one just after the blade, and three within the blade. The values for Y_O, Y_{OH}, Y_{SO3}, V_x, V_t, V_r, P, T, and ρ were compared at the boundaries of each blade pitch. The circumferential locations were labeled 0%, 33%, 66%, and 100%, with the 0% and 100% locations being the boundaries with the prescribed periodic boundary conditions. Figure 4.11 shows the axial stations and circumferential locations that were analyzed in this study.

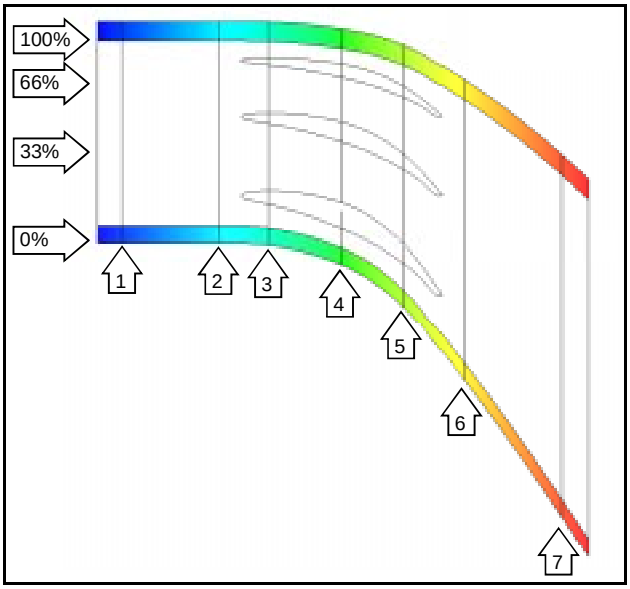

Figure 4.11 Stations for periodic boundary condition study

4.5.2 RESULTS

The results of the periodic boundary condition study are summarized in Table 4.5. Excluding V_r, the maximum error relative to the value at the 0% location was found to be 1.6%. The psuedo-2D grid had only two cells in the radial direction, and thus V_r had a very small value and was not resolved.

Summary of Results
(Error in % relative to 0% distance)

%	Distance	Y (O)	Y (OH)	Y (SO3)	Va	Vt	Vr	P	T	density
Station 1 (X = -0.090m)										
0	0.00616	0.00000	0.00000	0.00000	0.00000	0.00000	0.00000	0.00000	0.00000	0.00000
33	0.08647	1.57524	0.96817	0.51614	0.02657	0.04238	21.92809	0.00036	0.00000	0.00000
66	0.16677	1.58134	0.97314	0.51746	0.04114	0.00618	21.91245	0.00238	0.00062	0.00164
100	0.24707	0.00000	0.00019	0.00000	0.00000	0.00000	0.00344	0.00000	0.00000	0.00000
Station 2 (X = -0.050m)										
0	0.00616	0.00000	0.00000	0.00000	0.00000	0.00000	0.00000	0.00000	0.00000	0.00000
33	0.08647	0.09475	0.03310	0.07752	0.18508	0.47438	91.24584	0.00071	0.00000	0.00055
66	0.16677	0.09502	0.03194	0.07935	0.18861	0.47544	90.37488	0.00227	0.00062	0.00165
100	0.24707	0.00000	0.00000	0.00000	0.00000	0.00028	0.00307	0.00000	0.00000	0.00000
Station 3 (X = -0.030m)										
0	0.00781	0.00000	0.00000	0.00000	0.00000	0.00000	0.00000	0.00000	0.00000	0.00000
33	0.08811	0.11467	0.05943	0.08596	0.22545	0.73558	739.78837	0.00333	0.00312	0.00055
66	0.16841	0.11525	0.05820	0.08581	0.22115	0.80782	737.42081	0.00166	0.00249	0.00055
100	0.24872	0.00000	0.00000	0.00000	0.00000	0.00000	0.00467	0.00000	0.00000	0.00000
Station 4 (X = 0.000m)										
0	0.02329	0.00000	0.00000	0.00000	0.00000	0.00000	0.00000	0.00000	0.00000	0.00000
33	0.10359	0.00517	0.00145	0.04530	0.19617	0.38102	75.09076	0.00542	0.00629	0.01164
66	0.18389	0.00443	0.00022	0.04252	0.18115	0.37651	75.08537	0.00698	0.00564	0.01227
100	0.26420	0.00000	0.00000	0.00000	0.00000	0.00000	0.00287	0.00000	0.00000	0.00000
Station 5 (X = 0.025m)										
0	0.05418	0.00000	0.00000	0.00000	0.00000	0.00000	0.00000	0.00000	0.00000	0.00000
33	0.13449	0.00965	0.00695	0.02860	0.34149	0.38984	1680.61424	0.02638	0.00254	0.02429
66	0.21479	0.01210	0.00568	0.03716	0.34277	0.40235	1652.06698	0.02850	0.00320	0.02550
100	0.29510	0.00000	0.00017	0.00000	0.00000	0.00000	0.02222	0.00000	0.00000	0.00000
Station 6 (X = 0.050m)										
0	0.10459	0.00000	0.00000	0.00000	0.00000	0.00000	0.00000	0.00000	0.00000	0.00000
33	0.18490	0.04068	0.02562	0.01014	0.04683	0.04216	8.03507	0.00963	0.00445	0.00521
66	0.26521	0.05485	0.04277	0.05292	0.05177	0.03763	12.48811	0.01476	0.00763	0.00637
100	0.34551	0.00000	0.00000	0.00000	0.00000	0.00000	0.00286	0.00000	0.00000	0.00000
Station 7 (X = 0.090m)										
0	0.18742	0.00000	0.00000	0.00000	0.00000	0.00000	0.00000	0.00000	0.00000	0.00000
33	0.26773	1.19668	0.74615	0.45025	0.17822	0.01676	74.16898	0.03101	0.06989	0.10071
66	0.34804	1.17737	0.73834	0.45198	0.18307	0.01829	74.76751	0.02947	0.07052	0.10014
100	0.42835	0.02716	0.01392	0.01195	0.00321	0.00686	0.71326	0.00000	0.00127	0.00116
Maximum Error (%)		1.58	0.97	0.52	0.34	0.81	1680.61	0.03	0.07	0.10

Table 4.5 Summary of results from periodic boundary condition study

The detailed results for station 3 are given in Figure 4.12 as an example. The blue circle symbols in the figure are the 0%, 33%, 66%, and 100% circumferential locations.

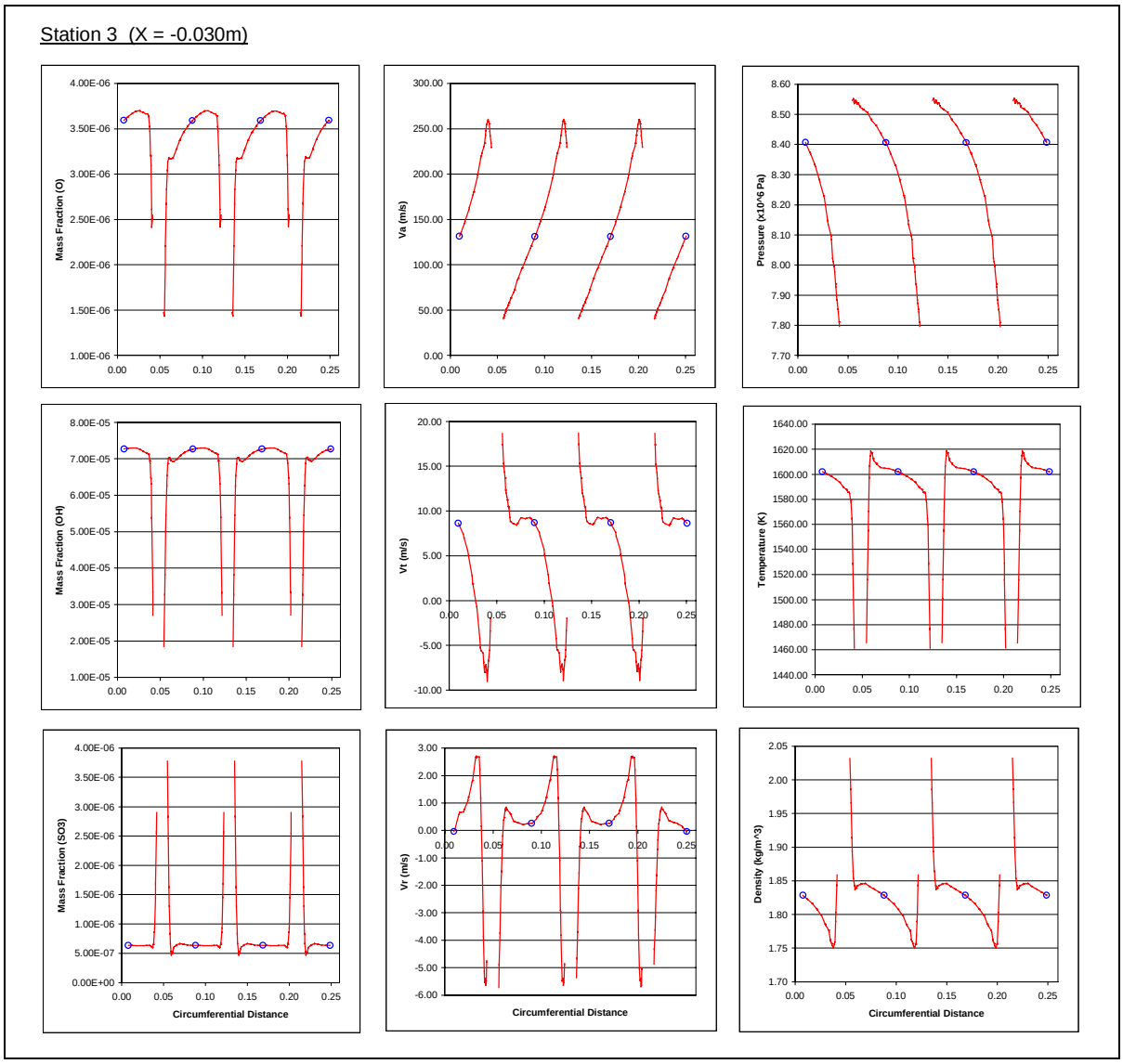

Figure 4.12 Detailed results for the periodic boundary condition study at station 3

These results suggests that the periodic boundary conditions do not introduce any significant error into the computation. Therefore, single pitch grids were used for the NASA/DERA engine test modeling where appropriate.

4.6 CHAPTER SUMMARY

The purpose of this chapter was to describe the validation exercises performed during the current research period. An attempt to benchmark the modeling tools through simulation of a flow reactor experiment was

presented. Although it was not completely successful, it provided the opportunity to test several code improvements, investigate the limitations of the modeling tools, and analyze flow features of the reactor. A chemical mechanism study which investigated the effects of the chemical mechanism on intra-engine chemistry modeling and selected a mechanism for use in the NASA/DERA engine test modeling was detailed. This chapter also discussed a convergence criteria study which resulted in improved chemistry convergence indicators. Finally, a periodic boundary condition study was presented.

In summary, the following is a list of all relevant points presented in this chapter:

- An attempt was made to model a VPFR experiment to benchmark the accuracy of the modeling tools, however, a limitation to the flow solver prevented this ultimate objective. The flow features from the simulation did not correlate well with those expected from experimental and empirical data.
- The VPFR validation exercise proved useful in validating some improvements to the modeling tools.
    - The new fully unstructured grid generator was successfully used to mesh the VPFR geometry
    - The multiple inlet/exit improvement was qualitatively validated.
- The modeling tools are limited to simulations of compressible flow and should be restricted to situations when the bulk of the flow field is above a Mach number of 0.2, an estimate for the compressibility limit of the code.
- The Princeton VPFR may operate with large scale unsteady stall.
- A comparative study was performed on four chemical mechanisms by repeating a 1D and 2D computation from prior work.
    - The species concentration trends were the same for all mechanisms studied.
    - The SO_x conversion ranged from 2.7% to 7.3% for a given case, which implies that the selection of chemical mechanism does impact intra-engine chemistry modeling.
    - Accurately representing key reactions in the mechanism produced reasonable results, thus prior work using Lukachko et al. (1998) was supported.
    - The Mueller et al. (2000)-truncated mechanism was selected for use intra-engine chemistry modeling. It is based on experimental data and is within 1% of the Mueller et al. (2000)-full mechanism.
- The original chemistry convergence criteria did not represent convergence of trace species well. They were improved by using the RMS average of individual species residuals for the species of interest to determine solution convergence.
- Periodic boundary conditions did not introduce any significant error into the computation, selected fluid and species variables at the boundary were within 1.6% of their corresponding value with no boundary present.

5 MODELING THE NASA/DERA ENGINE TEST

This chapter presents the first complete analysis which applies the intra-engine trace chemistry modeling methodology to a real engine. The goal of the simulation is to characterize the evolution of trace species in the post combustor flow path in order to provide engine exit plane emissions predictions, help guide the engine test plan, and research a few physical mechanisms thought to affect trace species chemistry.

5.1 CHAPTER OVERVIEW

The purpose of this chapter is to describe the modeling effort to simulate trace species evolution in the post-combustor gas path of an engine in support of the NASA/DERA engine test. The objective of the test is to provide measurements to help characterize aviation emissions and benchmark the models. The model is used to inform the test effort by providing pre-test predictions which were used to help formulate the test plan and to research a few fundamental mechanisms thought to influence trace species chemistry.

Three conditions are investigated: cruise, max power, and non-uniform max power. Details of the grid generation, fluid boundary condition specification, and species initial conditions specification are discussed. A time scale analysis is used to guide the modeling efforts. Two types of high fidelity models are used for the HPT1; a mixed-out case and a wake model case. Several properties of the solution are discussed, including: convergence, overall flow features, grid resolution, deviation angle, and flow-through times. A sample set of detailed flow-chemistry results from the high fidelity model is presented. Low fidelity models are used for HPT1 and HPT1 exit to nozzle exit. Low fidelity models for averaged and high and low temperature profiles in the HPT1 are compared to the high fidelity average. A HPT1 exit to nozzle exit profile is used to obtain a prediction of engine exit gas composition. A sample set of flow-chemistry results from the low fidelity model is presented.

This chapter also highlights several implications of the modeling results. Specifically, engine operating conditions, multi-dimensional non-uniformities, and the unsteady interaction of non-uniformities with downstream stations were all found to influence trace species evolution. They can all impact temperature,

pressure, gas composition, or residence time which are the key parameters influencing intra-engine chemistry. The scale as well as the magnitude of the non-uniformity impacts trace species evolution.

In summary, the following are the main points of this chapter:

- A first of its kind analysis was completed on the post-combustor gas path of the NASA/DERA engine to support an engine test aimed at characterizing aviation emissions.

- Pre-test simulations were used to guide the test plan, they suggested testing at the highest combustor exit temperature attainable, as well as, a lower power setting. Also, SO_3 and HOHO were selected as important species to monitor.

- A time scale analysis indicated that most SO_3 production occurs in the HPT1 at max power conditions. The analysis indicates that there is several orders of magnitude less sulfur conversion after the HPT1, and modeling resources were thus concentrated on the HPT1.

- HPT1 NGV blade-row flow-through time ranged from 0.18 to 0.26 ms and HPT1 rotor blade-row flow-through time ranged from 0.10 to 0.15 ms, as calculated in the high fidelity analysis.

- A summary of all high fidelity modeling results is contained in Table 5.5, Table 5.6, and Table 5.7. Examples of some detailed results of the high fidelity modeling can be found in Section 5.4.2.3 or Appendix C.

- A summary of all low fidelity modeling results is contained in Table 5.6 and Table 5.7. Examples of some detailed results of the low fidelity modeling can be found in Section 5.5.2.2 or Appendix C.

- Intra-engine post combustor chemistry is sensitive to engine operating conditions (i.e. combustor exit temperature). SO_3 and HONO concentrations increased with increased engine power level.

- Multi-dimensional non-uniformities have a considerable influence on intra-engine post combustor chemistry, which indicates that some important features can not be captured in low fidelity models.

- The temperature, pressure, gas composition, and residence time can vary significantly throughout a gas turbine engine. The scale as well as the magnitude of the non-uniformity impacts intra-engine chemistry.

- Correlation of the species mass fraction and temperature spatial variations in the high fidelity models suggests the primary influence on chemistry is temperature non-uniformity.

- The unsteady interaction non-uniformities with downstream blade-rows has a significant impact on intra-engine post-combustor chemistry.

- Local regions of flow or species non-uniformity persist through the subsequent blade rows.

Section 5.2 outlines the objectives of the engine test and modeling effort, provides some background information related to the engine test, and lists the modeling scenarios considered. Section 5.3 gives a time scale analysis for the engine test and gives an outline for the presentation of the details of the modeling effort. Section 5.4 details the set up and results of the high fidelity analysis. Section 5.5 details the set up and results of the low fidelity analysis. Section 5.6 describes the implications of the results from modeling effort. Section 5.7 is the chapter summary.

5.2 OBJECTIVES, BACKGROUND, AND MODELING SCENARIOS

NASA/DERA Engine Test Objectives

One of the project objectives outlined in Section 1.4 was a validation of engine modeling results through measurement studies. A collaboration of many research groups consisting mainly of teams from DERA, NASA, MIT/ARI, and UMR have formulated an engine test to address several emissions related phenomena. The main objective of the measurement campaign is to carry out ground-based simulation and measurement of chemical and physical processes relevant to aviation emissions characterization [8]. The NASA/DERA engine test aims to measure the emissions of a typical engine, evaluate the effects of various fuels and operating conditions on engine emissions, develop and evaluate various species measurement techniques, investigate intra-engine species evolution, and provide inputs to emissions models through characterizing the composition of the gas at the combustor and nozzle planes.

Modeling Objectives

The NASA/DERA engine test provides a unique opportunity to demonstrate the modeling methodology described in Section 2. The models were used to inform the test efforts by providing pre-test predictions for intra-engine species evolution. The pre-test predictions assisted in formulating the test plan by helping to ensure that operating conditions are selected so as to provide useful information about the intra-engine environment. The pre-test predictions are also useful in directing the measurement efforts by indicating the important species to monitor and providing estimates for the instrumentation requirements. Modeling of the engine test also provides the opportunity to benchmark the accuracy of the modeling methodology against measured data. A matched set (i.e. same engine and operating condition) of combustor and nozzle exit plane species data is required to evaluate the predictive capability of the intra-engine modeling tools. To date no such

data exists, primarily due to logistic and cost constraints associated with emissions measurements as described in Section 1.2.1. Finally, the simulations performed can be extended to investigate the effects of various fluid and chemical effects on the evolution of chemical species, as well as, the influence of various modeling approximations on the computed results in a real engine environment. In particular, the effects of engine operating condition, unsteady propagation of local non-uniformities, and 1D versus 2D modeling techniques are considered.

Background

The engine test is divided into two parts; a combustor rig test and an engine test. As of this writing, the experimental facility has been prepared, the test plan planned established, and the combustor rig test has been initiated. The complete engine test is planned for the summer of 2001. The pre-test simulations proved to be helpful in guiding the engine test plan by providing insight as to the operating conditions and species which would provide the most interesting information to the emissions characterization efforts.

An general overview of the engine is given in Table 5.1. Due to the proprietary nature of the combustor and engine design, the details of the geometric and performance data will not be discussed. Some parameters required as model inputs were not available and thus estimates were made using values typical of this type of engine or through extrapolation of the given data. For example, intra-stage fluid properties were not available and were derived from a velocity triangle analysis detailed in Appendix B. Also, the combustor plane exit species composition was unknown and thus derived in Section 5.4.1 using the initial conditions technique outlined in Section 2.3.2. Although the engine is an older model, it has been fitted with a modern combustor. Overall, the engine configuration and operating conditions studied in this analysis are believed to be typical of an older, but currently in-use civil aircraft.

Test Engine Specifications	
Type	Turbofan
Year of model introduction	1970's
Thrust	11,030-15,000 lbf (49.1-66.7 kN)
Pressure Ratio	16.8:1
Bypass Ratio	0.78:1
Turbine stages	2 High Pressure, 2 Low Pressure
Maximum combustor exit temperature	1,365 K
Dimensions	37 inch diameter and 115 inch length
Weight	2,417 lb (1,096 kg)

Table 5.1 Nominal NASA/DERA test engine description

For the engine test exhaust gas is sampled over a radial and circumferential grid (roughly 3x10) at the combustor and nozzle exit planes providing a two-dimensional gas composition profile for model inputs and benchmarking. The test will employ three fuels with varying sulfur content, although only one sulfur EI was modeled in the context of this thesis.

Modeling Scenarios

The engine modeling scenarios that were simulated in the context of this thesis were based on the nominal operating points for cruise and max power. Table 5.2 overviews the three simulations conducted which cover a range of combustor exit temperatures pertinent to many modern civil aircraft engines.

	Summary of NASA/DERA Engine Test Conditions		
Label	Cruise	Max power	Non-uniform max power
Description	Nominal cruise power setting	Nominal maximum power setting	Maximum power setting with a combustor exit temperature profile (nominally 1,600K)
Engine speed (rpm)	7,821	8,864	8,864
Ts at combustor exit (K)	1,123	1,357	1,430-1,840 (average~1,600)
Ps at combustor exit (Pa)	687,000	1,594,000	1,594,000
Ts at HPT1 exit (K)	983	1,186	1,186
Ps at HPT1 exit (Pa)	428,000	986,000	986,000
HPT1 rotor metal temperature (K)	826	999	999
HPT1 stator metal temperature (K)	791	956	956

Table 5.2 Summary of conditions modeled for NASA/DERA engine test [34]

These three test conditions provide a basis for investigating the effects of operating conditions on trace species evolution. As discussed previously in this section, the modeling strategy used for the NASA/DERA engine simulations called for high fidelity modeling of the first stage of the high pressure turbine followed by low fidelity modeling for the remainder of the post-combustor flow path. These computational simulations were extended to investigate the effects of several physical phenomena suspected to influence the evolution of trace species, namely circumferential non-uniformities and the unsteady interaction of the non-uniformities on downstream stations.

Two of the simulated conditions were used to investigate two types of circumferential non-uniformity. The HPT1 rotor calculation for the max power and non-uniform max power conditions were run both using a steady mixed-out initial condition and an unsteady wake model profile initial condition to investigate the effects of unsteady interaction of the non-uniformities on downstream stations (see Section 3.3.4 for more details on the wake model). Figure 5.1 gives a overview of all the modeling scenarios explored.

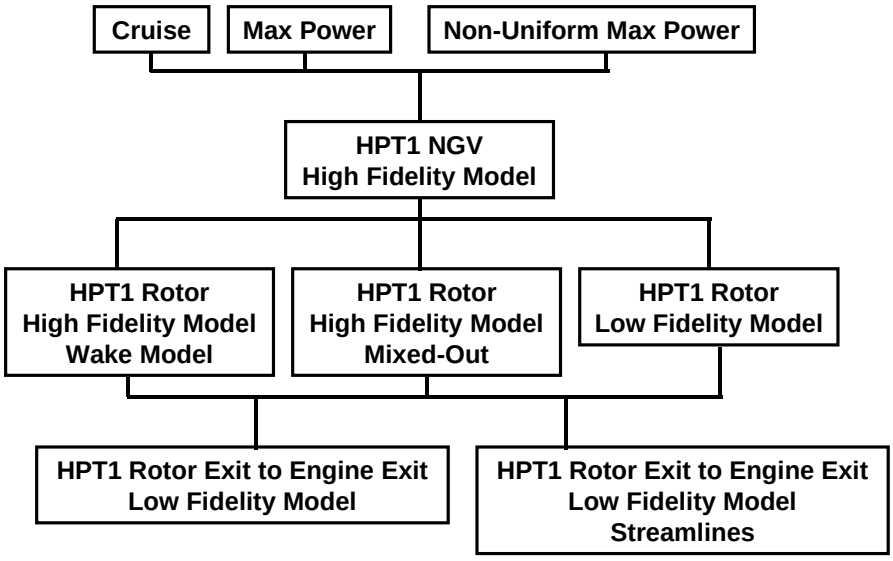

Figure 5.1 Overview of modeling scenarios

The cruise and max power case had constant values for each species and fluid parameter specified on the inlet plane. The non-uniform max power case had a circumferentially varying temperature profile specified. This variation in combustor exit temperature is typical of a cannular type gas turbine engine combustor. The actual profile used was scaled based on a pattern factor of about 40% from a exit temperature trace at the mid radial plane of a typical engine combustor (see Figure 5.2).

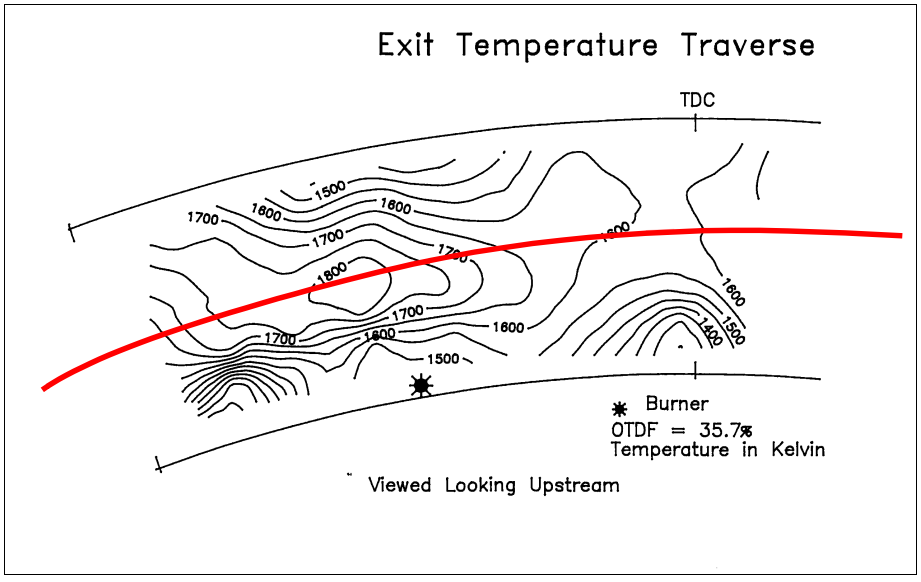

Figure 5.2 Typical combustor exit temperature trace and location for scaled profile of non-uniform max power case [34]

The profile was clocked such that the peak temperature, corresponding approximately to the injector locations, was aligned with a blade. This was considered a worst case scenario since the temperature difference between the combustor gas and the cooled blade would be greatest. Given the number of injectors and stator blades it is likely that this would occur somewhere within the circumference. The derived profile was then fit to the three NGV blade passages as shown in Figure 5.3 (0 to 18 degrees).

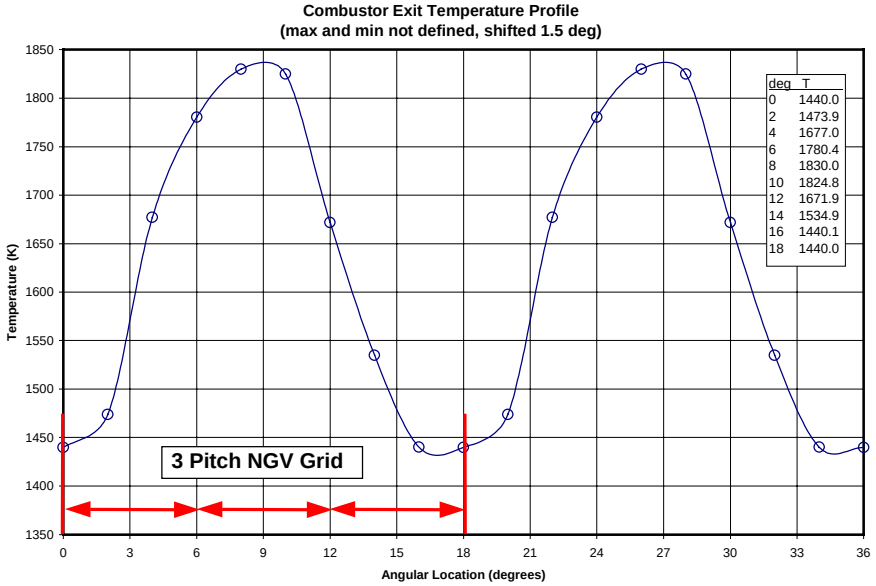

Figure 5.3 Combustor temperature profile used as initial condition for non-uniform max power case

Species of importance to evaluating the SO_x and NO_y evolution are SO_3, SO_2, H_2SO_4, O, OH, NO, NO_2, NO_3 and HONO. Several instrumentation teams will measure a multitude of primary and trace combustion products such as O_2, CO_2, CO, H_2O, unburned hydrocarbons, and soot particles. Initially, measurements were focused on SO_3 evolution, however, pre-test simulations showed that majority of the SO_2 conversion was completed in the combustor for the operating conditions considered (more so for the cruise condition). These results suggested concentrating the test efforts on the highest power setting attainable such that the combustor exit temperature is highest and the magnitude of change is greatest along the post-combustor gas path (i.e. between the measurement stations). Also, the focus was broadened to include HONO evolution which exhibits a greater change between the measurement stations for the planned test conditions. Furthermore, since NO_y chemistry remains active over this range of power settings it was still advantageous to explore multiple operating points. These modifications to the test plan would help to magnify the changes in HONO concentration through the measurement stations and provide the potential for comparison between two operating conditions.

An additional operating condition was proposed whereby the engine could be run at a temperature higher than the max power case by adjusting a compressor or fan stage [33]. However, limitations of the combustor rig constrained the maximum temperature for which a matched set of data could be obtained to a condition midway between the cruise and max power case. The final test plan focuses on the mid-cruise/max power case and calls for a limited sampling of data at the cruise conditions.

5.3 NASA/DERA ENGINE TEST MODELING

Application of a time scale analysis suggested that most changes in trace species occur through the first stage of the high pressure turbine. The three operating conditions described previously were considered; cruise, max power, and max power with a non-uniform combustor temperature profile.

5.3.1 TIME SCALE ANALYSIS

A time scale analysis was used to help determine the best allocation of computational resources. The severity parameter for sulfur, ΔS(VI), was analyzed since sulfur chemistry was the initial focus of the engine test. The analysis employed the chemical mechanism from Lukachko et al. [28] and used only the forward reactions. Figure 5.4 plots this severity parameter for the max power conditions at the entrance and exit to the HPT1.

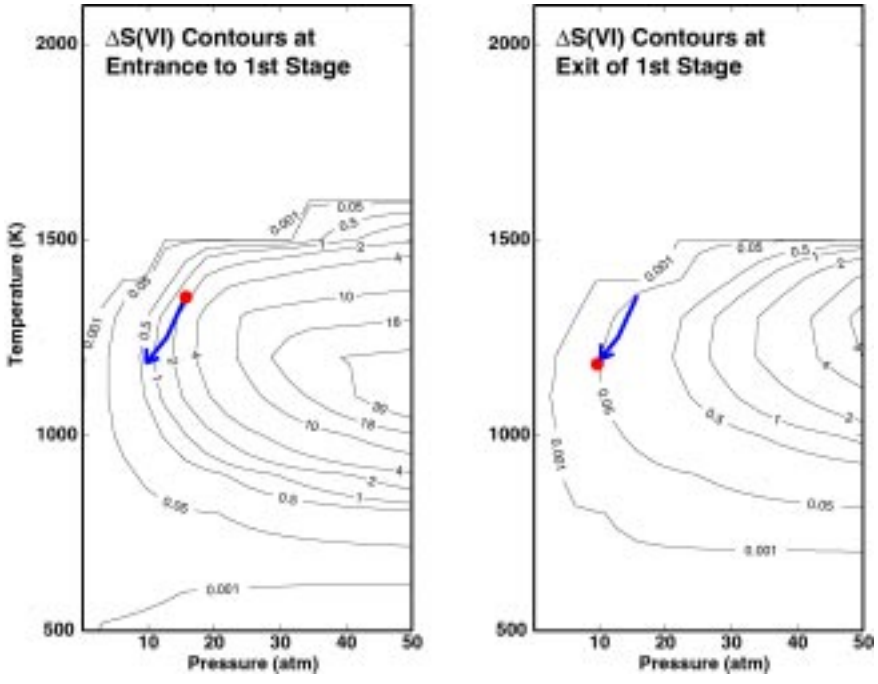

Figure 5.4 Time scale analysis severity parameter, ΔS(VI), for NASA/DERA engine test at max power condition

Integration along the path from the combustor exit to the HPT1 exit indicates that there will be less than 4% sulfur conversion in that stage. Integration along the path subsequent to this conversion, the severity parameter suggests several orders of magnitude less potential for sulfur conversion after the HPT1. Using these findings it was decided to use a high fidelity 2D model for the HPT1 combined with a low fidelity 1D model from the HPT1 exit to the nozzle exit to perform the pre-test modeling for the NASA/DERA engine test.

5.3.2 PRESENTATION OF MODELING EFFORT

A complete set of all the specific results accumulated during the course of this research would be overwhelming and not add much to the value to this thesis. In order to keep the write-up concise and not to obscure the key findings, the specific results were divided into two main parts with two subsections each. The two parts are: Section 5.4 High Fidelity Modeling and Section 5.5 Low Fidelity Modeling. The subsections are Set Up and Results. Finally, Section 5.6 Implications of Results contains an analysis of the results with regard to their impact on the research of intra-engine trace species evolution. The presentation layout gives a representative case for each distinct case without listing or plotting every chemical species or fluid variable for each operating condition and analysis technique. A diagram showing the important topics in the presentation layout is given in Figure 5.5.

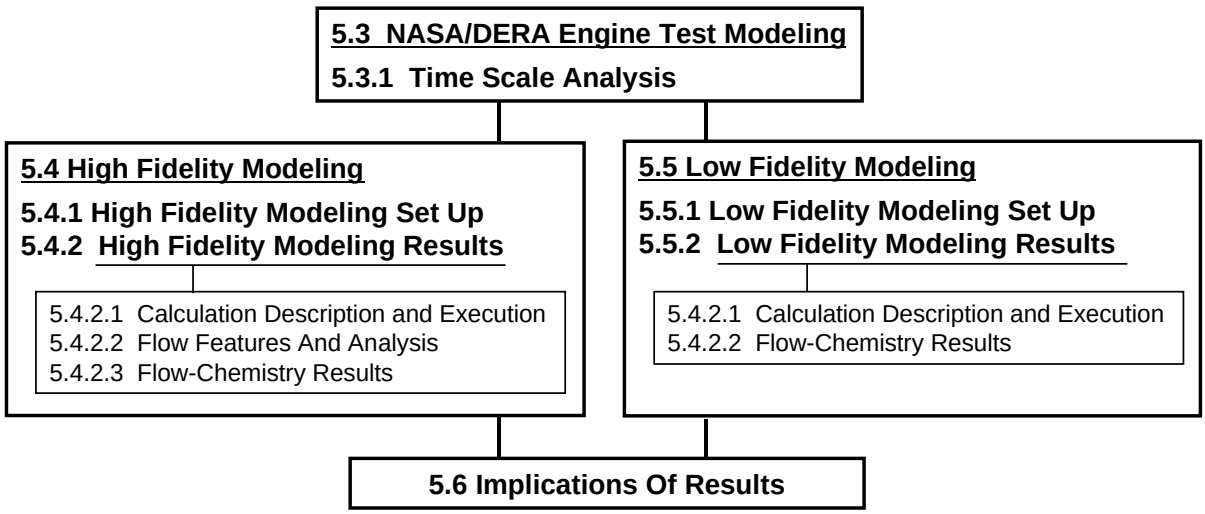

Figure 5.5 Presentation layout of NASA/DERA engine test modeling

5.4 HIGH FIDELITY MODELING

5.4.1 HIGH FIDELITY MODELING SET UP

Three set-up steps were required for the high fidelity modeling runs. First, 2D grids for the HPT1 NGV and rotor were generated (see Section 0). Second, fluid boundary conditions were extracted from a velocity triangle analysis (see Section 0). Third, species initial conditions were established (see Section 0). A set of input files to CNEWT for the max power condition is given in Appendix D as an example.

Grid Generation

The PRE grid generator was used create computational grids for the high fidelity models since it is best suited for typical turbomachinery geometries [49]. All of the grids used for the high fidelity modeling are essentially 2D grids, having only 2 cells in the radial direction. The grids are located on a plane at a 270 mm radius, the mid-span of the HPT1. Cells were clustered near the blade surfaces to help resolve the boundary layers and near the leading and trailing edge to capture the blade geometry accurately. However, the boundary layer is not fully resolved and the temperature at the blade surface is 1083.6 K compared to the specified value of 999.0 K for the max power conditions. The unresolved blade boundary layer would imply that any effects of the temperature deficit due to blade cooling are underestimated. Periodic boundary conditions on the circumferential boundaries were determined not to introduce any significant errors (see Section 4.5). Thus, a single blade pitch was used for computations in all cases where unsteady inlet conditions were not modeled.

Figure 5.6 shows the NGV grid. The inlet length for the NGV was set by the distance from the combustor exit plane to the blade leading edge. The exit length was extended roughly 0.8 axial chords downstream to minimize any impacts of the exit boundary conditions.

The periodicity of the combustor fuel nozzles matched approximately to three NGV pitches. Therefore, the non-uniform max power computations were done on a three pitch stator grid.

Also, three NGV pitches match up exactly with five rotor pitches. Thus the unsteady calculations which had periodic inlet non-uniformities were done on a five pitch rotor grid. The unsteady max power calculations used the solution from a single NGV pitch repeated three times and the non-uniform max power case used the solution from the three pitch NGV grid.

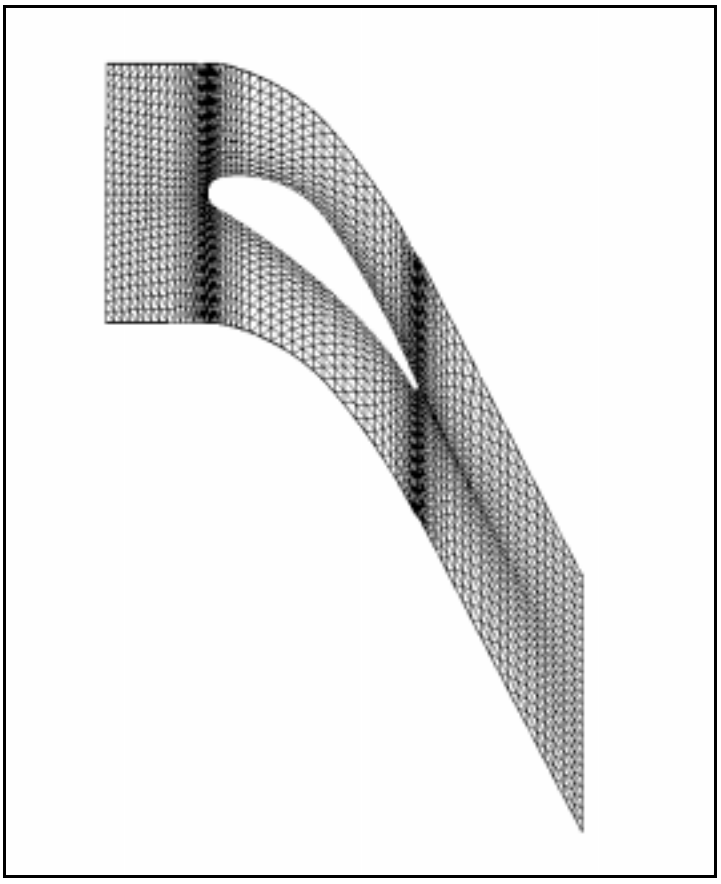

HPT1 NGV
Number of Blades = 60
I, J, K = 25, 80, 3
Cells = 23,160
Chord = 31.44 mm
Inlet = 10.95 mm
Axial Chord = 23.09 mm
Exit = 17.82 mm

Figure 5.6 Single pitch HPT1 NGV grid

Figure 5.7 shows the rotor grid. The inlet length for the rotor was set as half of the distance from the NGV trailing edge to the rotor leading edge. The inlet conditions for the high fidelity rotor calculations were extracted from the NGV solution at that plane. Again, the exit length was extended roughly 0.8 axial chords downstream.

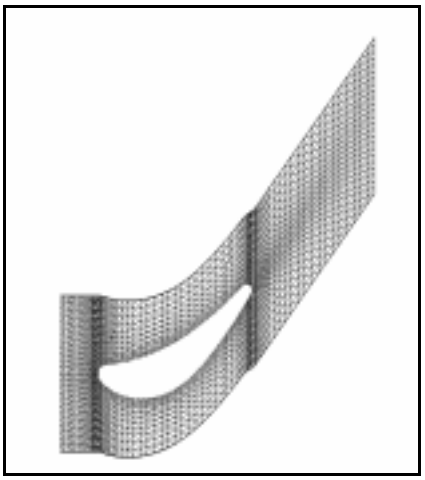

HPT1 Rotor
Number of Blades = 100
I, J, K = 20, 80, 3
Cells = 19,920
Chord = 19.18 mm
Inlet = 3.95 mm
Axial Chord = 16.79 mm
Exit = 13.19 mm

Figure 5.7 Single pitch HPT1 rotor grid

HPT1 Velocity Triangle Analysis

The necessary initial conditions for the flow parameters for the engine test run were derived by applying a mean line flow analysis using the limited performance data available. The data consisted of computed spool speed, mass flow, total pressure, and total temperature at several engine stations for the three operating conditions. The data was from a model which had been previously validated against experimental data [34]. There is no distinction between blade rows or stages since the model treats each turbine section (LP/HP) as a whole. Therefore, a velocity triangle analysis was used to obtain the necessary flow data required for the high fidelity modeling. The detailed procedure and example results from the velocity triangle analysis are given in Appendix B.

Based on the limited performance data obtained for the NASA/DERA engine, the velocity triangle analysis provided a reasonable set of boundary conditions necessary for the high fidelity modleing. The objective of the engine simulation, to predict species evolution and investigate the parameters which influence it, likely does not require an "exact" flow solution. Rather, a sucessful high fidelity modeling effort would mainly depend on capturing the important features of the flow field which dictate the temporal and spatial variations in flow and species variables. Some examples of such features are: flow-through time scale, pressure/temperature gradients, boundary layers, blade cooling, flow regime (i.e. no stall/separation), etc. which should be well represented with the boundary conditions derived from the velocity triangle analysis.

Chemistry Initial Conditions

Species initial conditions at the combustor exit for the NASA/DERA engine test case were estimated using the procedure presented in Section 2.3.2. A set of initial conditions at the appropriate combustor exit temperature

and pressure was derived for each of the three operating conditions investigated. The important input parameters used in the initial conditions code are listed in the table below:

	Chemistry Initial Condition Code Inputs		
Condition	**Cruise**	**Max power**	**Non-uniform max power**
T (K)	1,122.8	1,356.6	1,440-1,830
P (atm)	6.78	15.732	15.732
ϕ (equiv ratio)	0.35	0.35	0.35
η (comb eff)	0.9988	0.99988	0.99988
CO/H2/HC ratio	100/0/0	100/0/0	100/0/0
EI(NOx) (g/kg fuel)	21.0	21.0	21.0
NO/NOx ratio	0.99	0.99	0.99
EI(S) (g/kg fuel)	0.5	0.5	0.5
SO3/SOx ratio	0.06	0.06	various equilibrium (about 0.03 average)
EI(CO) (g/kg fuel)	5.09	0.51	0.51

Table 5.3 Chemistry inlet condition code inputs for NASA/DERA engine test

The main differences in the chemistry inlet specification technique relative to prior work in [1] and the Cambridge No 2 turbine rotor calculations discussed previously are that the $CO/H_2/HC$ ratio was changed from 78/22/0 to 100/0/0, the NO/NO_x ratio was changed from 0.90 to 0.99, and a kinetics calculation was used to resolve rapid numerical changes in the initial conditions due to inconsistencies in the resulting speciations. Due to lack of emissions data, the EI's represent a best estimate for an engine typical of this make and era. The $EI(NO_x)$ was adjusted to obtain approximately 300 ppm of NO_x to coincide with a rough visual average of NO_x contours of a similar gas turbine engine (see Figure 5.8). The EI(CO) was set by adjusting the combustion efficiency to achieve a value close to one interpolated from an emissions data base for a 1970's era engine with a pressure ratio of about 16 at the appropriate power setting [11]. The selected EI(NO) was also similar to the ones listed in the data base. The SO_3/SO_x was fixed at 6% for the cruise and max power setting based on experience from prior work [30] which showed that sulfur conversion in the combustor was limited. In contrast, the equilibrium level for these two cases resulted in a SO_3/SO_x ratio of about 38%. The temperature for the non-uniform max power condition spanned 1,440-1,830K which gave an equilibrium SO_3/SO_x ranging from about 1-8%, thus the equlibrium sulfur ratio was used in this case.

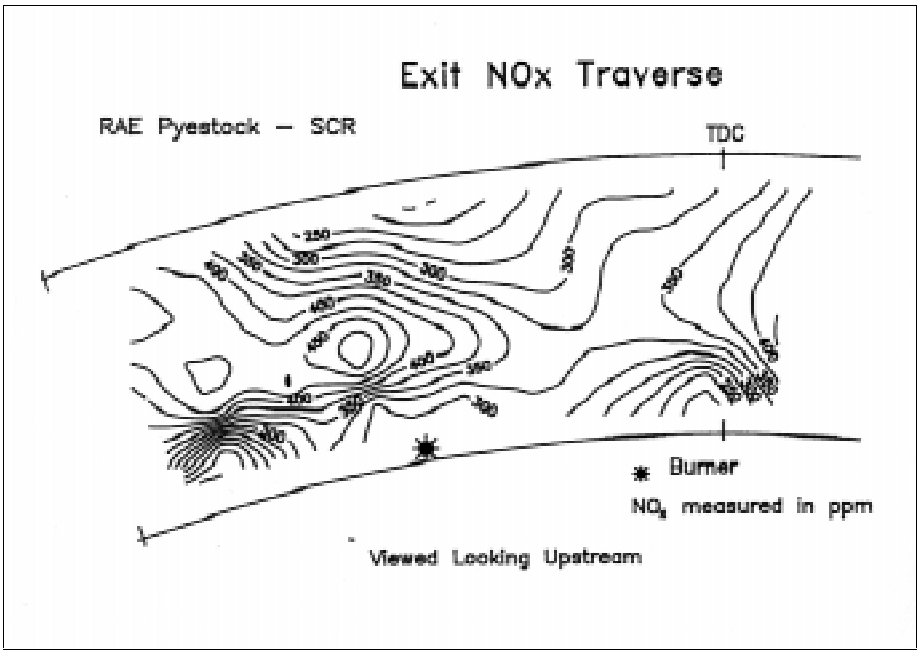

Figure 5.8 Typical NO_x contours at the combustor exit plane [34]

Rapid adjustments in the initial chemical composition were removed after running the results from the initial conditions code through the kinetics calculation step for 0.02 ms. This represents about 5% of the HPT1 flow-through time or less than 1% of the post-combustor gas path flow-through time. The initial compositions were not altered significantly by the constant temperature and pressure kinetics calculation step during that time and thus the general parameters in Table 5.3 describe the initial compositions adequately. The resulting initial chemical composition used for the NASA/DERA engine test simulations can be found in Table 5.5, Table 5.6, and Table 5.7 for each operating condition investigated. The Princeton-truncated chemical mechanism was used for all high and low fidelity modeling of the NASA/DERA engine test. Justification for the selected mechanism was presented in Section 4.3, and the complete set of species and reactions is described in Appendix A.

5.4.2 HIGH FIDELITY MODELING RESULTS

One goal of the high fidelity modeling was to improve the accuracy of the pre-test predictions by concentrating higher-order models in sections of the engine with the highest chemical reactivity for the species of interest. This would allow the pre-test predictions to be used more confidently as a guide for the test plan. The high fidelity modeling was also used to explore the influence of several flow phenomena on chemical evolution.

5.4.2.1 CALCULATION DESCRIPTION AND EXECUTION

Overview Of Analysis Types For Rotor Calculation

Figure 5.9 depicts the two types of high fidelity analysis were used for the HPT1 rotor in the current research. The first analysis uses the mass-averaged fluid and species quantities at the NGV exit plane as inlet conditions to the rotor domain and is called the "mixed-out case." The second analysis uses the wake model described in Section 3.3.4 to apply a rotating, circumferentially-varying fluid and species profile from the NGV exit plane as the inlet condition to the rotor domain and is called the "wake model case." These two techniques were used to evaluate the effects of non-uniformities on downstream blade rows.

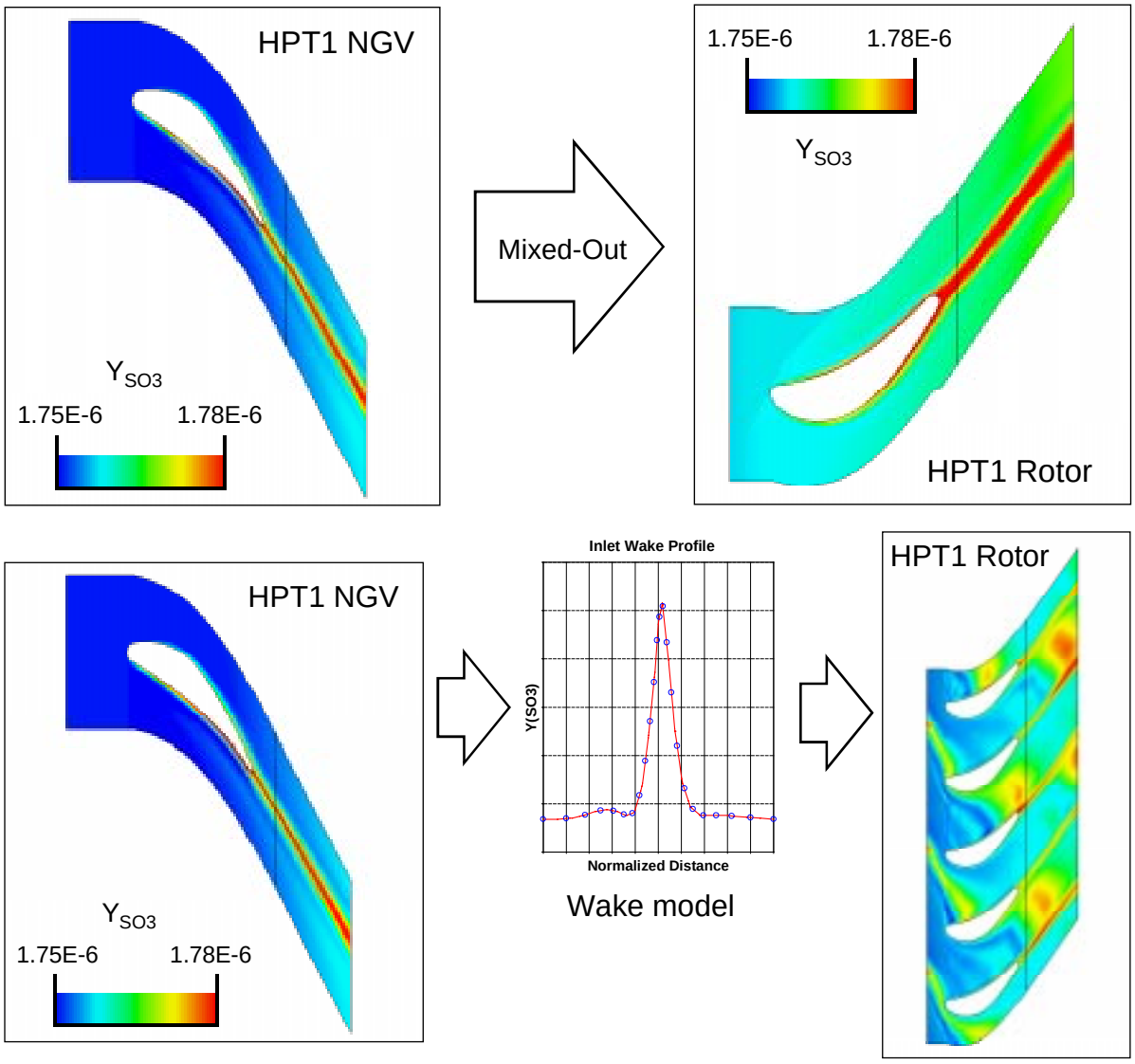

Figure 5.9 Two high fidelity analysis types, mixed-out (top) and wake model (bottom)

Solution Convergence

Each of the models run for the high fidelity analysis was run for at least 6,000 iterations. The insight gained from the convergence study (see Section 4.4) was used to help determine solution convergence. The fluid and several selected species convergence indicators were monitored, and all the solutions were deemed to be converged. The convergence history for the HPT1 NGV calculation at cruise condition to 10,000 iterations is shown in Figure 5.10 and Figure 5.11 as an example. As in this case, most of the runs were started with an initial guess for the flow and chemistry solutions set by specifying the inlet values throughout the domain. The fluid solution appears converged around 3,000 iterations and the chemistry solution at around 6,000 iterations. Some solutions were re-started using partially-converged solutions.

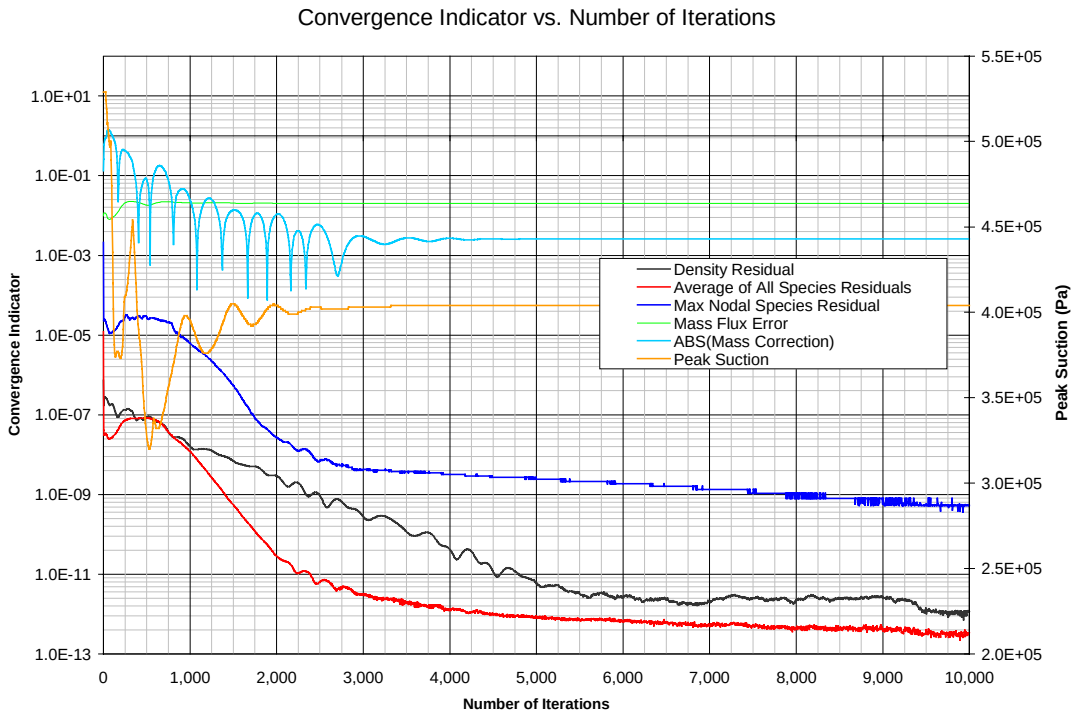

Figure 5.10 Fluid and basic species convergence indicators for NGV calculation at cruise condition

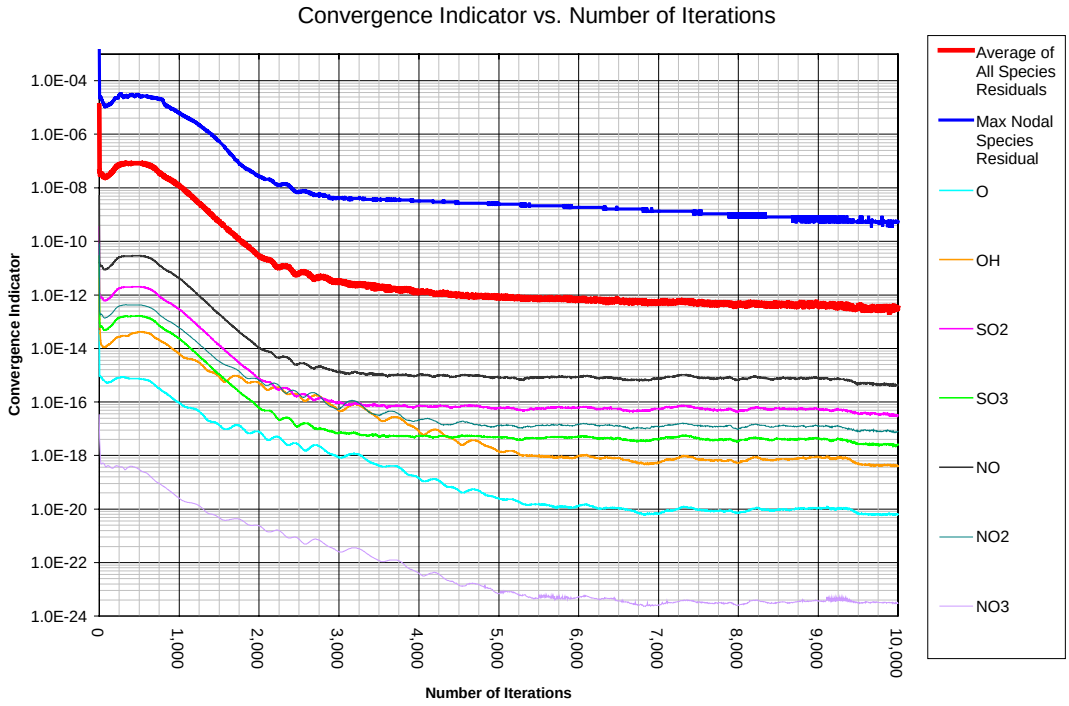

Figure 5.11 Selected species convergence indications for NGV calculation at cruise condition

The unsteady HPT1 rotor solutions were deemed to be converged when the convergence criteria became periodic about a constant value. Figure 5.12 and Figure 5.13 show example convergence histories for the HPT1 rotor calculation at the max power conditions. The unsteady solutions converge faster, although to higher residuals than the steady solutions. The higher residuals are due the need to resolve the fluid and chemistry variables in time (with a finite time-step) as well as the spatial domain.

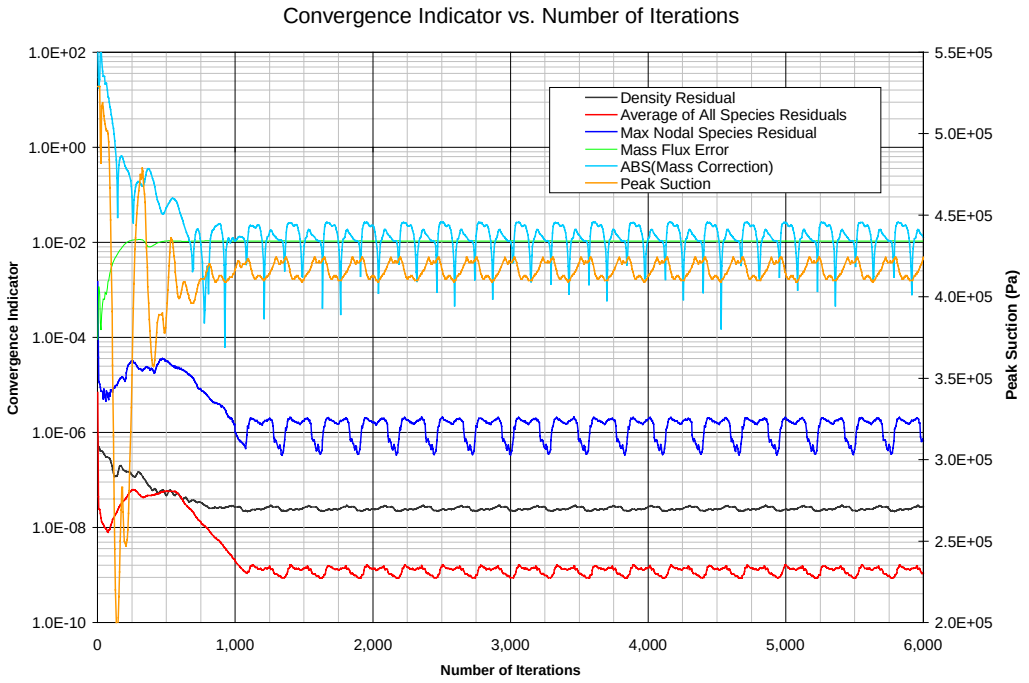

Figure 5.12 Fluid and basic species convergence indicators for unsteady rotor calculation at max power condition

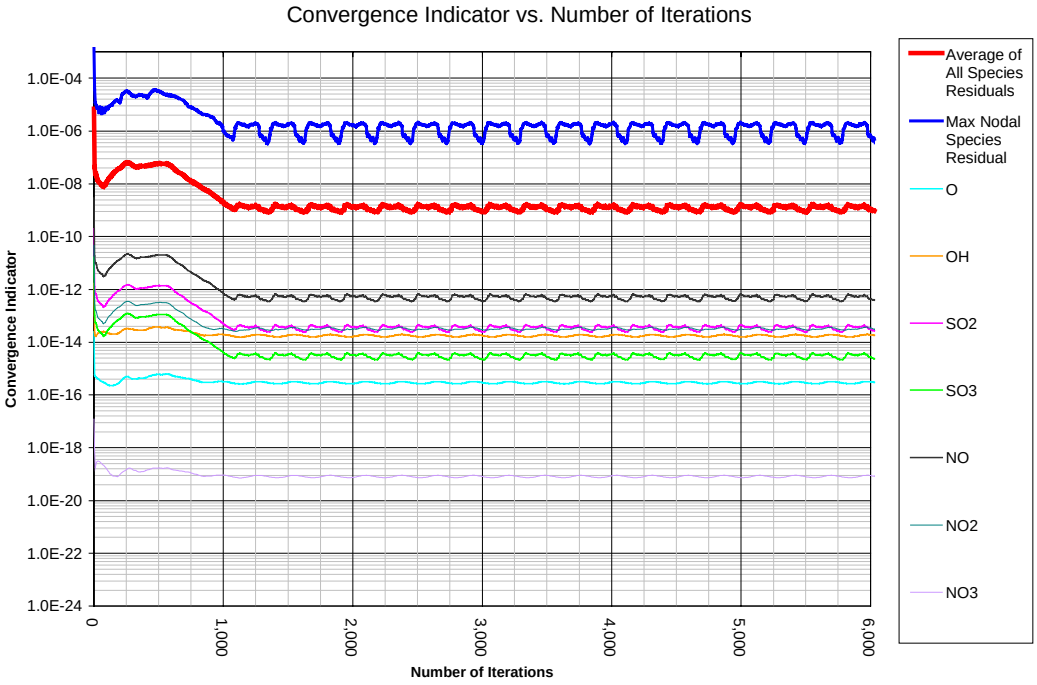

Figure 5.13 Selected species convergence indications for unsteady rotor calculation at max power condition

An full unsteady solution consists of the set of one complete cycle after convergence. Figure 5.14 shows the locations of a set of solution output files for an example unsteady rotor run at max power. In this case, ten evenly distributed locations in time were chosen for output over 275 iterations. All later runs spanned a minimum of 400 iterations per cycle for better resolution and typically consisted of 10 to 15 output locations per cycle.

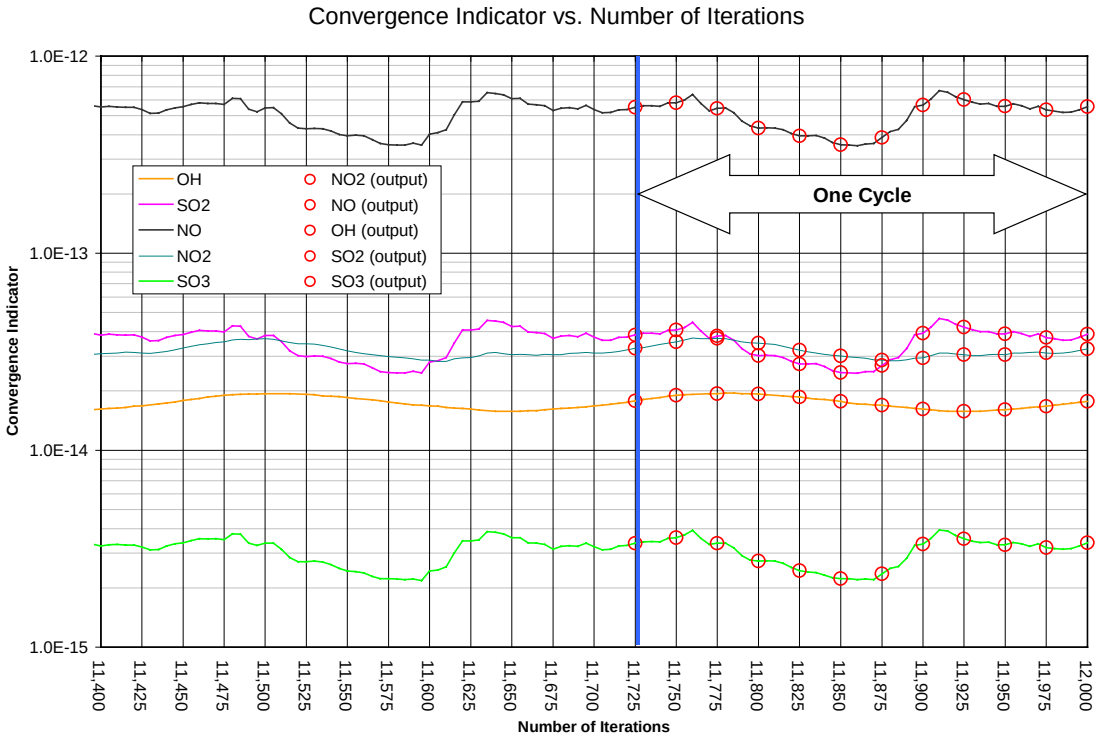

Figure 5.14 An example set of solution output files making up one cycle of a full unsteady solution

5.4.2.2 FLOW FEATURES AND ANALYSIS

Overall

In general, all of the solutions obtained in the high fidelity modeling phase were resonable. The features of the flow field and values of the fluid state variables were as expected. Table 5.4 contains a summary of the fluid quantities from the velocity triangle analysis and the high fidelity modeling.

Summary Of Fluid Quantities For HPT1 For Max Power Case							
	Station A	Station B			Station C		
Quantity	Velocity Triangle Analysis	Velocity Triangle Analysis	High Fidelity Model Result	Percent Difference	Velocity Triangle Analysis	High Fidelity Model Result	Percent Difference
Tt (K)	1,365.2	1,325.2	1,363.3	2.9%	1,200.2	1,300.2	8.3%
Ts (K)	1,356.6	1,250.4	1,287.5	3.0%	1,185.5	1,202.6	1.4%
Pt (Pa)	1,634,150	1,634,150	1,627,730	-0.4%	1,034,667	1,333,437	28.9%
Ps (Pa)	1,594,021	1,299,941	1,299,278	-0.1%	985,627	980,842	-0.5%
Vx (m/s)	139.8	200.35	201.4	0.5%	182.74	271.1	48.4%
Vt (m/s)	0	360.46	361.2	0.2%	-244.08	-379.9	55.6%

Table 5.4 Comparison of fluid quantities for HPT1 at max power

This table shows that the boundary conditions derived from the velocity triangle analysis were reasonable and that the high fidelity solution is valid. The results from the NGV high fidelity model at station B were used as input to the rotor high fidelity model rather that the estimate from the velocity triangle analysis since the high fidelity model results were thought to be more accurate. This caused a portion of the difference at station C in Table 5.4.

As a typical result, a field of streamlines overlayed with the Mach number contours is plotted in Figure 5.15 for the NGV max power case. From this figure it is evident that the flow is well behaved (i.e. not separated) and representative of a typical turbomachinery blade row.

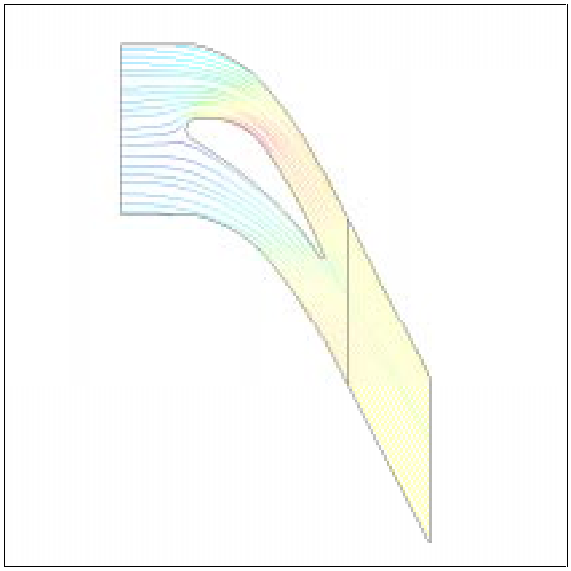

Figure 5.15 Mach number (0.15 to 0.75) plotted on streamlines for NGV at max power condition

Several flow features were checked to ensure the quality of each solution. In particular, the flow is not separated, the macroscopic features are feasible, the flow varables are reasonable relatve to the velocity trianlge

analysis, the deviation angle is reasonable, and the inlet/exit conditions are as specified. In general, all of the solutions from the high fidelity models were probed in a similar manner and the flow results were found to be similar.

Trailing Edge Resolution

One peculiar feature of the flow field was a very small region near the trailing edge which had a significantly higher Mach number. Upon close inspection, it appears that the high speed flow is caused by the tendancy of the fluid to accelerate around the TE from the pressure side to the suction side of the blade prior to the point of separation. The phenomena is magnified by the faceted shape of the TE and the limited grid resolution. This phenomena was much less pronounced in the prior calculations of the Cambridge No 2 turbine rotor because the TE was modeled as squared off which fixed the point of separation at the corners. Plots of the Mach number and total pressure for both cases are shown in Figure 5.16 for comparison. By modeling the true curvature of the TE, the point of separation and flow field in this region are not well resolved for the given grid spacing. The effect of this deficiency in the representation of the flow field is likely to be minimal on chemical species evolution. Two possiblilities to improve the situation would be to cut ("square off") the TE or to enhance the mesh in this region, however, both methods have drawbacks. Cutting the TE is in essence fixing the point of separation and thus dictates the shape of the wake. Reducing the initial grid spacing would start to skew the cells in that region and simply enhancing the grid using the boundary layer technique in POST will increase the number of cells drastically.

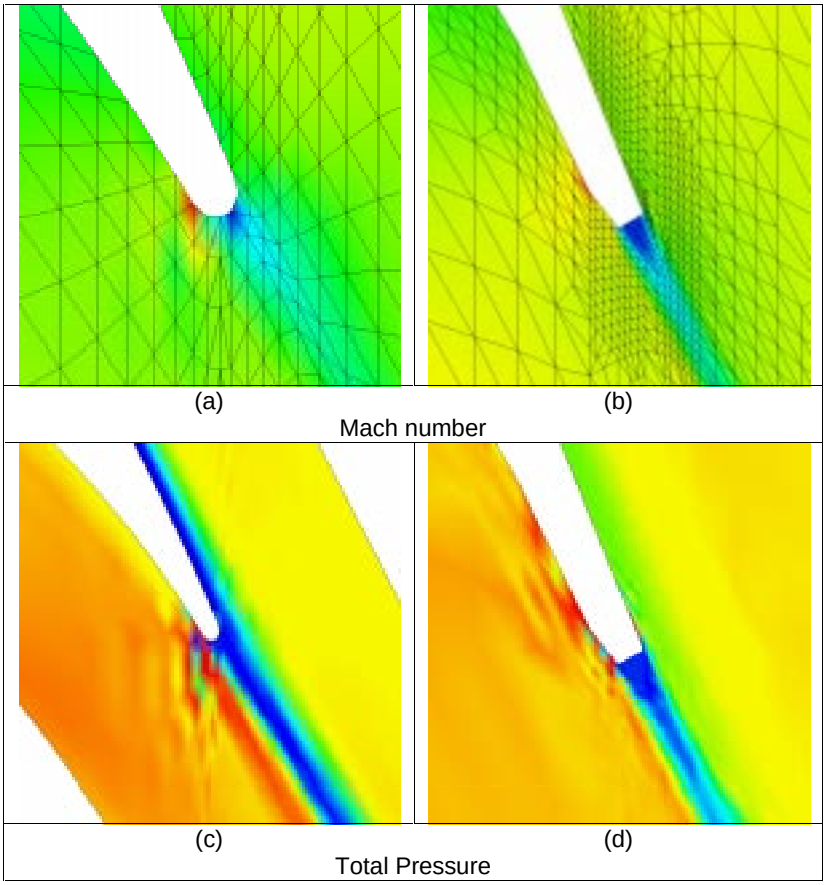

Figure 5.16 Mach number (a,b) and total pressure (c,d) near the trailing edge for the NASA/DERA engine (a,c) and Cambridge No 2 turbine rotor (b,d) geometries

Deviation Angle

The exit flow angle from a high fidelity model was measured and compared to the assumed value. Figure 5.17 shows streamlines (parallel to the blue line) near the trailing edge of the NGV at cruise conditions relative to the blade metal angle (red line). The deviation, measured as the angle between the two lines, was about 5-6° compared to the 2° assumed value of the velocity triangle analysis.

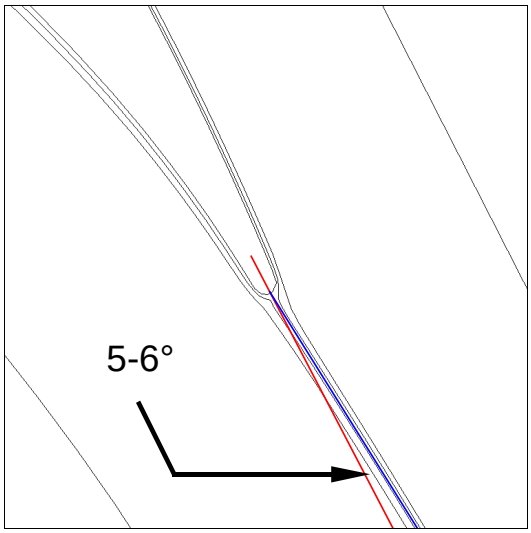

Figure 5.17 Streamlines near the trailing edge used to estimate the deviation angle

The deviation measured from the high fidelity model was between the estimate from Carter's Rule (7.5°) and the assumed value (2°). As mentioned, the flow parameters (including velocity vectors) from the high fidelity models at station B were used as input to the rotor high fidelity models, therefore, the assumed deviation of 2° was considered adequate to make the initial estimate of fluid boundary conditions.

Blade-Row Flow-through Time

The flow-through time for the HPT1 blade rows at cruise condition was estimated by integrating the total velocity along three streamlines as follows:

$$t = \int \frac{1}{V_T} ds \tag{5.23}$$

To give a feel for the range of flow-through times for various parcels of fluid, streamlines were chosen near the pressure and suction sides of the blade as well as one at mid passage. Figure 5.18 shows the streamlines and velocity profiles used for the calculation.

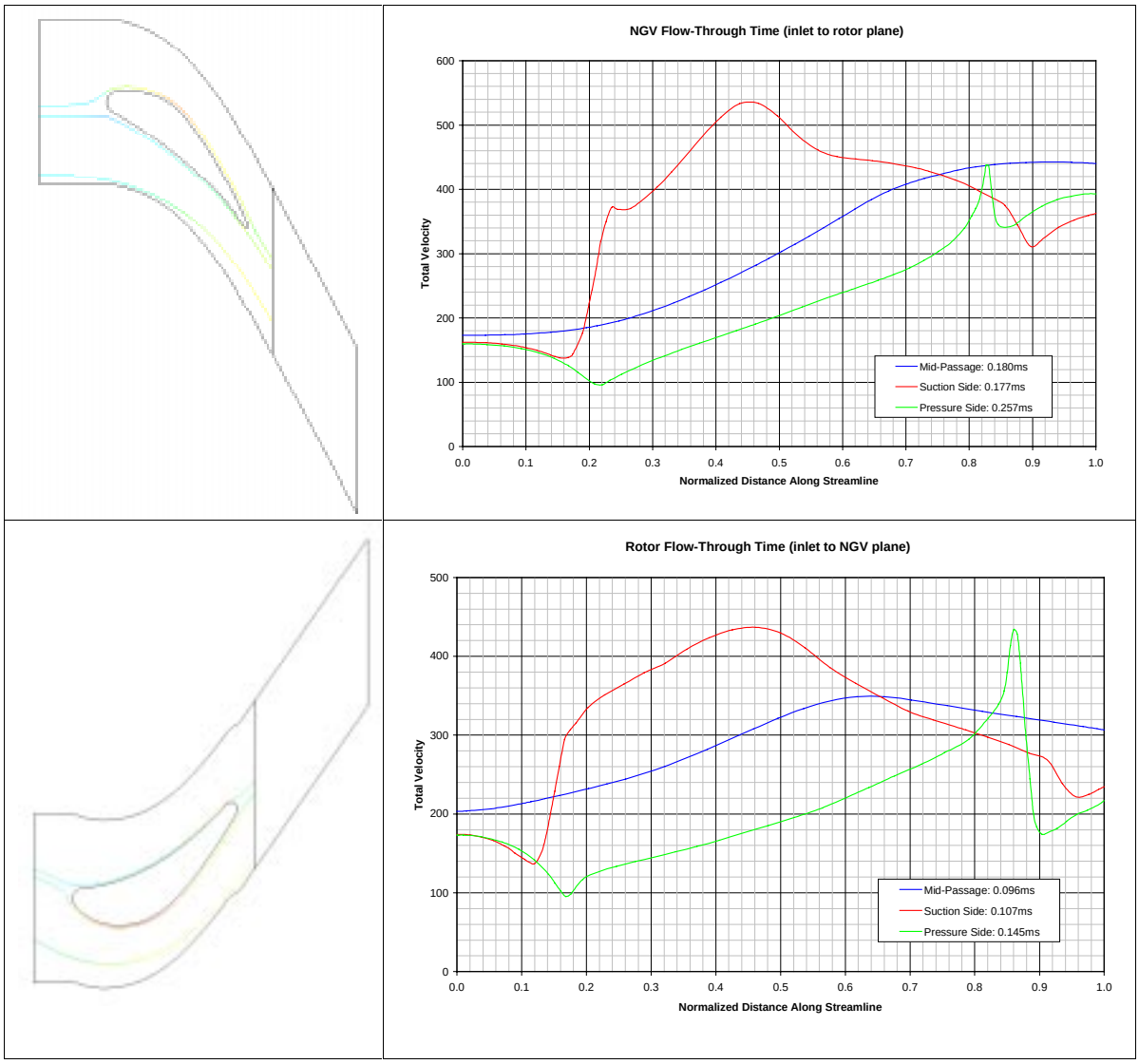

Figure 5.18 Blade row flow-through time calculation at cruise conditions

The flow-though time for the NGV at cruise conditions ranged from 0.18 to 0.26 ms. The corresponding time for the rotor ranged from 0.10 to 0.15 ms. This would imply a stage flow-through time of about 0.28 to 0.41 ms.

5.4.2.3 FLOW-CHEMISTRY RESULTS

A summary of all chemical species results from the HPT1 high fidelity modeling is given in Table 5.5, Table 5.6, and Table 5.7. In each table, the column labeled "Combustor Exit Initial Condition" is the result of the chemical initial condition procedure detailed in Section 2.3.2 and Section 5.4.1. The column labeled "HPT1 NGV Exit" is the mass-averaged species concentration at the plane midway between the NGV trailing edge and

rotor leading edge (at X = 0.04515 m in the NGV grid). As an example, the mass-averaged total pressure was computed as follows:

$$\overline{P_t}^{m} = \frac{\int\left(P + \frac{1}{2}\rho u^2\right)d\dot{m}}{\int d\dot{m}} \tag{5.24}$$

The column labeled "HPT1 Rotor Exit" is divided into two parts. The "mixed-out steady" column is the mass-averaged species concentration at the plane midway between the rotor trailing edge and the leading edge from the NGV on the following turbine stage, HPT2, for a mixed-out case (at X = 0.0106 m in the rotor grid). In the mixed-out case, the inlet condition for the rotor was simply specified as a constant value equal to the mass-averaged species concentration from the "HPT1 NGV Exit" for each species and also the mass-averaged temperature and pressure. In effect, all of the quantities were instantaneously mixed-out at the rotor inlet plane and thus all non-uniformities were removed. The "time ave. unsteady" column is the time-average of the mass-averaged species concentration at the same plane for the unsteady wake model case. As an example, the time-averaged mass-averaged total pressure was computed as follows:

$$\overline{P_t}^{tm} = \frac{\int\left(\overline{P_t}^{m} \cdot \dot{m}\right)dt}{\int \dot{m}\, dt} \tag{5.25}$$

In the unsteady wake model case, the actual 2D non-uniform species, temperature, and pressure profiles were applied to the rotor inlet using the wake model. The wake model which was discussed in detail in Section 3.3.4 preserves the upstream circumferential non-uniformities. Some example profiles for the max power case are given in the graphs on the third row of results in Figure 5.19 and Figure 5.20. The blue symbols on the graphs represent the data points input into the wake model.

Figure 5.19 and Figure 5.20 give example results for total temperature, total pressure, and a few selected species mass fractions from the high fidelity modeling for the NGV and mixed-out rotor cases. The first row is a spanwise view of the contour plot for the particular quantity where the black vertical line represents the blade-row exit plane. The second row is an axial view contour plot on that plane. The third row of the NGV plots is a plot of species mass fraction versus circumferential location at the center of that plane. And the last row lists the range for the contour plot and the mass averaged value on that plane.

The total temperature deficit in the NGV wake is about 9%. Also, notice that the SO_3 and HONO mass fraction profiles are inverse to the temperature wake profile, suggesting that the temperature gradients have the strongest influence on their local concentration and that blade cooling enhances their production.

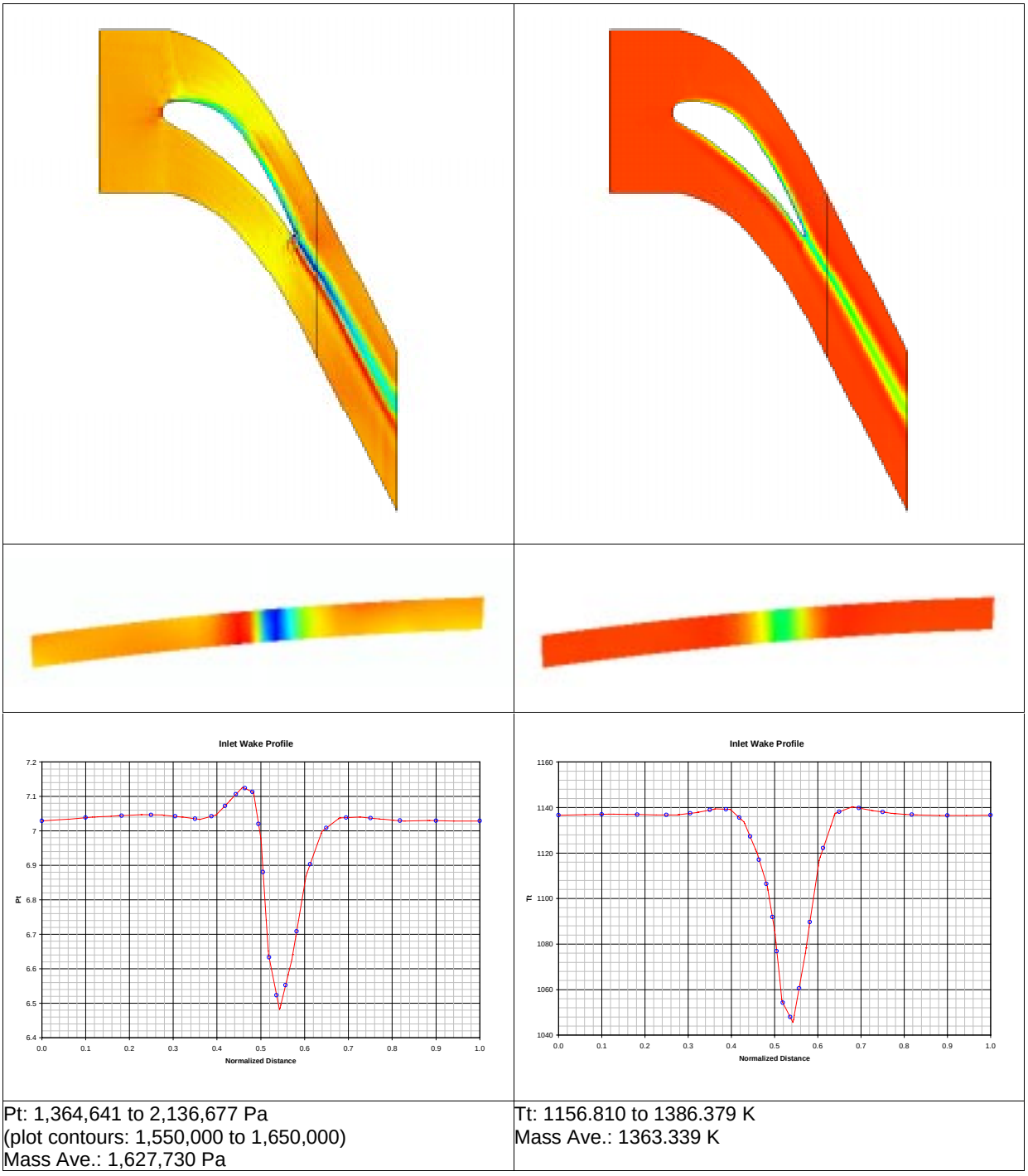

Pt: 1,364,641 to 2,136,677 Pa (plot contours: 1,550,000 to 1,650,000) Mass Ave.: 1,627,730 Pa	Tt: 1156.810 to 1386.379 K Mass Ave.: 1363.339 K

Figure 5.19 Total temperature and total pressure at NGV exit for max power case

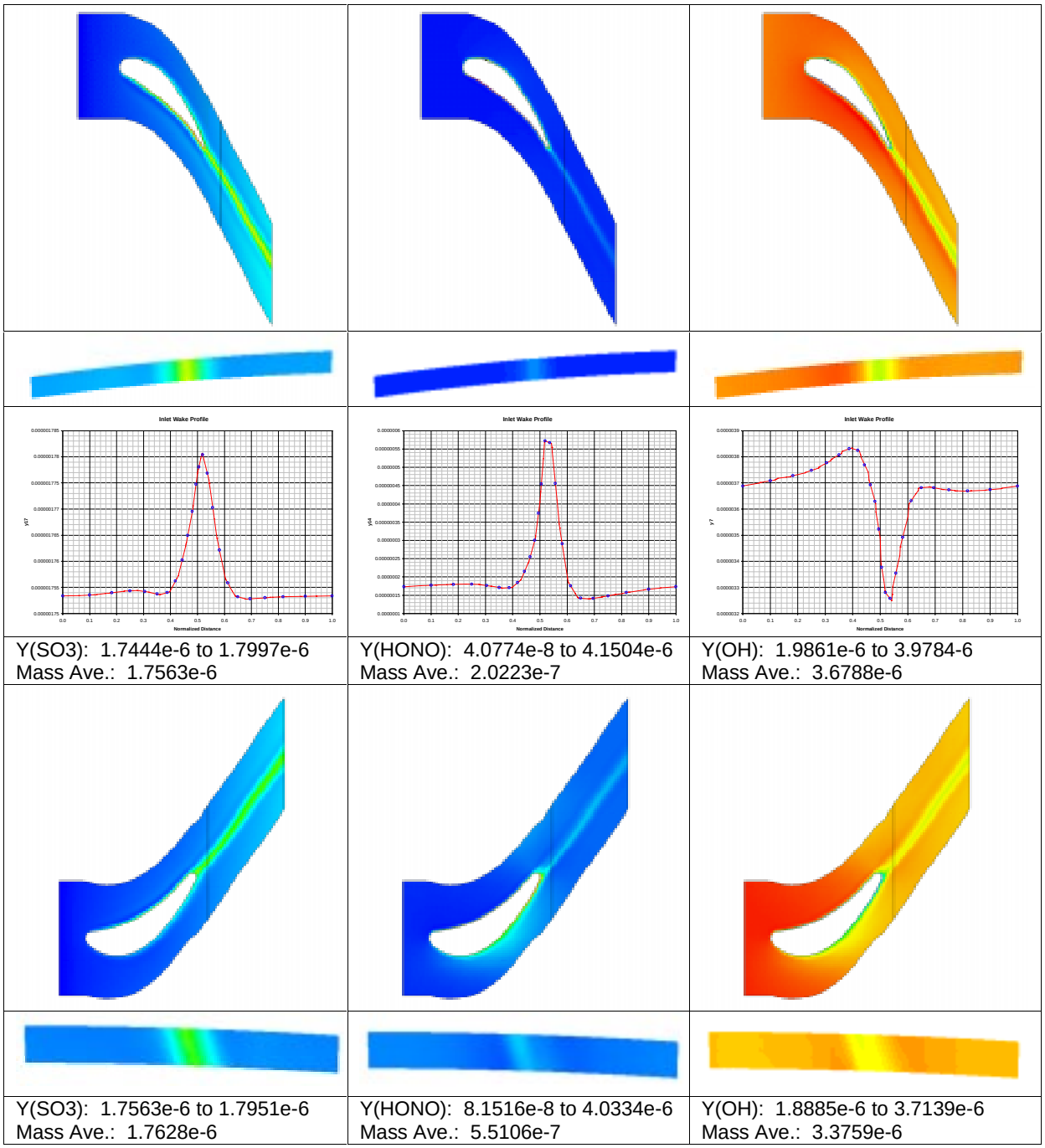

Y(SO3): 1.7444e-6 to 1.7997e-6 Mass Ave.: 1.7563e-6	Y(HONO): 4.0774e-8 to 4.1504e-6 Mass Ave.: 2.0223e-7	Y(OH): 1.9861e-6 to 3.9784-6 Mass Ave.: 3.6788e-6
Y(SO3): 1.7563e-6 to 1.7951e-6 Mass Ave.: 1.7628e-6	Y(HONO): 8.1516e-8 to 4.0334e-6 Mass Ave.: 5.5106e-7	Y(OH): 1.8885e-6 to 3.7139e-6 Mass Ave.: 3.3759e-6

Figure 5.20 SO_3, HONO, and OH at NGV and rotor exit for max power case

Some example results and profiles for the non-uniform max power case are given in Figure 5.21.

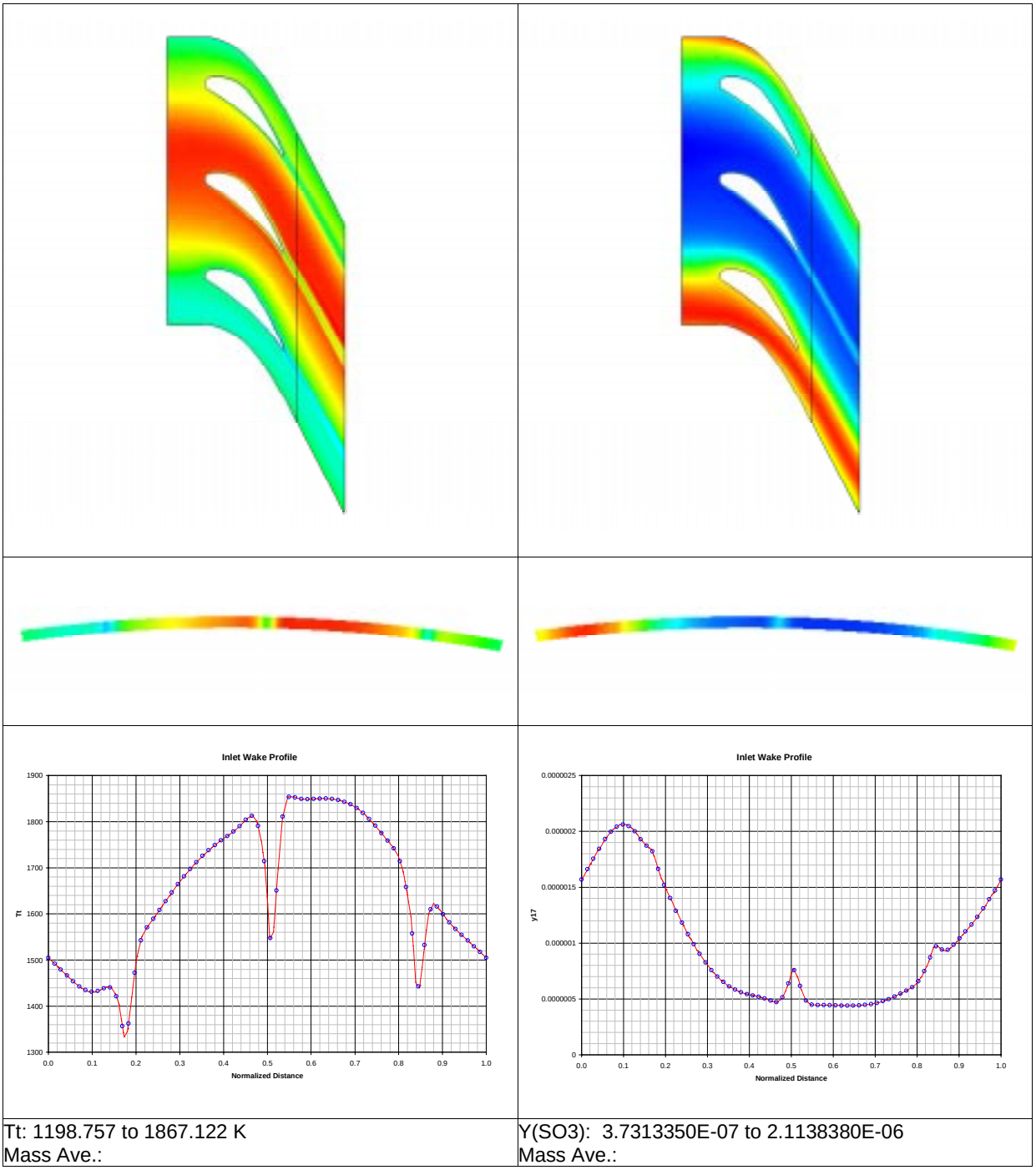

Tt: 1198.757 to 1867.122 K Mass Ave.:	Y(SO3): 3.7313350E-07 to 2.1138380E-06 Mass Ave.:

Figure 5.21 Total temperature and SO_3 at NGV exit for non-uniform max power case

The wake model rotor cases are unsteady (i.e. time varying) solutions due to the rotation of the upstream stator wakes and combustor profile relative to the rotor blades. Therefore, the specific results consist of a series of plots equally spaced out over a time interval equal to one cycle. An example result of the wake model case is shown in Figure 5.22 for the non-uniform max-power case. A similar result for the max power case is given in Appendix C. The time dependent results can also be viewed in the animations contained in the attached media detailed in Appendix E.

From the figure, it is evident that the localized regions of non-uniform SO_3 mass fraction persist downstream past the exit of the blade row. Also, notice that the non-uniformity from the combustor temperature profile is much larger than the non-uniformity from the wakes of the cooled blades (i.e. more of the flow is subject to the larger scale combustor non-uniformity).

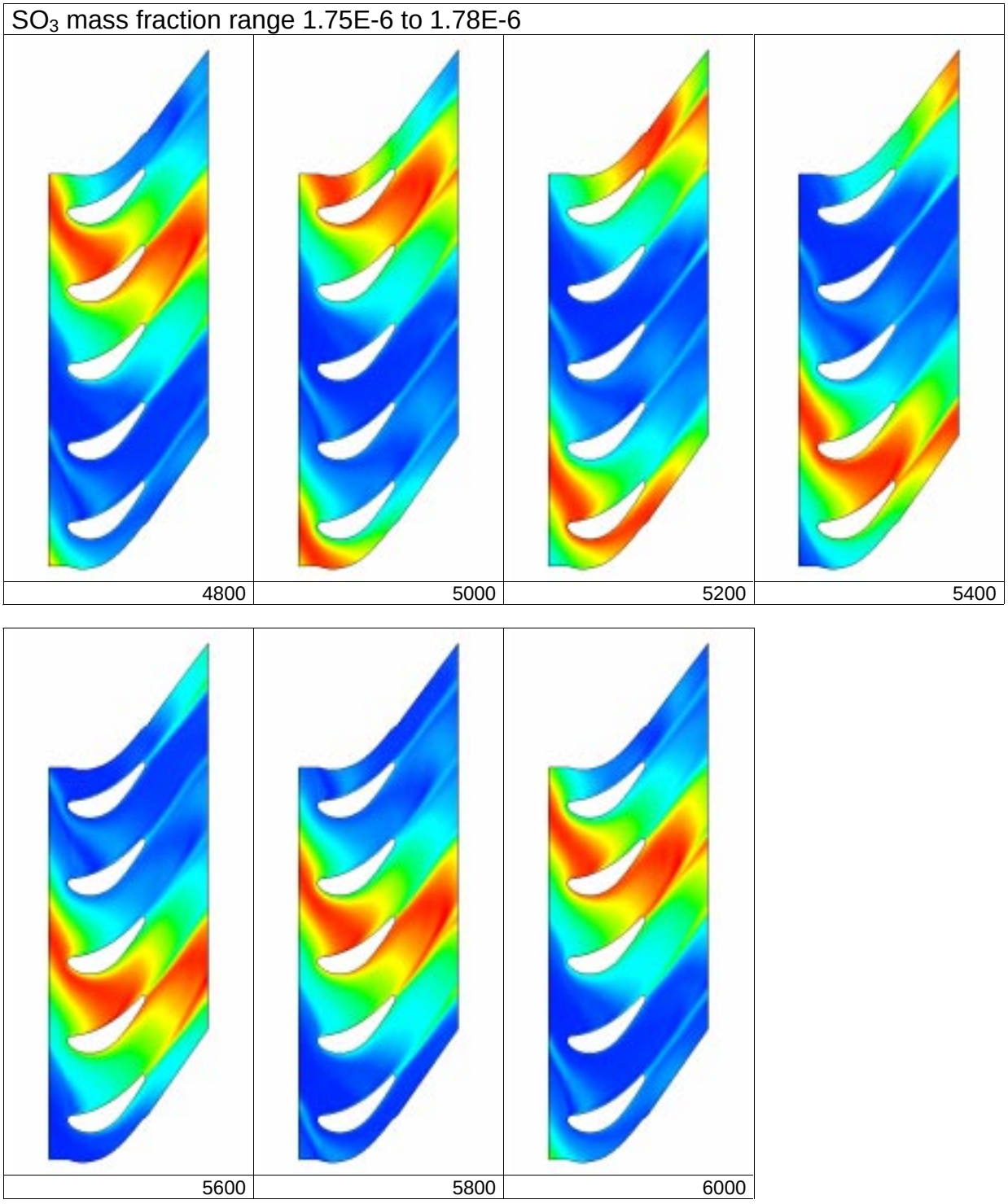

Figure 5.22 Example result of rotor wake model case, SO_3 mass fraction for non-uniform max power condition at selected times for one cycle

A summary of all the key results is given in Table 5.5, Table 5.6, and Table 5.7 for the cruise, max power, and non-uniform max power conditions, respectively. The species quantities are given in mole fraction. The unsteady wake model case and HPT1 exit to nozzle exit was not run for the cruise condition. Again, for a complete set of detailed results for the max power conditions see Appendix C.

Summary of 2-D Simulation Results: Cruise Condition						
		Combustor Exit	HPT1 NGV Exit	HPT1 Rotor Exit		Nozzle Exit
Number	Species	Initial Condition		mixed-out steady	time ave. unsteady	
1	CO	1.21890E-04	1.21772E-04	1.21739E-04	N/A	N/A
2	CO2	4.76468E-02	4.76469E-02	4.76469E-02	N/A	N/A
3	O2	1.33217E-01	1.33217E-01	1.33217E-01	N/A	N/A
4	H2O	4.78257E-02	4.78257E-02	4.78257E-02	N/A	N/A
5	H	1.68680E-10	1.64263E-10	1.52266E-10	N/A	N/A
6	O	4.88767E-09	4.92741E-09	4.53878E-09	N/A	N/A
7	OH	3.68109E-07	3.16391E-07	2.65419E-07	N/A	N/A
8	HO2	9.90554E-09	8.70358E-09	7.39922E-09	N/A	N/A
9	H2O2	4.64661E-10	6.84852E-10	7.97481E-10	N/A	N/A
10	NO	3.02737E-04	3.02550E-04	3.02462E-04	N/A	N/A
11	NO2	3.10783E-06	3.20137E-06	3.23082E-06	N/A	N/A
12	NO3	5.26957E-13	4.23230E-13	3.37662E-13	N/A	N/A
13	HNO	5.33968E-11	1.38233E-10	1.63320E-10	N/A	N/A
14	HONO	5.32214E-08	1.45864E-07	2.04203E-07	N/A	N/A
15	HNO3	1.50489E-10	5.45819E-10	8.45071E-10	N/A	N/A
16	SO2	9.83418E-06	9.83378E-06	9.83355E-06	N/A	N/A
17	SO3	6.29053E-07	6.29292E-07	6.29353E-07	N/A	N/A
18	HOSO	1.02269E-14	6.53196E-15	4.32394E-15	N/A	N/A
19	HSO3	3.29192E-13	4.87219E-13	6.07823E-13	N/A	N/A
20	HSO2	5.81476E-17	7.31318E-17	8.16752E-17	N/A	N/A
21	SO	1.24025E-14	7.82809E-15	4.90596E-15	N/A	N/A
22	HCO	2.09232E-16	1.78302E-16	1.45277E-16	N/A	N/A
23	H2	5.76045E-10	1.35492E-09	1.49002E-09	N/A	N/A
24	N2	7.70872E-01	7.70873E-01	7.70872E-01	N/A	N/A
25	AR	0.00000E+00	0.00000E+00	0.00000E+00	N/A	N/A
26	C(S)	0.00000E+00	0.00000E+00	0.00000E+00	N/A	N/A
27	N	0.00000E+00	0.00000E+00	0.00000E+00	N/A	N/A
28	H2SO4	2.71298E-10	4.32577E-10	5.97855E-10	N/A	N/A
29	S	8.93357E-26	8.93358E-26	8.93357E-26	N/A	N/A
Note: All quantities are species mole fractions						
(SO3+H2SO4)/SOx		6.014627%	6.017002%	6.017683%	N/A	N/A
Δ from comb exit		0.000000%	0.002375%	0.003057%	N/A	N/A
(HNO2+HNO3)/NOy		0.017448%	0.047862%	0.067032%	N/A	N/A
Δ from comb exit		0.000000%	0.030415%	0.049584%	N/A	N/A
CO/COx		0.255167%	0.254920%	0.254850%	N/A	N/A
Δ from comb exit		0.000000%	-0.000247%	-0.000317%	N/A	N/A

Table 5.5 Summary of results from HPT1 high fidelity modeling at cruise condition

Summary of 2-D Simulation Results: Max Power Condition						
		Combustor Exit	HPT1 NGV Exit	HPT1 Rotor Exit		Nozzle Exit
Number	Species	Initial Condition		mixed-out steady	time ave. unsteady	
1	CO	1.21338E-05	1.16222E-05	1.14829E-05	1.14873E-05	1.10103E-05
2	CO2	4.77591E-02	4.77596E-02	4.77597E-02	4.77594E-02	4.77602E-02
3	O2	1.33364E-01	1.33363E-01	1.33363E-01	1.33362E-01	1.33363E-01
4	H2O	4.78252E-02	4.78252E-02	4.78253E-02	4.78249E-02	4.78262E-02
5	H	2.25336E-10	2.39666E-10	2.69007E-10	2.65394E-10	1.83933E-14
6	O	4.70854E-08	6.14953E-08	7.79818E-08	7.69738E-08	3.60078E-12
7	OH	6.34676E-06	6.23653E-06	5.72297E-06	5.66955E-06	4.76565E-10
8	HO2	4.72951E-08	3.75148E-08	3.22171E-08	3.19551E-08	3.73416E-12
9	H2O2	5.65370E-09	1.43659E-08	3.38376E-08	3.42769E-08	8.11063E-08
10	NO	3.03146E-04	3.02607E-04	3.02235E-04	3.02198E-04	2.97325E-04
11	NO2	3.13150E-06	3.59479E-06	3.75165E-06	3.74791E-06	4.83243E-06
12	NO3	2.80802E-12	4.92369E-12	6.72411E-12	6.68833E-12	1.64124E-15
13	HNO	7.26096E-11	1.20328E-10	1.44131E-10	1.45020E-10	2.02452E-10
14	HONO	4.83244E-08	1.24018E-07	3.37947E-07	3.58021E-07	4.13637E-06
15	HNO3	1.41738E-10	4.18364E-10	1.12582E-09	1.20628E-09	3.14403E-08
16	SO2	9.83523E-06	9.83090E-06	9.82854E-06	9.82810E-06	9.80581E-06
17	SO3	6.28200E-07	6.32486E-07	6.34796E-07	6.34822E-07	6.32379E-07
18	HOSO	1.01540E-13	6.41894E-14	4.13414E-14	4.08055E-14	2.34491E-19
19	HSO3	2.11542E-12	2.89491E-12	3.81943E-12	3.87058E-12	3.07378E-14
20	HSO2	5.44402E-17	6.69217E-17	8.68047E-17	8.66727E-17	1.24059E-19
21	SO	2.16133E-13	2.09942E-13	1.87071E-13	1.83422E-13	3.42017E-19
22	HCO	5.51512E-17	4.47816E-17	4.05453E-17	4.01285E-17	1.28711E-21
23	H2	1.64534E-09	1.05576E-08	1.16103E-08	1.14921E-08	1.21473E-08
24	N2	7.70716E-01	7.70716E-01	7.70717E-01	7.70711E-01	7.70716E-01
25	AR	0.00000E+00	0.00000E+00	0.00000E+00	0.00000E+00	0.00000E+00
26	C(S)	0.00000E+00	0.00000E+00	0.00000E+00	0.00000E+00	0.00000E+00
27	N	0.00000E+00	0.00000E+00	0.00000E+00	0.00000E+00	0.00000E+00
28	H2SO4	1.28462E-10	1.68215E-10	2.22540E-10	2.28069E-10	2.53712E-08
29	S	2.19811E-21	2.19811E-21	2.19811E-21	2.19809E-21	2.19811E-21

Note: All quantities are species mole fractions

(SO3+H2SO4)/SOx	6.004995%	6.045985%	6.068084%	6.068569%	6.059928%
Δ from comb exit	0.000000%	0.040991%	0.063089%	0.063575%	0.054934%
(HNO2+HNO3)/NOy	0.015822%	0.040622%	0.110690%	0.117278%	1.360582%
Δ from comb exit	0.000000%	0.024801%	0.094869%	0.101456%	1.344760%
CO/COx	0.025400%	0.024329%	0.024037%	0.024047%	0.023048%
Δ from comb exit	0.000000%	-0.001071%	-0.001363%	-0.001353%	-0.002352%

Table 5.6 Summary of results from HPT1 high fidelity modeling at max power condition

Summary of 2-D Simulation Results: Non-Uniform Max Power Condition						
		Combustor Exit	HPT1 NGV Exit	HPT1 Rotor Exit		Nozzle Exit
Number	Species	Initial Condition		mixed-out steady	time ave. unsteady	
1	CO	1.15329E-05	8.35163E-06	7.38236E-06	7.79052E-06	5.03788E-06
2	CO2	4.78104E-02	4.78135E-02	4.78145E-02	4.78109E-02	4.78168E-02
3	O2	1.34160E-01	1.34167E-01	1.34172E-01	1.34181E-01	1.34182E-01
4	H2O	4.77659E-02	4.77844E-02	4.77958E-02	4.78122E-02	4.78231E-02
5	H	5.91935E-08	3.13144E-08	1.90711E-08	2.65527E-08	5.39530E-12
6	O	5.61601E-06	3.61282E-06	2.78809E-06	3.09000E-06	2.26319E-09
7	OH	1.20450E-04	8.40250E-05	6.14268E-05	6.45515E-05	1.76425E-07
8	HO2	6.76771E-07	4.43111E-07	4.21141E-07	4.71472E-07	1.12166E-09
9	H2O2	3.81133E-08	4.82831E-08	1.07656E-07	8.13361E-08	2.56225E-07
10	NO	3.03484E-04	3.02503E-04	3.01528E-04	2.98333E-04	2.87829E-04
11	NO2	2.88219E-06	3.83386E-06	4.75487E-06	1.05940E-05	1.09828E-05
12	NO3	7.33999E-12	1.97938E-11	6.09685E-11	9.39380E-11	5.28522E-13
13	HNO	3.88249E-10	3.50353E-10	6.70221E-10	4.79792E-10	3.15691E-10
14	HONO	2.62278E-08	5.56272E-08	1.09335E-07	1.20774E-07	7.47313E-06
15	HNO3	7.55054E-11	2.47416E-10	5.20103E-10	1.41816E-09	1.07858E-07
16	SO2	1.01206E-05	1.01041E-05	1.00939E-05	1.01001E-05	1.00311E-05
17	SO3	3.41779E-07	3.58292E-07	3.68528E-07	3.58658E-07	4.29548E-07
18	HOSO	3.87086E-12	2.08593E-12	1.28268E-12	1.62738E-12	1.92871E-16
19	HSO3	6.59378E-12	6.38182E-12	8.06975E-12	6.88370E-12	2.11402E-12
20	HSO2	3.77560E-15	2.22706E-15	2.10835E-15	2.05852E-15	7.21925E-18
21	SO	6.86930E-11	3.42928E-11	1.46333E-11	2.15939E-11	6.72918E-16
22	HCO	6.08598E-15	1.91539E-15	1.19428E-15	1.27618E-15	1.44639E-19
23	H2	8.14864E-07	5.79348E-07	4.34916E-07	5.26470E-07	1.09997E-07
24	N2	7.69808E-01	7.69809E-01	7.69810E-01	7.69761E-01	7.69810E-01
25	AR	0.00000E+00	0.00000E+00	0.00000E+00	0.00000E+00	0.00000E+00
26	C(S)	0.00000E+00	0.00000E+00	0.00000E+00	0.00000E+00	0.00000E+00
27	N	4.01390E-12	4.00640E-12	4.00640E-12	3.86511E-12	4.00640E-12
28	H2SO4	3.05830E-11	4.19789E-11	3.13587E-11	5.12671E-11	1.80619E-09
29	S	4.11071E-16	4.10394E-16	4.10395E-16	3.99506E-16	4.10395E-16
Note: All quantities are species mole fractions						

(SO3+H2SO4)/SOx	3.267025%	3.424855%	3.522683%	3.429555%	4.106721%
Δ from comb exit	0.000000%	0.157831%	0.255658%	0.162531%	0.839697%
(HNO2+HNO3)/NOy	0.008585%	0.018236%	0.035854%	0.039538%	2.474273%
Δ from comb exit	0.000000%	0.009651%	0.027269%	0.030953%	2.465688%
CO/COx	0.024116%	0.017464%	0.015437%	0.016292%	0.010535%
Δ from comb exit	0.000000%	-0.006652%	-0.008679%	-0.007825%	-0.013582%

Table 5.7 Summary of results from HPT1 high fidelity modeling at max power condition

5.5 LOW FIDELITY MODELING

5.5.1 LOW FIDELITY MODELING SET UP

Low fidelity models were use to model both the HPT1 and the HPT1 exit to nozzle exit flow paths. Several steps were required to prepare for these runs. First, the 1D temperature, pressure, and velocity profiles were extracted from the high fidelity models of the HPT1 NGV and rotor blade rows. A mass-averaged profile as well as profiles along several streamlines were investigated. Next, the available engine performance data was used to generate similar 1D profiles for the HPT1 exit to nozzle exit. A set of input files to CALCHEM for the max power condition is given in Appendix D as an example.

HPT1

The low fidelity models of the HPT1 would give a direct comparison of the results of a high fidelity versus a low fidelity model. The HPT1 is a good region of the engine to make these comparisons since it is expected to have the highest chemical reactivity.

The domains of the high fidelity models for the NGV and rotor were both divided into ten equally spaced axial stations at which mass-averaged flow and species quantities were obtained. The static temperature, static pressure, and axial velocity were assembled into the 1D profile and used for the low fidelity modeling of the HPT1. The normalized 1D profiles of flow parameters for the max power mixed-out case are shown in Figure 5.23. The circle data points represent the locations of the mass average planes. The magenta lines show the entrance and exit plane of each domain and the cyan lines show the location of the respective blade within the domain.

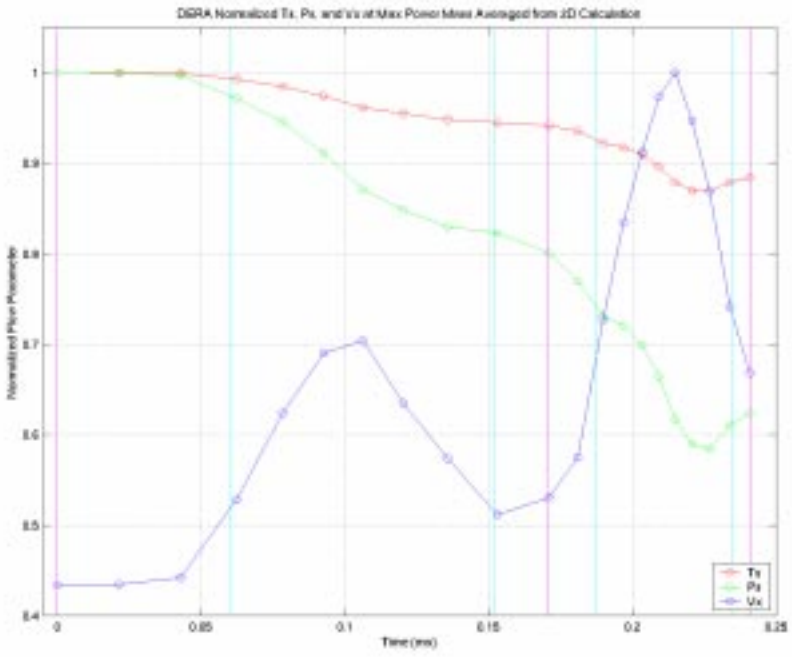

Figure 5.23 HPT1 normalized 1D profile

The 1D profiles were also created for the non-uniform max power mixed-out case, the normalized intra-stage profiles are similar to those in Figure 5.23 for the max power case.

Streamlines

Representative low and high temperature streamlines were also selected at the exit of the NGV and rotor domains. Flow and species quantities were extracted along those streamlines for both the max power and non-uniform max power cases. The high temperature streamline was between the blades near the pressure surface and the low temperature streamline was in the boundary layer near the suction surface for both the NGV and rotor. Figure 5.24 shows the streamlines selected for the max power case. The corresponding high and low temperature 1D profiles extracted from those streamlines are shown in Figure 5.25. The streamline profiles were used to perform a 1D analysis which would be expected to show the range in magnitude of species change due to 2D non-uniformity.

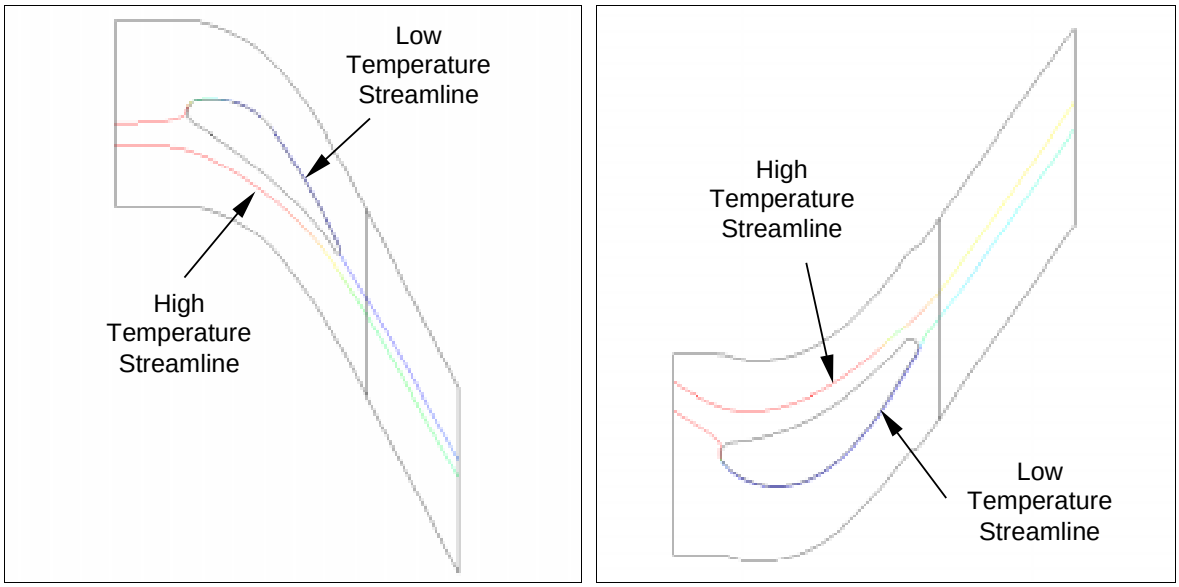

Figure 5.24 High and low temperature streamlines selected for 1D profiles

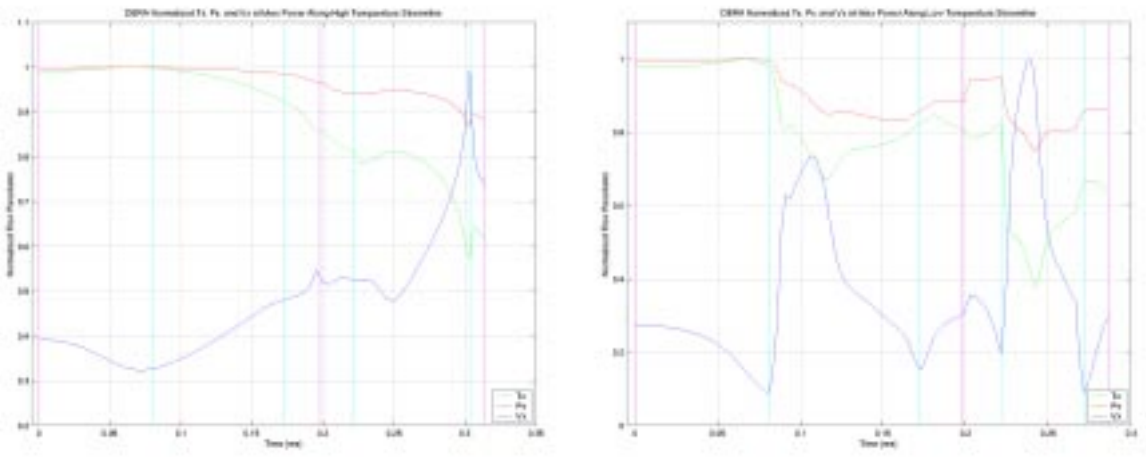

Figure 5.25 1D profile for high (left) and low (right) temperature streamlines

The 1D profiles for the streamlines were also created for the non-uniform max power mixed-out case. The normalized intra-stage profiles are similar to those in Figure 5.25 for the max power case.

HPT1 Exit To Nozzle Exit

Initially, the limited engine data from the DERA model was used to construct a 1D profile for the low fidelity modeling for the HPT1 exit to nozzle exit using pressure, temperature, and Mach number data at the available engine stations. However, the species evolution results contained significant discontinuities due to the coarse and discontinuous engine data. Therefore, the HPT1 1D profile was scaled to fit the other three stages of the turbines in attempt to provide a more accurate profile for the 1D calculations. Also, an attempt was made to insert more points to smooth the remainder of the post turbine flow path. The large number of points required to fully represent the details of this complicated flow path contradicted the goal of a simplified 1D analysis, therefore, several polynomial curve fits were used to obtain a simpler profile. Figure 5.26 shows the coarse profile obtained from the available data and the improved profile using the scaled HPT1 profile and curve fitting. The circle data labels in lower portion of the figure are the points obtained from the curve fitting.

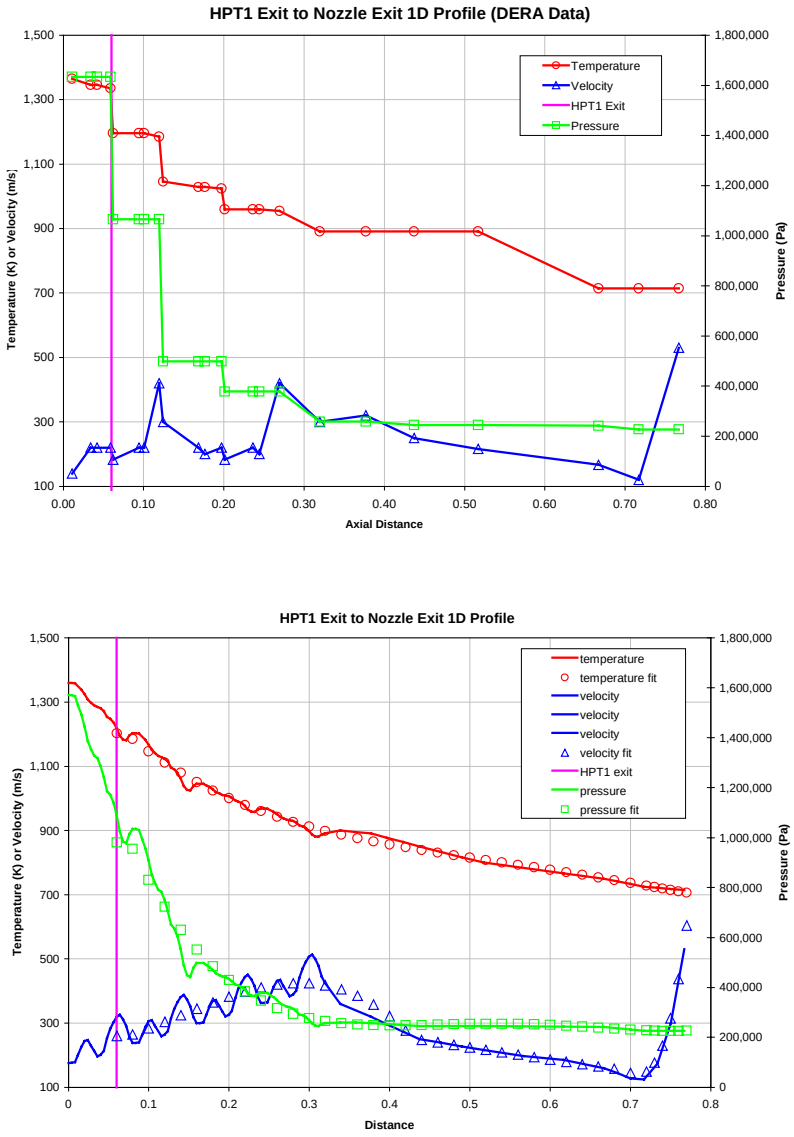

Figure 5.26 HPT1 exit to nozzle exit 1D profile, available data (top) and curve fit (bottom)

Figure 5.27 shows the final normalized HPT1 exit to nozzle exit 1D profiles used for the low fidelity modeling. The magenta lines approximate the locations of the inlet and exit planes for the HPT2, LPT1, and LPT2 turbine stages.

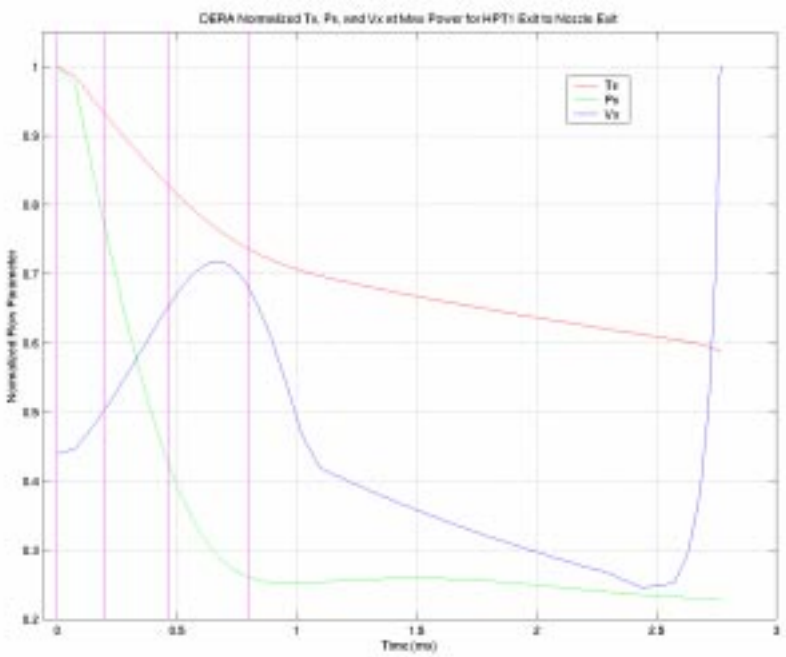

Figure 5.27 Normalized HPT1 exit to nozzle exit 1D profiles used in low fidelity models

5.5.2 LOW FIDELITY MODELING RESULTS

The low fidelity modeling for the NASA/DERA engine test consisted of 1D fluid-chemistry solutions for the HPT1 and the HPT1 exit to nozzle exit for the max power and non-uniform max power conditions. The low fidelity modeling was primarily used to track the evolution of species from the end of the high fidelity HPT1 model to the engine nozzle exit in order to obtain an engine exit plane gas composition. Also, the low fidelity modeling was used on the HPT1 so as to provide a direct comparison between the low and high fidelity modeling techniques.

5.5.2.1 CALCULATION DESCRIPTION AND EXECUTION

Solution Convergence And Profile Resolution

Convergence of the low fidelity solutions is automatically achieved within CALCHEM by setting the error tolerance variables RTOL and ATOL which were set at, 1.0E-6 and 1.0E-9 for these calculations, respectively (see [68] for more details). The input profiles used in the low fidelity modeling calculations typically had between 20 to 80 points specified. The linear interpolation option of CALCHEM was used to add roughly 10 to 50 additional points to yield a solution result with about 500 to 1,000 points along the 1D profiles.

HPT1 and Engine Flow-Through Time

The flow-through times ranged from 0.24 ms for the mass averaged case to 0.32 ms for the high temperature streamline of the HPT1 at max power conditions. For the 1D analysis the flow-through time was computed by integrating the axial velocity along the axial distance rather than the total velocity along the actual streamline path. These estimated flow-through times for the HPT1 were consistent with those from the high fidelity modeling (see 5.4.2.2). The flow-through time for the HPT1 exit to nozzle exit was 2.77 ms for the max power condition, giving an overall flow-through time for the post-combustor gas path of about 3 ms.

5.5.2.2 FLOW-CHEMISTRY RESULTS

A summary of the important chemical species results from HPT1 low fidelity modeling is given in Table 5.6 and Table 5.7. In each table, the column labeled "Nozzle Exit" is the result of the 1D low fidelity modeling of the HPT1 exit to nozzle exit using the mixed-out HPT1 results as input to the low fidelity models.

The results from the low fidelity model were plotted as mass fraction versus time for three subsets of species. The plots are divided into two halves, the left graph shows the species evolution within the HPT1, and the right graph shows the species evolution from the HPT1 exit to the nozzle exit. Notice that the axis scales are different on both graphs. The species subsets were divided by family: SO_x (SO_2, SO_3, H_2SO_4, HSO_3, SO), NO_y (NO, NO_2, HONO, HNO_3, HNO, NO_3), and CO, OH, and O. The plots contain the three 1D calculations for the mass average, high temperature streamline, and low temperature streamline profiles, as well as, the mass-averaged species from the high fidelity modeling (labeled "2D Mass Average"). As an example, the NO_y plots are given in Figure 5.28 and Figure 5.29 for the max power and non-uniform max power case, respectively. For a complete set of detailed results for the max power conditions see Appendix C.

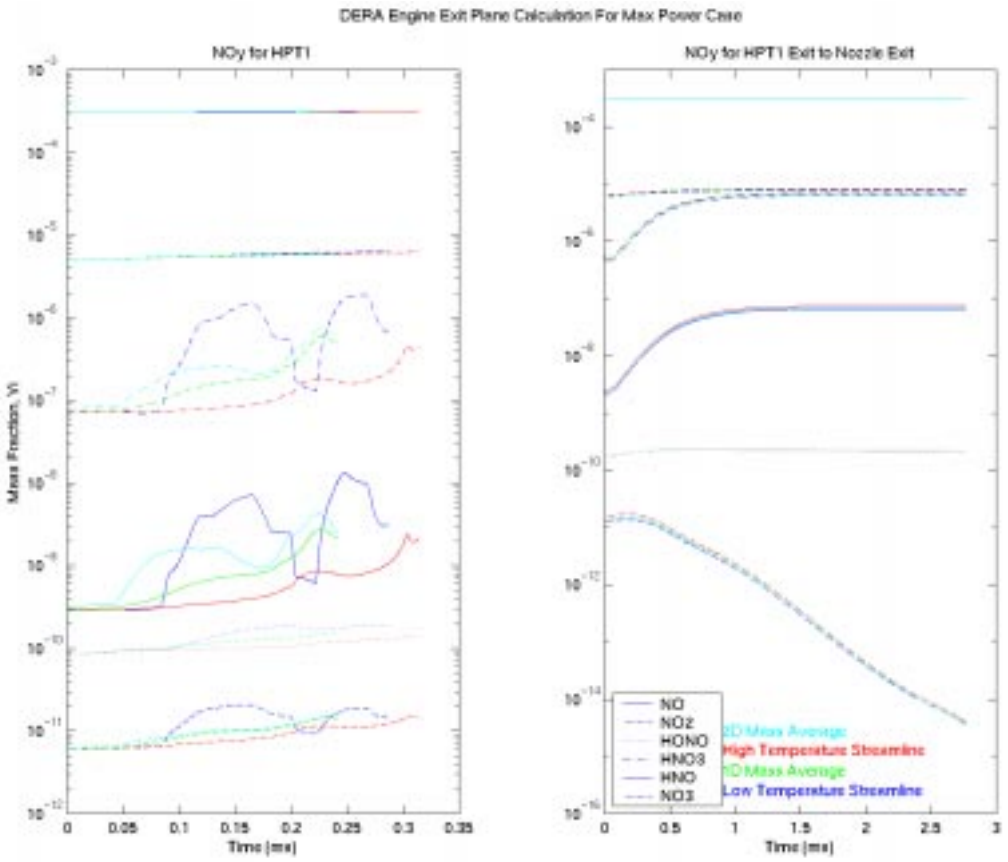

Figure 5.28 Example low fidelity modeling results, NOy species evolution in the HPT1 and from the HPT1 exit to nozzle exit for the max power condition

NOTE: The legend on the chart lists the species in the proper sequence for the lines (top to bottom), however, the line style is not correct (dashed, dotted, solid, etc is wrong).

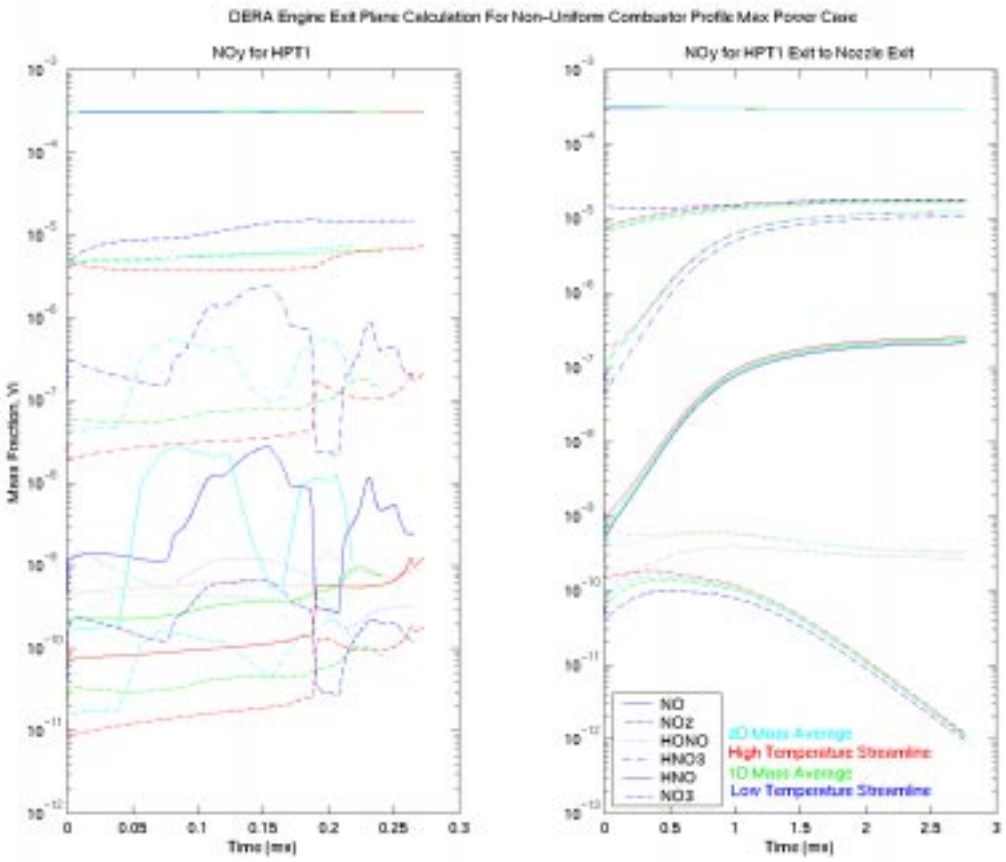

Figure 5.29 Example low fidelity modeling results, NOy species evolution in the HPT1 and from the HPT1 exit to nozzle exit for the non-uniform max power condition

NOTE: The legend on the chart lists the species in the proper sequence for the lines (top to bottom), however, the line style is not correct (dashed, dotted, solid, etc is wrong).

5.6 IMPLICATIONS OF RESULTS

5.6.1 EFFECTS OF ENGINE OPERATING CONDITIONS

The three operating points studied for the NASA/DERA engine test simulation are typical of an older, but currently in-use engine. They can be used to assess the effects of engine operating conditions on trace species evolution and engine emissions. The cruise case has a combustor exit temperature of 1120 K and pressure of 6.8 atm, while for the max power case they are 1360 K and 15.7 atm, and for the non-uniform max power case the temperature is nominally 1600 K. It was found that SO_3 and HONO concentrations increased with

increased engine power level. The increase in $(SO_3+H_2SO_4)/SO_x$ from the mixed-out case was 0.003%, 0.06%, and 0.26% over the HPT1 stage for the cruise, max power, and non-uniform max power cases, respectively. Since the max power and non-uniform max power cases have the same pressure and the values are quoted from the mixed-out case, one can attribute these trends primarily to the increased combustor exit temperature. It is expected that this trend is general, however, the magnitude of the changes is also influenced by the degree and scale of the non-uniformities (see Section 5.6.2 and 5.6.3). The increase in $(SO_3+H_2SO_4)/SO_x$ at the nozzle exit was 0.05% for the max power case and 0.84% for the non-uniform max power case using the mixed-out results. The nozzle exit plane results also show the sensitivity of the SO_x chemistry to temperature since the $(SO_3+H_2SO_4)/SO_x$ decreases slightly for the max power case and increases significantly for the non-uniform max power case. This implies that further oxidation is occurring for the non-uniform max power case after the HPT1 which suggests that it is still in a higher temperature range which is favorable to SO_3 production. Also, the increase in $(HNO_2+HNO_3)/NO_y$ for the mixed-out case was 0.05%, 0.09%, and 0.03% over the HPT1 stage for the cruise, max power, and non-uniform max power cases, respectively. The increase in $(HNO_2+HNO_3)/NO_y$ at the nozzle exit was 1.3% for the max power case and 2.5% for the non-uniform max power case using the mixed-out results. These results further suggest that there is a region in the temperature range at which HONO production is favored, which is at lower temperatures than for SO_3, and that HONO concentrations at the nozzle exit also increase with higher temperatures. Overall, the various operating conditions studied in the NASA/DERA engine test simulations further support the conclusions from the 1D parametric study in previous work by Lukachko [1] that post-combustor chemistry is sensitive to combustor exit temperature. Also, the conclusions indicate that newer and future engine designs which tend to have higher combustor exit temperatures will be more prone to conversion to SO_3, H_2SO_4, HONO, and HNO_3 in the post-combustor gas path.

5.6.2 EFFECTS OF MULTI-DIMENSIONAL NON-UNIFORMITIES

The high fidelity models used for the HPT1 of the NASA/DERA engine test simulation also give insight into the effects of non-uniformities, occurring due to multi-dimensional effects, on trace species evolution. The temperature, pressure, and velocity can vary significantly throughout the blade passages due to geometry induced blade-to-blade gradients, blade cooling, viscous boundary layers, and non-uniform combustor temperature profiles. Spatial variations in species concentrations in the 2D solutions suggest that these non-uniformities have an effect on chemical evolution. The correlation of the species and temperature spatial variations in the high fidelity models further suggests the primary influence on chemistry is temperature gradients. For example, a 9% temperature deficit equated to a 1.4% increase in SO_3 mass fraction in the wake of the NGV for the max power case. The species concentrations for the max power case were plotted versus axial distance in Figure 5.28 for the max power case and Figure 5.29 for the non-uniform max power case through the HPT1 by mass-averaging the 2D calculation at several axial planes and for a 1D calculation using

the mass averaged T, P, and V_x profiles. There was a significant difference between the 1D and 2D computations. The 1D computation under-predicted the SO_3 and HONO by 0.25% and 11.25% for the max power case and 2.7% and 21.3% for the non-uniform max power case, respectively. This trend is general and the difference is expected to depend on the magnitude of the temperature, pressure, or residence time discrepancies captured in the 2D model, as well as, the scale of those non-uniformities.

Another way to look at these effects is to consider the different pressure, temperature, and velocity profiles encountered by fluid elements traveling along different streamlines. The species concentrations along a high and low temperature streamline were also plotted versus axial distance. The results from the two streamlines differ significantly from the averaged values, as well as each other. These results further support the conclusions from previous work by Lukachko [1] that multi-dimensional non-uniformities have a considerable influence on trace chemistry evolution which indicates that some important features can not be captured in 1D models. Furthermore, other non-uniformities such as endwall boundary layers/cooling (similar to blade cooling), cooling air mass addition (addition of O_2), regions of separation or re-circulation (large residence time), or afterburner duct geometry (large residence time) would also be expected to affect trace species evolution.

5.6.3 EFFECTS OF THE UNSTEADY INTERACTION OF NON-UNIFORMITIES WITH DOWNSTREAM STATIONS

The high fidelity model for the rotor of the HPT1 was used to investigate the effects of the persistence of non-uniformities on subsequent blade rows. Two cases were investigated, focusing on temperature non-uniformities; the max power case which has smaller scale non-uniformities mainly caused by the wakes from the upstream cooled stator blades, and a non-uniform combustor exit temperature profile case which has a larger scale non-uniformity caused by combustion variations from the discrete fuel injector nozzles as well as the non-uniformity from the upstream cooled stator blades. Qualitatively, local regions of non-uniformity can be seen to persist through the downstream blade row in Figure 5.22. The mass-averaged exit plane species concentrations were time averaged over one cycle for the unsteady cases. The $(SO_3+H_2SO_4)/SO_x$ is 0.0005% higher and the $(HNO_2+HNO_3)/NO_y$ is 0.007% higher at the rotor exit plane for the max power case with the effects of the unsteady non-uniformities relative to the mixed-out case. The low reactivity of the SO_3 chemistry for this condition makes it difficult to make a definitive statement about the unsteady effects of the non-uniformity on SO_3, although, it appears to enhance the oxidation of both trace species. Including the unsteady non-uniformities increases the HONO ratio by 26% relative to the mixed-out case.

The $(SO_3+H_2SO_4)/SO_x$ is 0.09% lower and the $(HNO_2+HNO_3)/NO_y$ is 0.004% higher at the rotor exit plane for the unsteady non-uniform combustor exit temperature max power case. This case shows that the effect of the

unsteady non-uniformities again tends to enhance the oxidation of HONO, however, it significantly diminishes the conversion of SO_3. In other words, mixing out the non-uniformities over predicts the conversion of SO_3 by about 60%. Taken together, these results suggest that the unsteady non-uniformities have a significant impact on trace species evolution and the direction of the influence depends on the operating condition (i.e. temperature), species being considered, and/or size of the non-uniformity. The most plausible explanation for the disparity is that two competing effects could shift the overall effect in either direction depending on the specific conditions. For example, mixing out the species gradients could cause a net shift away from equilibrium leaving more potential for conversion, whereas, mixing out the temperature gradients could shift the equilibrium level so as to reduce the potential for conversion.

5.7 CHAPTER SUMMARY

The purpose of this chapter was to describe the modeling effort to simulate trace species evolution in the post-combustor gas path on an engine in support of the NASA/DERA engine test. The objective of the test is to provide measurements to help characterize aviation emissions and benchmark the models. The model was used to inform the test effort by providing pre-test predictions which were used to help formulate the test plan and to research a few fundamental mechanisms thought to influence trace species chemistry.

Three conditions were investigated: cruise, max power, and non-uniform max power. Details of the grid generation, fluid boundary condition specification, and species initial conditions specification were discussed. A time scale analysis was used to guide the modeling efforts. Two types of high fidelity models were used for the HPT1; a mixed-out case and a wake model case. Several properties of the solution were discussed, including: convergence, overall flow features, grid resolution, deviation angle, and flow-through times. A sample set of detailed flow-chemistry results from the high fidelity model was presented. Low fidelity models were used for HPT1 and HPT1 exit to nozzle exit. Low fidelity models for averaged and high and low temperature profiles in the HPT1 were compared to the high fidelity average. A HPT1 exit to nozzle exit profile was used to obtain a prediction of engine exit gas composition. A sample set of flow-chemistry results from the low fidelity model was presented.

This chapter also highlighted several implications of the modeling results. Specifically, engine operating conditions, multi-dimensional non-uniformities, and the unsteady interaction of non-uniformities with downstream stations were all found to influence trace species evolution. They can all impact temperature, pressure, gas composition, or residence time which are the key parameters influencing intra-engine chemistry. The scale as well as the magnitude of the non-uniformity impacts trace species evolution.

In summary, the following is a list of all relevant points presented in this chapter:

- A first of its kind analysis was completed on the post-combustor gas path of the NASA/DERA engine to support an engine test aimed at characterizing aviation emissions.

- The engine is typical of an older, but currently in-use civil aircraft engine. Three conditions were simulated: cruise, max power, and non-uniform max power.

- Pre-test simulations were used to guide the test plan. They helped to ensure that the operating conditions selected provide useful information about intra-engine chemistry. Also, they helped direct the measurement efforts by indicating important species to monitor and giving estimates for the instrumentation requirements.

- The pre-test simulations suggested testing at the highest combustor exit temperature attainable, as well as, a lower power setting. Also, SO_3 and HOHO were selected as important species to monitor.

- A time scale analysis indicated that most SO_3 production occurs in the HPT1 at max power conditions (approximately 4%). The analysis indicated that there is several orders of magnitude less sulfur conversion after the HPT1, and modeling resources were thus concentrated on the HPT1.

- PRE was used to generate grids of the NGV and rotor. A velocity triangle analysis was used to derive necessary intra-stage fluid parameters for the high fidelity modeling. The species initial condition for each condition were derived using the technique outlined in Section 2.3.2.

- Two types of high fidelity modeling were employed, a mixed-out case and a wake model case. All solutions were deemed converged using the criteria from Section 4.4. Also, the flow features such as deviation angle, streamlines, and inlet/exit conditions were checked to ensure the quality of each solution.

- The boundary layers and trailing edge geometry were not fully resolved for the grids used, however, they are not expected to have a significant impact on the trace chemistry results.

- HPT1 NGV blade-row flow-through time ranged from 0.18 to 0.26 ms and HPT1 rotor blade-row flow-through time ranged from 0.10 to 0.15 ms. The flow-through times computed from the low fidelity modeling were similar.

- A summary of all high fidelity modeling results is contained in Table 5.5, Table 5.6, and Table 5.7. Examples of some detailed results of the high fidelity modeling can be found in Section 5.4.2.3 or Appendix C.

- Low fidelity models were used to model the HPT1 and HPT1 exit to nozzle exit flow paths. A high and low temperature streamline, as well as the averaged profile, through the HPT1 were investigated. The HPT1 low fidelity model can be compared to the HPT1 high fidelity model to investigate the impacts of 2D versus 1D modeling.

- The HPT1 exit to nozzle exit low fidelity model profile was improved using a curve fit to results from the HPT1 high fidelity modeling and the available data.

- A summary of all low fidelity modeling results is contained in Table 5.6 and Table 5.7. Examples of some detailed results of the low fidelity modeling can be found in Section 5.5.2.2 or Appendix C.

- Intra-engine post combustor chemistry is sensitive to engine operating conditions (i.e. combustor exit temperature). SO_3 and HONO concentrations increased with increased engine power level.

    - The increase in $(SO_3+H_2SO_4)/SO_x$ from the mixed-out case was 0.003%, 0.06%, and 0.26% over the HPT1 stage for the cruise, max power, and non-uniform max power cases, respectively. The corresponding increase in $(HNO_2+HNO_3)/NO_y$ was 0.05%, 0.09%, and 0.03%.
    - The increase in $(SO_3+H_2SO_4)/SO_x$ at the nozzle exit was 0.05% for the max power case and 0.84% for the non-uniform max power case using the mixed-out results. The corresponding increase in $(HNO_2+HNO_3)/NO_y$ at the nozzle exit was 1.3% and 2.5%.

- Multi-dimensional non-uniformities have a considerable influence on intra-engine post combustor chemistry, which indicates that some important features can not be captured in low fidelity models.

    - The temperature, pressure, gas composition, and residence time can vary significantly throughout a gas turbine engine. These non-uniformities can arise due to geometry induced blade-to-blade gradients, blade cooling, viscous boundary layers, and non-uniform combustor temperature profiles to name a few.
    - Correlation of the species mass fraction and temperature spatial variations in the high fidelity models suggests the primary influence on chemistry is temperature non-uniformity.
    - There were significant differences in the species evolution in low fidelity and high fidelity models of the HPT1. The low fidelity computation under-predicted the SO_3 and HONO by 0.25% and 11.25% for the max power case and 2.7% and 21.3% for the non-uniform max power case, respectively.
    - A high and low temperature streamline were investigated with low fidelity models. The results from the two streamlines differ significantly from the averaged values, as well as each other indicating the importance of modeling non-uniformities.
    - The scale as well as the magnitude of the non-uniformity captured in the high fidelity model impacts intra-engine chemistry.

- The unsteady interaction non-uniformities with downstream blade-rows has a significant impact on intra-engine post-combustor chemistry. The direction of the influence depends on the operating condition (i.e. temperature), species being considered, and/or size of the non-uniformity.

- Local regions of flow or species non-uniformity persist through the subsequent blade rows.
- With the small scale non-uniformities (wakes from cooled blades) in the max power case, the $(SO_3+H_2SO_4)/SO_x$ is 0.0005% higher and the $(HNO_2+HNO_3)/NO_y$ is 0.007% higher at the rotor exit plane with the effects of the unsteady non-uniformities relative to the mixed-out case. In other words, including the unsteady non-uniformities increases the HONO ratio by 26% relative to the mixed-out case.
- With the large scale non-uniformities (combustor temperature profile and wakes from cooled blades) in the non-uniform max power case, the $(SO_3+H_2SO_4)/SO_x$ is 0.09% lower and the $(HNO_2+HNO_3)/NO_y$ is 0.004% higher at the rotor exit plane with the effects of the unsteady non-uniformities relative to the mixed-out case. In other words, mixing out the non-uniformities over predicts the conversion of SO_3 by about 60%.

6 THESIS SUMMARY AND CONTRIBUTIONS

This chapter will present a summary of the research discussed in this thesis and describe specific contributions of this research.

6.1 THESIS SUMMARY

Trace species of aircraft emissions were shown to have potential impacts on the local and global atmosphere, including changes in radiative forcing and ozone depletion. A summary of prior work was provided, which has concluded that most trace species chemistry occurs early, thus the need exists for better characterization of trace species in the intra-engine environment.

This thesis presented an overview of a modeling methodology developed to simulate the evolution of trace species in the post-combustor flow path of gas turbine engines. The modeling methodology incorporates various levels of detail to accurately and efficiently predict levels of intra-engine trace species by considering key parameters affecting their evolution, specifically temperature, pressure, residence time, and species concentration. The model is intended to improve the overall understanding of the fundamental physical processes that effect trace species evolution and to serve as a predictive design tool which can direct the development of new engine technologies which reduce undesirable aviation emissions.

Modeling tools and improvements made to these tools were discussed. The existing tools consist of the PRE grid generation code, PROCESS grid pre-conditioner code, POST grid post processor code, CNEWT and CALCHEM flow chemistry solvers, and CNEWTVS6 flow visualization code. Improvements in modeling tools were made, which allow for more complicated geometries, multiple inlet and exits, improved execution time for solutions with chemistry, and a specification of a pressure, temperature, and species concentration deficits associated with a wake of an upstream blade or blade row.

Several validation exercises were performed to benchmark these modeling tools. An attempt was made to model a VPFR experiment to demonstrate the accuracy of the modeling tools, however, a limitation to the flow solver prevented this ultimate objective. The validation exercise did nonetheless provide the opportunity to test several code improvements, investigate the limitations of the modeling tools, and analyze flow features of the reactor. A chemical mechanism study which investigated the effects of the chemical mechanism on intra-

engine chemistry and selected a mechanism for the use in the NASA/DERA engine test modeling was detailed. The original chemistry convergence criteria did not represent convergence of trace species well, so they were improved by using the RMS average of individual species residuals for the species of interest to determine solution convergence. Also, periodic boundary conditions were shown not to introduce any significant error into the computation. Selected fluid and species variables at the boundary were within 1.6% of their corresponding value with no boundary present.

Of most significance to the thesis was a modeling effort done to simulate trace species evolution in the post combustor gas path on an engine in support of the NASA/DERA engine test. The objective of the test was to provide measurements to help characterize aviation emissions and benchmark the models. The model was used to inform the test effort by providing pre-test predictions which were used to help formulate the test plan and to research a few fundamental mechanisms thought to influence trace species chemistry.

Three conditions were investigated: cruise, max power, and non-uniform max power. Details of the grid generation, fluid boundary condition specification, and species initial conditions specification were discussed. A time scale analysis was used to guide the modeling efforts. Two types of high fidelity models were used for the HPT1; a mixed-out case and a wake model case. Several properties of the solution were discussed, including: convergence, overall flow features, grid resolution, deviation angle, and flow-through times. A sample set of detailed flow-chemistry results from the high fidelity model was presented. Low fidelity models were used for the HPT1 and HPT1 exit to nozzle exit. Low fidelity models for averaged and high and low temperature streamline profiles in the HPT1 were compared to the high fidelity average. A HPT1 exit to nozzle exit profile was used to obtain a prediction of engine exit gas composition. A sample set of flow-chemistry results from the low fidelity model was presented. Engine operating conditions, multi-dimensional non-uniformities, and the unsteady interaction of non-uniformities with downstream stations were all found to influence trace species evolution. They encompass non-uniformities in temperature, pressure, gas composition, or residence time which are the key parameters influencing intra-engine chemistry. The scale as well as the magnitude of the non-uniformity impacts trace species evolution

6.2 CONTRIBUTIONS

Specifically, relevant contributions and points presented in this thesis include:

- A modeling methodology and modeling tools which can be used to simulate intra-engine chemistry. Many aspects of the model have been validated and there is an ongoing effort to continue its validation.

- The intra-engine trace chemistry modeling methodology involves a time scale analysis, specifying chemistry initial conditions, and a detailed simulation using high or low fidelity models.

- Time scale analyses are useful in formulating a overall modeling strategy by indicating the critical areas of the engine flow path to investigate with higher fidelity modeling.

- A time scale analysis is a simple parametric study which incorporates thermodynamic potential, chemical kinetics, and residence time. The output is a plot of severity parameter for a given species of interest, although, a preliminary estimate of species evolution can be obtained.

- Time scale analyses can also be used to provide insight into the physical phenomena influencing trace species evolution. A few example time scale analyses were used to show:

    - Blade cooling can enhance sulfur conversion.
    - Engine operating condition can influence sulfur conversion, take-off conditions can have higher sulfur conversion than cruise conditions.
    - The OH pathway to SO_3 can be more active than the O pathway.

- A simple method for specifying chemistry initial conditions involves perturbing an equilibrium composition , re-balancing the species based on mass, and doing a stabilizing kinetics calculation.

- High and low fidelity models involve integrating the equations of mass, momentum, and energy over a discrete domain coupled with chemical kinetics to simulate intra-engine chemistry. A high fidelity model can incorporate many multi-dimensional effects (i.e. non-uniformities) while a low fidelity model uses average quantities.

- CNEWT and CALCHEM have been useful modeling tools for studying intra-engine trace species flow-chemistry problems. CNEWT is a code created by Lukachko [1] which was built upon the NEWT turbomachinery CFD code from Dawes [51]. CALCHEM is a simple, 1D version of CNEWT.

- Other supporting codes necessary for turbine chemistry modeling are PRE, PROCESS, POST, and CNEWTVS6.

- The improvements made to existing modeling tools include:

    - A new CAD solid model based grid generator which allows for the simulation of more complicated, arbitrary geometries. The output is a truly unstructured grid. The tools were in a developmental stage and a few difficulties were encountered with the translation step and numerical issues in the volume mesher. The VPFR was successfully meshed with the new grid generator.
    - Addition of multiple inlet/exit capability which allows for simulation of mixing flows. A test case and the Princeton VPFR were used to validate the multiple inlet/exit code modifications.
    - Addition of parallel chemistry subroutines. A test case showed a factor of 3.4 improvement in time on 6 compute nodes. The accuracy of the parallel chemistry modifications was verified.

    - Implemented a wake model boundary condition for temperature and chemical species which allows for the investigation of unsteady effects including flow-chemistry interactions.

- An attempt was made to model a VPFR experiment to benchmark the accuracy of the modeling tools, however, a limitation to the flow solver prevented this ultimate objective. The flow features from the simulation did not correlate well with those expected from experimental and empirical data.

- The VPFR validation exercise proved useful in validating some improvements to the modeling tools.

    - The new fully unstructured grid generator was successfully used to mesh the VPFR geometry
    - The multiple inlet/exit improvement was qualitatively validated.

- The modeling tools are limited to simulations of compressible flow and should be restricted to situations when the bulk of the flow field is above a Mach number of 0.2, an estimate for the compressibility limit of the code.

- The Princeton VPFR may operate with large scale unsteady stall.

- A comparative study was performed on four chemical mechanisms by repeating a 1D and 2D computation from prior work.

    - The species concentration trends were the same for all mechanisms studied.
    - The SO_x conversion ranged from 2.7% to 7.3% for a given case, which implies that the selection of chemical mechanism does impact intra-engine chemistry modeling.
    - Accurately representing key reactions in the mechanism produced reasonable results, thus prior work using Lukachko et al. (1998) was supported.
    - The Mueller et al. (2000)-truncated mechanism was selected for use intra-engine chemistry modeling. It is based on experimental data and is within 1% of the Mueller et al. (2000)-full mechanism.

- The original chemistry convergence criteria did not represent convergence of trace species well. They were improved by using the RMS average of individual species residuals for the species of interest to determine solution convergence.

- A first of its kind analysis was completed on the post-combustor gas path of the NASA/DERA engine to support an engine test aimed at characterizing aviation emissions.

- The engine is typical of an older, but currently in-use civil aircraft engine. Three conditions were simulated: cruise, max power, and non-uniform max power.

- Pre-test simulations were used to guide the test plan. They helped to ensure that the operating conditions selected provide useful information about intra-engine chemistry. Also, they helped direct the measurement efforts by indicating important species to monitor and giving estimates for the instrumentation requirements.

- The pre-test simulations suggested testing at the highest combustor exit temperature attainable, as well as, a lower power setting. Also, SO_3 and HOHO were selected as important species to monitor.

- A time scale analysis indicated that most SO_3 production occurs in the HPT1 at max power conditions (approximately 4%). The analysis indicated that there is several orders of magnitude less sulfur conversion after the HPT1, and modeling resources were thus concentrated on the HPT1.

- PRE was used to generate grids of the NGV and rotor. A velocity triangle analysis was used to derive necessary intra-stage fluid parameters for the high fidelity modeling. The species initial condition for each condition were derived using the technique outlined in Section 2.3.2.

- Two types of high fidelity modeling were employed, a mixed-out case and a wake model case. All solutions were deemed converged using the criteria from Section 4.4. Also, the flow features such as deviation angle, streamlines, and inlet/exit conditions were checked to ensure the quality of each solution.

- The boundary layers and trailing edge geometry were not fully resolved for the grids used, however, they are not expected to have a significant impact on the trace chemistry results.

- HPT1 NGV blade-row flow-through time ranged from 0.18 to 0.26 ms and HPT1 rotor blade-row flow-through time ranged from 0.10 to 0.15 ms. The flow-through times computed from the low fidelity modeling were similar.

- A summary of all high fidelity modeling results is contained in Table 5.5, Table 5.6, and Table 5.7. Examples of some detailed results of the high fidelity modeling can be found in Section 5.4.2.3 or Appendix C.

- Low fidelity models were used to model the HPT1 and HPT1 exit to nozzle exit flow paths. A high and low temperature streamline, as well as the averaged profile, through the HPT1 were investigated. The HPT1 low fidelity model can be compared to the HPT1 high fidelity model to investigate the impacts of 2D versus 1D modeling.

- The HPT1 exit to nozzle exit low fidelity model profile was improved using a curve fit to results from the HPT1 high fidelity modeling and the available data.

- A summary of all low fidelity modeling results is contained in Table 5.6 and Table 5.7. Examples of some detailed results of the low fidelity modeling can be found in Section 5.5.2.2 or Appendix C.

- Intra-engine post combustor chemistry is sensitive to engine operating conditions (i.e. combustor exit temperature). SO_3 and HONO concentrations increased with increased engine power level.
    - The increase in $(SO_3+H_2SO_4)/SO_x$ from the mixed-out case was 0.003%, 0.06%, and 0.26% over the HPT1 stage for the cruise, max power, and non-uniform max power cases, respectively. The corresponding increase in $(HNO_2+HNO_3)/NO_y$ was 0.05%, 0.09%, and 0.03%.
    - The increase in $(SO_3+H_2SO_4)/SO_x$ at the nozzle exit was 0.05% for the max power case and 0.84% for the non-uniform max power case using the mixed-out results. The corresponding increase in $(HNO_2+HNO_3)/NO_y$ at the nozzle exit was 1.3% and 2.5%.
- Multi-dimensional non-uniformities have a considerable influence on intra-engine post combustor chemistry, which indicates that some important features can not be captured in low fidelity models.
    - The temperature, pressure, gas composition, and residence time can vary significantly throughout a gas turbine engine. These non-uniformities can arise due to geometry induced blade-to-blade gradients, blade cooling, viscous boundary layers, and non-uniform combustor temperature profiles to name a few.
    - Correlation of the species mass fraction and temperature spatial variations in the high fidelity models suggests the primary influence on chemistry is temperature non-uniformity.
    - There were significant differences in the species evolution in low fidelity and high fidelity models of the HPT1. The low fidelity computation under-predicted the SO_3 and HONO by 0.25% and 11.25% for the max power case and 2.7% and 21.3% for the non-uniform max power case, respectively.
    - A high and low temperature streamline were investigated with low fidelity models. The results from the two streamlines differ significantly from the averaged values, as well as each other indicating the importance of modeling non-uniformities.
    - The scale as well as the magnitude of the non-uniformity captured in the high fidelity model impacts intra-engine chemistry.
- The unsteady interaction non-uniformities with downstream blade-rows has a significant impact on intra-engine post-combustor chemistry. The direction of the influence depends on the operating condition (i.e. temperature), species being considered, and/or size of the non-uniformity.
    - Local regions of flow or species non-uniformity persist through the subsequent blade rows.
    - With the small scale non-uniformities (wakes from cooled blades) in the max power case, the $(SO_3+H_2SO_4)/SO_x$ is 0.0005% higher and the $(HNO_2+HNO_3)/NO_y$ is 0.007% higher at the rotor exit plane with the effects of the unsteady non-uniformities relative to the mixed-out case. In other words, including the unsteady non-uniformities increases the HONO ratio by 26% relative to the mixed-out case.
    - With the large scale non-uniformities (combustor temperature profile and wakes from cooled blades) in the non-uniform max power case, the $(SO_3+H_2SO_4)/SO_x$ is 0.09% lower and the $(HNO_2+HNO_3)/NO_y$ is 0.004% higher at the rotor exit plane with the effects of the unsteady non-uniformities relative to the mixed-out case. In other words, mixing out the non-uniformities over predicts the conversion of SO_3 by about 60%.

APPENDIX A

PRINCETON VPFR VALIDATION MODELING

The Princeton University's Variable Pressure Flow Reactor (VPFR) is an experimental apparatus specifically designed to measure chemical kinetic data at the high temperatures and pressures typical of energy conversion systems. The VPFR is ideally suited to evaluate the capability of the modeling tools to represent many flow features of interest, mixing, and passively reacting flow. The approach was to model a published flow reactor experiment and compare the simulation data to the experimental data in an attempt to benchmark the accuracy of the modeling tools. The plan was to first simulate the flow-only, then flow with inert species, and finally passively reacting flow. In the end, the objectives of the flow reactor were reduced due to the restriction of the modeling tools to simulation of compressible flows since the flow-only solution did not accurately represent the actual VPFR experimental data.

The objectives of the Princeton VPFR validation modeling effort can be found in Section 4.2.1 and a summary of results can be found in Section 4.2.2.

VPFR MODELING SET UP

Grid Generation

The flow reactor is essentially a cylindrical tube with an inlet section, a baffle, an injector assembly, a diffuser, and a test section. Figure A.1 shows the basic flow reactor geometry and identifies some important features.

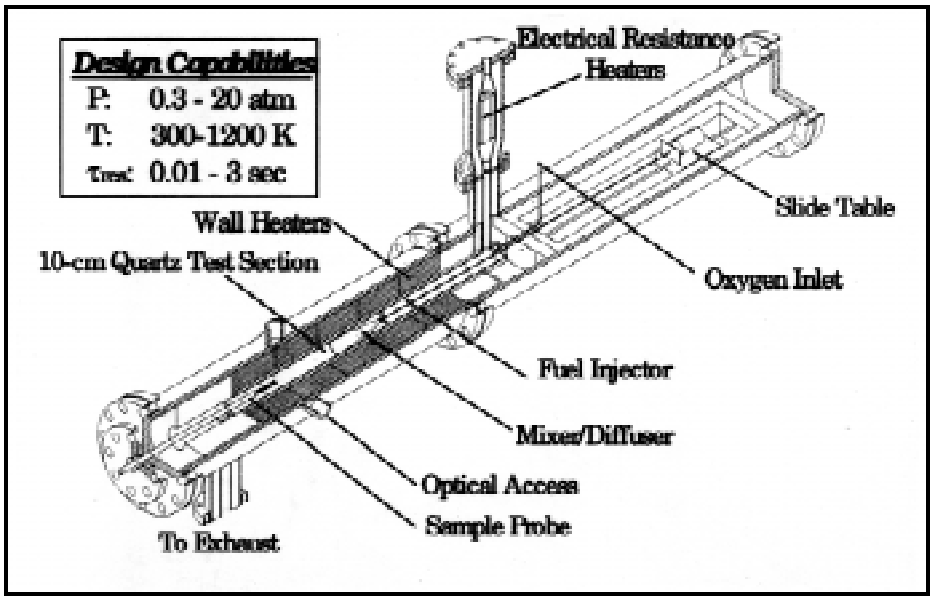

Figure A.1 Cut-away view of Princeton VPFR [26]

The flow reactor geometry is not similar to a turbomachinery blade passage, and although it appears to be quite simple it is fairly complex from a modeling perspective. The flow reactor geometry has a length to radius aspect ratio of 40:1 and a maximum to minimum scale ratio, considering the length of the test section relative to the diameter of the injector holes, of 200:1. The new fully unstructured grid generator was employed to mesh the flow reactor. The strategy was to simplify the grid as much as possible to reduce the computational burden. Only a $1/16^{th}$ sector of the flow reactor was modeled to capitalize on the symmetry about the injector holes. The injectors nozzles were modeled simply as short tubes extending perpendicularly from the main flow, the flow in the length of tube feeding the injector nozzle was deemed unimportant for this study. There was one main inlet, two injector inlets, and one main exit for the domain. A rigorous set of grid controls were used to concentrate the grid points near the baffle and injector assembly to help capture the mixing and along the centerline of the test section where majority of the experimental measurements were made. There was no attempt to resolve viscous layers near the outer walls initially, because although desirable, the large number of cells required to resolve them was prohibitive. Once a reasonable initial solution was obtained selective grid refinement was planned.

A 3D solid model of the flow reactor was generated and converted to a geometry file for the fully unstructured grid generator. The geometry file required an extensive amount of repair to be useable with the new grid generation tools, the details of which will not be discussed here. A file containing the grid controls was created and the grid generator was successfully used to create a surface mesh and volume mesh of the flow reactor geometry. The final flow reactor mesh consisted of about 170,000 cells. Some of the details of the grid

generation procedure are detailed in Section 3.3.1 and [66]. The solid model and final flow reactor grid are shown in Figure A.2.

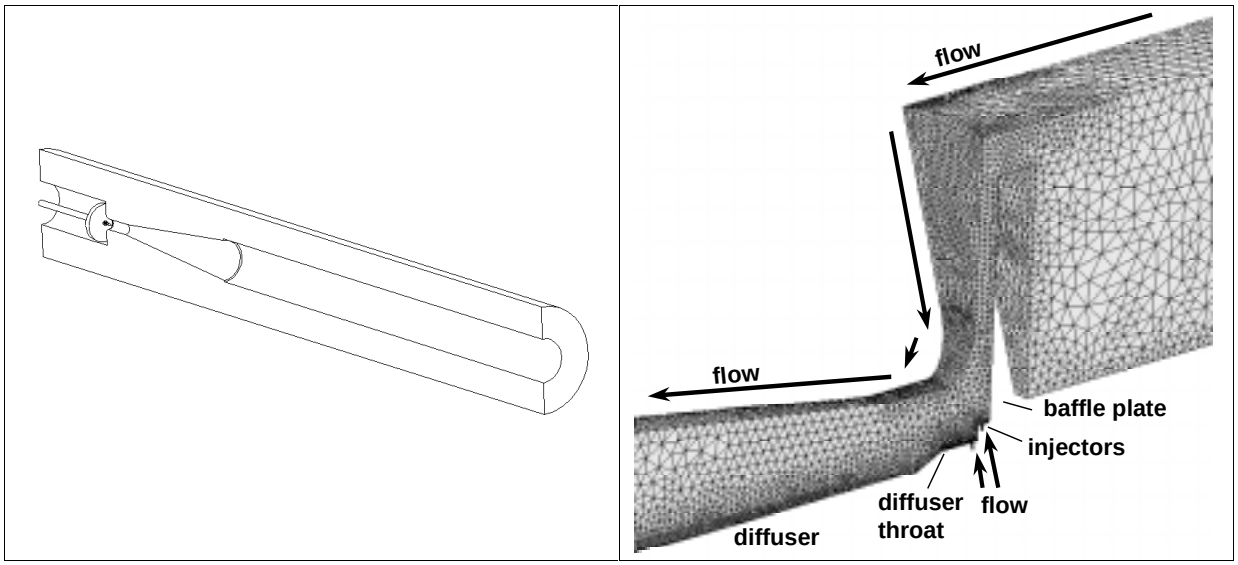

Figure A.2 VPFR solid model and grid detail near baffle and injector assembly

As mentioned in Section 3.3.1, the new grid generator had difficulty meshing geometries with large aspect ratios. This was overcome in the flow reactor grid by scaling the radial dimension in the solid model by a factor of 2 to reduce the aspect ratio then re-scaling the resultant grid back to the original aspect ratio.

To improve convergence time the grid is typically initialized with an approximate guess for the fluid variables (temperature, pressure, density, and velocity). In particular, an axial velocity in the direction of flow was estimated and used for the flow reactor. However, due to the complex nature of the flow path in the reactor it was found to be better to start with zero initial velocity. In the inlet and test section the flow is nearly axial, however, near the injection site it moves radially outward around the baffle and then radially inward into the diffuser. In other words, the baffle is perpendicular to the flow which means that the fluid near the baffle had a poor initial guess. Therefore, the grid with a prescribed axial velocity would cause the code to enter the "panic smoothing" routine which is triggered by an abnormally low pressure since the fluid on the downstream side of the baffle was moving away from the baffle causing a low pressure region. In most cases, the code would eventually crash once the pressure became very small. Initializing the grid with a zero velocity resolved this problem at the expense of having a large transient in the beginning of the solution and long convergence time.

Experimental Conditions And Modeling Assumptions

Several aspects of the experimental operating conditions need to be considered relative to the modeling assumptions inherent in CNEWT when evaluating the applicability of the code to the flow reactor problem. A

few such assumptions considered were heat release, steadiness, and compressibility. In the end, the objectives of the flow reactor simulation were compromised because the code is not suited to model the incompressible flow characteristic of the flow reactor. Therefore the simulations did not accurately represent the flow field and the mixing and reacting flow simulations were not perused. Unfortunately, the flow reactor validation effort was underway before the detailed operating conditions were known. Several solutions were run and many difficulties associated with modeling the operating point using the CNEWT code were encountered (see "Steady Non-Reacting Flow Solutions" and "Unsteady Non-Reacting Flow Solution" latter in this appendix for more details). However, many of the initial objectives were accomplished through the execution of these solutions.

Passively Reacting Flow Assumption

The reactants are diluted with an inert gas to reduce the experimentally observed reaction rates thereby making time evolution species concentration measurements easier. Furthermore, since the initial concentrations of the reactants are small the heat release from chemical reaction is minimized making the experimental conditions easier to control. The dilute nature of the flow reactor experiments is amiable to the assumption of passively reacting flow currently used in CNEWT.

Steady Versus Unsteady Flow Assumption

The crude solutions initially obtained suggested that there was the possibility of flow separation in the diffuser which may cause the flow reactor to operate in an unsteady regime. Although the solver can be run in an unsteady mode, the added complexity of unsteadiness was undesirable for the validation effort. However, an unsteady case was run to further investigate the hypothesis and provide more insight into the ability of the code to model unsteady flows. Details of the unsteady runs are given in "Unsteady Non-Reacting Flow Solution."

Compressible Versus Incompressible Flow Assumption

The flow reactor was designed to encourage a rapid mixing of the fuel, oxygen, and carrier gas to ensure an uniform distribution of species in the bulk gas [26]. It was also designed to have a well characterized uniform velocity field so that the sampling position can accurately be converted to residence time [26]. The VPFR operates in a range of Reynolds numbers from 3,000 to 15,000. In this operating regime the flow is thought to be fully turbulent and free from large scale separation. The fluid velocity in the test section is roughly 1 to 10 m/s for these flow conditions [26], which is necessary to keep the length of the flow reactor reasonable. This equates to a Mach number (M) in the test section on the order of 0.01, which is well into the incompressible regime (roughly $M < 0.3$). The CNEWT code was developed for turbomachinery applications and thus is intended for compressible flows. In brief, the solution routine uses differences in pressure to characterize the flow field, which in the case of incompressible flow are extremely small thereby introducing significant error due to the numerical accuracy of the computer. However, while the code has been known to give accurate

results for Mach numbers as low as 0.2 to 0.3 [69] it is in general not well suited to simulate the experimental conditions typical of the VPFR operation. Modifying the code by changing the flow variables to double precision could extend the compressibility limits of the code by helping to resolve the pressure differences [69], however, it is uncertain how much this modification would help.

In general, the error introduced by exceeding the compressibility limit was large and the fluid solution did not represent experimental or empirical features well. Initially, a similarity approach was attempted to improve the solution quality by using non-dimensional analysis. The Mach number could be increased (to $0.1 < M < 0.3$) while maintaining the incompressibility assumption by altering the numeric artificial viscosity. The Reynolds number is defined as:

$$\mathrm{Re}_D = \frac{\rho \cdot V \cdot D}{\mu} \tag{A.1}$$

Matching the Reynolds number of the simulation to the experiment is an important step to reproducing the flow features. However, it was found to be practically impossible to scale the reactor with complete similarity [59], [60]. Using the available independent variables, it is very difficult to match the non-dimensional numbers necessary to equate the various other parameters required to accomplish modeling with even partial similarity for this situation [59]. The fluid flow features, mixing, and chemical kinetics are all important to accurately represent the flow reactor, some of the difficulties encountered in the similarity approach for this situation will be detailed further in "Steady Non-Reacting Flow Solution.

Other possibilities to overcome the compressibility problem with the flow reactor modeling effort was to use the double precision fluid variables, implement a pre-conditioner to the current solution algorithm [70] or adopt a entirely new solution algorithm. Using the double precision option was not expected to resolve the problem and the other options were not easily implemented and were outside the context of the research agenda.

EXPECTED FLOW REACTOR RESULTS

Diffuser Pressure Recovery Coefficient

The pressure recovery coefficient is one method to measure the performance of a diffuser. It is defined as:

$$c_p = \frac{p_e - p_t}{p_{ot} - p_t} \tag{A.2}$$

There are ample data in the literature relating diffuser design parameters and operating conditions to this pressure recovery coefficient. These pressure recovery maps are useful to diffuser designers. In the context of

the VPFR validation modeling the pressure recovery coefficient is used as a simple method to evaluate the accuracy of the solutions. The Princeton VPFR has a conical diffuser with the following design parameters:

Wall Angle: $2\theta = 10$
Aspect Ratio: $L/D = 15$
Area Ratio: $AR = 13.7$

From the pressure recovery maps in Figure A.3 [39] with the above design parameters, a throat Mach number of 0.2, Reynolds number of 30,000, and throat blockage from 0.03 to 0.12 the expected pressure recovery coefficient ranges from 0.56 to 0.72.

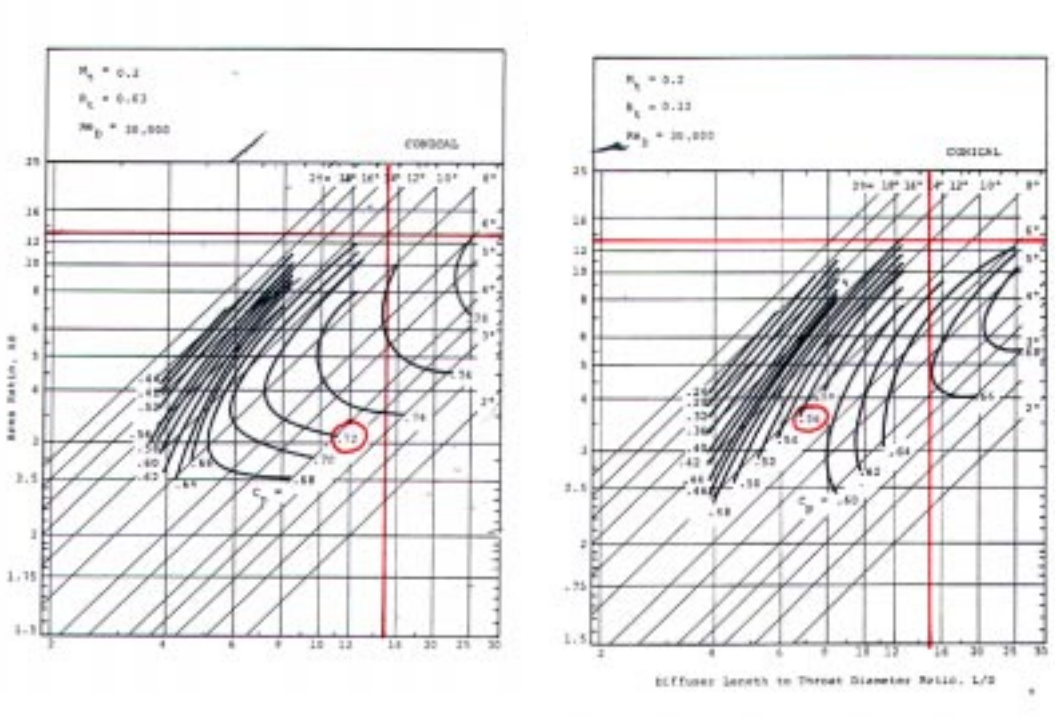

Figure A.3 Pressure recovery maps for constant dA/dx diffusers [41]

Diffuser Operating Regime

The operating regime for diffusers has also been experimentally characterized based on the diffuser design parameters. Although the flow regime map in Figure A.4 is for straight channel diffusers, it can loosely be applied to a conical diffuser by neglecting the wall angle and looking at the aspect ratio and area ratio. From the figure it is expected that the VPFR designed operating point is in the regime of fully developed two dimensional stall (intersection of red lines). In "Steady Non-Reacting Flow Solutions" it will be shown that the simulation predicts the point where the flow first separates is at a location in the diffuser with an L/D ~ 8.5 and AR ~ 2.5 (intersection of blue lines).

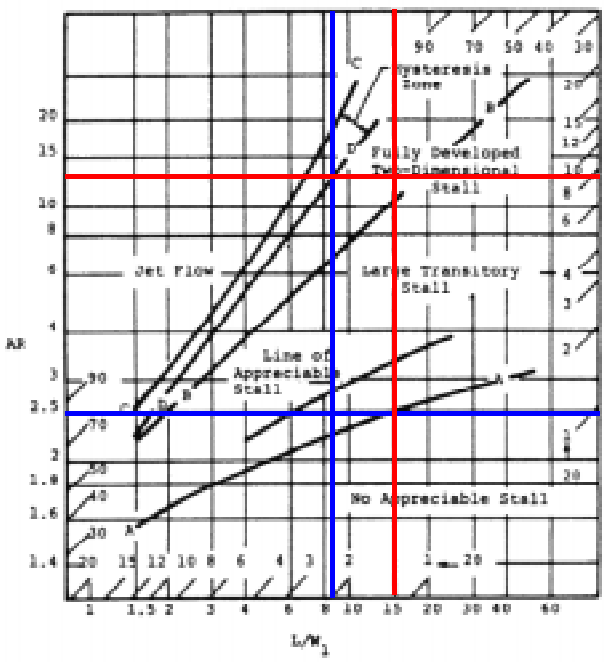

VPFR operating point
intersection of red lines (L/D = 15, AR = 13.7)
Fully developed two dimensional stall

Initial separation form computation
intersection of blue lines (L/D ~ 8.5, AR ~ 2.5)
Near line of appreciable stall

Figure A.4 Diffuser flow regime map [39]

Velocity Profiles

The most informative method to evaluate the quality of the computational solution was to compare the velocity profiles to experimental data and empirical correlations. The VPFR was designed to operate such that the velocity profiles transition quickly to fully-developed turbulent velocity profiles [26]. These profiles have a characteristic "top hat" shape (see Figure A.5 and Figure A.6).

Empirical Correlation

The Power Law is one empirical correlation commonly used to predict velocity profiles in pipe flow:

$$\frac{u}{V_c} = \left(1 - \frac{r}{R}\right)^{\frac{1}{n}} \qquad \text{(A.3)}$$

Where V_c is the centerline velocity, u is the time average x component of velocity, and R is the pipe radius. For the flow reactor case, n, which is a function of Reynolds number, is about 6. Figure A.5 shows the expected velocity profile for the VPFR derived from the Power Law.

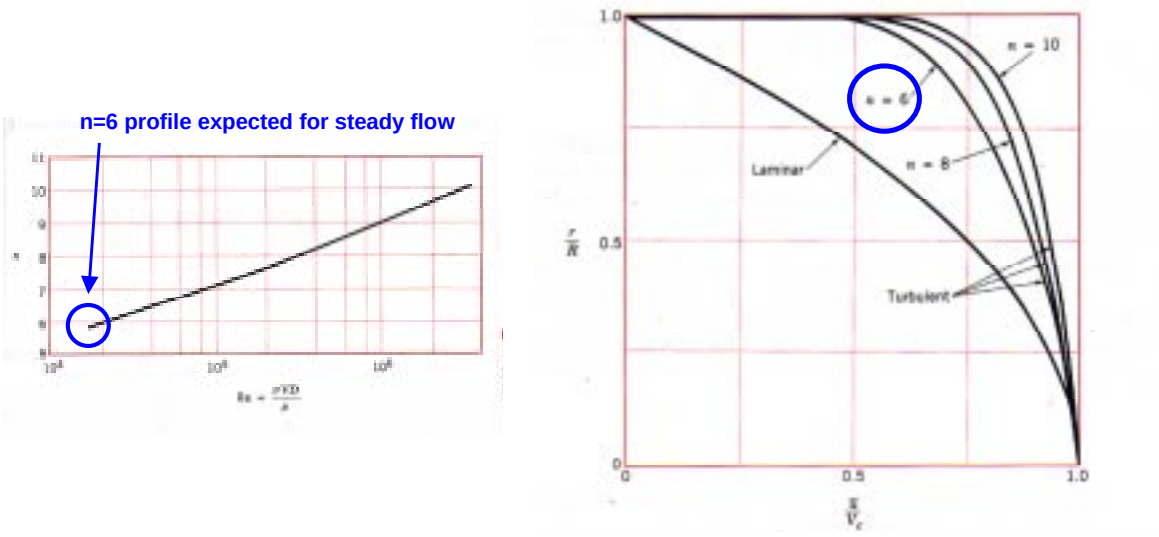

Figure A.5 Typical velocity profiles from Power Law [38]

Experimental Data

For comparison, some velocity profile data specific to the Princeton VPFR is given in Figure A.6.

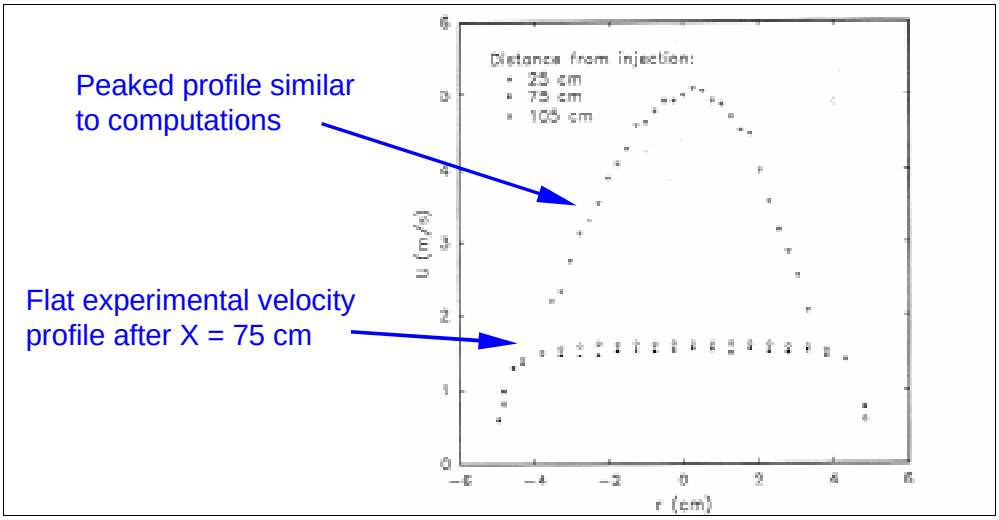

Figure A.6 Experimental velocity profiles for Princeton VPFR [26]

Another point of comparison are other experimentally measured velocity profiles for conical diffusers, such as that given in Figure A.7. The red labels in the figure indicate the profiles for diffusers with design parameters similar to those of the Princeton VPFR. This figure shows that the profiles become more asymmetric and peaked with higher AR and L/D.

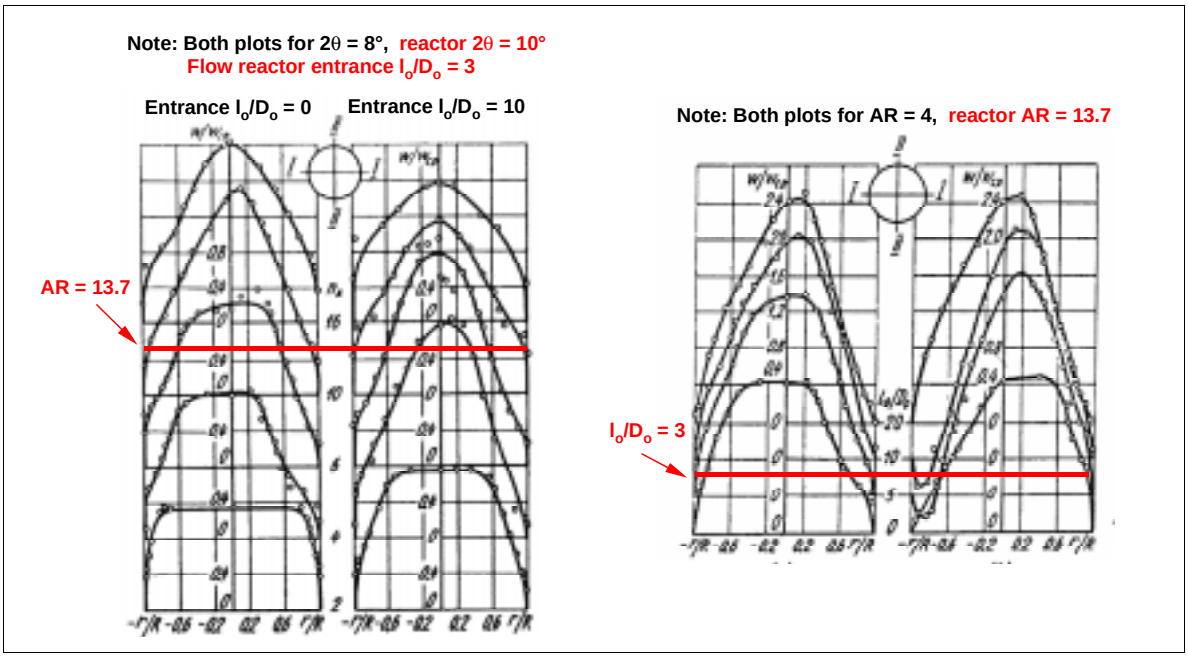

Figure A.7 General velocity profiles in diffusers [40]

STEADY NON-REACTING FLOW SOLUTIONS

Several modeling runs were made in an attempt to simulate the flow reactor and characterize the capability and limitations of the CNEWT code. Two cases were selected for presentation in this thesis to illustrate the major findings of the flow reactor validation effort. The first case, labeled "Run 1," has the lowest Reynolds number in the test section for which a converged solution could be obtained. The second case, labeled "Run 12," has a higher Reynolds number. Further differences between the cases and details of the solutions follow in "Low Reynolds Number Solution (Run 1)" and "High Reynolds Number Solution (Run 12)".

General Results

A summary of results from the two selected cases is given in Table A.1. The Reynolds number for both solutions is several times larger than the experimental conditions of the VPRF.

	Run 1	Run 12
ΔP (kPa)	1	30
V_x max (m/s)	-85	-452
V_x min (m/s)	11	163
M_{max}	0.25	1.7
P_t	93,004	55,181
P_{ot}	96,677	122,028
P_e	96,994	106,128
C_p	1.09	0.76
V_x average exit (m/s)	-4.7	-16
Re_D	31,400	116,700
Mass flow in (kg/s)	2.7e-3	8.4e-3
Mass flow out (kg/s)	2.5e-3	1.1e-2
Mass flow error	7.2%	Injectors ??
Shock position (cm)	none	5

Table A.1 Summary of selected results for VPFR validation runs

Figure A.8 shows a cross-section of the flow reactor with locations of nine axial stations from 15 to 95 cm. In the simulations presented here, the flow travels in the negative X direction (right to left in the figure).

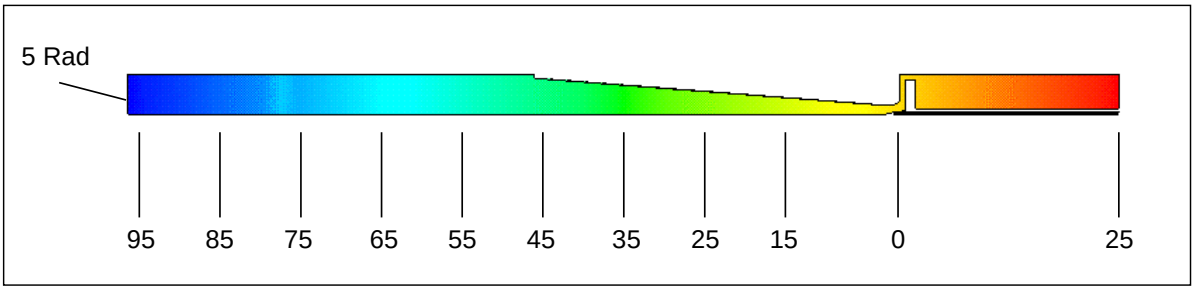

Figure A.8 Axial position X (cm) for flow reactor modeling

Low Reynolds Number Solution (Run 1)

Run 1, a low Re solution, was solved on a preliminary coarse grid which had about 60,000 cells and no injector flow. It was started with a ΔP across the reactor main inlet to exit of 30 kPa which yielded a Mach number of 1.23 at the throat of the diffuser and a Reynolds number of 82,400 in the test section. The convergence history, which was typical of most flow reactor runs, is plotted in Figure A. 9.

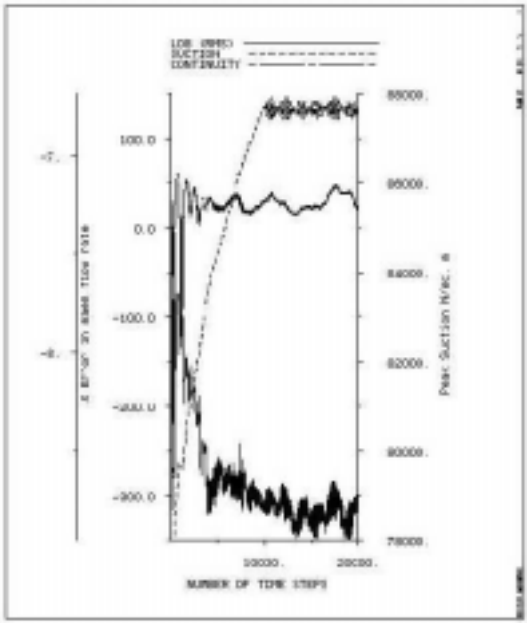

Figure A. 9 Flow reactor Run 1 convergence history

The peak suction (lowest pressure in the domain) converged to about 87 kPa, log(RMS) (the root mean square residual) was below 1.0E-8, and the continuity (mass flow error) oscillated between 10% and 60%. The mass flow error and oscillations were larger for lower Mach number flows, and Run 1 represents the edge of solution stability. The large mass flow error was eventually attributed to the codes inability to compute incompressible flows.

As mentioned previously, a similarity approach was planned as a potential method to overcome the compressibility issue and continue the flow reactor validation efforts. In an attempt to match the experimental conditions for the Princeton VPFR, the inlet pressure was sequentially reduced until the Mach number at the throat of the diffuser was less than 0.3, which occurred at a pressure difference of 1 kPa. Contours of axial velocity are given in Figure A.10. The average Mach number was 0.013 in the test section.

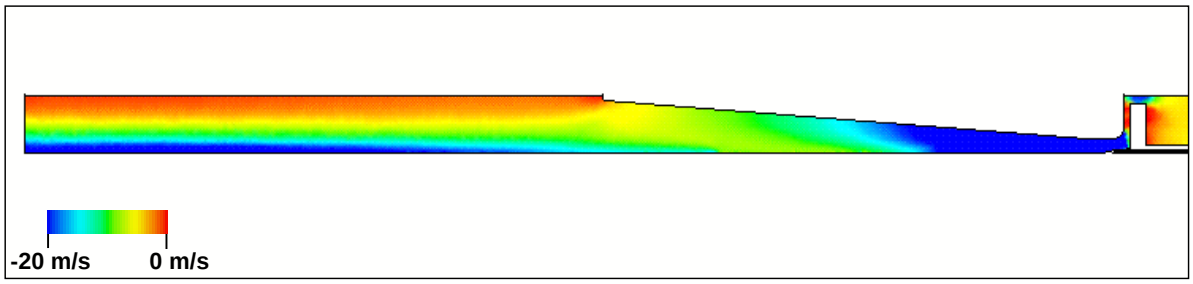

Figure A.10 Axial velocity from -85 to 11 m/s (note: contours clipped for presentation)

The diffuser and test section were divided into nine axial stations (see Figure A.8) and velocity profiles were obtained at each. The profiles are given in Figure A.11 for Run 1.

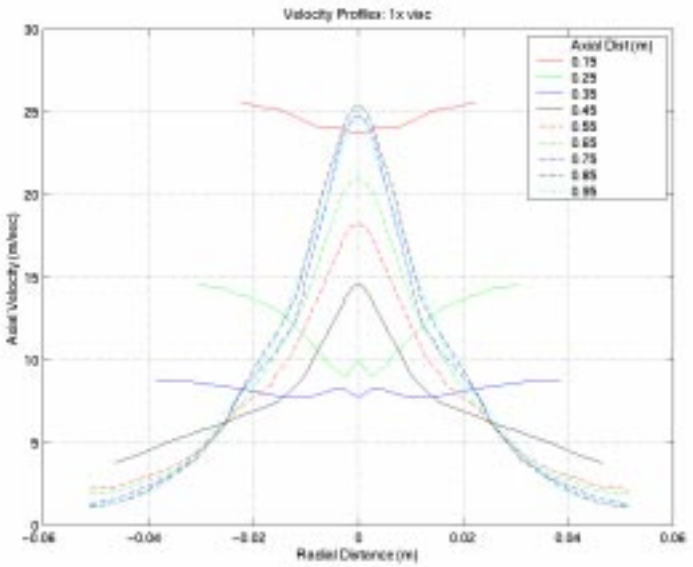

Figure A.11 Velocity profiles at nine axial stations

The velocity profiles for Run 1 are not similar to the "top hat" profiles typical of fully developed turbulent flow. They are peaked and the curvature is opposite to that which is expected. The results from Run 1 exhibit no recirculation, however the infective velocity profiles indicate the possibility of separated jet flow. Furthermore, the pressure coefficient was unrealistically greater than unity. Considering the very low Mach number in the bulk of the test section ($M \sim 0.01 << 0.3$), it was suspected that the majority of the error encountered was associated with using the code beyond the compressibility limit. However, potential discrepancies caused by the mismatched Reynolds number or boundary layer grid resolution were still investigated.

Carrying on with the plan to match the Reynolds number by increasing the artificial viscosity, three additional solutions were started from Run 1. The laminar and turbulent viscosity were increased by a factor of 10, 20, and 50 for these solutions. The results of this study are summarized in the following table:

	Run 1	Run 2	Run 3	Run 4
Description	1x μ	10x μ	20x μ	50x μ
V_x max (m/s)	-85	-73	-72	-61
V_x min (m/s)	11	10	9	7
M_{max}	0.247	0.210	0.206	0.176
P_t	93,004	94,444	95,314	96,401
P_{ot}	96,677	96,898	97,018	97,211
P_e	96,994	96,999	96,999	96,999
C_p	1.09	1.04	0.99	0.74
V_x average exit (m/s)	-4.7	-3.8	-3.2	-2.3
Re_D	31,400	2,590	1,080	300
Mass flow in (kg/s)	2.7E-3	2.3E-3	1.9E-3	1.3E-3
Mass flow out (kg/s)	2.5E-3	1.8E-3	1.5E-3	1.5E-3
Mass flow error	7.2 %	25.1 %	29.8 %	12.7 %

Table A.2 Summary of Reynolds number matching study

The Reynolds number for the 10x case was already beyond the goal of reaching 3,000 to 15,000. The profiles for that case were very similar to Run 1 and are not repeated here. Instead the velocity profiles for Run 4, the extreme case with 50x viscosity, are shown in Figure A.12. As the numerical viscosity increased, the velocity profiles became more inflected and still remained peaked, thus matching the Reynolds number did not move toward a more realistic solution. In fact, increasing the viscosity lowered the flow Mach number pushing the flow more into the incompressible regime which would make the error associated with the incompressibility higher.

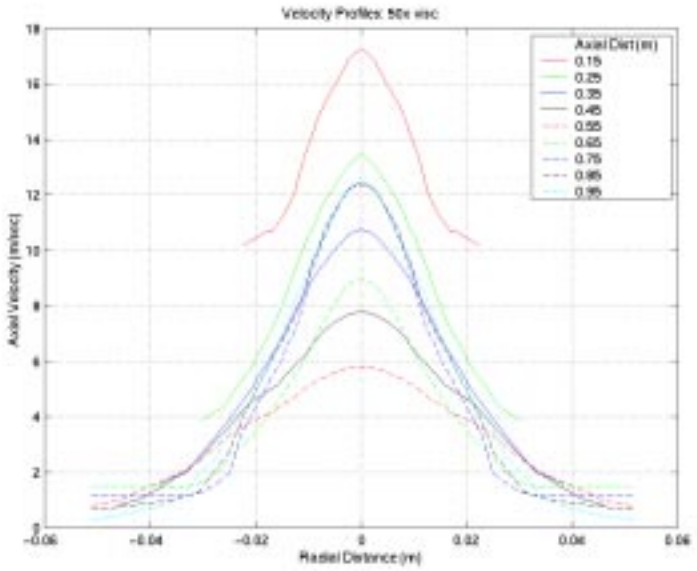

Figure A.12 Velocity profies for 50x viscosity case (Run 4)

Also, it was initially thought that the wall functions or grid boundary layer resolution could be causing the poor solution quality. The grid post processor was used to refine the grid near the outer walls of the diffuser and test section. The first node from the outer wall for the coarse grid was 5.9 mm away. Several levels of refinement were used until a grid with nearly 670,000 cells was created with the first node located 0.6 mm from the outer wall, see Figure A.13. The results of this study are summarized in the following table:

	Run 1	**Run 5**	**Run 6**
Grid	coarse	2 level refinement	3 level refinement
Cells	60,166	205,682	668,681
V_x max (m/s)	-85	-71	-85
V_x min (m/s)	11	10	11
M_{max}	0.247	0.209	0.245
P_t	93,004	94,438	93,338
P_{ot}	96,677	96,984	96,543
P_e	96,994	97,000	97,000
C_p	1.086	1.006	1.143
V_x average exit (m/s)	-4.7	-3.9	-4.3
Re_D	31,400	26,300	28,600
Mass flow in (kg/s)	2.7E-3	2.3E-3	2.5E-3
Mass flow out (kg/s)	2.5E-3	2.2E-3	2.6E-3
Mass flow error	7.2 %	5.9 %	3.4 %

Table A.3 Summary of boundary layer grid refinement study

The velocity profiles from Run 6 with the highest degree of boundary layer refinement are shown in Figure A.14. Again, the velocity profiles did not move in the direction of resembling the experimentally or empirically derived profiles. The velocity profiles were still peaked/inflected and the pressure recovery coefficient was unreasonable, lending further evidence that the main source of error in these flow reactor simulations is due to the compressibility limits of the code.

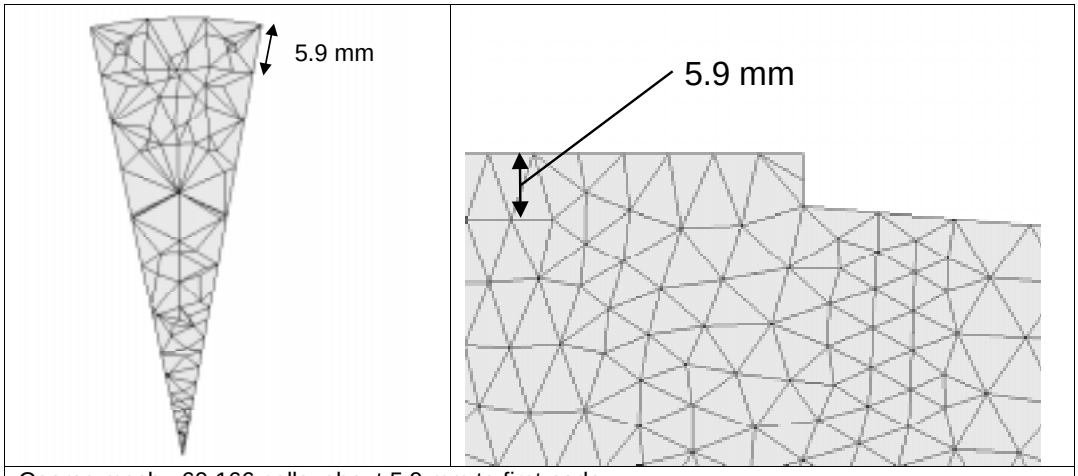

Coarse mesh: 60,166 cells, about 5.9 mm to first node

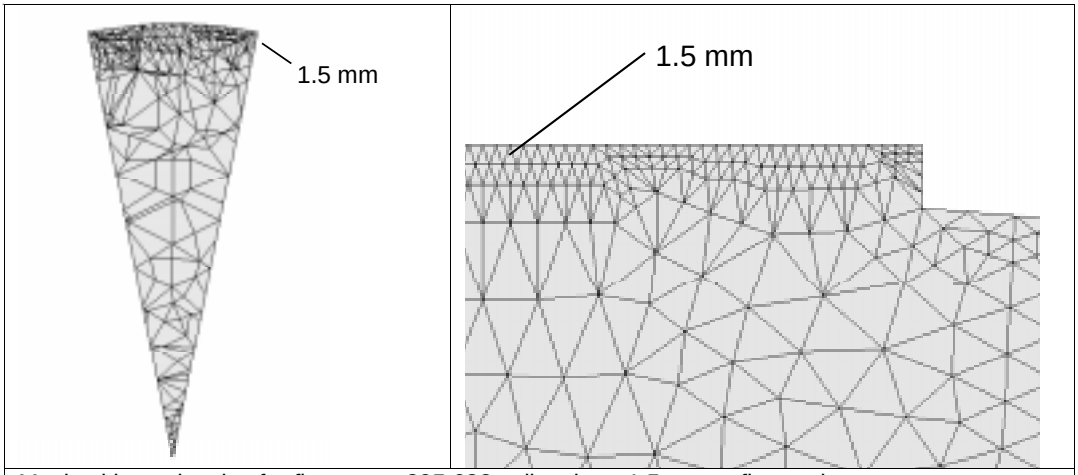

Mesh with two levels of refinement: 205,682 cells, about 1.5 mm to first node

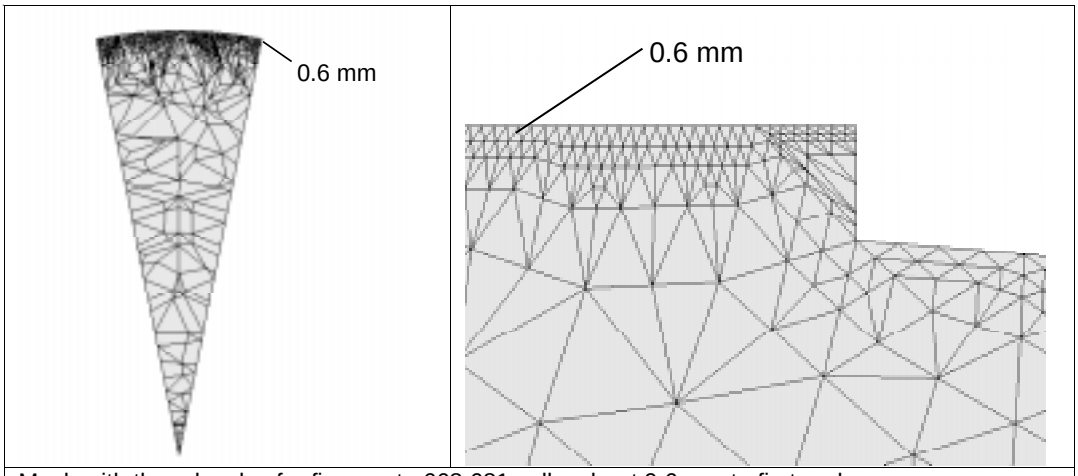

Mesh with three levels of refinement: 668,681 cells, about 0.6 mm to first node

Figure A.13 Mesh refinement in flow reactor test section

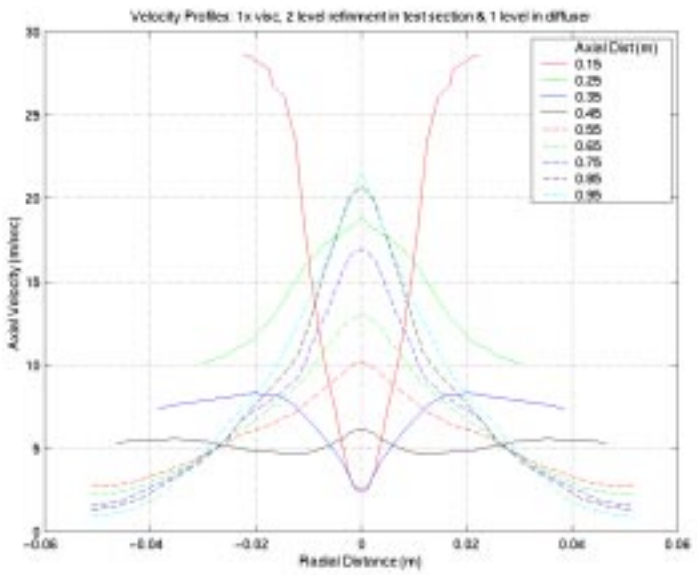

Figure A.14 Velocity profiles for case with refined boundary layer grid (Run 6)

High Reynolds Number Solution (Run 12)

The second case to be discussed in some detail, Run 12, was solved on a finer grid which had about 270,000 cells (see Figure A.2). It was maintained at a higher ΔP of 30 kPa from the main inlet to exit and had flow at the two injector inlets. The injector inlets were set at a pressure ratio of about 9 to 1 relative to the pressure at the main exit. In this case the mass flow error was not computed correctly because the injector mass flow could not be easily accounted. Figure A. 15 shows the axial velocity contours plotted on streamlines for a solution dumped at 10,000 and 35,000 iterations.

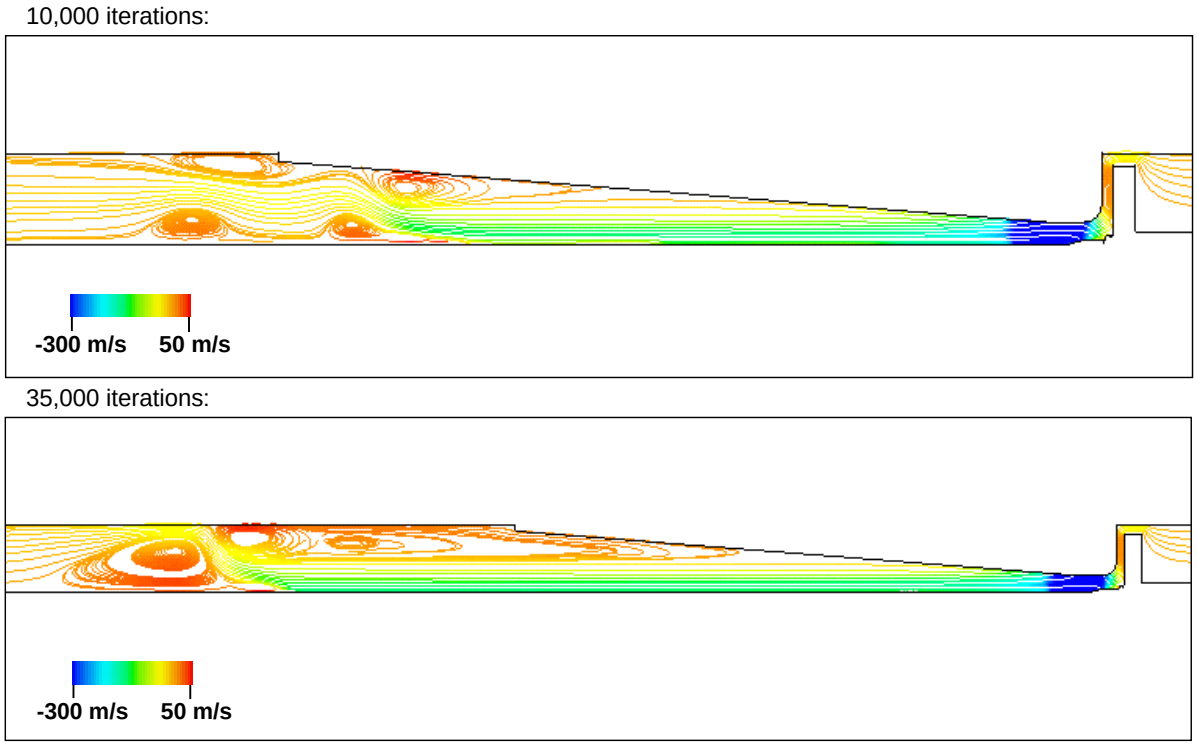

Figure A. 15 Axial velocity from -452 to 163 m/s at 10,000 (top) and 35,000 (bottom) iterations (note: contours clipped for presentation)

The average Mach number in the test section was 0.05. This solution shows that the flow separates in the diffuser and recirculation zones begin to form. The point of separation is roughly 23 cm downstream of the injection site. This point corresponds to a L/D of about 8.5 and a AR of about 2.5 and was anticipated based on the flow regime map presented in Figure A.4.

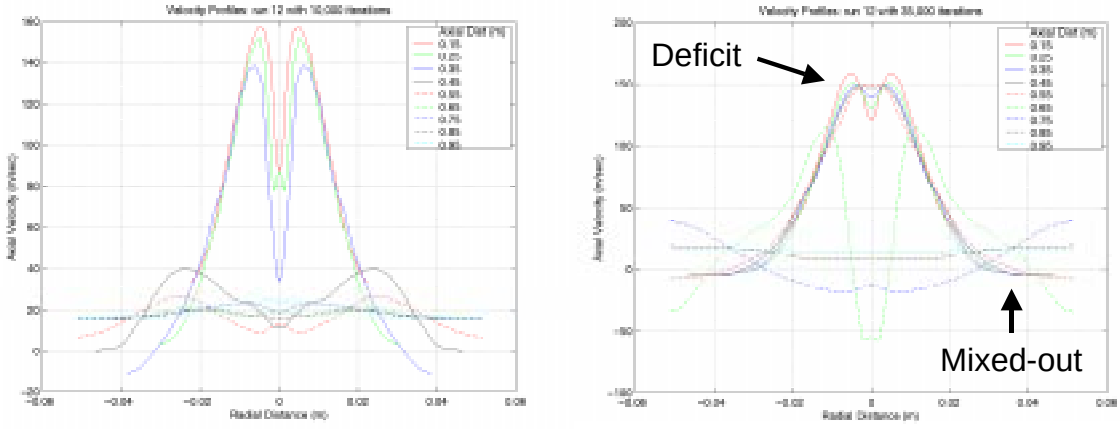

Figure A.16 Axial velocity profiles at nine axial stations for 10,000 and 35,000 iteration solutions

The velocity profiles were peaked prior to the recirculation, followed by flat profiles characteristic of the experimental data. The flat profiles after the stall cells are likely due to the large scale mixing, exchange of low momentum fluid at the wall with high momentum fluid in the core. The profiles show a deficit near the centerline which is typical of flow around a bluff body (the injector). These observations would suggest that the diffuser is operating with large scale unsteady stall similar to the expected operation based on the flow regime map. The flat experimental velocity profiles of the Princeton VPFR could be due to this averaged unsteadiness rather than high turbulence at the diffuser inlet. However, the code was being run in steady mode with a non-uniform time step, therefore, further investigation into the unsteadiness was required (see Unsteady Non-Reacting Flow Solution).

In the higher ΔP solution, Run 12, the diffuser was choked and there was a shock positioned 5 cm into the diffuser. Figure A.17 shows the supersonic region where the flow accelerates from the diffuser throat to the shock where the maximum Mach number was 1.7.

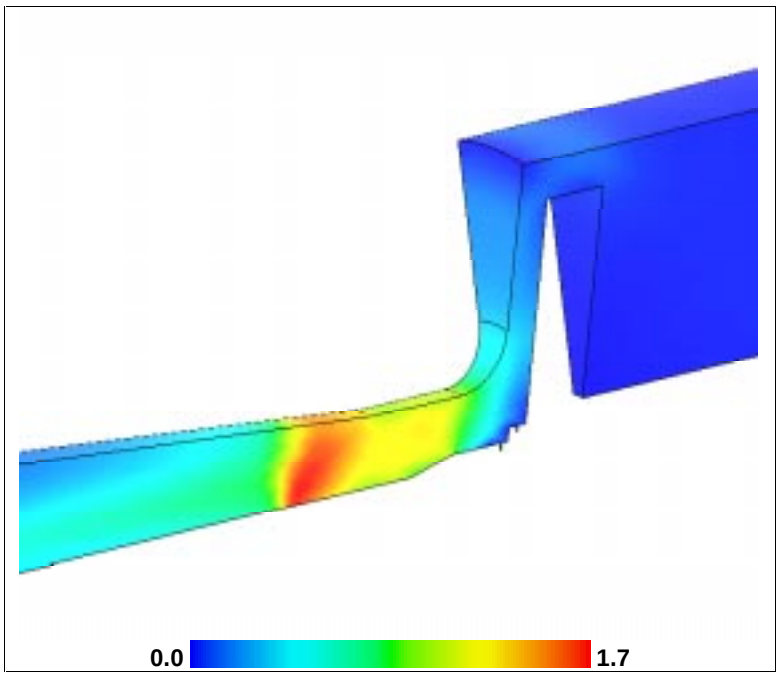

Figure A.17 Mach number contours near diffuser throat showing subsonic to supersonic transition

The pressure recovery coefficient for this case was 0.76. However, this lower value was due to the losses associated with the shock rather than a better representation of the diffuser operation at the desired flow conditions.

The presence of the shock was an additional complication when considering the plan for a similarity solution. It was apparent from Run 1 that having a Mach number of about 0.2 to 0.3 solely in the throat of the diffuser was not sufficient to overcome the compressibility limits of the code. The bulk of the flow field would have to be

above a Mach number of 0.2 to obtain an accurate solution. The flow reactor geometry is such that the throat of the diffuser chokes well before the Mach number in the test section increases to a reasonable level for the flow solver. From a compressible flow table for an ideal gas (with $\gamma = 1.4$), assuming isentropic flow with an area ratio of 13.7, the Mach number at the diffuser exit would only reach about 0.04 when the throat chokes [38]. Or in other words, to use geometric scaling and assuming a desired Mach number in the test section of less than 0.25, the maximum diffuser area ratio would be 2.4. With this Mach number and area ratio, the velocity in the test section is much higher and the length of the test section must be increased to capture the same flow reactor residence time. The test section becomes prohibitively long (about 25 m), making lab measurements difficult and the geometry harder to mesh (worse aspect ratio).

Figure A.18 shows a detail of the Z-direction velocity contours overlaid on streamlines near the injectors. This figure gives qualitative evidence that the multiple inlet/exit code modifications are functioning properly. At this point, no attempt has been made to quantitatively evaluate the ability of the code to simulate the mixing process associated with the injected fluid.

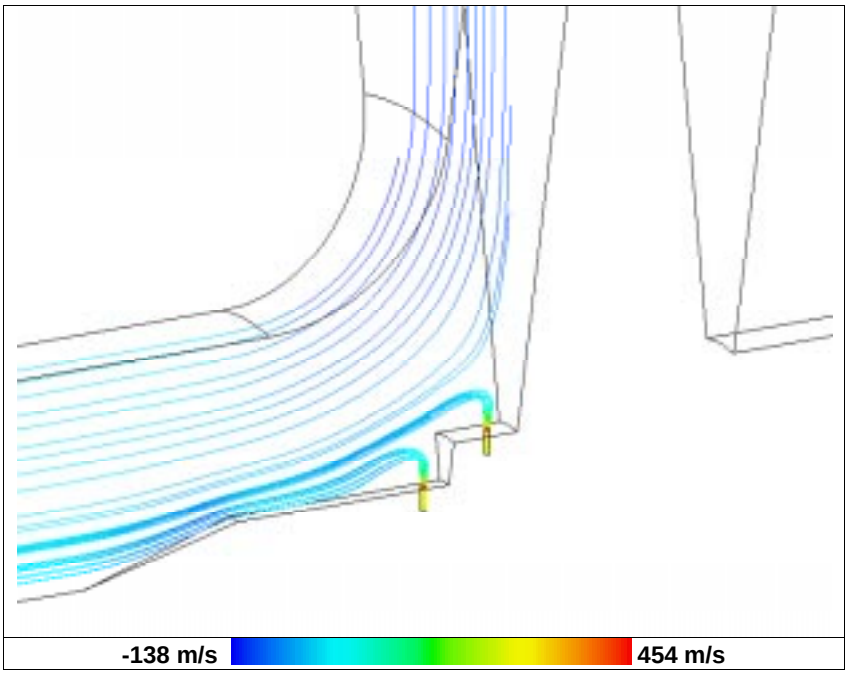

Figure A.18 Z direction velocity component near injectors

Matching the momentum ratio of the injection jet and the opposing primary flow is another complex problem with regard to performing a similarity solution.

UNSTEADY NON-REACTING FLOW SOLUTION

After discovering the flow separation in Run 12 and knowing that the diffuser may operate in a unsteady fashion, it was decided to continue Run 12 using a uniform time step to get a proper unsteady solution. The choice of time step was constrained by the size of the smallest cell. Choosing too large a time step would cause the code to crash because the flow could not be resolved on the scale of that smallest cell. The fine mesh near the injector limited the time step to 0.2455E-06 seconds per iteration.

This unsteady case gives more insight into the operating characteristics of the flow reactor and the capability of the code to simulate unsteady flow. Figure A.19 shows contours of axial velocity overlaid on streamlines at 60,000 iterations, just prior to the time when the large initial transient leaves the domain.

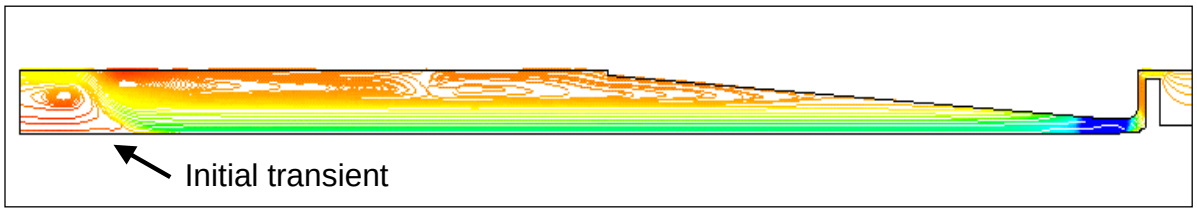

Figure A.19 Axial velocity just before 60,000 iterations

Figure A.20 shows the instantaneous velocity profiles for the unsteady Run 12 at 100,000 iterations. The shape of the velocity profiles are similar to the steady case and are no more representative of the "top hat" profiles expected of fully developed turbulent flow. The deficit near the centerline from the bluff body and inflected profile shape are still evident. In fact, the negative velocity near the outer radius is indicative of reversed flow and signifies separation.

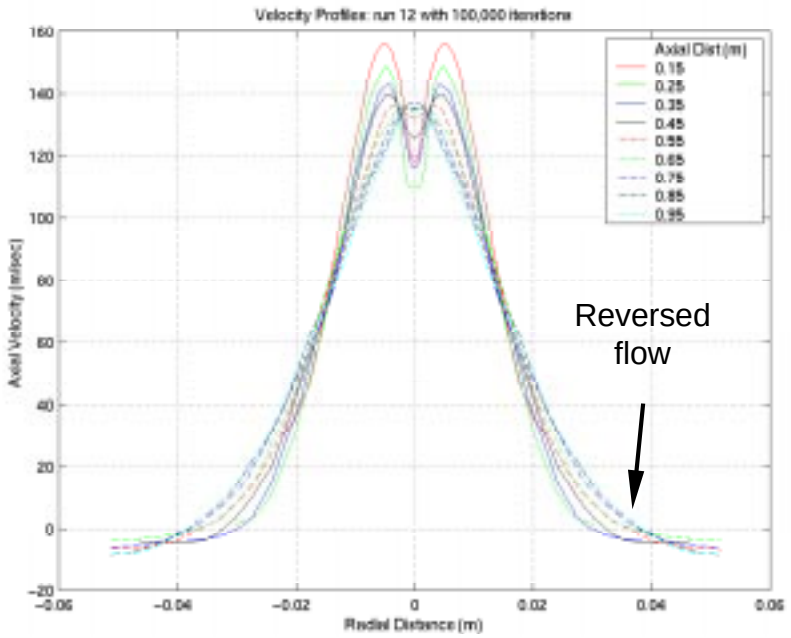

Figure A.20 Velocity profiles for unsteady Run 12 at 100,000 iterations (not time averaged)

The unsteady Run 12 solution was continued for one cycle after the initial transient left the domain. The limitations on time step meant that nearly 30 days of computational time were required to compute that one cycle. A recirculation vortex was observed to form near the outer wall at the point of first separation then travel downstream while growing in size until it is shed into the test section, see Figure A.21. The periodic vortex shedding was estimated to occur at a frequency of 151 Hz by computing the time elapsed between one cycle in the unsteady computation.

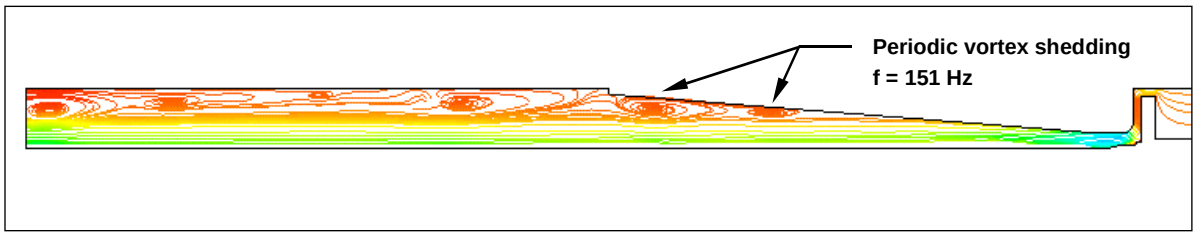

Figure A.21 Streamlines with axial velocity contours for unsteady Run 12 showing one cycle of the periodic vortex shedding

An animation of the initial transient leaving the domain and one cycle of the periodic vortex shedding can be found in Figure F.9 and Figure F.10, respectively (see Appendix F).

Acoustic Resonance Calculation

The VPFR was suspected to have an acoustic resonance at certain operating conditions [26]. It was hypothesized that these acoustic pressure waves could be linked to the vortex shedding frequency. Using the wave equation, the resonant frequency for the modeled portion of the flow reactor was estimated as:

$$f = \frac{c}{\lambda} = \frac{c}{2 \cdot L} = \frac{(340\ \text{m/s})}{2 \cdot (0.964\ \text{m})} = 176\ \text{Hz} \qquad \text{(A.4)}$$

This theoretical frequency compared well to the value of 151 Hz predicted in the unsteady simulation. The simulation did not include the entire length of test section of the real flow reactor. Using L = 1.7 m for the actual length from the baffle to the exit of the flow reactor, the vortex shedding frequency for the experimental facility is predicted to be about 100 Hz.

VPFR MODELING SUMMARY

Limitations of the flow solver hampered the ultimate objective of validating the modeling tools through a successful reacting flow simulation of the Princeton VPFR. Although the validation exercise was not completed, many code improvements were tested, a considerable amount was learned about the limitations of the tools, and some potential issues with the flow reactor design were identified.

Refer to Section 4.2.2 for a more detailed summary of the results from the Princeton VPFR validation modeling exercise.

APPENDIX B

TURBINE CHEMISTRY MECHANISM

Several turbine chemistry chemical mechanisms were evaluated for use in the calculations. The mechanism referred to as the "Mueller et al. (2000)-truncated mechanism" was selected for the NASA/DERA engine simulations. The mechanism has 29 species and 73 reactions. For more information regarding the selection of chemical mechanism see Section 4.3. This appendix lists the output from CHEMKIN which describes the mechanism.

```
CHEMKIN INTERPRETER OUTPUT: CHEMKIN-II Version 3.9  Aug. 1994
                            DOUBLE PRECISION

                          --------------------
                          ELEMENTS     ATOMIC
                          CONSIDERED   WEIGHT
                          --------------------
                           1. C       12.0112
                           2. H       1.00797
                           3. O       15.9994
                           4. S       32.0640
                           5. N       14.0067
                           6. AR      39.9480
                          --------------------
 ------------------------------------------------------------------------------
                            C
                        P   H
                        H   A
                        A   R
 SPECIES                S   G  MOLECULAR  TEMPERATURE  ELEMENT COUNT
 CONSIDERED             E   E  WEIGHT     LOW    HIGH  C  H  O  S  N  AR
 ------------------------------------------------------------------------------
   1. CO                G   0   28.01055   300   5000   1  0  1  0  0  0
   2. CO2               G   0   44.00995   300   5000   1  0  2  0  0  0
   3. O2                G   0   31.99880   300   5000   0  0  2  0  0  0
   4. H2O               G   0   18.01534   300   5000   0  2  1  0  0  0
   5. H                 G   0    1.00797   300   5000   0  1  0  0  0  0
   6. O                 G   0   15.99940   300   5000   0  0  1  0  0  0
   7. OH                G   0   17.00737   300   5000   0  1  1  0  0  0
   8. HO2               G   0   33.00677   200   3500   0  1  2  0  0  0
   9. H2O2              G   0   34.01474   300   5000   0  2  2  0  0  0
  10. NO                G   0   30.00610   300   5000   0  0  1  0  1  0
  11. NO2               G   0   46.00550   300   5000   0  0  2  0  1  0
  12. NO3               G   0   62.00490   300   5000   0  0  3  0  1  0
  13. HNO               G   0   31.01407   300   5000   0  1  1  0  1  0
  14. HONO              G   0   47.01347   300   5000   0  1  2  0  1  0
  15. HNO3              G   0   63.01287   300   5000   0  1  3  0  1  0
  16. SO2               G   0   64.06280   300   5000   0  0  2  1  0  0
  17. SO3               G   0   80.06220   300   5000   0  0  3  1  0  0
  18. HOSO              G   0   65.07077   300   5000   0  1  2  1  0  0
```

```
19. HOSO2           G  0   81.07017   300   5000   0  1  3  1  0  0
20. HSO2            G  0   65.07077   300   5000   0  1  2  1  0  0
21. SO              G  0   48.06340   300   5000   0  0  1  1  0  0
22. HCO             G  0   29.01852   300   5000   1  1  1  0  0  0
23. H2              G  0    2.01594   300   5000   0  2  0  0  0  0
24. N2              G  0   28.01340   300   5000   0  0  0  0  2  0
25. AR              G  0   39.94800   300   5000   0  0  0  0  0  1
26. C(S)            S  0   12.01115   300   5000   1  0  0  0  0  0
27. N               G  0   14.00670   200   6000   0  0  0  0  1  0
28. H2SO4           G  0   98.07754   300   5000   0  2  4  1  0  0
29. S               G  0   32.06400   300   5000   0  0  0  1  0  0
--------------------------------------------------------------------------------


                                                    (k = A T**b exp(-E/RT))
    REACTIONS CONSIDERED                              A        b        E

 1. H2+M=H+H+M                                     4.57E+19   -1.4   104400.0
       H2              Enhanced by    2.500E+00
       H2O             Enhanced by    1.200E+01
       CO              Enhanced by    1.900E+00
       CO2             Enhanced by    3.800E+00
       AR              Enhanced by    7.500E-01
 2. O+H2=H+OH                                      5.08E+04    2.7     6290.0
 3. O+O+M=O2+M                                     6.16E+15   -0.5        0.0
       H2              Enhanced by    2.500E+00
       H2O             Enhanced by    1.200E+01
       CO              Enhanced by    1.900E+00
       CO2             Enhanced by    3.800E+00
       AR              Enhanced by    7.500E-01
 4. H+O2=O+OH                                      1.91E+14    0.0    16440.0
 5. H+O2(+M)=HO2(+M)                               1.48E+12    0.6        0.0
    Low pressure limit:  0.34820E+17 -0.41100E+00 -0.11150E+04
    TROE centering:      0.50000E+00  0.10000E-29  0.10000E+31
       H2              Enhanced by    2.500E+00
       H2O             Enhanced by    1.200E+01
       CO              Enhanced by    1.900E+00
       CO2             Enhanced by    3.800E+00
       AR              Enhanced by    7.500E-01
 6. H+O+M=OH+M                                     4.71E+18   -1.0        0.0
       H2              Enhanced by    2.500E+00
       H2O             Enhanced by    1.200E+01
       CO              Enhanced by    1.900E+00
       CO2             Enhanced by    3.800E+00
       AR              Enhanced by    7.500E-01
 7. OH+H2=H2O+H                                    2.16E+08    1.5     3430.0
 8. H2O+O=OH+OH                                    2.97E+06    2.0    13400.0
 9. H2O2(+M)=OH+OH(+M)                             2.95E+14    0.0    48430.0
    Low pressure limit:  0.12000E+18  0.00000E+00  0.45500E+05
    TROE centering:      0.50000E+00  0.10000E-89  0.10000E+91
       H2              Enhanced by    2.500E+00
       H2O             Enhanced by    1.200E+01
       CO              Enhanced by    1.900E+00
       CO2             Enhanced by    3.800E+00
       AR              Enhanced by    7.500E-01
10. OH+H+M=H2O+M                                   2.21E+22   -2.0        0.0
       H2              Enhanced by    2.500E+00
       H2O             Enhanced by    1.200E+01
       CO              Enhanced by    1.900E+00
       CO2             Enhanced by    3.800E+00
       AR              Enhanced by    7.500E-01
11. HO2+O=O2+OH                                    3.25E+13    0.0        0.0
12. HO2+H=H2+O2                                    1.66E+13    0.0      823.0
13. HO2+H=OH+OH                                    7.08E+13    0.0      295.0
14. HO2+OH=H2O+O2                                  2.89E+13    0.0     -497.0
15. HO2+HO2=H2O2+O2                                4.20E+14    0.0    11982.0
    Declared duplicate reaction...
```

```
16. HO2+HO2=H2O2+O2                                 1.30E+11    0.0    -1629.0
    Declared duplicate reaction...
17. H2O2+O=OH+HO2                                   9.55E+06    2.0     3970.0
18. H2O2+H=H2O+OH                                   2.41E+13    0.0     3970.0
19. H2O2+H=HO2+H2                                   4.82E+13    0.0     7950.0
20. H2O2+OH=H2O+HO2                                 1.00E+12    0.0        0.0
    Declared duplicate reaction...
21. H2O2+OH=H2O+HO2                                 5.80E+14    0.0     9557.0
    Declared duplicate reaction...
22. HNO+H=NO+H2                                     4.40E+11    0.7      650.0
23. NO+O(+M)=NO2(+M)                                1.30E+15   -0.8        0.0
    Low pressure limit:  0.47200E+25 -0.28700E+01  0.15510E+04
    TROE centering:      0.95700E+00  0.10000E-89  0.83320E+04
       AR               Enhanced by    7.500E-01
24. NO+H(+M)=HNO(+M)                                1.52E+15   -0.4        0.0
    Low pressure limit:  0.31000E+20 -0.13200E+01  0.73520E+03
    TROE centering:      0.82000E+00  0.10000E-89  0.10000E+91
       AR               Enhanced by    7.500E-01
25. NO+OH(+M)=HONO(+M)                              1.99E+12   -0.1     -721.0
    Low pressure limit:  0.50800E+24 -0.25100E+01 -0.67600E+02
    TROE centering:      0.62000E+00  0.10000E-89  0.10000E+91
       AR               Enhanced by    7.500E-01
26. NO2+H2=HONO+H                                   7.33E+11    0.0    28810.0
27. NO2+O=O2+NO                                     1.05E+14   -0.5        0.0
28. NO2+O(+M)=NO3(+M)                               1.33E+13    0.0        0.0
    Low pressure limit:  0.14900E+29 -0.40800E+01  0.24670E+04
    TROE centering:      0.82600E+00  0.10000E-89  0.31910E+04
       AR               Enhanced by    7.500E-01
29. NO2+H=NO+OH                                     1.32E+14    0.0      362.0
30. NO2+OH(+M)=HNO3(+M)                             2.41E+13    0.0        0.0
    Low pressure limit:  0.64200E+33 -0.54900E+01  0.23500E+04
    TROE centering:      0.83700E+00  0.10000E-89  0.16570E+04
       AR               Enhanced by    7.500E-01
31. HO2+NO=NO2+OH                                   2.11E+12    0.0     -479.0
32. NO2+NO2=NO3+NO                                  9.64E+09    0.7    20920.0
33. NO2+NO2=2NO+O2                                  1.63E+12    0.0    26120.0
34. HNO+O=OH+NO                                     1.81E+13    0.0        0.0
35. HNO+OH=H2O+NO                                   1.30E+07    1.9     -956.0
36. HNO+NO2=HONO+NO                                 6.02E+11    0.0     1987.0
37. HONO+O=OH+NO2                                   1.20E+13    0.0     5961.0
38. HONO+OH=H2O+NO2                                 1.70E+12    0.0     -520.0
39. HCO+M=H+CO+M                                    1.86E+17   -1.0    17000.0
       H2               Enhanced by    2.500E+00
       H2O              Enhanced by    1.200E+01
       CO               Enhanced by    1.900E+00
       CO2              Enhanced by    3.800E+00
40. HCO+O2=CO+HO2                                   7.58E+12    0.0      410.0
41. HCO+O=CO+OH                                     3.02E+13    0.0        0.0
42. HCO+H=CO+H2                                     7.23E+13    0.0        0.0
43. HCO+OH=CO+H2O                                   3.02E+13    0.0        0.0
44. CO+O(+M)=CO2(+M)                                1.80E+10    0.0     2384.0
    Low pressure limit:  0.13500E+25 -0.27880E+01  0.41910E+04
       H2               Enhanced by    2.500E+00
       H2O              Enhanced by    1.200E+01
       CO               Enhanced by    1.900E+00
       CO2              Enhanced by    3.800E+00
45. CO+O2=CO2+O                                     2.53E+12    0.0    47700.0
46. CO+OH=CO2+H                                     1.40E+05    1.9    -1347.0
47. CO+HO2=CO2+OH                                   3.01E+13    0.0    23000.0
48. NO+HCO=HNO+CO                                   7.23E+12    0.0        0.0
49. NO2+HCO=CO+HONO                                 1.26E+23   -3.3     2354.0
50. NO2+HCO=H+CO2+NO                                8.43E+15   -0.8     1927.0
51. NO2+CO=CO2+NO                                   9.03E+13    0.0    33780.0
52. SO3+O=SO2+O2                                    4.40E+11    0.0     6100.0
53. SO3+SO=SO2+SO2                                  1.00E+12    0.0     4000.0
54. SO2+O(+M)=SO3(+M)                               9.20E+10    0.0     2384.0
    Low pressure limit:  0.40000E+29 -0.40000E+01  0.52500E+04
       N2               Enhanced by    1.300E+00
```

```
       H2O              Enhanced by    1.000E+01
 55. SO2+OH(+M)=HOSO2(+M)                          1.21E+12    0.0        0.0
     Low pressure limit:  0.18700E+32 -0.46100E+01  0.20500E+04
     TROE centering:      0.35000E+00  0.10000E-29  0.10000E+31
       H2O              Enhanced by    1.000E+01
 56. SO2+OH=SO3+H                                  4.90E+01    2.7    23800.0
 57. SO+O(+M)=SO2(+M)                              3.20E+13    0.0        0.0
     Low pressure limit:  0.29000E+25 -0.29000E+01  0.00000E+00
     TROE centering:      0.55000E+00  0.10000E-29  0.10000E+31
       N2               Enhanced by    1.500E+00
       H2O              Enhanced by    1.000E+01
 58. SO+OH=SO2+H                                   5.20E+13    0.0        0.0
 59. SO+OH+M=HOSO+M                                8.00E+21   -2.2      830.0
 60. SO+O2=SO2+O                                   6.20E+03    2.4     3050.0
 61. HOSO+M=SO2+H+M                                5.90E+34   -5.7    50900.0
 62. HOSO+OH=SO2+H2O                               1.00E+12    0.0        0.0
 63. HOSO+O2=SO2+HO2                               1.00E+12    0.0     1000.0
 64. HSO2+M=SO2+H+M                                1.20E+28   -4.1    18900.0
 65. HSO2+M=HOSO+M                                 1.10E+21   -2.0    29900.0
 66. HOSO2=HOSO+O                                  5.40E+18   -2.3   106300.0
 67. HOSO2+M=SO3+H+M                               3.20E+16   -0.8    53700.0
 68. HOSO2+H=SO2+H2O                               1.00E+12    0.0        0.0
 69. HOSO2+O=SO3+OH                                5.00E+12    0.0        0.0
 70. HOSO2+OH=SO3+H2O                              1.00E+12    0.0        0.0
 71. HOSO2+O2=SO3+HO2                              7.80E+11    0.0      656.0
 72. SO2+NO2=SO3+NO                                6.30E+12    0.0    27000.0
 73. SO3+H2O=H2SO4                                 7.23E+08    0.0        0.0

 NOTE:  A units mole-cm-sec-K, E units cal/mole


NO ERRORS FOUND ON INPUT...CHEMKIN LINKING FILE WRITTEN.

WORKING SPACE REQUIREMENTS ARE
   INTEGER:     1569
   REAL:        1675
   CHARACTER:     35
```

APPENDIX C

HPT1 VELOCITY TRIANGLE ANALYSIS

Due to the limited data available for the NASA/DERA engine, a velocity triangle analysis was used to obtain the intra-stage data needed for the HPT1 high fidelity modeling. This type of analysis is common in turbomachinery textbooks, and further details can be found in [7], [36], or [37]. This appendix presents the specific procedure along with some example results for the velocity triangle analysis referred to in Section 0:

The axial stations of interest were labeled as follows:

Station A: Combustor exit (8) (numbers refer to DERA data designation)
Station B: HPT1 rotor inlet (9)
Station C: HPT1 rotor exit
Station "Overall HPT exit": HPT2 rotor exit (11)

The subscripts a, b, and c are used to designate these stations in this analysis, as well as, Figure C. and Table C.. The annulus area was calculated at each station. The properties of air R=288.7 J/kgK and γ=1.34 were assumed to be constant over the temperature range of interest, 800-1,300K.

The fluid density was calculated using the ideal gas law and the relationship between total and static pressure/temperature by using an initial guess for the Mach number as follows:

$$P_a = \frac{P_{Ta}}{\left(1+\frac{\gamma-1}{2}M_a^{\,2}\right)^{\frac{\gamma}{\gamma-1}}} \tag{C.1}$$

$$T_a = \frac{T_{Ta}}{\left(1+\frac{\gamma-1}{2}M_a^{\,2}\right)} \tag{C.2}$$

$$\rho_a = \frac{P_a}{RT_a} \tag{C.3}$$

Then, the axial velocity and Mach number were calculated as follows:

$$u_{xa} = \frac{\dot{m}_a}{\rho_a A_a} \tag{C.4}$$

$$M_a = \frac{u_{xa}}{\sqrt{\gamma \cdot R \cdot T_a}} \tag{C.5}$$

An iteration was performed using equations (C.1) to (C.5) until the Mach number was consistent. The combustor exit flow was assumed to enter the NGV with zero incidence angle, thus:

$$V_a = u_{xa} \tag{C.6}$$

A similar iterative procedure was used to compute u_{xb}. However, since the total temperature and pressure were not explicitly given within the stages, negligible total pressure loss was assumed to occur through the HPT1 NGV and thus, the "Overall HPT exit" values (which were similar to the combustor exit) were used for this intra-stage station. Also, the Mach number was computed using the absolute velocity, V_b. The flow was initially assumed to have zero deviation, thus the blade metal angle at the trailing edge, β_b, and u_{xb} were used to compute V_b as follows:

$$V_b = \frac{u_{xb}}{\cos(\beta_b)} \tag{C.7}$$

$$M_b = \frac{V_b}{\sqrt{\gamma \cdot R \cdot T_b}} \tag{C.8}$$

Vector addition was used to subtract the tangential velocity of the rotor, ωr, from V_b to get the velocity, V_b', and inlet angle, β_b' , relative to the rotor reference frame as follows:

$$v_b = \sqrt{V_b^{\,2} - u_{xb}^2} \tag{C.9}$$

$$v_b' = v_b - \omega \cdot r \tag{C.10}$$

$$V_b' = \sqrt{u_{xb}^2 + v_b'^2} \tag{C.11}$$

$$\beta_b' = \tan^{-1}\left(\frac{v_b'}{u_{xb}}\right) \tag{C.12}$$

Again, since the HPT1 rotor exit condition was not given explicitly the turbine was assumed to have a 50% reaction, thus the work per stage was assumed to be equal. A power balance using Station A and the "Overall HPT exit" values was done assuming a polytropic efficiency of 0.90 to obtain the total temperature and pressure at station C, T_{Tc} and P_{Tc} respectively. An iteration was performed to obtain T_{Tc} and the turbine temperature and pressure ratios were computed to obtain P_{Tc} as follows:

$$\dot{m}_1 c_p \left(T_{Tc} - T_{Ta}\right) = \dot{m}_2 c_p \left(T_{T2} - T_{Tc}\right) \quad \Rightarrow \quad T_{Tc} \tag{C.13}$$

$$\tau_{t1} = \frac{T_{Tc}}{T_{Ta}} \tag{C.14}$$

$$\pi_{t1} = \frac{P_{Tc}}{P_{Ta}} = \tau_{t1}^{\left(\frac{\gamma-1}{\gamma \cdot \eta_{poly}}\right)} \tag{C.15}$$

$$P_{Tc} = \pi_{T1} \cdot P_{Ta} \tag{C.16}$$

Finally, an iterative proceedure over equations (C.5) to (C.12) was used to compute the velocity vectors at the HPT1 rotor exit. Again a zero deviation was assumed (β_c' = rotor blade metal angle at the triling edge) and the Mach number was computed using the absolute velocity, V_c', as follows:

$$V_c' = \frac{u_{xc}}{\cos(\beta_c')} \tag{C.17}$$

$$v_c' = \sqrt{V_c'^2 - u_{xc}^2} \tag{C.18}$$

$$v_c = v_c' - \omega \cdot r \tag{C.19}$$

$$V_c = \sqrt{u_{xc}^2 + v_c^2} \tag{C.20}$$

$$\beta_c = \tan^{-1}\left(\frac{v_c}{u_{xc}}\right) \tag{C.21}$$

$$M_c = \frac{u_{xc}}{\sqrt{\gamma \cdot R \cdot T_c}} \tag{C.22}$$

The results of this analysis were reasonable since the fluid flow angle at the exit of the stage is nearly axial as is typical in the design of a turbine stage, β_c = 3.7°. However, the incidence angle to the rotor, although reasonable, was fairly large β_b' = 37.1°. Therefore, a deviation of the flow from the blade metal angles was

assumed. The deviation was initially set at 2° for both blades. This lowered the rotor incidence angle to –2.2° and changed the rotor exit angle to 28.7° As an example, the resultant velocity triangles and underlying data from this analysis for the mamimum power condition with 2° assumed deviation are given in Figure C. and Table C..

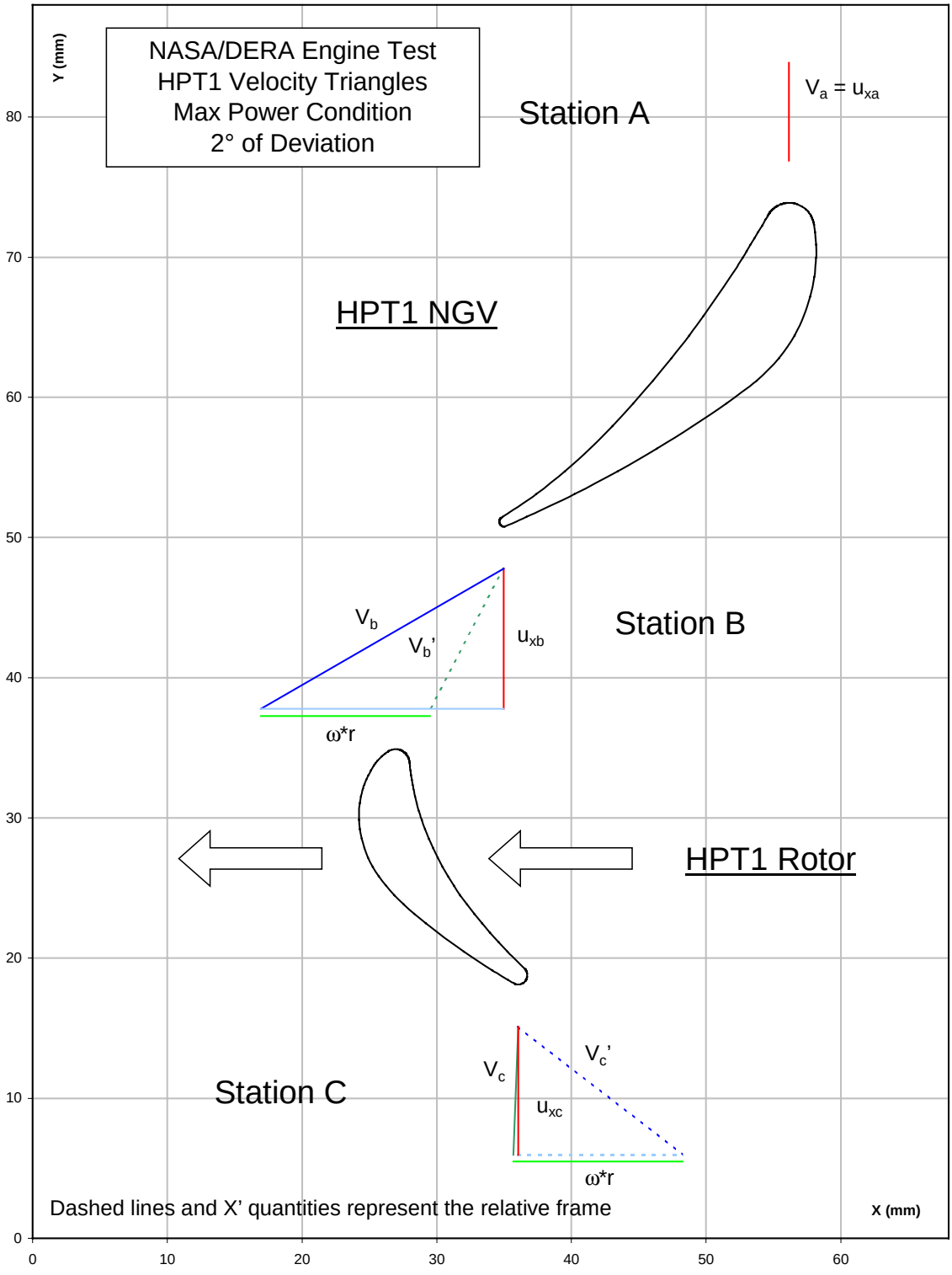

Figure C.1 Velocity triangle diagram for maximum power condition with 2° deviation

NASA/DERA Engine Test, HPT1 Velocity Triangles, Max Power Condition, Assumed 2 degrees of Deviation

Station A Combustor exit condition (8)		Station B HT1 rotor inlet (10)			Station C HPT1 rotor exit		Station overall HPT exit HPT2 rotor exit (11)	
R =	270.38 mm	Nblades =	100		t =	0 mm		
Nblades =	60	t =	0 mm	0	Do =	23.52136781 in		
t =	0 mm	Do =	22.7 in	22.97781	Di =	19.25826812 in		
Do =	22.86 in	Di =	19.74 in	19.686	delta D =	4.263099693 in		
Di =	19.1 in	delta D =	2.96 in	3.291812	A =	143.236089 in^2		
delta D =	3.76 in	A =	98.66360224 in^2	110.3023		0.092410195 m^2		
A =	123.9119541 in^2		0.06365381 m^2	0.071163				
	0.079943036 m^2	A ave =	0.06740822 m^2					
Ma =	0.192940589	Mb =	0.592963766		Mc =	0.270039769		
γ =	1.34						Stage 2	
Pta =	1,634,150.0 Pa	Ptb =	1,634,150.0 Pa		Ptc =	1,034,667.2 Pa	Pt2 =	498,714.0 Pa
Tta =	1,365.2 K	Ttb =	1,325.2 K		Ttc =	1,200.2 K	Tt2 =	1,045.8 K
Pa =	1,594,021.3 Pa	Pb =	1,299,940.8 Pa		Pc =	985,627.1 Pa	m dot =	48.6348 kg/s
Ta =	1,356.6 K	Tb =	1,250.4 K		Tc =	1,185.5 K	cp =	1137.741 J/kg*K
R =	288.7 J/kg*K						Δt2 =	154.3 K
ρ =	4.070 kg/m^3	ρ =	3.601 kg/m^3		ρ =	2.880 kg/m^3	W2 =	8540228 W
m dot =	45.479 kg/s	m dot =	48.6348 kg/s		m dot =	48.6348 kg/s		
uxa =	139.77 m/s	uxb =	200.35 m/s		uxc =	182.74 m/s	Stage 1	
							m dot =	45.479 kg/s
							cp =	1137.741 J/kg*K
							Δt1 =	165.0 K
							W1 =	8540228 W
βa =	0 deg	Exit Slope Ave =	-1.957070591		Exit Slope Ave =	1.437640026		
		βb =	62.93443178 deg		βc' =	55.17812707 deg	delta(W) =	0 W
		c =	31.44 mm		c =	19.18 mm		
		σ =	1.110399751		σ =	1.129000595		
		δt =	2 deg		δt =	2 deg		
Tt (HPCe) =	698.858 K	βb - δt =	60.93443178 deg		βb - δt =	53.17812707 deg		
T (HPCe) =	694.463 K	ω =	928.215 rad/s					
T met ngv =	998.997 K							
T met rot =	956.207 K	Vb =	412.40 m/s		Vc' =	304.90 m/s	η poly =	0.9
		vb =	360.46 m/s		vc' =	244.08 m/s	τ t1 =	0.879105
Ma =	0.192941463	Mb =	0.592963765				π t1 =	0.633153
delta Ma =	-0.00000087	delta Mb =	0.00000000					
Va =	139.77 m/s	ω*r =	250.97 m/s					
		vb' =	109.49 m/s		vc =	-6.89 m/s		
		Vb' =	228.31 m/s		Vc =	182.87 m/s		
					Mc =	0.270039781		
					delta Mc =	-0.00000001		
		βb' =	28.66 deg		βc =	-2.16 deg		

Inputs
Iterate
Output
Solution converged:
YES

Table C.1 Data for the maximum power 2° deviation velocity triangle diagram of Figure C.

In an attempt to obtain a more accuate estimate of the deviation an empirical correlation, Carter's Rule, was employed as follows [36]:

$$\phi = \beta_1 + \beta_2 \tag{C.23}$$

$$\sigma = \frac{c}{s} \tag{C.24}$$

$$\delta_t = \frac{\phi}{8 \cdot \sqrt{\sigma}} \tag{C.25}$$

This resulted in a deviation of 7.5° and 7.3° for the NGV and rotor, respectively. Using these deviation values, the rotor incidence angle was 7.0° and the rotor exit angle was -14.8°.

Another possibility to increase the accuracy of the velocity trianlgle analysis was investigated. A total pressure loss coefficient ("profile loss") at Station B was attempted rather than assuming a negligible total pressure loss across the NGV. However, using empirical cascade correlations for a stator which are a function of the solidity

($\sigma = c_{axial}/s$) the pressure loss coefficient was found to be w = 0.03 and the effect on the result for P_{Tb} and β_b was found to be less than 2% [36].

Overall, the velocity triangle analysis provided reasonable fluid property data for the high fidelity modeling. Including the profile loss had a negligible effect on the results and thus it was ignored to keep the analysis simple. Also, it is difficult to justify a particular deviation angle. The NASA/DERA engine test simultaions used a deviation angle of 2° since it was thought to be a conservative approach and gave a nearly axial exit flow angle. As another point of reference, the HPT2 NGV has a chord angle of 41° versus 45° for the HPT1 NGV. This would imply that the blades are both roughly designed to have a zero inlet swirl, supporting the notion that the exit flow angle be nearly axial.

APPENDIX D

DETAILED RESULTS FROM NASA/DERA ENGINE SIMULATION OF MAX POWER CASE

This appendix contains a complete set of calculation results for the max power condition. From the high fidelity modeling effort the following items are given in order for the mixed-out case, first for the NGV and then for the rotor:

- Fluid and chemistry convergence history
- Range and mass averaged quantities of fluid and chemistry variables at exit plane
- Total temperature and total pressure contours
- Mass fraction contours of trace species

Then, for the high fidelity rotor wake model case:

- Time series of SO_3 mass fraction for one blade passing cycle (see Appendix D for an animation)

And finally, from the low fidelity modeling effort the following items are given:

- SO_x species evolution
- NO_y species evolution
- CO, OH, and O species evolution

The CNEWT and CALCHEM input file used to obtain these results are given in Appendix E.

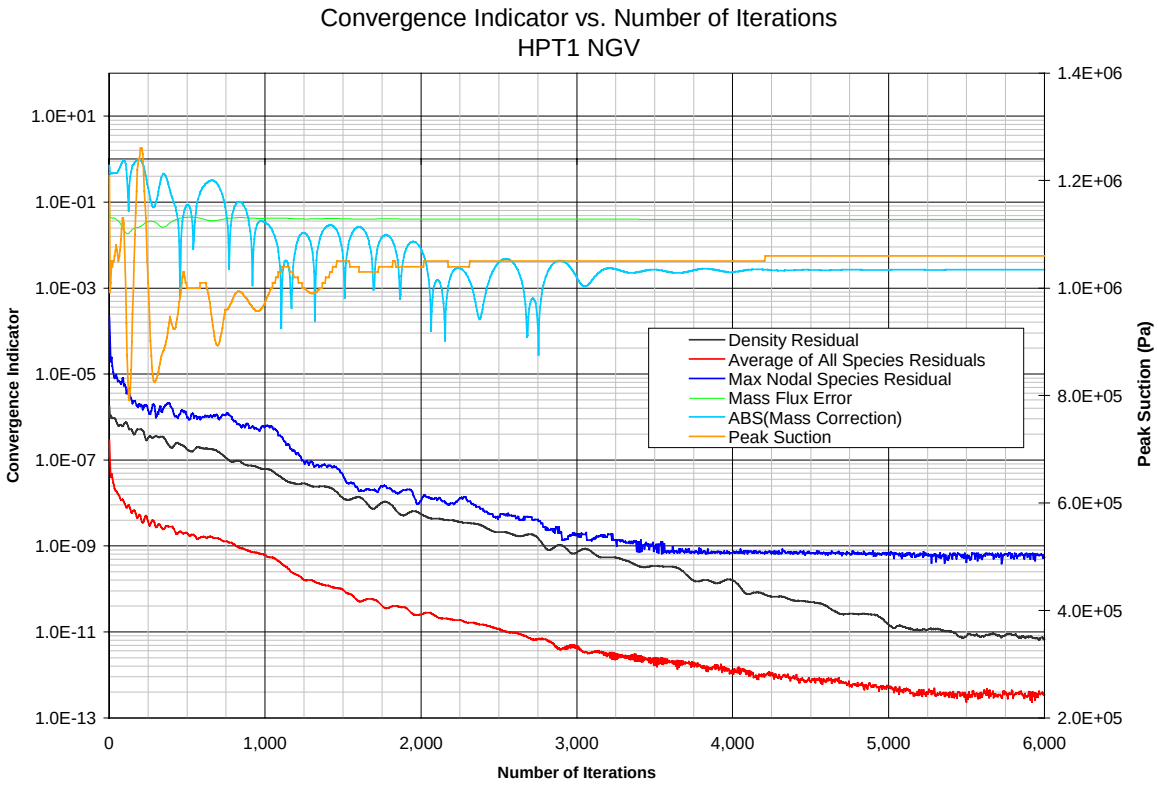
Convergence Indicator vs. Number of Iterations
HPT1 NGV
Convergence Indicator
Peak Suction (Pa)
Number of Iterations
1.0E+01
1.0E-01
1.0E-03
1.0E-05
1.0E-07
1.0E-09
1.0E-11
1.0E-13
1.4E+06
1.2E+06
1.0E+06
8.0E+05
6.0E+05
4.0E+05
2.0E+05
0
1,000
2,000
3,000
4,000
5,000
6,000
Density Residual
Average of All Species Residuals
Max Nodal Species Residual
Mass Flux Error
ABS(Mass Correction)
Peak Suction

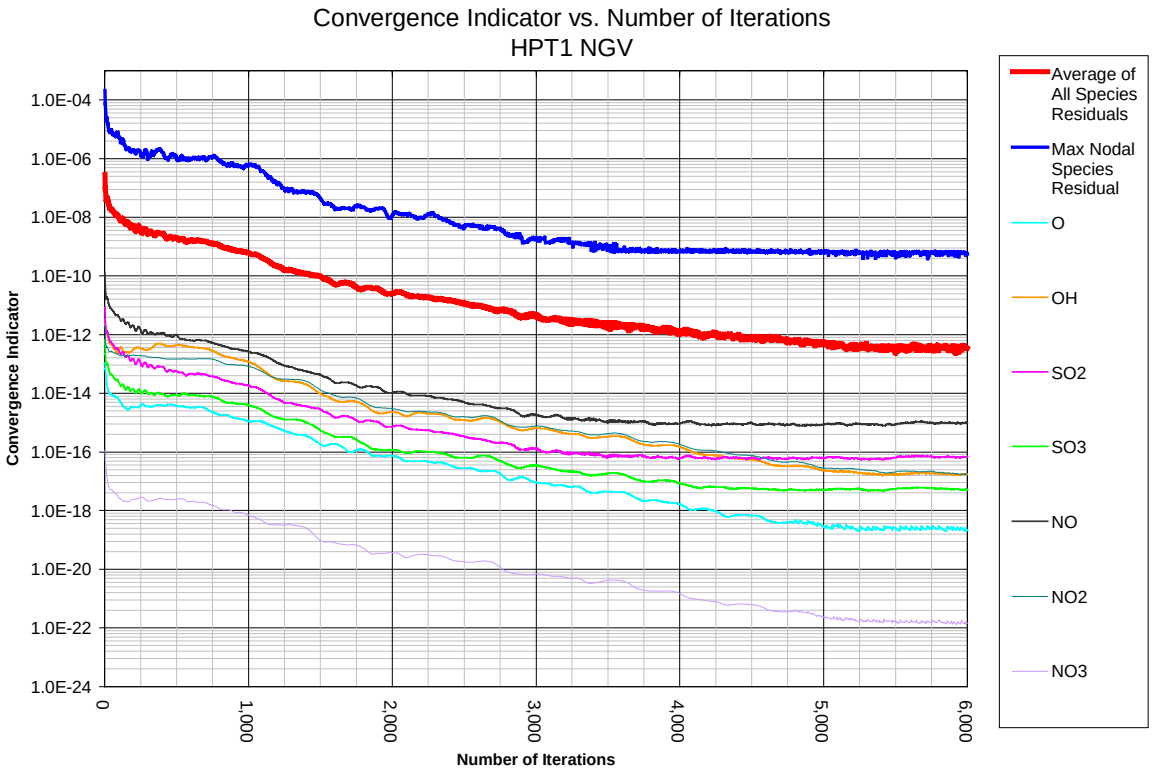
Convergence Indicator vs. Number of Iterations
HPT1 NGV
Convergence Indicator
Number of Iterations
1.0E-04
1.0E-06
1.0E-08
1.0E-10
1.0E-12
1.0E-14
1.0E-16
1.0E-18
1.0E-20
1.0E-22
1.0E-24
0
1,000
2,000
3,000
4,000
5,000
6,000
Average of All Species Residuals
Max Nodal Species Residual
O
OH
SO2
SO3
NO
NO2
NO3

range and mass averaged quantities at cutting plane
cutting plane at 0.04515

Num	Spec	min	max	mass ave
1	CO	1.0960670E-05	1.1788260E-05	1.1291178E-05
2	CO2	7.2901480E-02	7.2902828E-02	7.2902240E-02
3	O2	0.1480127	0.1480136	0.1480131
4	H2O	2.9883171E-02	2.9883521E-02	2.9883305E-02
5	H	2.8244520E-12	9.4324088E-12	8.3788480E-12
6	O	2.6128790E-08	4.4815678E-08	3.4125186E-08
7	OH	1.9860620E-06	3.9784268E-06	3.6788304E-06
8	HO2	2.4688800E-08	5.8078822E-08	4.2947221E-08
9	H2O2	5.4499472E-09	9.8093857E-08	1.6948434E-08
10	NO	3.1216681E-04	3.1549390E-04	3.1493246E-04
11	NO2	4.9967889E-06	6.4257251E-06	5.7360417E-06
12	NO3	5.9383180E-12	3.1245451E-11	1.0588782E-11
13	HNO	7.8105612E-11	1.7963479E-10	1.2943577E-10
14	HONO	4.0774090E-08	4.1504150E-06	2.0222627E-07
15	HNO3	-1.4242200E-10	5.3347769E-08	9.1435254E-10
16	SO2	2.1805350E-05	2.1853461E-05	2.1843829E-05
17	SO3	1.7444370E-06	1.7997299E-06	1.7563391E-06
18	HOSO	2.7650279E-14	2.5342201E-13	1.4487009E-13
19	HSO3	5.0049240E-12	1.1248480E-10	8.1400182E-12
20	HSO2	1.2148050E-16	5.7409781E-16	1.5103668E-16
21	SO	9.1956160E-14	3.9928561E-13	3.4998060E-13
22	HCO	2.5679660E-17	5.7935929E-17	4.5071751E-17
23	H2	1.1504340E-10	1.0300690E-09	7.3819911E-10
24	N2	0.7488416	0.7488421	0.7488415
25	AR	0.0000000E+00	0.0000000E+00	0.0000000E+00
26	C(S)	0.0000000E+00	0.0000000E+00	0.0000000E+00
27	N	0.0000000E+00	0.0000000E+00	0.0000000E+00
28	H2SO4	3.7797829E-10	6.7893300E-09	5.7222255E-10
29	S	2.4445289E-21	2.4445451E-21	2.4445346E-21

X/X	7.1622198E-03	5.9027892E-02	
Y/R	0.2616538	0.2712400	
Z/T	-6.3572727E-02	2.0361030E-02	
Tt	1156.810	1386.379	1363.339
dens	3.119411	4.331536	
Ps	10.55461	16.76656	12.99278
Vx	-123.4683	450.0187	201.4363
Vt	-430.1193	261.4255	361.1647
Vr	-84.10556	25.99604	-5.2535836E-02
TK	0.5282233	285292.6	
TE	12.38410	6.1178208E+10	
Ts	1083.624	1374.872	1287.489
Mach	3.7381984E-03	0.9269373	
Pt	13.64641	21.36677	16.27730
Pred	10.55461	16.76656	
S	0.6861496	0.8642535	

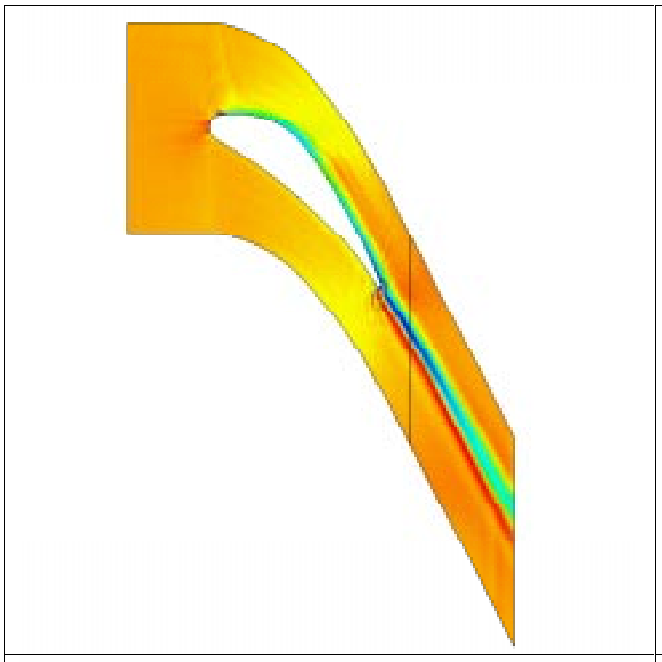

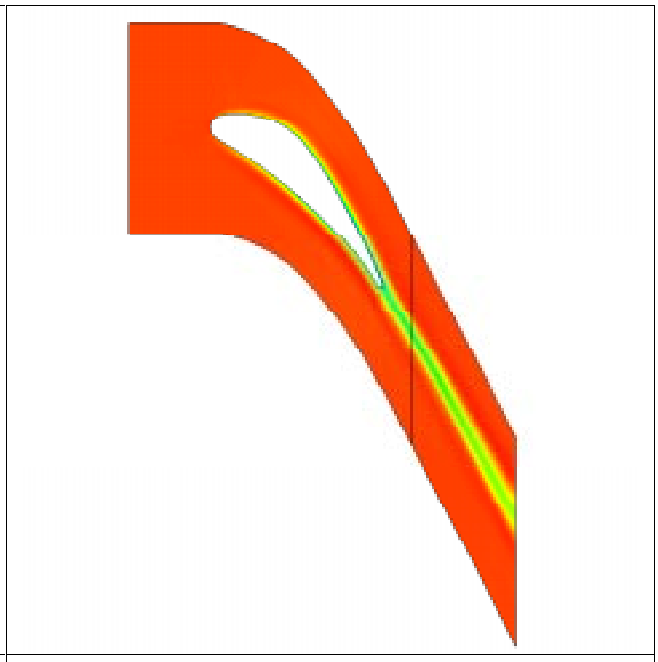

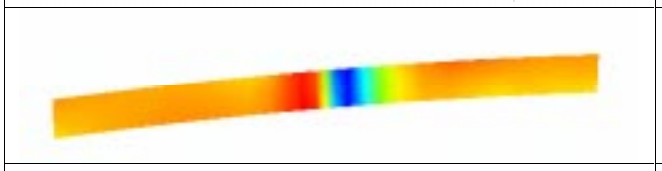

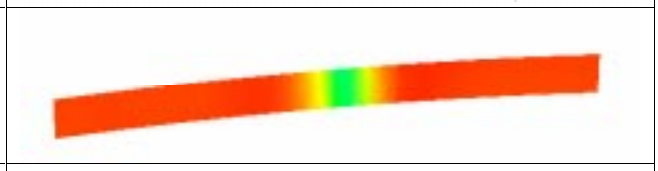

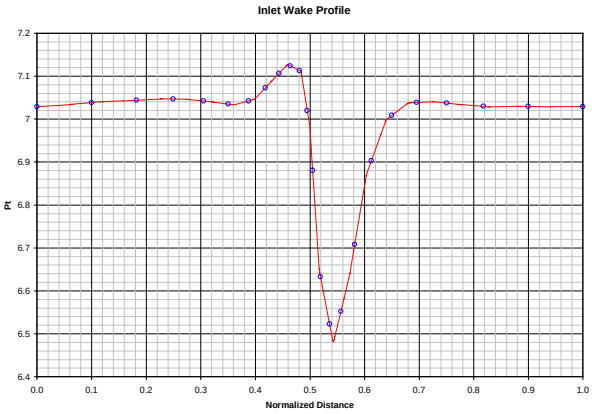

Pt: 1,364,641 to 21,366,770 Pa
(1,550,000 to 1,650,000 plot)
Mass Ave.: 1,627,730 Pa

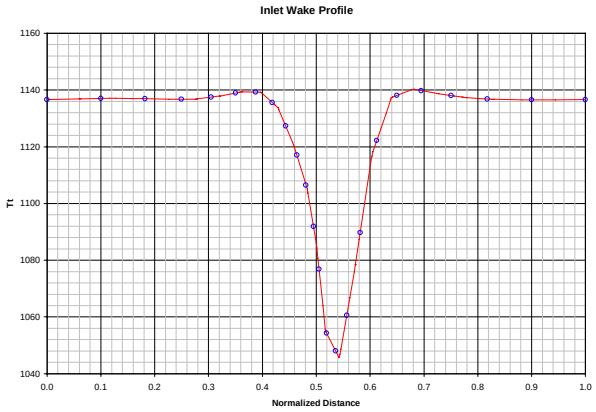

Tt: 1156.810 to 1386.379 K
Mass Ave.: 1363.339 K

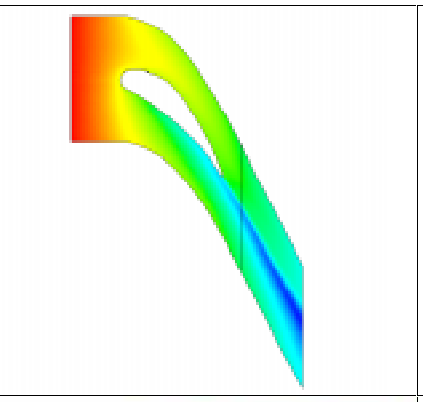
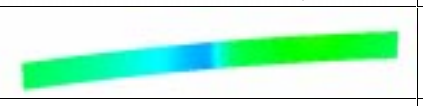
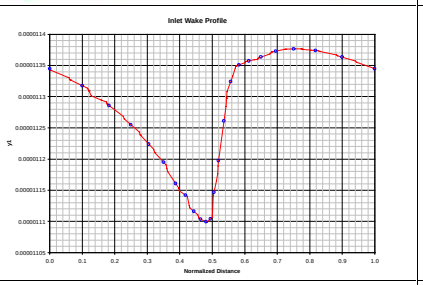

Y(CO): 1.0961e-5 to 1.1788e-5
Mass Ave.: 1.1291e-5

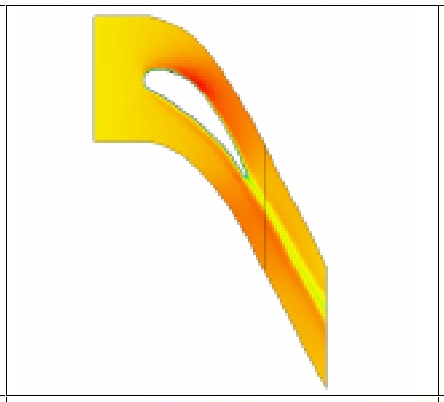

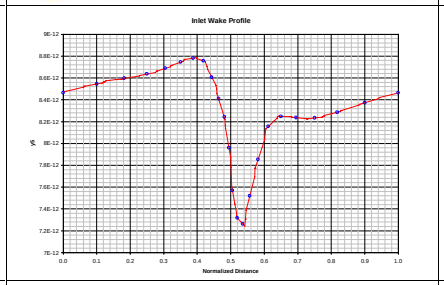

Y(H): 2.8245e-12 to 9.4324e-12
Mass Ave.: 8.3788e-12

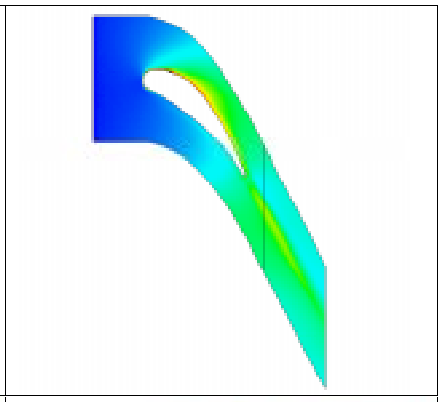
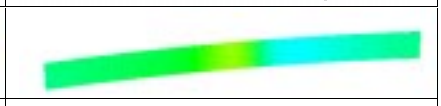
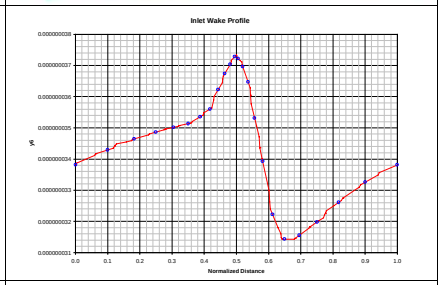

Y(O): 2.6129e-8 to 4.4816e-8
Mass Ave.: 3.4125e-8

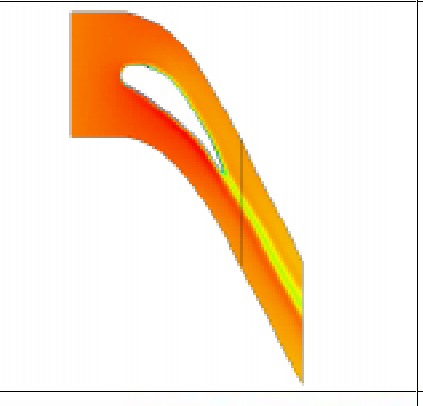

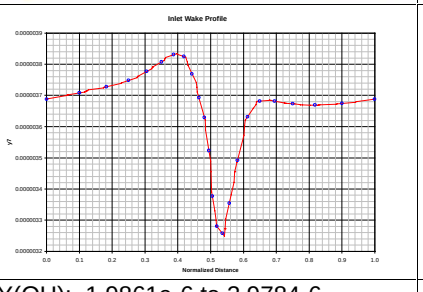

Y(OH): 1.9861e-6 to 3.9784-6
Mass Ave.: 3.6788e-6

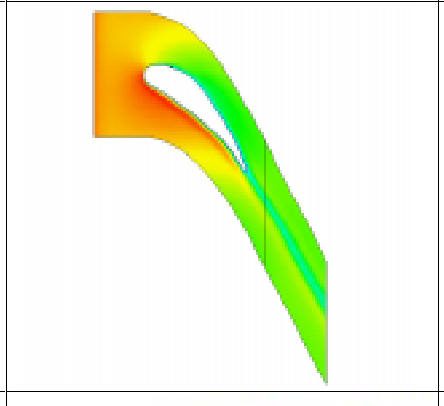
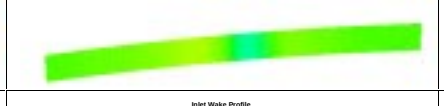
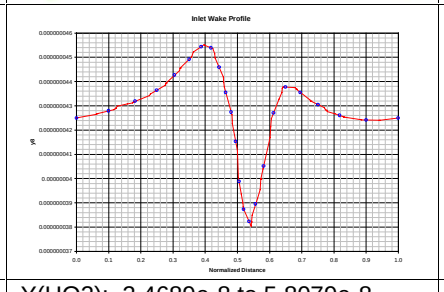

Y(HO2): 2.4689e-8 to 5.8079e-8
Mass Ave.: 4.2947e-8

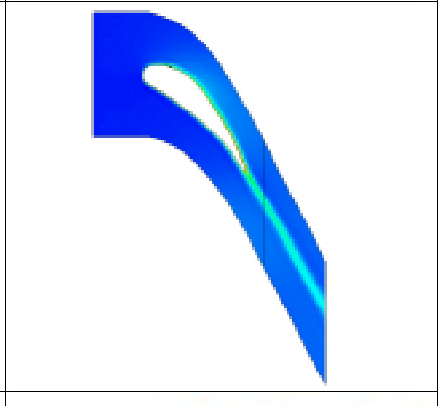
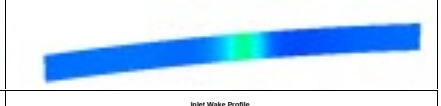
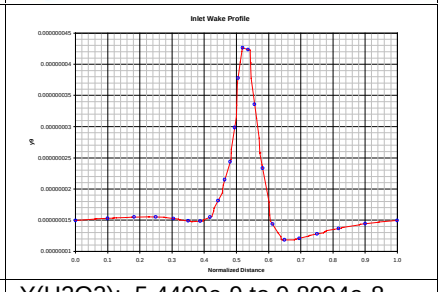

Y(H2O2): 5.4499e-9 to 9.8094e-8
Mass Ave.: 1.6948e-8

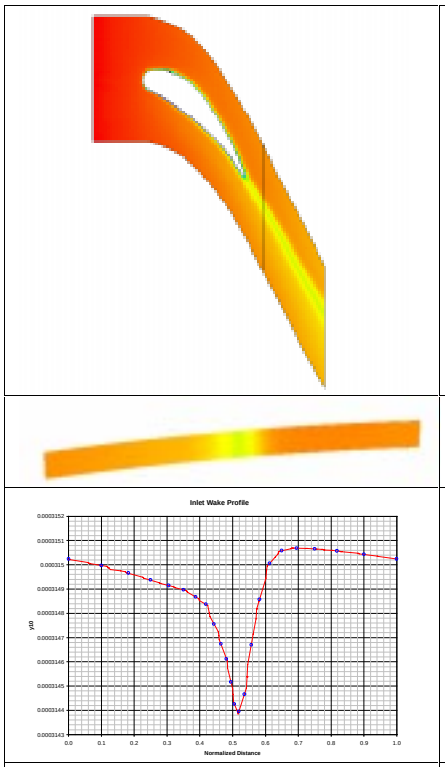
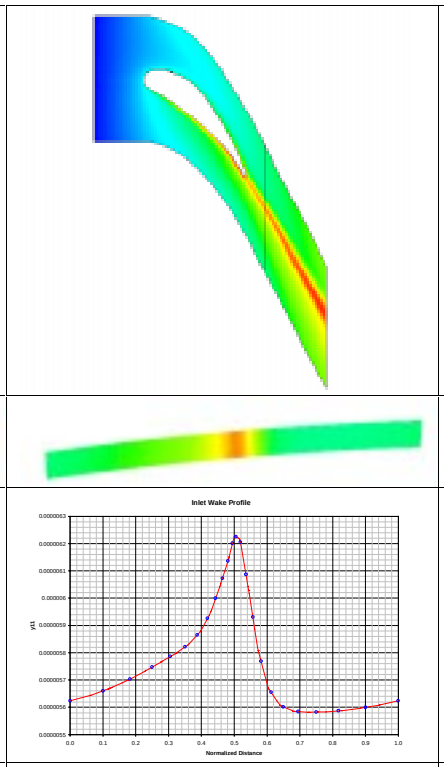
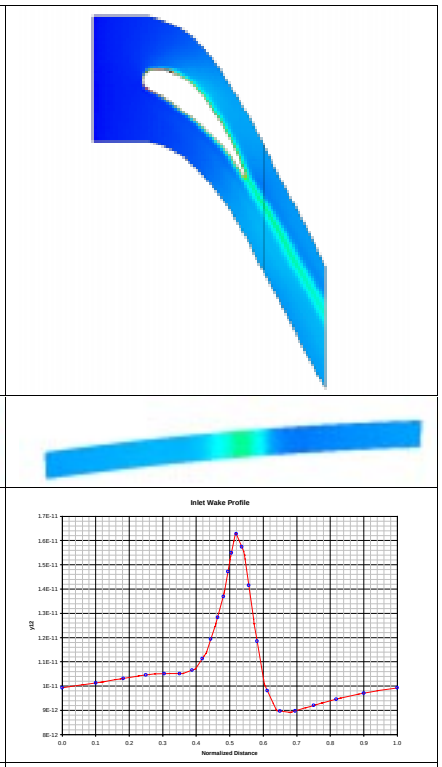

Y(NO): 3.1217e-4 to 3.1549e-4
Mass Ave.: 3.1493e-4

Y(NO2): 4.9968e-6 to 6.4257e-6
Mass Ave.: 5.7360e-6

Y(NO3): 5.9383e-12 to 3.1245e-11
Mass Ave.: 1.0589e-11

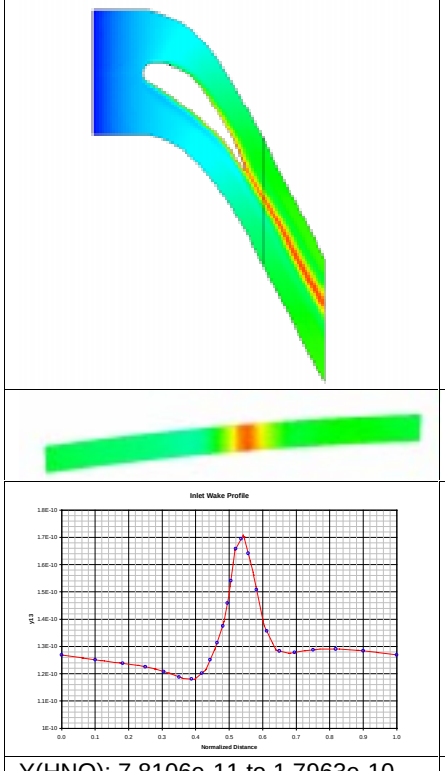
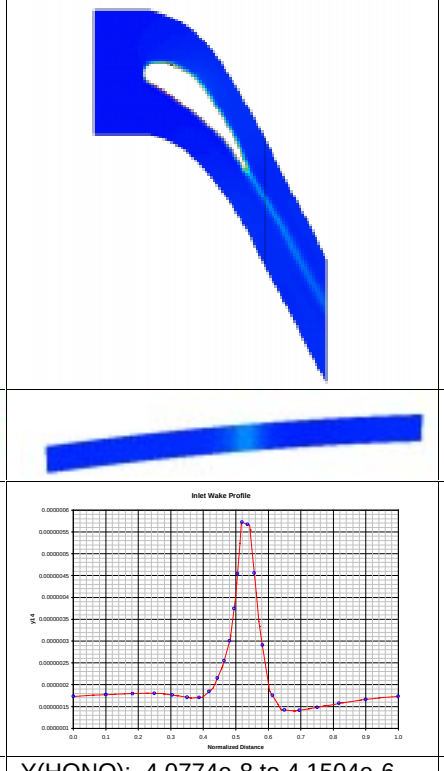
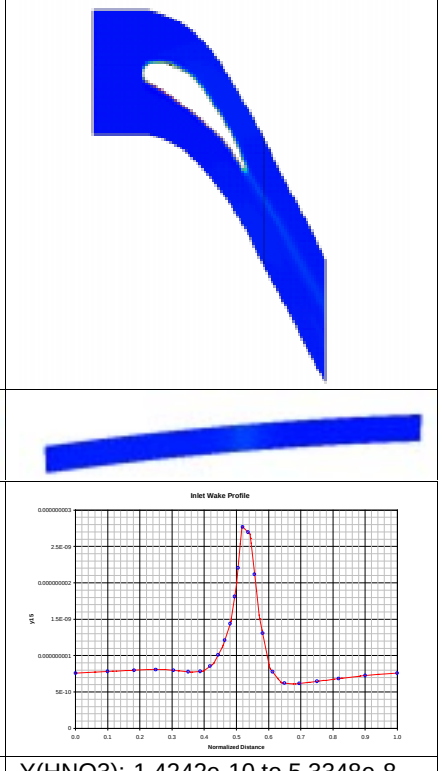

Y(HNO): 7.8106e-11 to 1.7963e-10
Mass Ave.: 1.2944e-10

Y(HONO): 4.0774e-8 to 4.1504e-6
Mass Ave.: 2.0223e-7

Y(HNO3):-1.4242e-10 to 5.3348e-8
Mass Ave.: 9.1435e-10

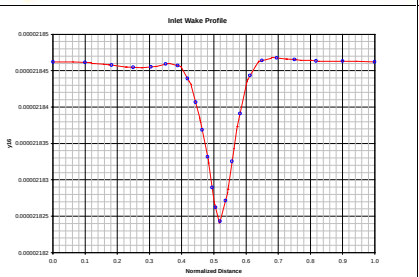

Y(SO2): 2.1805e-5 to 2.1853e-5
Mass Ave.: 2.1844e-5

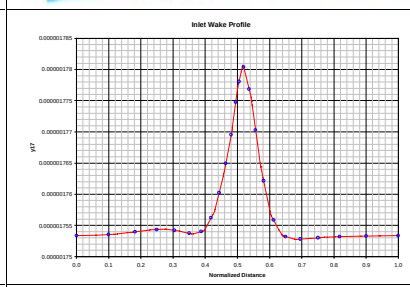

Y(SO3): 1.7444e-6 to 1.7997e-6
Mass Ave.: 1.7563e-6

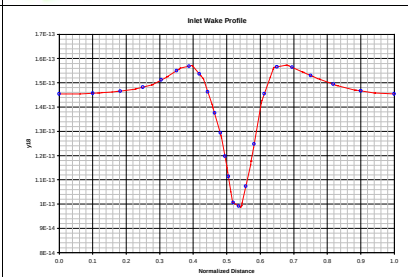

Y(HOSO): 2.7650e-14 to 2.5342e-13
Mass Ave.: 1.4487e-13

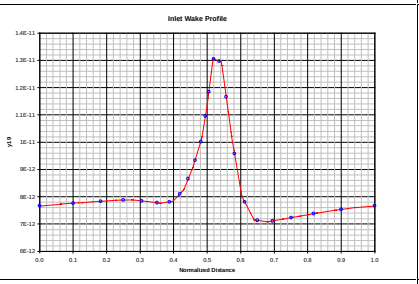

Y(HSO3): 5.0049e-12 to 1.1248e-10
Mass Ave.: 8.1400e-12

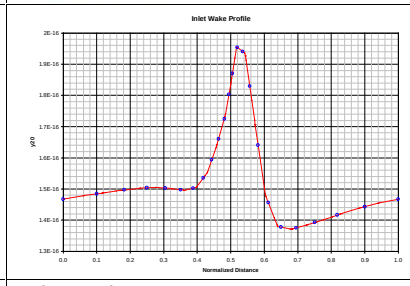

Y(HSO2): 1.2148e-16 to 5.7410e-16
Mass Ave.: 1.5104e-16

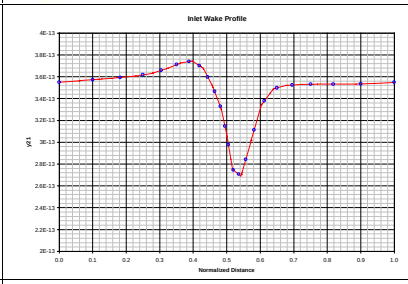

Y(SO): 9.1956e-14 to 3.9929e-13
Mass Ave.: 3.4998e-13

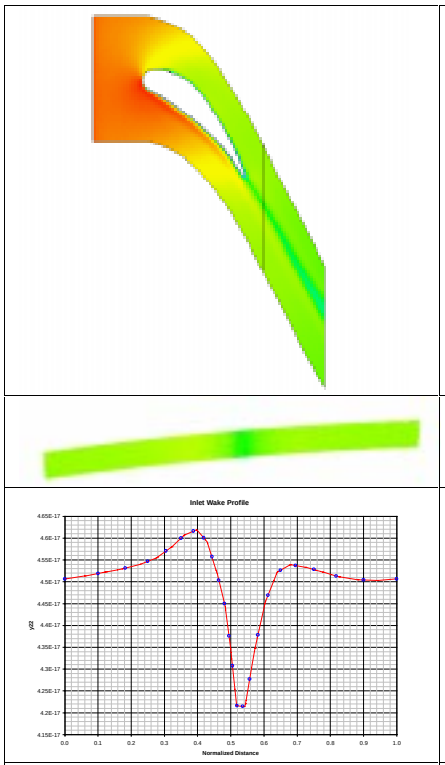

Y(HCO): 2.5680e-17 to 5.7936e-17
Mass Ave.: 4.5072e-17

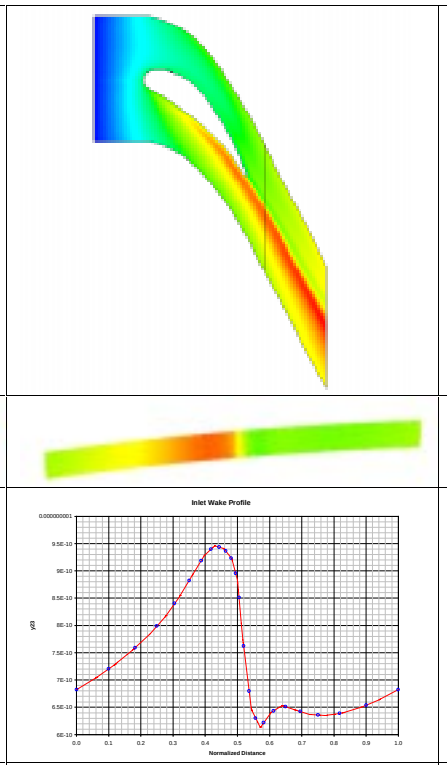

Y(H2): 1.1504e-10 to 1.0301e-9
Mass Ave.: 7.3820e-10

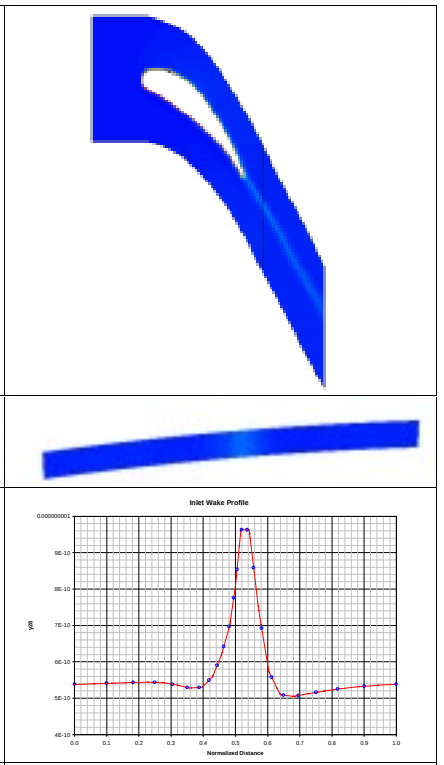

Y(H2SO4): 3.7798e-10 to 6.7893e-9
Mass Ave.: 5.7222e-10

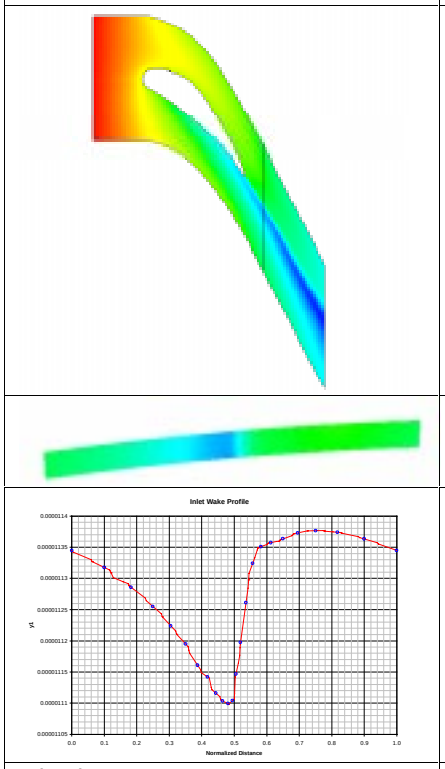

Y(CO): 0.1182e-3 to 0.1184e-3
Mass Ave.: 1.1831298e-4

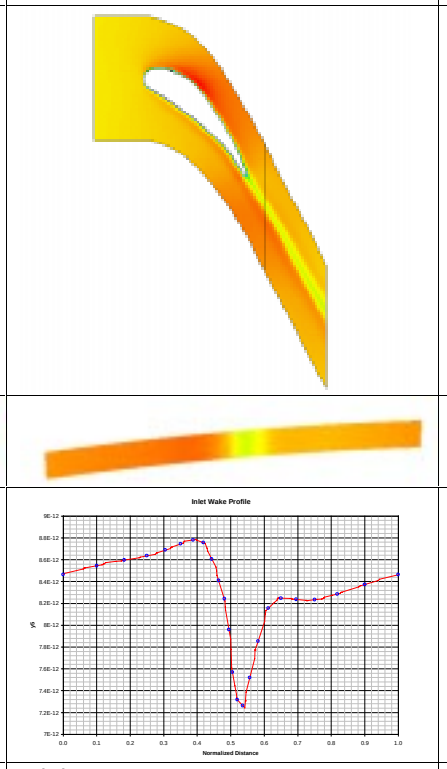

Y(H): 0.1744e-11 to 0.7114e-11
Mass Ave.: 5.7431872e-12

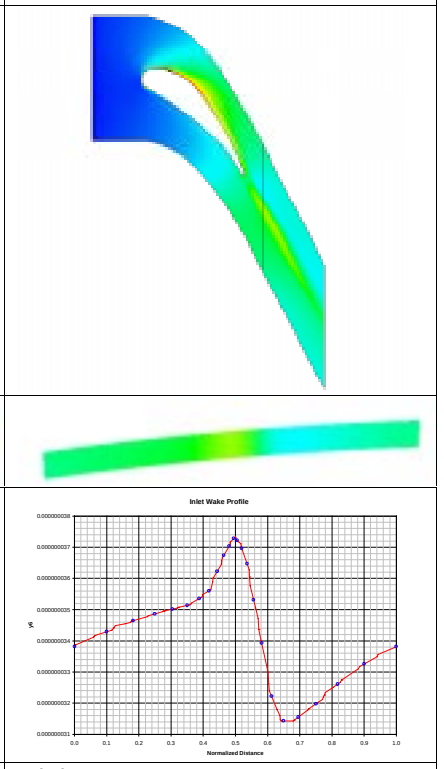

Y(O): 0.1381e-8 to 0.3256e-8
Mass Ave.: 2.7345592e-9

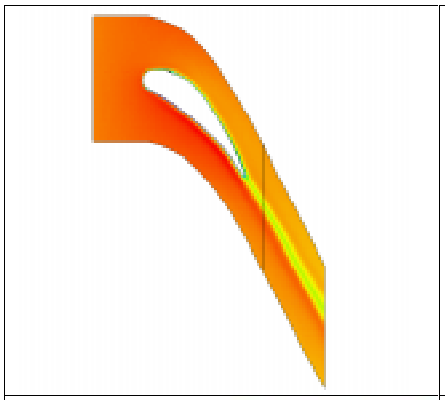
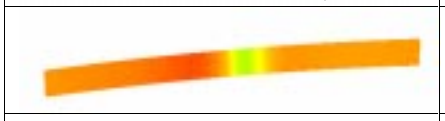
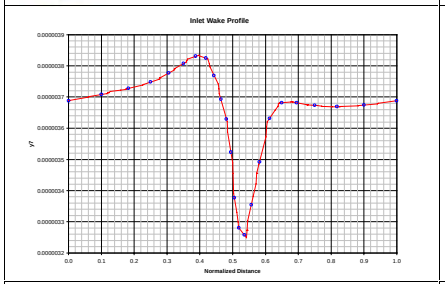

Y(OH): 0.9709e-7 to 0.2440e-6
Mass Ave.: 1.8664913e-7

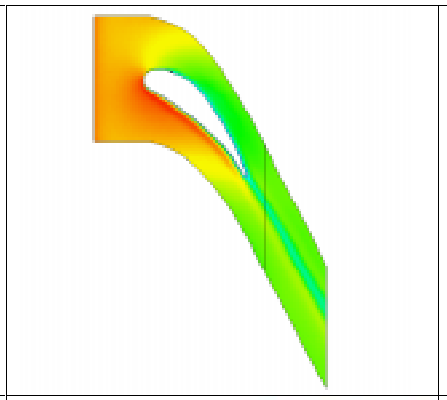
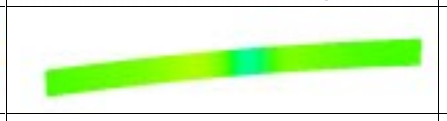
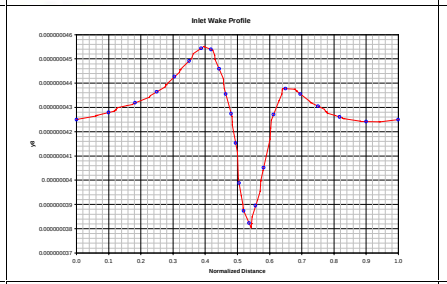

Y(HO2): 0.5840e-8 0.1280e-7
Mass Ave.: 9.9647286e-9

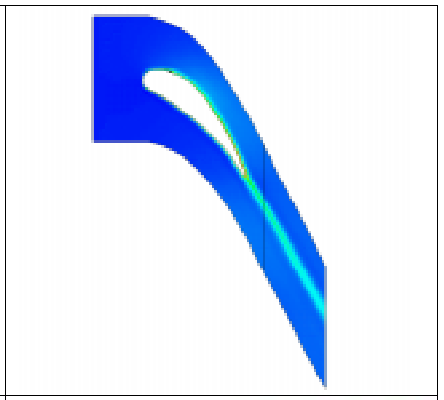
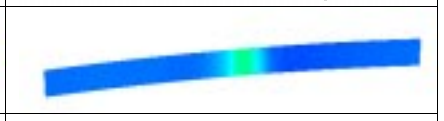
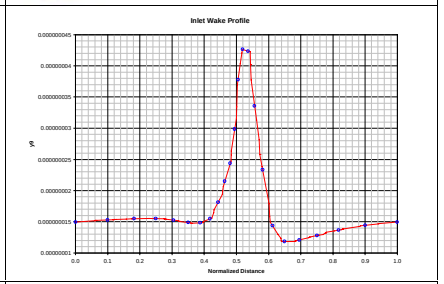

Y(H2O2): 0.5482e-9 to 0.9895e-9
Mass Ave.: 8.0803236e-10

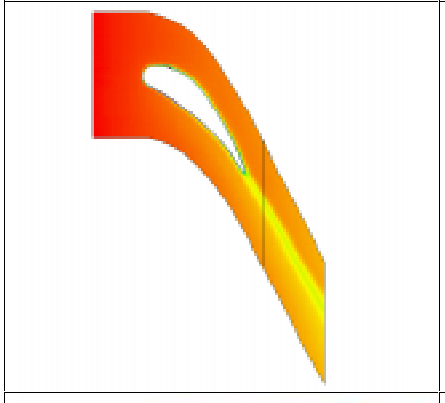
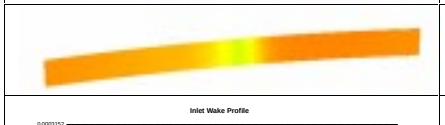
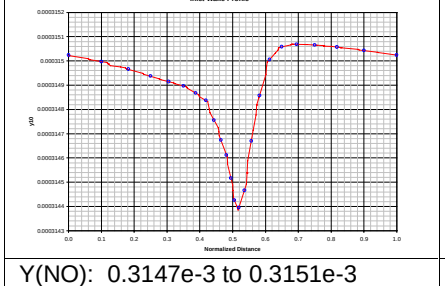

Y(NO): 0.3147e-3 to 0.3151e-3
Mass Ave.: 3.1489908e-4

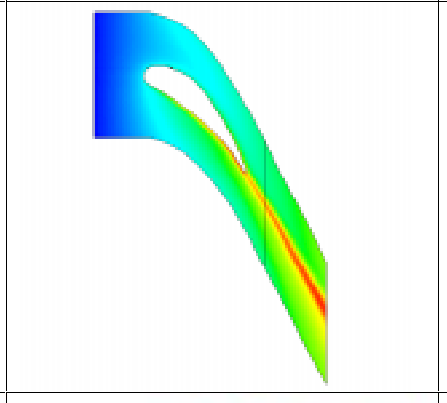
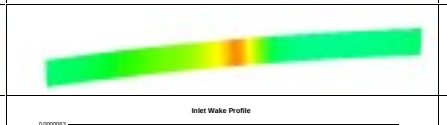
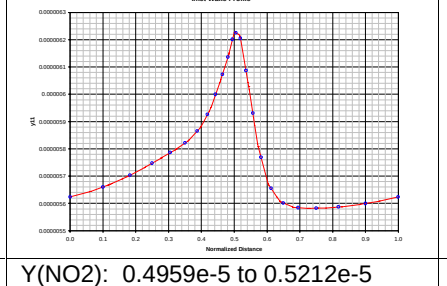

Y(NO2): 0.4959e-5 to 0.5212e-5
Mass Ave.: 5.1086913e-6

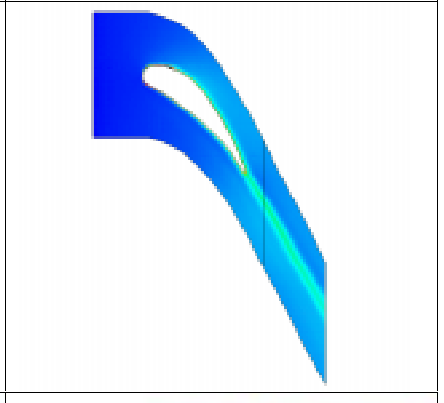
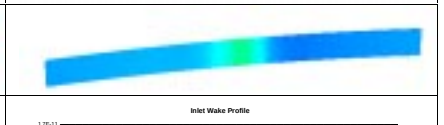
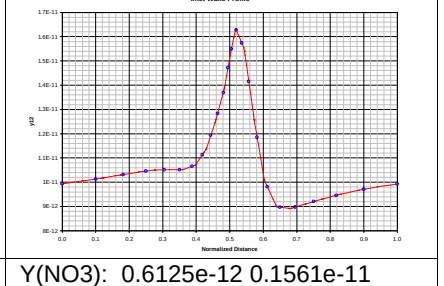

Y(NO3): 0.6125e-12 0.1561e-11
Mass Ave.: 9.1026232e-13

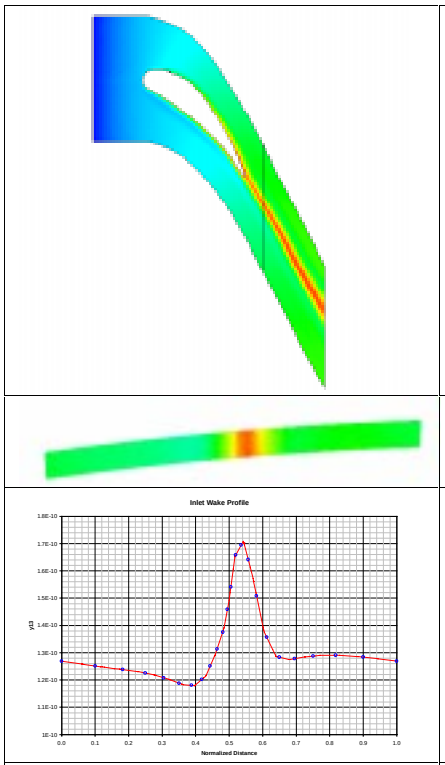
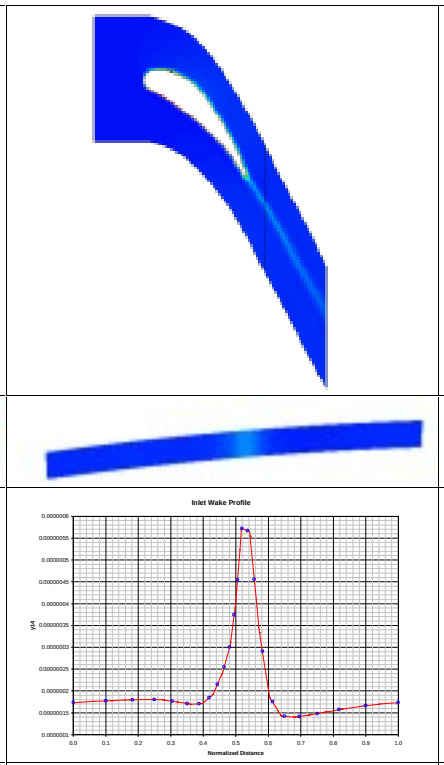
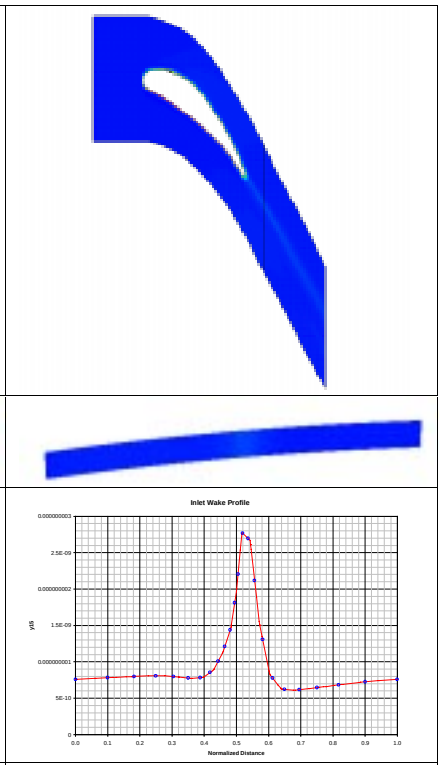

Y(HNO): 0.5744e-10 to 0.2084e-9
Mass Ave.: 1.4870816e-10

Y(HONO): 0.7931e-7 to 0.4635e-6
Mass Ave.: 2.3786764e-7

Y(HNO3): 0.1836e-9 0.5146e-8
Mass Ave.: 1.1930059e-99

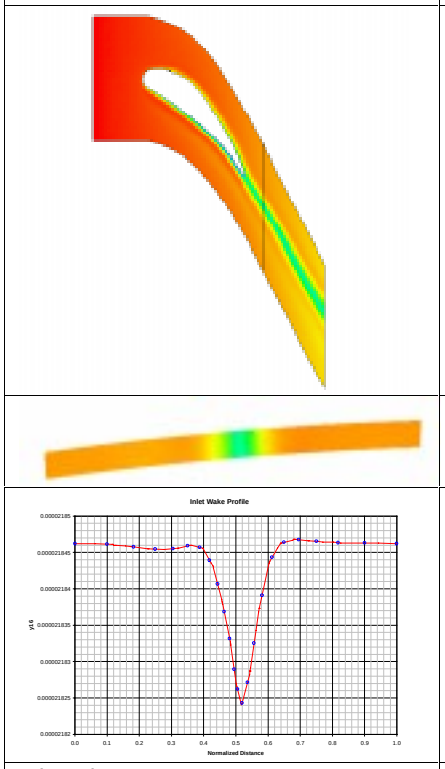
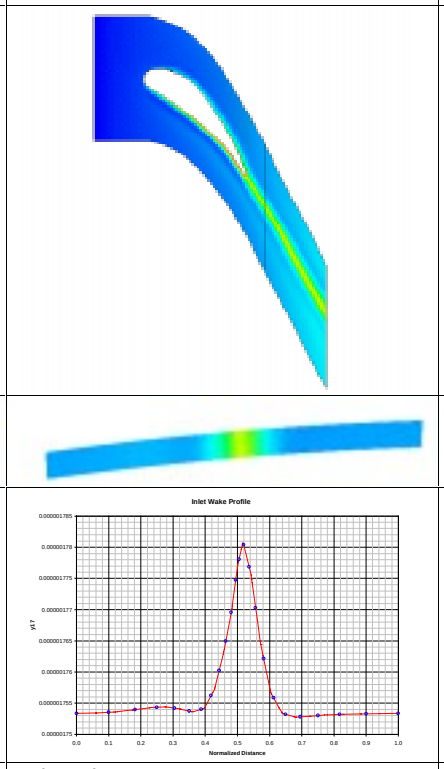
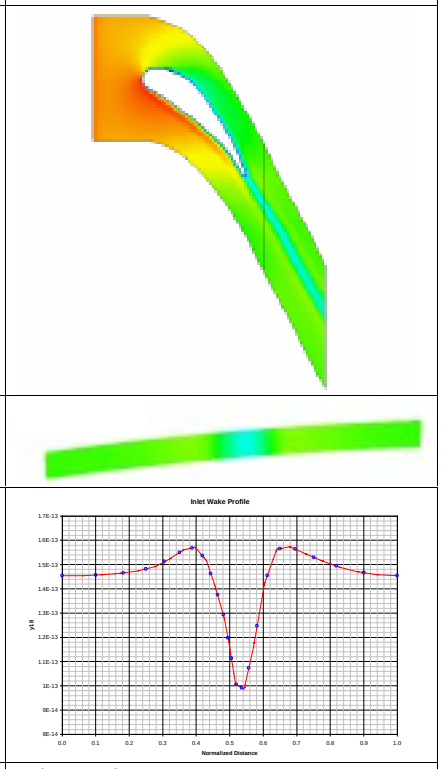

Y(SO2): 0.2185e-4 to 0.2185e-4
Mass Ave.: 2.1851994e-5

Y(SO3): 0.1732e-5 to 0.1750e-5
Mass Ave.: 1.7476095e-6

Y(HOSO): 0.2800e-14 to 0.2575e-13
Mass Ave.: 1.4743281e-14

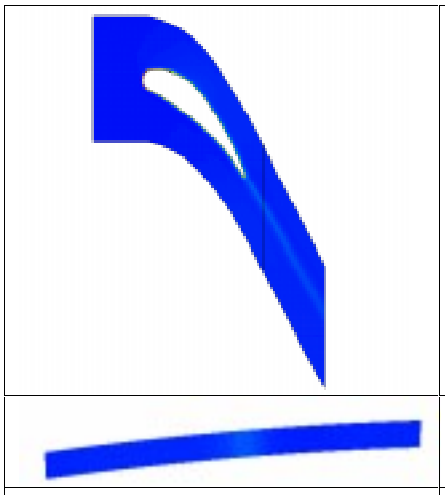

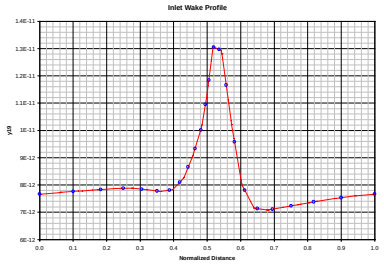

Y(HSO3): 0.6570e-12 to 0.3095e-10
Mass Ave.: 1.3700932e-12

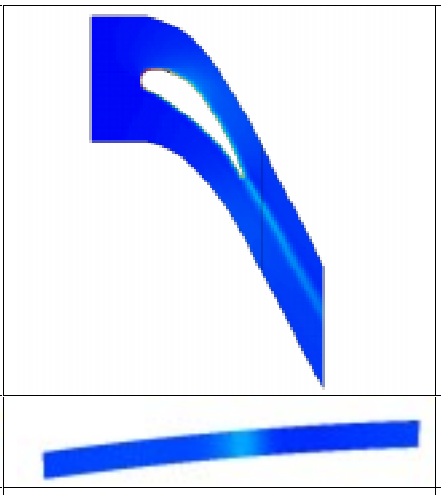

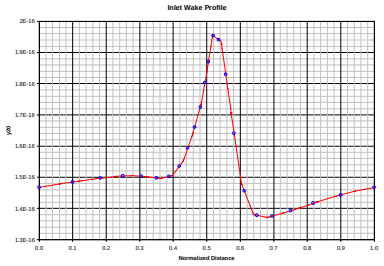

Y(HSO2): 0.1312e-15 to 0.8096e-15
Mass Ave.: 1.6506563e-16

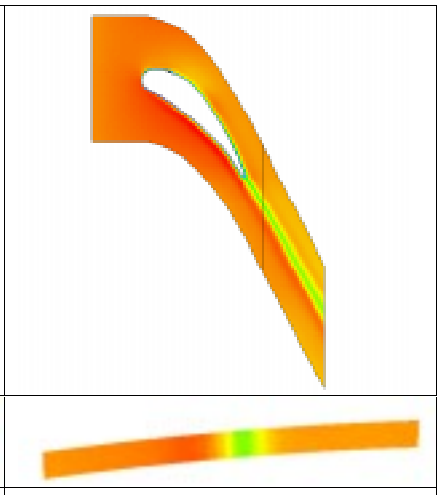

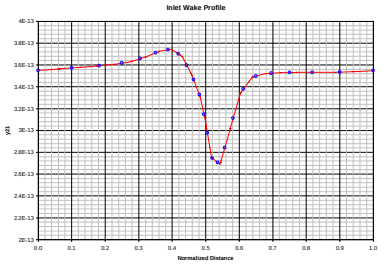

Y(SO): 0.2181e-14 to 0.2360e-13
Mass Ave.: 1.3050741e-14

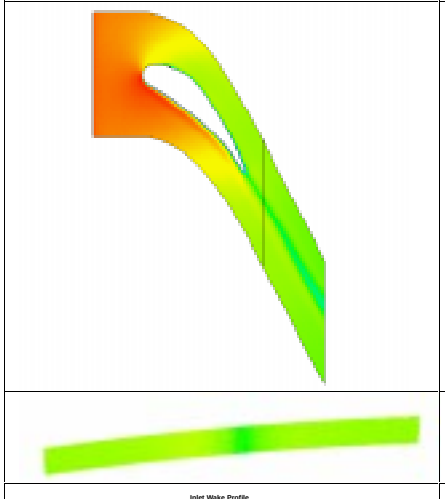

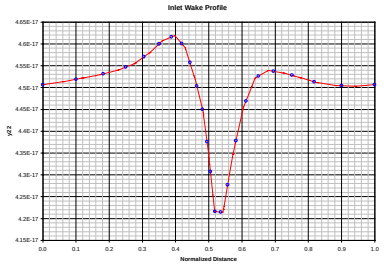

Y(HCO): 0.7836e-16 to 0.2348e-15
Mass Ave.: 1.7947180e-16

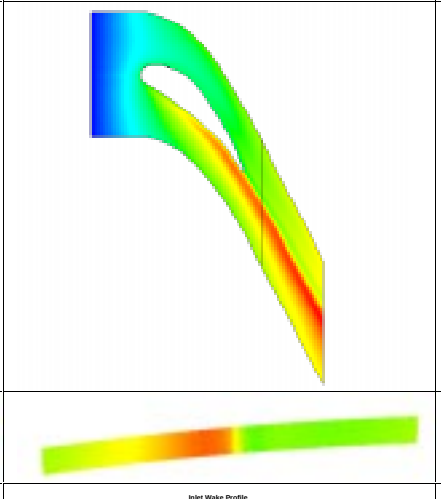

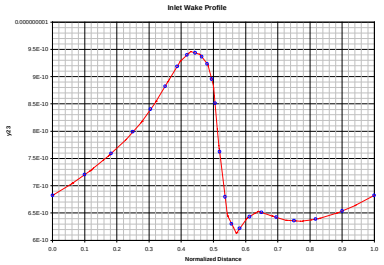

Y(H2): 0.4028e-10 to 0.1340e-9
Mass Ave.: 9.4745010e-11

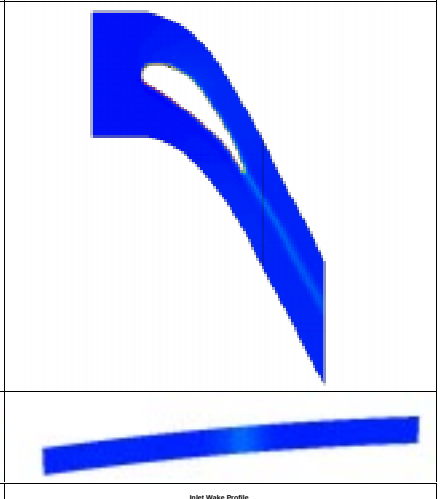

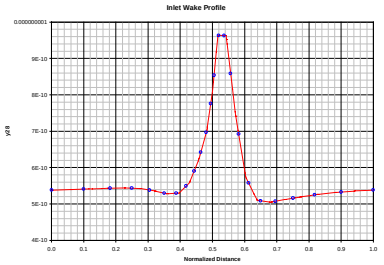

Y(H2SO4): 0.6635e-9 to 0.2421e-7
Mass Ave.: 1.4716267e-9

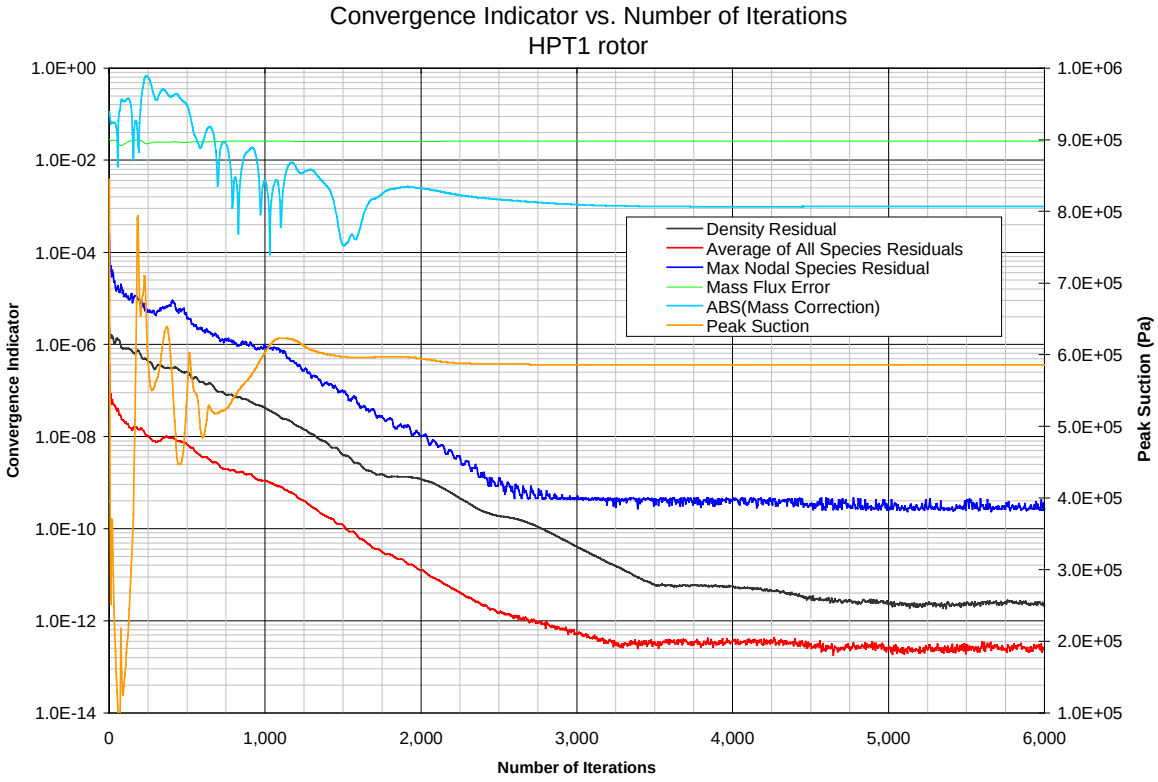
Convergence Indicator vs. Number of Iterations
HPT1 rotor
Convergence Indicator
Peak Suction (Pa)
Number of Iterations
Density Residual
Average of All Species Residuals
Max Nodal Species Residual
Mass Flux Error
ABS(Mass Correction)
Peak Suction
1.0E+00
1.0E-02
1.0E-04
1.0E-06
1.0E-08
1.0E-10
1.0E-12
1.0E-14
1.0E+06
9.0E+05
8.0E+05
7.0E+05
6.0E+05
5.0E+05
4.0E+05
3.0E+05
2.0E+05
1.0E+05
0
1,000
2,000
3,000
4,000
5,000
6,000

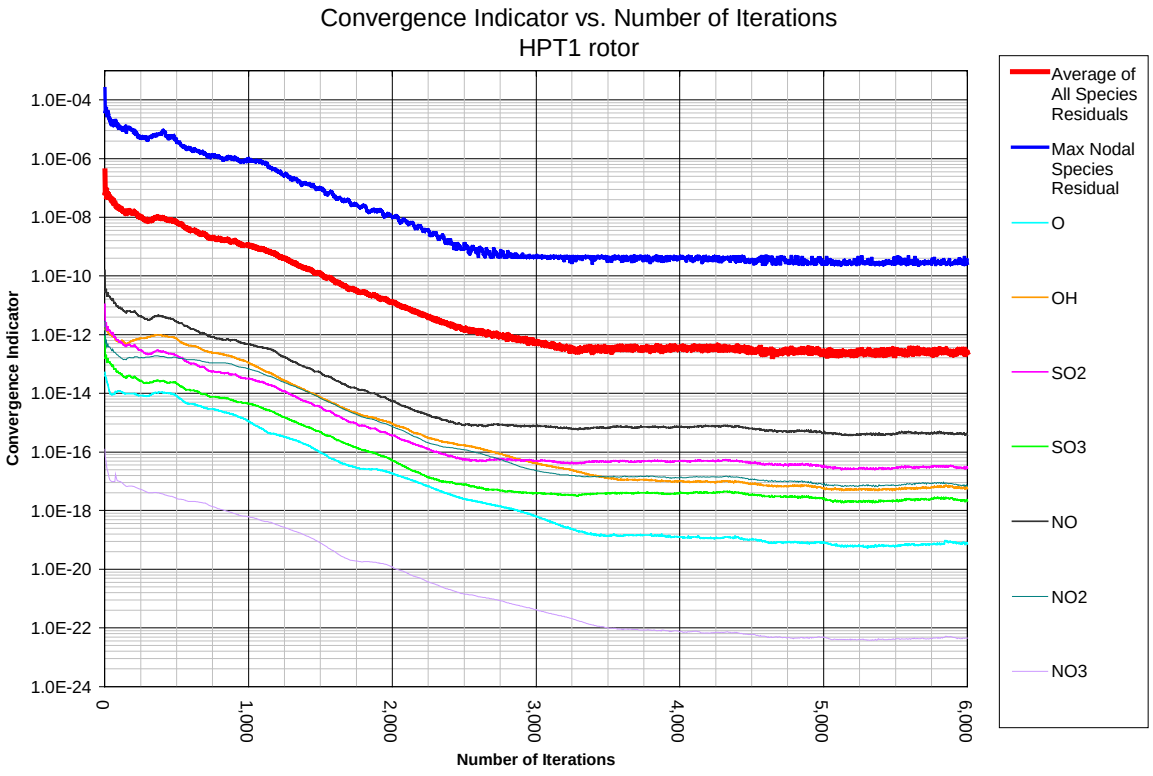
Convergence Indicator vs. Number of Iterations
HPT1 rotor
Convergence Indicator
Number of Iterations
Average of All Species Residuals
Max Nodal Species Residual
O
OH
SO2
SO3
NO
NO2
NO3
1.0E-04
1.0E-06
1.0E-08
1.0E-10
1.0E-12
1.0E-14
1.0E-16
1.0E-18
1.0E-20
1.0E-22
1.0E-24
0
1,000
2,000
3,000
4,000
5,000
6,000

range and mass averaged quantities at cutting plane
cutting plane at 0.01060

num	species	min	max	mass ave
1	CO	1.1028110E-05	1.1291180E-05	1.1155897E-05
2	CO2	7.2902203E-02	7.2902679E-02	7.2902434E-02
3	O2	0.1480128	0.1480133	0.1480130
4	H2O	2.9883269E-02	2.9883681E-02	2.9883401E-02
5	H	3.0306020E-12	1.1951770E-11	9.4046255E-12
6	O	3.0920891E-08	5.6032619E-08	4.3273968E-08
7	OH	1.8885230E-06	3.7138709E-06	3.3758893E-06
8	HO2	2.3738091E-08	4.5069211E-08	3.6882440E-08
9	H2O2	1.0050790E-08	8.7000387E-08	3.9920529E-08
10	NO	3.1211879E-04	3.1495970E-04	3.1454579E-04
11	NO2	5.7360421E-06	6.3211310E-06	5.9863410E-06
12	NO3	8.3264983E-12	3.6301271E-11	1.4460729E-11
13	HNO	1.2877401E-10	1.8293370E-10	1.5504040E-10
14	HONO	8.1516284E-08	4.0333512E-06	5.5106256E-07
15	HNO3	-3.1286479E-10	6.1903712E-08	2.4605282E-09
16	SO2	2.1808110E-05	2.1843831E-05	2.1838596E-05
17	SO3	1.7563390E-06	1.7951180E-06	1.7627525E-06
18	HOSO	2.1189459E-14	1.6339089E-13	9.3304000E-14
19	HSO3	5.8176632E-12	1.5686860E-10	1.0739637E-11
20	HSO2	1.3123580E-16	7.0853009E-16	1.9591100E-16
21	SO	8.1447761E-14	3.6073450E-13	3.1185338E-13
22	HCO	2.3288410E-17	4.5266589E-17	4.0807966E-17
23	H2	7.3819911E-10	8.7823260E-10	8.1180129E-10
24	N2	0.7488415	0.7488420	0.7488419
25	AR	0.0000000E+00	0.0000000E+00	0.0000000E+00
26	C(S)	0.0000000E+00	0.0000000E+00	0.0000000E+00
27	N	0.0000000E+00	0.0000000E+00	0.0000000E+00
28	H2SO4	4.2082671E-10	9.0190957E-09	7.5702011E-10
29	S	2.4445289E-21	2.4445469E-21	2.4445352E-21

X/X	-1.1852840E-02	2.2079229E-02	
Y/R	0.2671618	0.2712400	
T/Z	-1.2139130E-02	3.3451378E-02	
Tt	1124.372	1333.011	1300.225
dens	2.046658	3.929755	
Ps	5.856664	14.15914	9.808423
Vx	-72.06285	712.5885	271.0783
Vt	-484.9583	490.9988	-379.8698
Vr	-52.12230	43.46152	-0.2326850
TK	0.5275032	527503.2	
TE	20.16434	6.5262518E+11	
Ts	851.8360	1315.987	1202.610
Mach	3.7721284E-03	1.512067	
Pt	9.385468	23.24667	13.33437
Pred	5.856664	14.15914	
S	0.6160989	0.8636632	

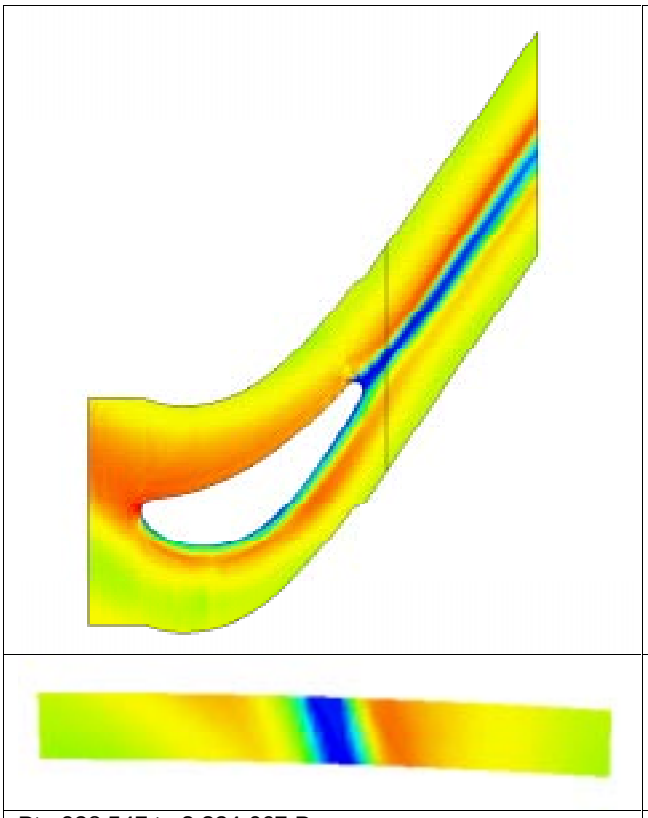	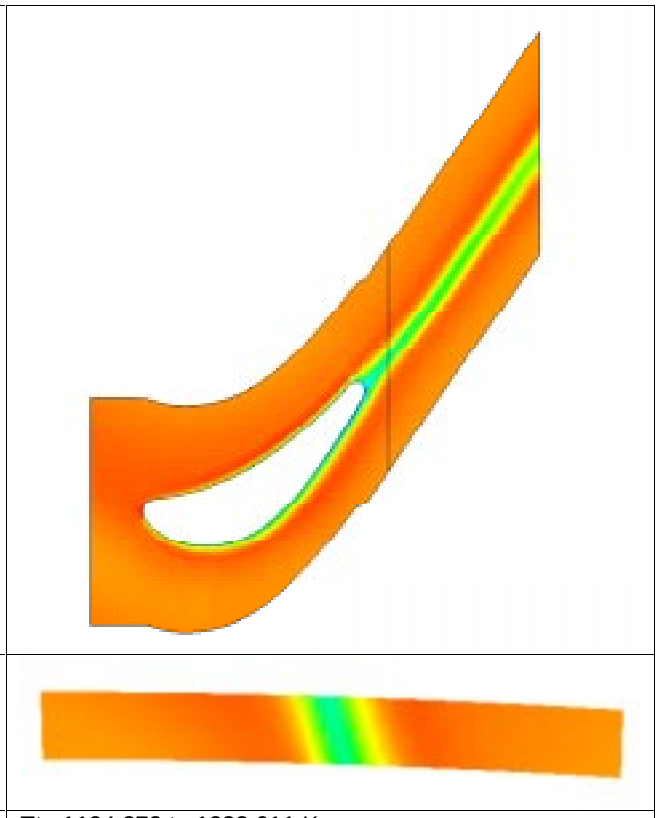
Pt: 938,547 to 2,324,667 Pa (1,200,000-1,400,000 plot) Mass Ave.: 1,333,437 Pa	Tt: 1124.372 to 1333.011 K Mass Ave.: 1300.225 K

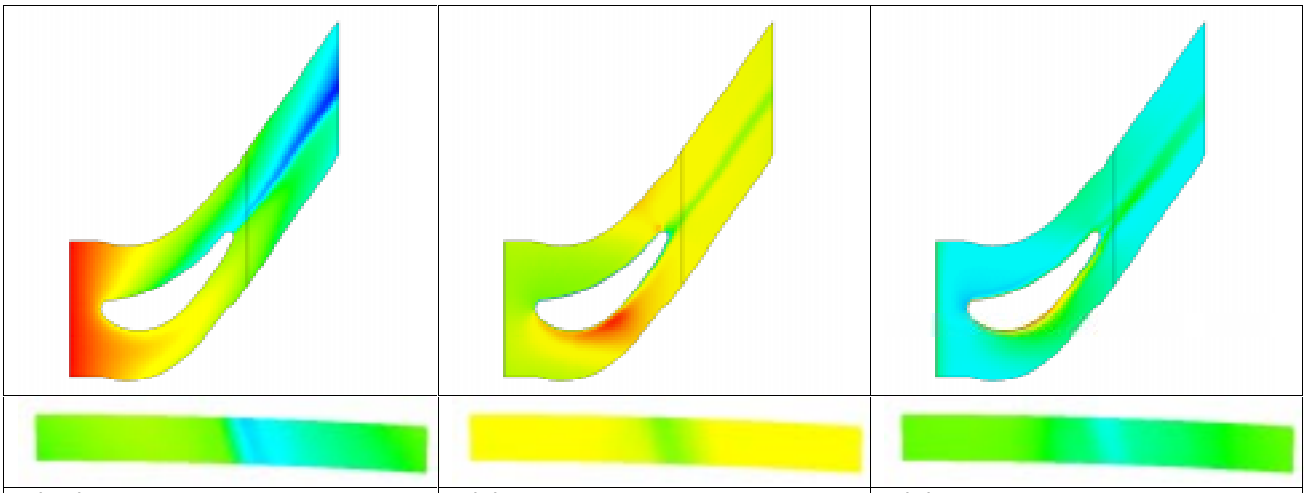		
Y(CO): 1.1028e-5 to 1.1291e-5 Mass Ave.: 1.1156e-5	Y(H): 3.0306e-12 to 1.1952e-11 Mass Ave.: 9.4046e-12	Y(O): 3.0921e-8 to 5.6033e-8 Mass Ave.: 4.3274e-8
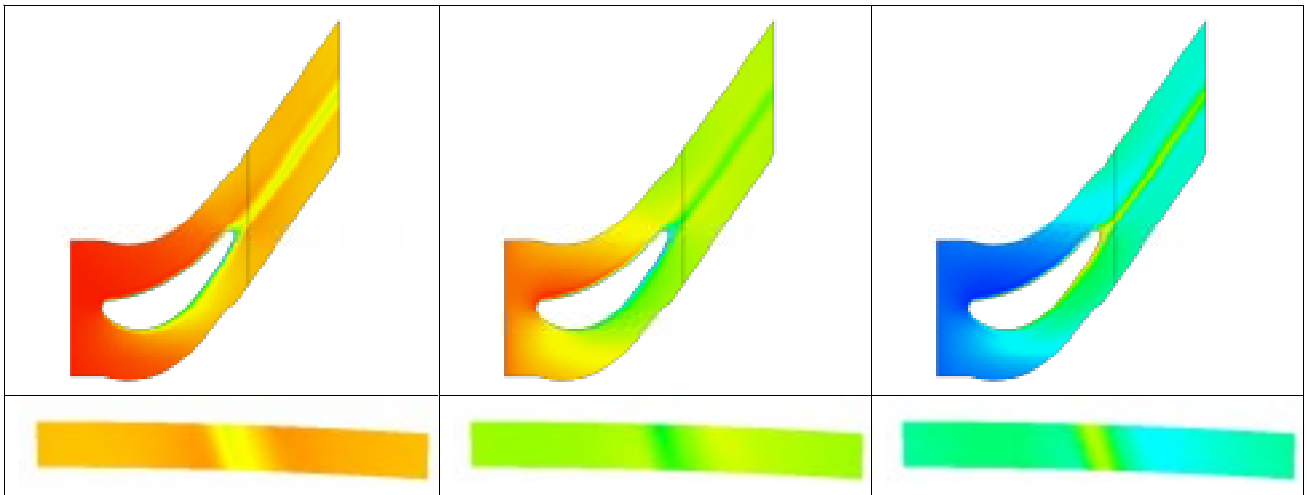		
Y(OH): 1.8885e-6 to 3.7139e-6 Mass Ave.: 3.3759e-6	Y(HO2): 2.3738e-8 to 4.5069e-8 Mass Ave.: 3.6882e-8	Y(H2O2): 1.0051e-8 to 8.7000e-8 Mass Ave.: 3.9921e-8
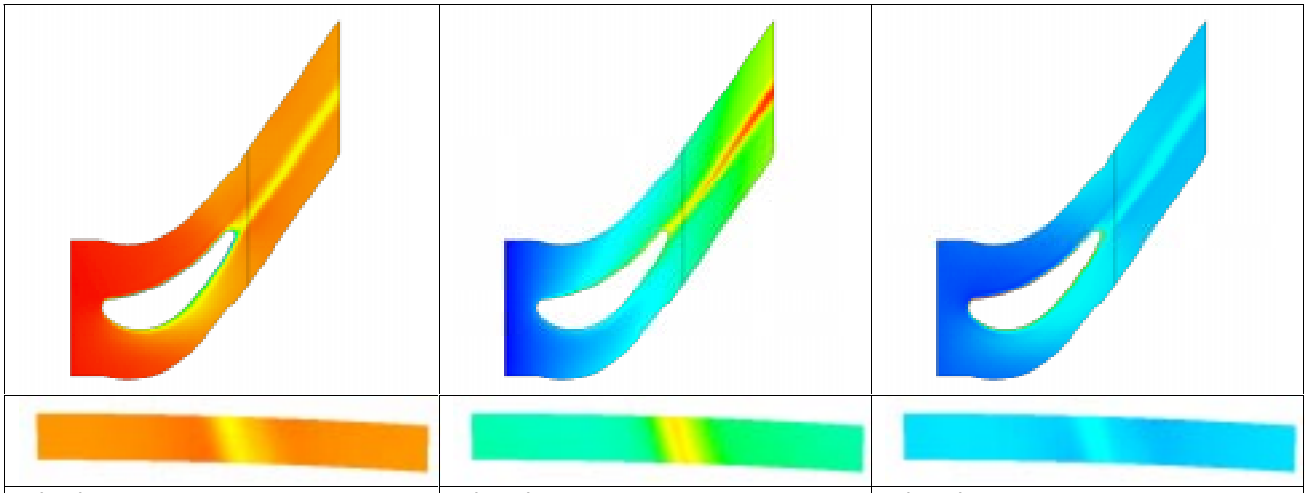		
Y(NO): 3.1212e-4 to 3.1496e-4 Mass Ave.: 3.1455e-4	Y(NO2): 5.7360e-6 to 6.3211e-6 Mass Ave.: 5.9863e-6	Y(NO3): 8.3265e-12 to 3.6301e-11 Mass Ave.: 1.4461e-11

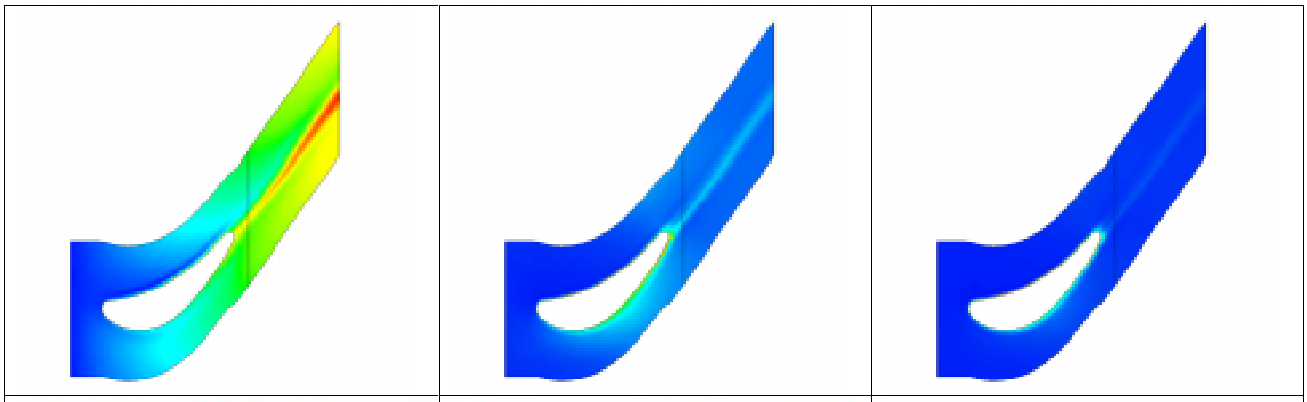

Y(HNO): 1.2877e-10 to 1.8293e-10
Mass Ave.: 1.5504e-10

Y(HONO): 8.1516e-8 to 4.0334e-6
Mass Ave.: 5.5106e-7

Y(HNO3):-3.1286e-10 to 6.1904e-8
Mass Ave.: 2.4605e-9

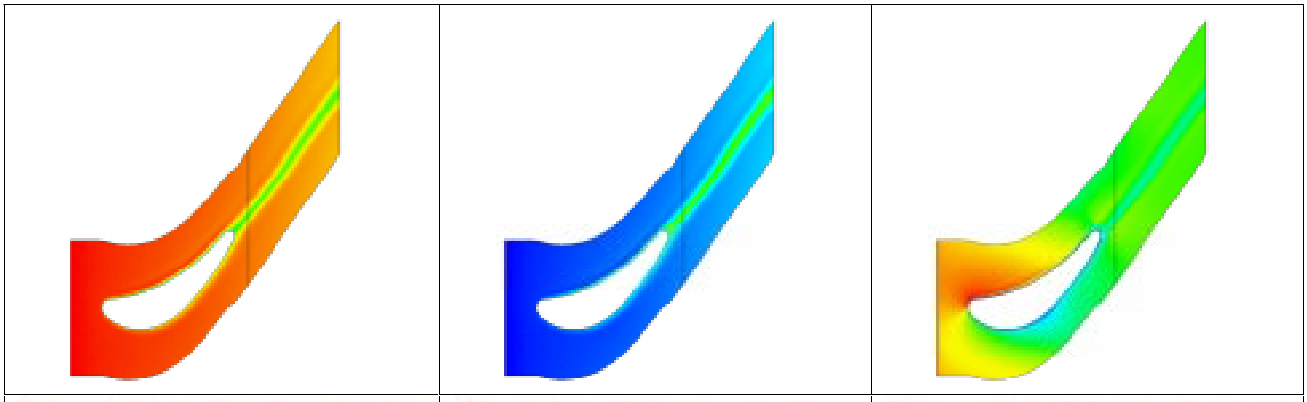

Y(SO2): 2.1808e-5 to 2.1844e-5
Mass Ave.: 2.1839e-5

Y(SO3): 1.7563e-6 to 1.7951e-6
Mass Ave.: 1.7628e-6

Y(HOSO): 2.1189e-14 to 1.6339e-13
Mass Ave.: 9.3304e-14

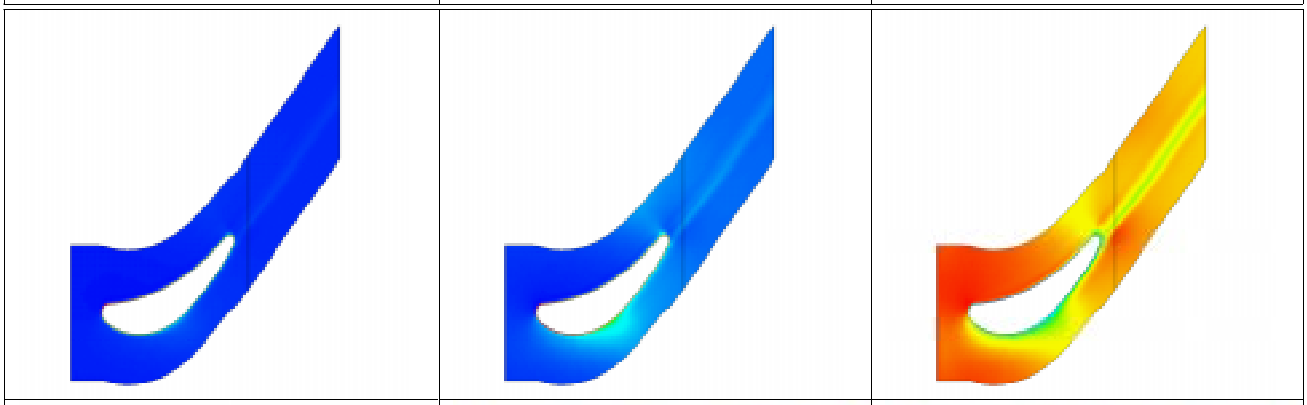

Y(HSO3): 5.8177e-12 to 1.5687e-10
Mass Ave.: 1.0740e-11

Y(HSO2): 1.3124e-16 to 7.0853e-16
Mass Ave.: 1.9591e-16

Y(SO): 8.1448e-14 to 3.6073e-13
Mass Ave.: 3.1185e-13

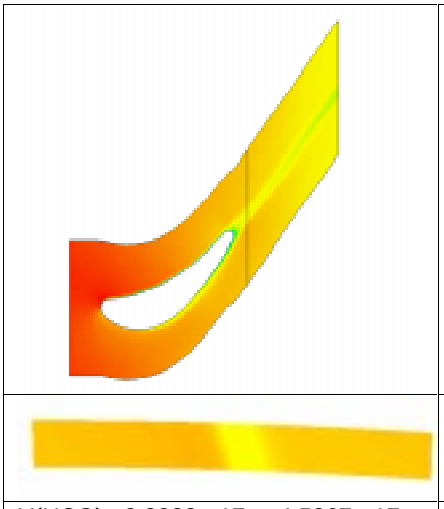	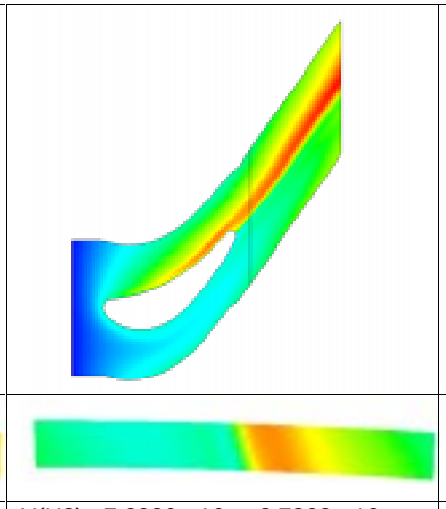	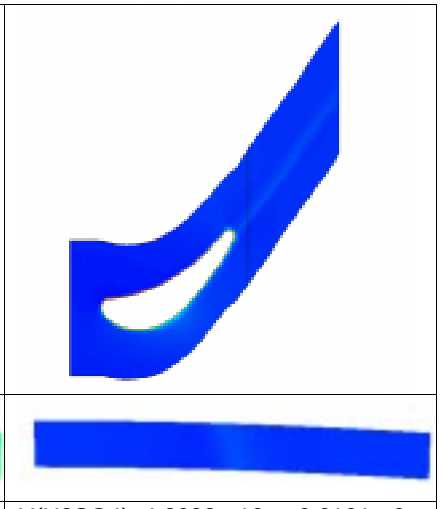
Y(HCO): 2.3288e-17 to 4.5267e-17 Mass Ave.: 4.0808e-17	Y(H2): 7.3820e-10 to 8.7823e-10 Mass Ave.: 8.1180e-10	Y(H2SO4): 4.2083e-10 to 9.0191e-9 Mass Ave.: 7.5702e-10

Rotor Wake Model Case – SO_3 Mass Fraction at selected times for one cycle
SO_3 mass fraction range 1.75E-6 to 1.78E-6

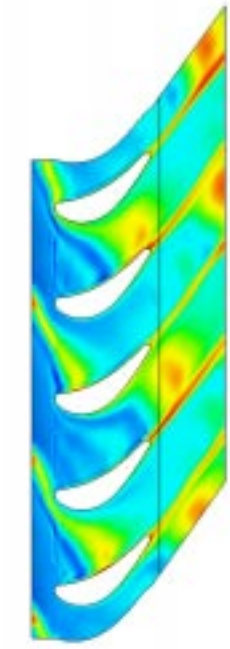	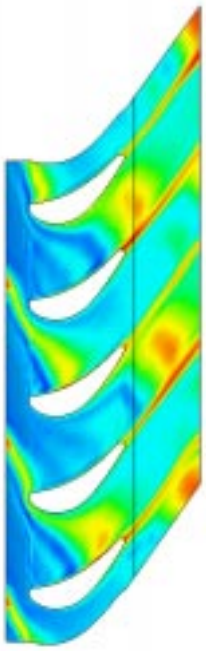	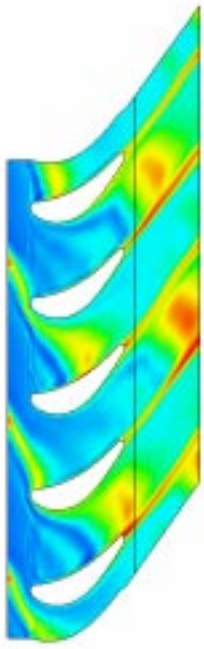	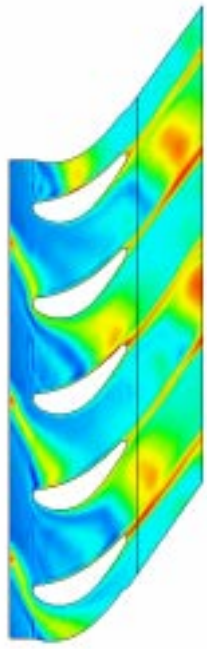
7325	7375	7425	7475

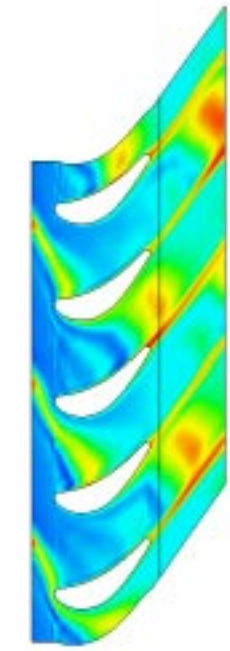	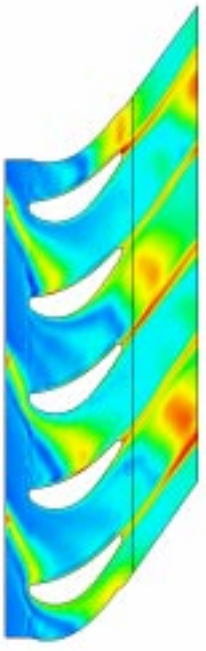	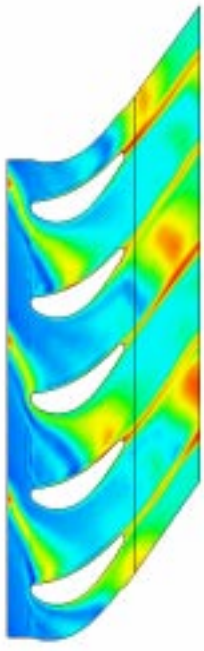	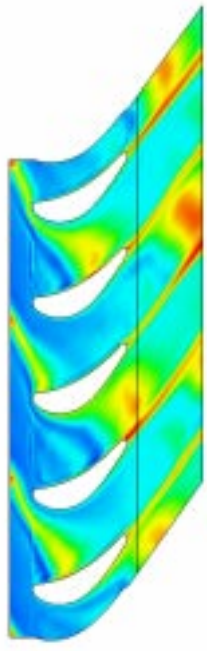
7525	7575	7625	7675

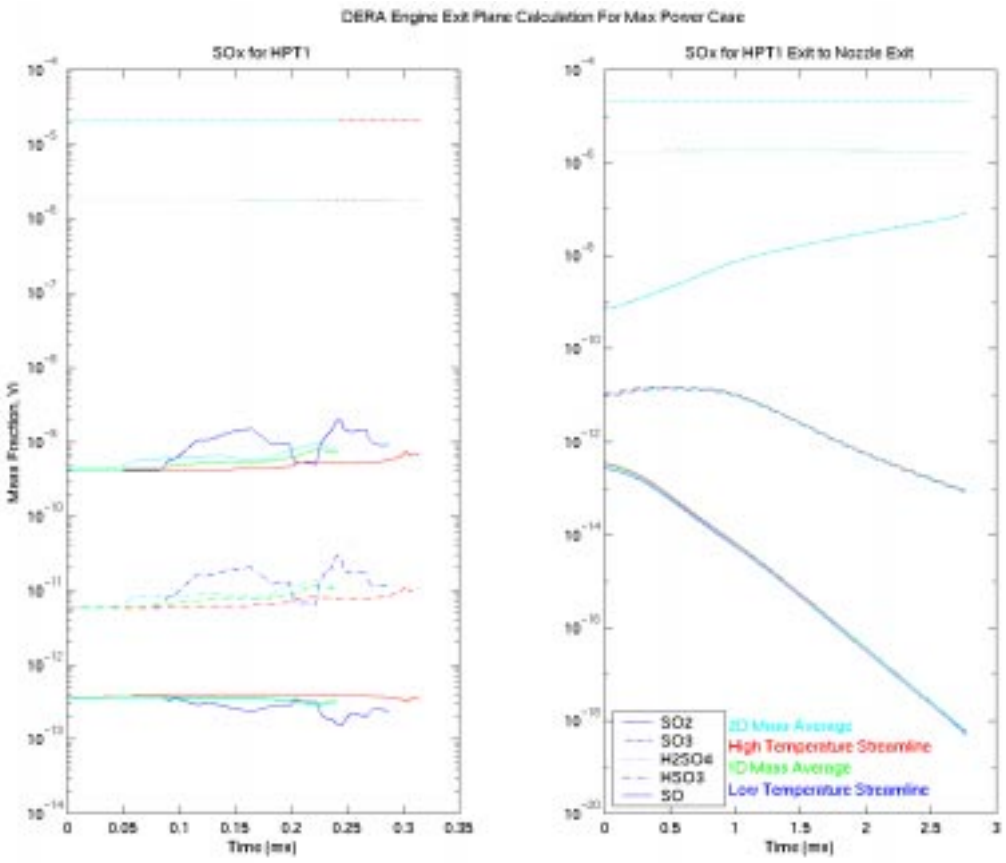

NOTE: The legend on the chart lists the species in the proper sequence for the lines (top to bottom), however, the line style is not correct (dashed, dotted, solid, etc is wrong).

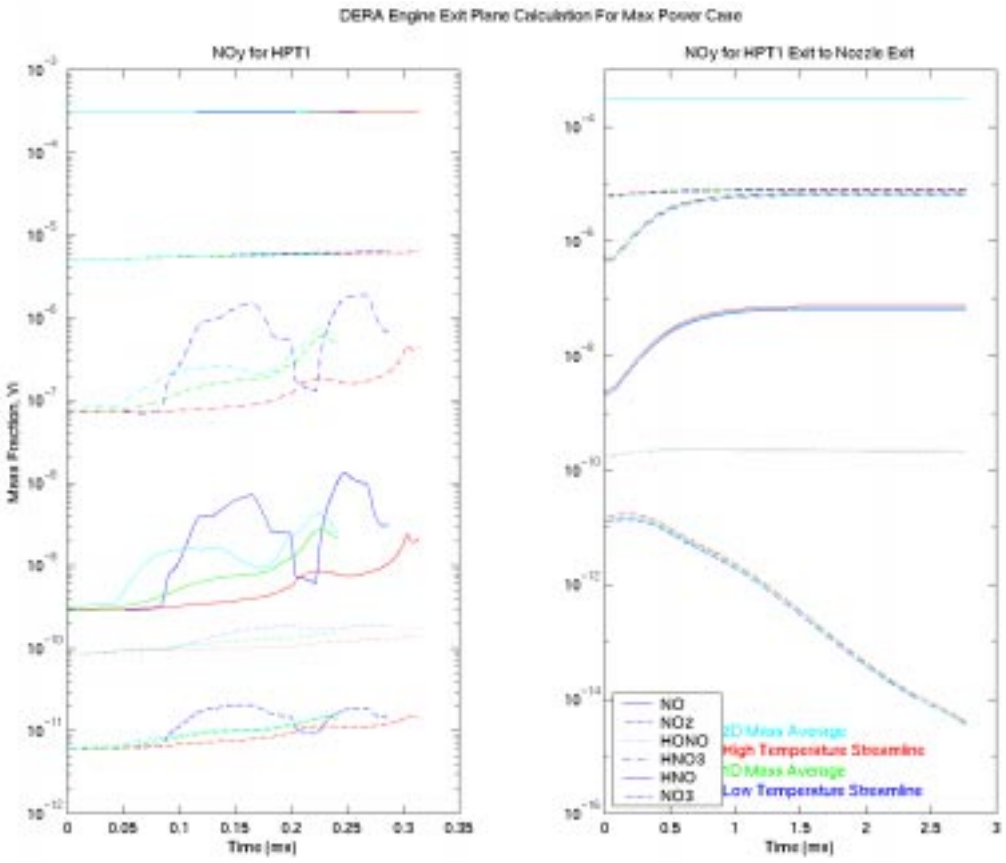

NOTE: The legend on the chart lists the species in the proper sequence for the lines (top to bottom), however, the line style is not correct (dashed, dotted, solid, etc is wrong).

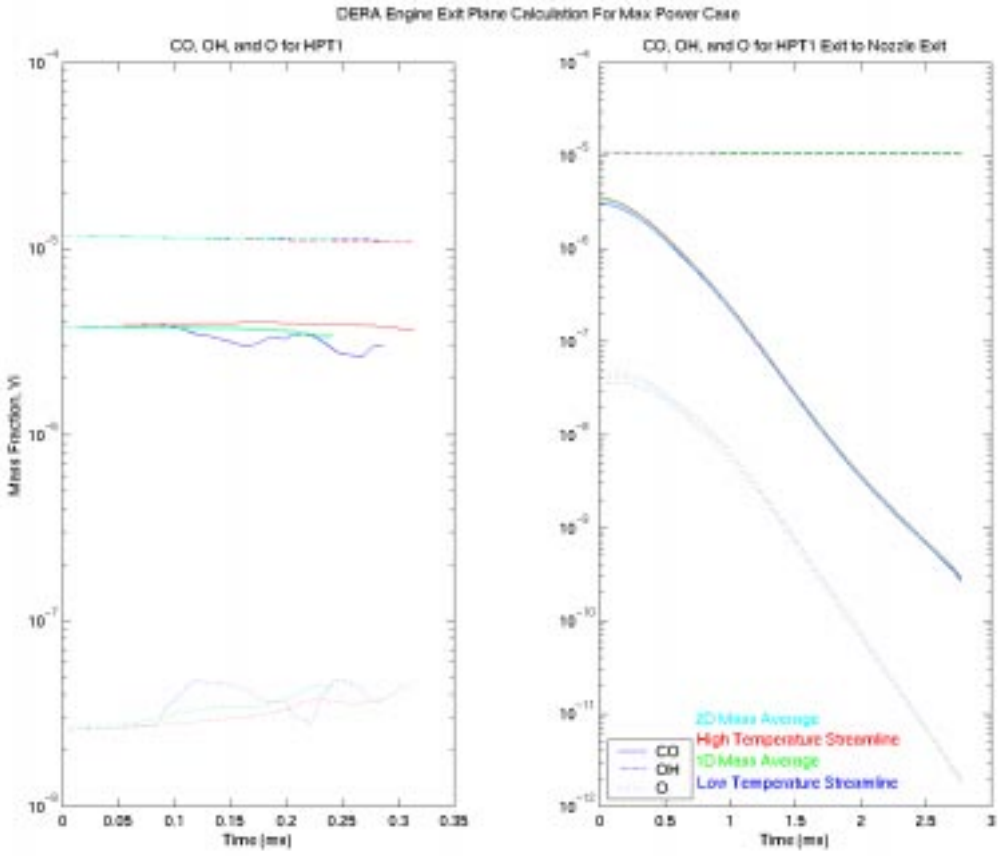

NOTE: The legend on the chart lists the species in the proper sequence for the lines (top to bottom), however, the line style is not correct (dashed, dotted, solid, etc is wrong).

APPENDIX E

CNEWT AND CALCHEM INPUT FILES FOR MAX POWER CONDITION

This appendix contains the CNEWT run files used for the high fidelity modeling and CALCHEM input files used for the low fidelity modeling of the NASA/DERA engine test max power condition.

There are three CNEWT run files listed in the following order:

- HPT1 NGV - Max power
- HPT1 rotor - Max power - Mixed-out
- HPT1 rotor - Max power - Unsteady wake model

Followed by four CALCHEM input files listed in the following order:

- HPT1 - Max power - Mass averaged
- HPT1 - Max power - High temperature streamline
- HPT1 - Max power - Low temperature streamline
- HPT1 exit to nozzle exit - Max power - Mass Averaged

HPT1 NGV - Max power:

```
CNEWT:mid-span of DERA HPT1 NGV:max power condition
 3550    0    2    1    1    0   <--- change KNORM=1 for stronger blade bc
   1.00000   0.00000   0.50000   0.00200   0.25000
1634150.  1365.20000  00.00000   0.00000 000.00000 1299940.8 1299940.8 998.99700
1138.     1.34      0.0000546 0000.0    0.031
    1    2    3    3   -4
    3    0    1   29   1   1          <--- MASKIN=0; code will not read lines after MIN
   25   80    3
   0.26924   0.27124
1634150.0 1634150.0 1634150.0
  1365.2    1365.2    1365.2
     0.        0.        0.
     0.        0.        0.
     0.        0.        0.
     1.        1.        1.
 1.1788260e-05 1.1788260e-05 1.1788260e-05
 7.2901490e-02 7.2901490e-02 7.2901490e-02
 1.4801360e-01 1.4801360e-01 1.4801360e-01
 2.9883310e-02 2.9883310e-02 2.9883310e-02
 7.8778370e-12 7.8778370e-12 7.8778370e-12
 2.6128790e-08 2.6128790e-08 2.6128790e-08
 3.7438540e-06 3.7438540e-06 3.7438540e-06
 5.4143820e-08 5.4143820e-08 5.4143820e-08
 6.6700590e-09 6.6700590e-09 6.6700590e-09
 3.1549390e-04 3.1549390e-04 3.1549390e-04
 4.9967900e-06 4.9967900e-06 4.9967900e-06
 6.0388730e-12 6.0388730e-12 6.0388730e-12
 7.8105610e-11 7.8105610e-11 7.8105610e-11
 7.8798570e-08 7.8798570e-08 7.8798570e-08
 3.0977400e-10 3.0977400e-10 3.0977400e-10
 2.1853460e-05 2.1853460e-05 2.1853460e-05
 1.7444370e-06 1.7444370e-06 1.7444370e-06
 2.2916830e-13 2.2916830e-13 2.2916830e-13
 5.9482370e-12 5.9482370e-12 5.9482370e-12
 1.2286700e-16 1.2286700e-16 1.2286700e-16
 3.6030010e-13 3.6030010e-13 3.6030010e-13
 5.5508550e-17 5.5508550e-17 5.5508550e-17
 1.1504340e-10 1.1504340e-10 1.1504340e-10
 7.4884180e-01 7.4884180e-01 7.4884180e-01
 0.0000000e+00 0.0000000e+00 0.0000000e+00
 0.0000000e+00 0.0000000e+00 0.0000000e+00
 0.0000000e+00 0.0000000e+00 0.0000000e+00
 4.3699380e-10 4.3699380e-10 4.3699380e-10
 2.4445370e-21 2.4445370e-21 2.4445370e-21
-0.028    0.343     0.        <--- boundary staionary wrto. blade
1.        1.        1.        1.        1.        0.999     0.995     0.992
0.99100   0.992     0.995     0.999     1.        1.        1.        1.
1.        1.        1.        1.        1.        0.999     0.995     0.992
0.99100   0.992     0.995     0.999     1.        1.        1.        1.
1.
5.        5.        4.        3.        2.        2.        2.        2.
2.        2.        2.        2.        3.        4.        5.        5.
5.        5.        4.        3.        2.        2.        2.        2.
2.        2.        2.        2.        3.        4.        5.        5.
```

HPT1 rotor - Max power – Mixed-out:

```
CNEWT:mid-span of DERA HPT1 rotor:max power condition,mixed-out
 4800    0    2    1    1    0   <--- change KNORM=1 for stronger blade bc
   1.00000   0.00000   0.50000   0.00200   0.25000
1627730.0 1363.33900 -60.84980   0.00000 361.16470  985627.1  985627.1 956.20700
1138.     1.34      0.0000546 -8863.8     0.019
    1    2    3    3   -4
    3    0    1   29   1   1          <--- MASKIN=0; code will not read lines after MIN
   25   80    3
   0.26924   0.27124
 1627730.0 1627730.0 1627730.0
  1363.339  1363.339  1363.339
   -60.850   -60.850   -60.850
     0.        0.        0.
   361.165   361.165   361.165
     1.        1.        1.
 1.1291178E-05 1.1291178E-05 1.1291178E-05
 7.2902240E-02 7.2902240E-02 7.2902240E-02
 0.1480131     0.1480131     0.1480131
 2.9883305E-02 2.9883305E-02 2.9883305E-02
 8.3788480E-12 8.3788480E-12 8.3788480E-12
 3.4125186E-08 3.4125186E-08 3.4125186E-08
 3.6788304E-06 3.6788304E-06 3.6788304E-06
 4.2947221E-08 4.2947221E-08 4.2947221E-08
 1.6948434E-08 1.6948434E-08 1.6948434E-08
 3.1493246E-04 3.1493246E-04 3.1493246E-04
 5.7360417E-06 5.7360417E-06 5.7360417E-06
 1.0588782E-11 1.0588782E-11 1.0588782E-11
 1.2943577E-10 1.2943577E-10 1.2943577E-10
 2.0222627E-07 2.0222627E-07 2.0222627E-07
 9.1435254E-10 9.1435254E-10 9.1435254E-10
 2.1843829E-05 2.1843829E-05 2.1843829E-05
 1.7563391E-06 1.7563391E-06 1.7563391E-06
 1.4487009E-13 1.4487009E-13 1.4487009E-13
 8.1400182E-12 8.1400182E-12 8.1400182E-12
 1.5103668E-16 1.5103668E-16 1.5103668E-16
 3.4998060E-13 3.4998060E-13 3.4998060E-13
 4.5071751E-17 4.5071751E-17 4.5071751E-17
 7.3819911E-10 7.3819911E-10 7.3819911E-10
 0.7488415     0.7488415     0.7488415
 0.0000000E+00 0.0000000E+00 0.0000000E+00
 0.0000000E+00 0.0000000E+00 0.0000000E+00
 0.0000000E+00 0.0000000E+00 0.0000000E+00
 5.7222255E-10 5.7222255E-10 5.7222255E-10
 2.4445346E-21 2.4445346E-21 2.4445346E-21
-0.028    0.343     0.        <--- boundary staionary wrto. blade
1.        1.        1.        1.        1.        0.999     0.995     0.992
0.99100   0.992     0.995     0.999     1.        1.        1.        1.
1.        1.        1.        1.        1.        0.999     0.995     0.992
0.99100   0.992     0.995     0.999     1.        1.        1.        1.
1.
5.        5.        4.        3.        2.        2.        2.        2.
2.        2.        2.        2.        3.        4.        5.        5.
5.        5.        4.        3.        2.        2.        2.        2.
2.        2.        2.        2.        3.        4.        5.        5.
```

HPT1 rotor - Max power - Unsteady wake model:

```
CNEWT:mid-span of DERA HPT1 rotor:max power condition,3 pitch inlet wake
10000    0    2    1    1    0   <--- change KNORM=1 for stronger blade bc
  -2.01000   0.00000   0.50000   0.00200   0.25000
1627730.0 1363.33900 -60.84980   0.00000 361.16470  985627.1  985627.1 956.20700
1138.     1.34      0.0000546 -8863.8   0.019
    1    2    3    3   -4
    0   70    1   29    1   1          <--- MASKIN=70, MIN=0
  121   75    3
-0.042507 0.269035  -8863.8
 1.6319600E+06 1.6334097E+06 1.6344153E+06 1.6348285E+06 1.6339272E+06 1.6326136E+06 1.6342565E+06 1.6400197E+06
 1.6458172E+06 1.6480668E+06 1.6445275E+06 1.6254299E+06 1.6019341E+06 1.5646283E+06 1.5530312E+06 1.5615181E+06
 1.5864542E+06 1.6136267E+06 1.6284102E+06 1.6339775E+06 1.6340041E+06 1.6323421E+06 1.6321173E+06 1.6319600E+06
 1.6334097E+06 1.6344153E+06 1.6348285E+06 1.6339272E+06 1.6326136E+06 1.6342565E+06 1.6400197E+06 1.6458172E+06
 1.6480668E+06 1.6445275E+06 1.6254299E+06 1.6019341E+06 1.5646283E+06 1.5530312E+06 1.5615181E+06 1.5864542E+06
 1.6136267E+06 1.6284102E+06 1.6339775E+06 1.6340041E+06 1.6323421E+06 1.6321173E+06 1.6319600E+06 1.6334097E+06
 1.6344153E+06 1.6348285E+06 1.6339272E+06 1.6326136E+06 1.6342565E+06 1.6400197E+06 1.6458172E+06 1.6480668E+06
 1.6445275E+06 1.6254299E+06 1.6019341E+06 1.5646283E+06 1.5530312E+06 1.5615181E+06 1.5864542E+06 1.6136267E+06
 1.6284102E+06 1.6339775E+06 1.6340041E+06 1.6323421E+06 1.6321173E+06 1.6319600E+06
 1.3733000E+03 1.3736851E+03 1.3734623E+03 1.3733692E+03 1.3744791E+03 1.3763530E+03 1.3763435E+03 1.3711324E+03
 1.3602751E+03 1.3468093E+03 1.3327657E+03 1.3123256E+03 1.2930020E+03 1.2666420E+03 1.2636717E+03 1.2829062E+03
 1.3204067E+03 1.3591487E+03 1.3768992E+03 1.3778210E+03 1.3751360E+03 1.3735196E+03 1.3731996E+03 1.3733000E+03
 1.3736851E+03 1.3734623E+03 1.3733692E+03 1.3744791E+03 1.3763530E+03 1.3763435E+03 1.3711324E+03 1.3602751E+03
 1.3468093E+03 1.3327657E+03 1.3123256E+03 1.2930020E+03 1.2666420E+03 1.2636717E+03 1.2829062E+03 1.3204067E+03
 1.3591487E+03 1.3768992E+03 1.3778210E+03 1.3751360E+03 1.3735196E+03 1.3731996E+03 1.3733000E+03 1.3736851E+03
 1.3734623E+03 1.3733692E+03 1.3744791E+03 1.3763530E+03 1.3763435E+03 1.3711324E+03 1.3602751E+03 1.3468093E+03
 1.3327657E+03 1.3123256E+03 1.2930020E+03 1.2666420E+03 1.2636717E+03 1.2829062E+03 1.3204067E+03 1.3591487E+03
 1.3768992E+03 1.3778210E+03 1.3751360E+03 1.3735196E+03 1.3731996E+03 1.3733000E+03
 1.1344700E-05 1.1317641E-05 1.1285575E-05 1.1255040E-05 1.1223797E-05 1.1194730E-05 1.1160670E-05 1.1141855E-05
 1.1116077E-05 1.1103603E-05 1.1099339E-05 1.1104153E-05 1.1146548E-05 1.1197313E-05 1.1260912E-05 1.1324297E-05
 1.1350943E-05 1.1357249E-05 1.1363410E-05 1.1372702E-05 1.1376438E-05 1.1374067E-05 1.1363370E-05 1.1344700E-05
 1.1317641E-05 1.1285575E-05 1.1255040E-05 1.1223797E-05 1.1194730E-05 1.1160670E-05 1.1141855E-05 1.1116077E-05
 1.1103603E-05 1.1099339E-05 1.1104153E-05 1.1146548E-05 1.1197313E-05 1.1260912E-05 1.1324297E-05 1.1350943E-05
 1.1357249E-05 1.1363410E-05 1.1372702E-05 1.1376438E-05 1.1374067E-05 1.1363370E-05 1.1344700E-05 1.1317641E-05
 1.1285575E-05 1.1255040E-05 1.1223797E-05 1.1194730E-05 1.1160670E-05 1.1141855E-05 1.1116077E-05 1.1103603E-05
 1.1099339E-05 1.1104153E-05 1.1146548E-05 1.1197313E-05 1.1260912E-05 1.1324297E-05 1.1350943E-05 1.1357249E-05
 1.1363410E-05 1.1372702E-05 1.1376438E-05 1.1374067E-05 1.1363370E-05 1.1344700E-05
 7.2902292E-02 7.2902292E-02 7.2902292E-02 7.2902292E-02 7.2902292E-02 7.2902292E-02 7.2902292E-02 7.2902292E-02
 7.2902292E-02 7.2902292E-02 7.2902292E-02 7.2902292E-02 7.2902292E-02 7.2902292E-02 7.2902292E-02 7.2902292E-02
 7.2902292E-02 7.2902292E-02 7.2902292E-02 7.2902292E-02 7.2902292E-02 7.2902292E-02 7.2902292E-02 7.2902292E-02
 7.2902292E-02 7.2902292E-02 7.2902292E-02 7.2902292E-02 7.2902292E-02 7.2902292E-02 7.2902292E-02 7.2902292E-02
 7.2902292E-02 7.2902292E-02 7.2902292E-02 7.2902292E-02 7.2902292E-02 7.2902292E-02 7.2902292E-02 7.2902292E-02
 7.2902292E-02 7.2902292E-02 7.2902292E-02 7.2902292E-02 7.2902292E-02 7.2902292E-02 7.2902292E-02 7.2902292E-02
 7.2902292E-02 7.2902292E-02 7.2902292E-02 7.2902292E-02 7.2902292E-02 7.2902292E-02 7.2902292E-02 7.2902292E-02
 7.2902292E-02 7.2902292E-02 7.2902292E-02 7.2902292E-02 7.2902292E-02 7.2902292E-02 7.2902292E-02 7.2902292E-02
 7.2902292E-02 7.2902292E-02 7.2902292E-02 7.2902292E-02 7.2902292E-02 7.2902292E-02
 1.4801300E-01 1.4801300E-01 1.4801300E-01 1.4801300E-01 1.4801300E-01 1.4801300E-01 1.4801300E-01 1.4801300E-01
 1.4801300E-01 1.4801300E-01 1.4801300E-01 1.4801300E-01 1.4801300E-01 1.4801300E-01 1.4801300E-01 1.4801300E-01
 1.4801300E-01 1.4801300E-01 1.4801300E-01 1.4801300E-01 1.4801300E-01 1.4801300E-01 1.4801300E-01 1.4801300E-01
 1.4801300E-01 1.4801300E-01 1.4801300E-01 1.4801300E-01 1.4801300E-01 1.4801300E-01 1.4801300E-01 1.4801300E-01
 1.4801300E-01 1.4801300E-01 1.4801300E-01 1.4801300E-01 1.4801300E-01 1.4801300E-01 1.4801300E-01 1.4801300E-01
 1.4801300E-01 1.4801300E-01 1.4801300E-01 1.4801300E-01 1.4801300E-01 1.4801300E-01 1.4801300E-01 1.4801300E-01
 1.4801300E-01 1.4801300E-01 1.4801300E-01 1.4801300E-01 1.4801300E-01 1.4801300E-01 1.4801300E-01 1.4801300E-01
 1.4801300E-01 1.4801300E-01 1.4801300E-01 1.4801300E-01 1.4801300E-01 1.4801300E-01 1.4801300E-01 1.4801300E-01
 1.4801300E-01 1.4801300E-01 1.4801300E-01 1.4801300E-01 1.4801300E-01 1.4801300E-01
 2.9883300E-02 2.9883300E-02 2.9883300E-02 2.9883300E-02 2.9883300E-02 2.9883300E-02 2.9883300E-02 2.9883300E-02
 2.9883300E-02 2.9883300E-02 2.9883300E-02 2.9883300E-02 2.9883300E-02 2.9883300E-02 2.9883300E-02 2.9883300E-02
 2.9883300E-02 2.9883300E-02 2.9883300E-02 2.9883300E-02 2.9883300E-02 2.9883300E-02 2.9883300E-02 2.9883300E-02
 2.9883300E-02 2.9883300E-02 2.9883300E-02 2.9883300E-02 2.9883300E-02 2.9883300E-02 2.9883300E-02 2.9883300E-02
 2.9883300E-02 2.9883300E-02 2.9883300E-02 2.9883300E-02 2.9883300E-02 2.9883300E-02 2.9883300E-02 2.9883300E-02
 2.9883300E-02 2.9883300E-02 2.9883300E-02 2.9883300E-02 2.9883300E-02 2.9883300E-02 2.9883300E-02 2.9883300E-02
 2.9883300E-02 2.9883300E-02 2.9883300E-02 2.9883300E-02 2.9883300E-02 2.9883300E-02 2.9883300E-02 2.9883300E-02
 2.9883300E-02 2.9883300E-02 2.9883300E-02 2.9883300E-02 2.9883300E-02 2.9883300E-02 2.9883300E-02 2.9883300E-02
 2.9883300E-02 2.9883300E-02 2.9883300E-02 2.9883300E-02 2.9883300E-02 2.9883300E-02
 8.4637200E-12 8.5439389E-12 8.5969422E-12 8.6354514E-12 8.6883739E-12 8.7451264E-12 8.7811106E-12 8.7561593E-12
 8.6063023E-12 8.4093940E-12 8.2426977E-12 7.9595924E-12 7.5705733E-12 7.3163417E-12 7.2633166E-12 7.5201166E-12
 7.8549552E-12 8.1559254E-12 8.2472808E-12 8.2364694E-12 8.2332469E-12 8.2851215E-12 8.3733926E-12 8.4637200E-12
 8.5439389E-12 8.5969422E-12 8.6354514E-12 8.6883739E-12 8.7451264E-12 8.7811106E-12 8.7561593E-12 8.6063023E-12
 8.4093940E-12 8.2426977E-12 7.9595924E-12 7.5705733E-12 7.3163417E-12 7.2633166E-12 7.5201166E-12 7.8549552E-12
 8.1559254E-12 8.2472808E-12 8.2364694E-12 8.2332469E-12 8.2851215E-12 8.3733926E-12 8.4637200E-12 8.5439389E-12
 8.5969422E-12 8.6354514E-12 8.6883739E-12 8.7451264E-12 8.7811106E-12 8.7561593E-12 8.6063023E-12 8.4093940E-12
 8.2426977E-12 7.9595924E-12 7.5705733E-12 7.3163417E-12 7.2633166E-12 7.5201166E-12 7.8549552E-12 8.1559254E-12
 8.2472808E-12 8.2364694E-12 8.2332469E-12 8.2851215E-12 8.3733926E-12 8.4637200E-12
 3.3813600E-08 3.4291738E-08 3.4642331E-08 3.4864049E-08 3.5017839E-08 3.5132846E-08 3.5351533E-08 3.5603954E-08
 3.6222523E-08 3.6740560E-08 3.7039767E-08 3.7281342E-08 3.7219986E-08 3.6967498E-08 3.6469722E-08 3.5309451E-08
 3.3929308E-08 3.2220627E-08 3.1432577E-08 3.1552902E-08 3.1978402E-08 3.2608269E-08 3.3260385E-08 3.3813600E-08
 3.4291738E-08 3.4642331E-08 3.4864049E-08 3.5017839E-08 3.5132846E-08 3.5351533E-08 3.5603954E-08 3.6222523E-08
```

3.6740560E-08 3.7039767E-08 3.7281342E-08 3.7219986E-08 3.6967498E-08 3.6469722E-08 3.5309451E-08 3.3929308E-08
3.2220627E-08 3.1432577E-08 3.1552902E-08 3.1978402E-08 3.2608269E-08 3.3260385E-08 3.3813600E-08 3.4291738E-08
3.4642331E-08 3.4864049E-08 3.5017839E-08 3.5132846E-08 3.5351533E-08 3.5603954E-08 3.6222523E-08 3.6740560E-08
3.7039767E-08 3.7281342E-08 3.7219986E-08 3.6967498E-08 3.6469722E-08 3.5309451E-08 3.3929308E-08 3.2220627E-08
3.1432577E-08 3.1552902E-08 3.1978402E-08 3.2608269E-08 3.3260385E-08 3.3813600E-08
3.6878900E-06 3.7080213E-06 3.7277736E-06 3.7479838E-06 3.7766963E-06 3.8073647E-06 3.8308082E-06 3.8246800E-06
3.7690451E-06 3.6930851E-06 3.6294911E-06 3.5229465E-06 3.3766549E-06 3.2804493E-06 3.2578806E-06 3.3545979E-06
3.4920339E-06 3.6311205E-06 3.6818206E-06 3.6812374E-06 3.6729106E-06 3.6689327E-06 3.6743286E-06 3.6878900E-06
3.7080213E-06 3.7277736E-06 3.7479838E-06 3.7766963E-06 3.8073647E-06 3.8308082E-06 3.8246800E-06 3.7690451E-06
3.6930851E-06 3.6294911E-06 3.5229465E-06 3.3766549E-06 3.2804493E-06 3.2578806E-06 3.3545979E-06 3.4920339E-06
3.6311205E-06 3.6818206E-06 3.6812374E-06 3.6729106E-06 3.6689327E-06 3.6743286E-06 3.6878900E-06 3.7080213E-06
3.7277736E-06 3.7479838E-06 3.7766963E-06 3.8073647E-06 3.8308082E-06 3.8246800E-06 3.7690451E-06 3.6930851E-06
3.6294911E-06 3.5229465E-06 3.3766549E-06 3.2804493E-06 3.2578806E-06 3.3545979E-06 3.4920339E-06 3.6311205E-06
3.6818206E-06 3.6812374E-06 3.6729106E-06 3.6689327E-06 3.6743286E-06 3.6878900E-06
4.2494400E-08 4.2789645E-08 4.3188823E-08 4.3644891E-08 4.4264530E-08 4.4912680E-08 4.5437244E-08 4.5387788E-08
4.4586922E-08 4.3546491E-08 4.2736072E-08 4.1526559E-08 3.9883513E-08 3.8735799E-08 3.8232551E-08 3.8949119E-08
4.0514640E-08 4.2704330E-08 4.3773599E-08 4.3552703E-08 4.3050069E-08 4.2603554E-08 4.2413847E-08 4.2494400E-08
4.2789645E-08 4.3188823E-08 4.3644891E-08 4.4264530E-08 4.4912680E-08 4.5437244E-08 4.5387788E-08 4.4586922E-08
4.3546491E-08 4.2736072E-08 4.1526559E-08 3.9883513E-08 3.8735799E-08 3.8232551E-08 3.8949119E-08 4.0514640E-08
4.2704330E-08 4.3773599E-08 4.3552703E-08 4.3050069E-08 4.2603554E-08 4.2413847E-08 4.2494400E-08 4.2789645E-08
4.3188823E-08 4.3644891E-08 4.4264530E-08 4.4912680E-08 4.5437244E-08 4.5387788E-08 4.4586922E-08 4.3546491E-08
4.2736072E-08 4.1526559E-08 3.9883513E-08 3.8735799E-08 3.8232551E-08 3.8949119E-08 4.0514640E-08 4.2704330E-08
4.3773599E-08 4.3552703E-08 4.3050069E-08 4.2603554E-08 4.2413847E-08 4.2494400E-08
1.4940000E-08 1.5278168E-08 1.5490873E-08 1.5513094E-08 1.5253305E-08 1.4886596E-08 1.4851887E-08 1.5485478E-08
1.8140504E-08 2.1484439E-08 2.4347309E-08 2.9846094E-08 3.7765007E-08 4.2632635E-08 4.2347613E-08 3.3549172E-08
2.3321989E-08 1.4368399E-08 1.1843122E-08 1.2080676E-08 1.2780012E-08 1.3653457E-08 1.4418485E-08 1.4940000E-08
1.5278168E-08 1.5490873E-08 1.5513094E-08 1.5253305E-08 1.4886596E-08 1.4851887E-08 1.5485478E-08 1.8140504E-08
2.1484439E-08 2.4347309E-08 2.9846094E-08 3.7765007E-08 4.2632635E-08 4.2347613E-08 3.3549172E-08 2.3321989E-08
1.4368399E-08 1.1843122E-08 1.2080676E-08 1.2780012E-08 1.3653457E-08 1.4418485E-08 1.4940000E-08 1.5278168E-08
1.5490873E-08 1.5513094E-08 1.5253305E-08 1.4886596E-08 1.4851887E-08 1.5485478E-08 1.8140504E-08 2.1484439E-08
2.4347309E-08 2.9846094E-08 3.7765007E-08 4.2632635E-08 4.2347613E-08 3.3549172E-08 2.3321989E-08 1.4368399E-08
1.1843122E-08 1.2080676E-08 1.2780012E-08 1.3653457E-08 1.4418485E-08 1.4940000E-08
3.1502400E-04 3.1499689E-04 3.1496590E-04 3.1493705E-04 3.1491441E-04 3.1489664E-04 3.1486729E-04 3.1483700E-04
3.1475565E-04 3.1467365E-04 3.1461182E-04 3.1451682E-04 3.1442564E-04 3.1439556E-04 3.1446591E-04 3.1467016E-04
3.1485724E-04 3.1500566E-04 3.1505820E-04 3.1506870E-04 3.1506562E-04 3.1505710E-04 3.1504266E-04 3.1502400E-04
3.1499689E-04 3.1496590E-04 3.1493705E-04 3.1491441E-04 3.1489664E-04 3.1486729E-04 3.1483700E-04 3.1475565E-04
3.1467365E-04 3.1461182E-04 3.1451682E-04 3.1442564E-04 3.1439556E-04 3.1446591E-04 3.1467016E-04 3.1485724E-04
3.1500566E-04 3.1505820E-04 3.1506870E-04 3.1506562E-04 3.1505710E-04 3.1504266E-04 3.1502400E-04 3.1499689E-04
3.1496590E-04 3.1493705E-04 3.1491441E-04 3.1489664E-04 3.1486729E-04 3.1483700E-04 3.1475565E-04 3.1467365E-04
3.1461182E-04 3.1451682E-04 3.1442564E-04 3.1439556E-04 3.1446591E-04 3.1467016E-04 3.1485724E-04 3.1500566E-04
3.1505820E-04 3.1506870E-04 3.1506562E-04 3.1505710E-04 3.1504266E-04 3.1502400E-04
5.6239200E-06 5.6602822E-06 5.7030755E-06 5.7473146E-06 5.7861705E-06 5.8216338E-06 5.8648701E-06 5.9257070E-06
5.9992466E-06 6.0721584E-06 6.1363353E-06 6.2009919E-06 6.2247980E-06 6.2046267E-06 6.0865673E-06 5.9306476E-06
5.7684544E-06 5.6547121E-06 5.6017010E-06 5.5844275E-06 5.5824495E-06 5.5869516E-06 5.5995508E-06 5.6239200E-06
5.6602822E-06 5.7030755E-06 5.7473146E-06 5.7861705E-06 5.8216338E-06 5.8648701E-06 5.9257070E-06 5.9992466E-06
6.0721584E-06 6.1363353E-06 6.2009919E-06 6.2247980E-06 6.2046267E-06 6.0865673E-06 5.9306476E-06 5.7684544E-06
5.6547121E-06 5.6017010E-06 5.5844275E-06 5.5824495E-06 5.5869516E-06 5.5995508E-06 5.6239200E-06 5.6602822E-06
5.7030755E-06 5.7473146E-06 5.7861705E-06 5.8216338E-06 5.8648701E-06 5.9257070E-06 5.9992466E-06 6.0721584E-06
6.1363353E-06 6.2009919E-06 6.2247980E-06 6.2046267E-06 6.0865673E-06 5.9306476E-06 5.7684544E-06 5.6547121E-06
5.6017010E-06 5.5844275E-06 5.5824495E-06 5.5869516E-06 5.5995508E-06 5.6239200E-06
9.9303600E-12 1.0133041E-11 1.0315558E-11 1.0459090E-11 1.0512444E-11 1.0515709E-11 1.0654593E-11 1.1131837E-11
1.1930260E-11 1.2833108E-11 1.3693774E-11 1.4720614E-11 1.5492479E-11 1.6275552E-11 1.5740753E-11 1.4153022E-11
1.1850625E-11 9.8119282E-12 8.9716894E-12 8.9745790E-12 9.2030030E-12 9.4603498E-12 9.7055531E-12 9.9303600E-12
1.0133041E-11 1.0315558E-11 1.0459090E-11 1.0512444E-11 1.0515709E-11 1.0654593E-11 1.1131837E-11 1.1930260E-11
1.2833108E-11 1.3693774E-11 1.4720614E-11 1.5492479E-11 1.6275552E-11 1.5740753E-11 1.4153022E-11 1.1850625E-11
9.8119282E-12 8.9716894E-12 8.9745790E-12 9.2030030E-12 9.4603498E-12 9.7055531E-12 9.9303600E-12 1.0133041E-11
1.0315558E-11 1.0459090E-11 1.0512444E-11 1.0515709E-11 1.0654593E-11 1.1131837E-11 1.1930260E-11 1.2833108E-11
1.3693774E-11 1.4720614E-11 1.5492479E-11 1.6275552E-11 1.5740753E-11 1.4153022E-11 1.1850625E-11 9.8119282E-12
8.9716894E-12 8.9745790E-12 9.2030030E-12 9.4603498E-12 9.7055531E-12 9.9303600E-12
1.2691400E-10 1.2515727E-10 1.2381082E-10 1.2254941E-10 1.2080821E-10 1.1883032E-10 1.1807289E-10 1.2019209E-10
1.2517224E-10 1.3132024E-10 1.3749699E-10 1.4588913E-10 1.5407723E-10 1.6582781E-10 1.6942488E-10 1.6411289E-10
1.5083575E-10 1.3571490E-10 1.2835028E-10 1.2782938E-10 1.2876088E-10 1.2905563E-10 1.2839354E-10 1.2691400E-10
1.2515727E-10 1.2381082E-10 1.2254941E-10 1.2080821E-10 1.1883032E-10 1.1807289E-10 1.2019209E-10 1.2517224E-10
1.3132024E-10 1.3749699E-10 1.4588913E-10 1.5407723E-10 1.6582781E-10 1.6942488E-10 1.6411289E-10 1.5083575E-10
1.3571490E-10 1.2835028E-10 1.2782938E-10 1.2876088E-10 1.2905563E-10 1.2839354E-10 1.2691400E-10 1.2515727E-10
1.2381082E-10 1.2254941E-10 1.2080821E-10 1.1883032E-10 1.1807289E-10 1.2019209E-10 1.2517224E-10 1.3132024E-10
1.3749699E-10 1.4588913E-10 1.5407723E-10 1.6582781E-10 1.6942488E-10 1.6411289E-10 1.5083575E-10 1.3571490E-10
1.2835028E-10 1.2782938E-10 1.2876088E-10 1.2905563E-10 1.2839354E-10 1.2691400E-10
1.7317200E-07 1.7721829E-07 1.7970502E-07 1.8004258E-07 1.7648628E-07 1.7095664E-07 1.7075896E-07 1.8447604E-07
2.1490865E-07 2.5504971E-07 2.9995857E-07 3.7428040E-07 4.5420162E-07 5.7189776E-07 5.6724403E-07 4.5590030E-07
2.9083002E-07 1.7581928E-07 1.4185696E-07 1.4128161E-07 1.4811355E-07 1.5722138E-07 1.6620917E-07 1.7317200E-07
1.7721829E-07 1.7970502E-07 1.8004258E-07 1.7648628E-07 1.7095664E-07 1.7075896E-07 1.8447604E-07 2.1490865E-07
2.5504971E-07 2.9995857E-07 3.7428040E-07 4.5420162E-07 5.7189776E-07 5.6724403E-07 4.5590030E-07 2.9083002E-07
1.7581928E-07 1.4185696E-07 1.4128161E-07 1.4811355E-07 1.5722138E-07 1.6620917E-07 1.7317200E-07 1.7721829E-07
1.7970502E-07 1.8004258E-07 1.7648628E-07 1.7095664E-07 1.7075896E-07 1.8447604E-07 2.1490865E-07 2.5504971E-07
2.9995857E-07 3.7428040E-07 4.5420162E-07 5.7189776E-07 5.6724403E-07 4.5590030E-07 2.9083002E-07 1.7581928E-07
1.4185696E-07 1.4128161E-07 1.4811355E-07 1.5722138E-07 1.6620917E-07 1.7317200E-07
7.5791800E-10 7.8111140E-10 7.9861544E-10 8.0693481E-10 7.9701261E-10 7.7744679E-10 7.8280420E-10 8.5455809E-10
1.0077276E-09 1.2096770E-09 1.4373165E-09 1.8106757E-09 2.2032795E-09 2.7677292E-09 2.6948357E-09 2.1152827E-09
1.3072919E-09 7.7766358E-10 6.2276265E-10 6.1713629E-10 6.4497725E-10 6.8376726E-10 7.2404147E-10 7.5791800E-10
7.8111140E-10 7.9861544E-10 8.0693481E-10 7.9701261E-10 7.7744679E-10 7.8280420E-10 8.5455809E-10 1.0077276E-09
1.2096770E-09 1.4373165E-09 1.8106757E-09 2.2032795E-09 2.7677292E-09 2.6948357E-09 2.1152827E-09 1.3072919E-09
7.7766358E-10 6.2276265E-10 6.1713629E-10 6.4497725E-10 6.8376726E-10 7.2404147E-10 7.5791800E-10 7.8111140E-10
7.9861544E-10 8.0693481E-10 7.9701261E-10 7.7744679E-10 7.8280420E-10 8.5455809E-10 1.0077276E-09 1.2096770E-09

1.4373165E-09 1.8106757E-09 2.2032795E-09 2.7677292E-09 2.6948357E-09 2.1152827E-09 1.3072919E-09 7.7766358E-10
6.2276265E-10 6.1713629E-10 6.4497725E-10 6.8376726E-10 7.2404147E-10 7.5791800E-10
2.1846200E-05 2.1846130E-05 2.1845767E-05 2.1845456E-05 2.1845528E-05 2.1845912E-05 2.1845708E-05 2.1843922E-05
2.1840660E-05 2.1836863E-05 2.1833167E-05 2.1828942E-05 2.1826232E-05 2.1824303E-05 2.1827146E-05 2.1832525E-05
2.1839086E-05 2.1844319E-05 2.1846388E-05 2.1846740E-05 2.1846521E-05 2.1846337E-05 2.1846300E-05 2.1846200E-05
2.1846130E-05 2.1845767E-05 2.1845456E-05 2.1845528E-05 2.1845912E-05 2.1845708E-05 2.1843922E-05 2.1840660E-05
2.1836863E-05 2.1833167E-05 2.1828942E-05 2.1826232E-05 2.1824303E-05 2.1827146E-05 2.1832525E-05 2.1839086E-05
2.1844319E-05 2.1846388E-05 2.1846740E-05 2.1846521E-05 2.1846337E-05 2.1846300E-05 2.1846200E-05 2.1846130E-05
2.1845767E-05 2.1845456E-05 2.1845528E-05 2.1845912E-05 2.1845708E-05 2.1843922E-05 2.1840660E-05 2.1836863E-05
2.1833167E-05 2.1828942E-05 2.1826232E-05 2.1824303E-05 2.1827146E-05 2.1832525E-05 2.1839086E-05 2.1844319E-05
2.1846388E-05 2.1846740E-05 2.1846521E-05 2.1846337E-05 2.1846300E-05 2.1846200E-05
1.7533500E-06 1.7535321E-06 1.7539587E-06 1.7543418E-06 1.7542017E-06 1.7537326E-06 1.7540143E-06 1.7562079E-06
1.7602275E-06 1.7649223E-06 1.7695277E-06 1.7747588E-06 1.7780490E-06 1.7803816E-06 1.7768499E-06 1.7702612E-06
1.7621491E-06 1.7558544E-06 1.7532033E-06 1.7528148E-06 1.7530174E-06 1.7532016E-06 1.7532878E-06 1.7533500E-06
1.7535321E-06 1.7539587E-06 1.7543418E-06 1.7542017E-06 1.7537326E-06 1.7540143E-06 1.7562079E-06 1.7602275E-06
1.7649223E-06 1.7695277E-06 1.7747588E-06 1.7780490E-06 1.7803816E-06 1.7768499E-06 1.7702612E-06 1.7621491E-06
1.7558544E-06 1.7532033E-06 1.7528148E-06 1.7530174E-06 1.7532016E-06 1.7532878E-06 1.7533500E-06 1.7535321E-06
1.7539587E-06 1.7543418E-06 1.7542017E-06 1.7537326E-06 1.7540143E-06 1.7562079E-06 1.7602275E-06 1.7649223E-06
1.7695277E-06 1.7747588E-06 1.7780490E-06 1.7803816E-06 1.7768499E-06 1.7702612E-06 1.7621491E-06 1.7558544E-06
1.7532033E-06 1.7528148E-06 1.7530174E-06 1.7532016E-06 1.7532878E-06 1.7533500E-06
1.4539800E-13 1.4567049E-13 1.4655058E-13 1.4819564E-13 1.5120238E-13 1.5499828E-13 1.5679555E-13 1.5366882E-13
1.4625191E-13 1.3752474E-13 1.2939141E-13 1.1973194E-13 1.1136875E-13 1.0056010E-13 9.9187928E-14 1.0731573E-13
1.2473472E-13 1.4545968E-13 1.5651731E-13 1.5637891E-13 1.5301333E-13 1.4938816E-13 1.4664500E-13 1.4539800E-13
1.4567049E-13 1.4655058E-13 1.4819564E-13 1.5120238E-13 1.5499828E-13 1.5679555E-13 1.5366882E-13 1.4625191E-13
1.3752474E-13 1.2939141E-13 1.1973194E-13 1.1136875E-13 1.0056010E-13 9.9187928E-14 1.0731573E-13 1.2473472E-13
1.4545968E-13 1.5651731E-13 1.5637891E-13 1.5301333E-13 1.4938816E-13 1.4664500E-13 1.4539800E-13 1.4567049E-13
1.4655058E-13 1.4819564E-13 1.5120238E-13 1.5499828E-13 1.5679555E-13 1.5366882E-13 1.4625191E-13 1.3752474E-13
1.2939141E-13 1.1973194E-13 1.1136875E-13 1.0056010E-13 9.9187928E-14 1.0731573E-13 1.2473472E-13 1.4545968E-13
1.5651731E-13 1.5637891E-13 1.5301333E-13 1.4938816E-13 1.4664500E-13 1.4539800E-13
7.6656300E-12 7.7597340E-12 7.8350000E-12 7.8765823E-12 7.8478174E-12 7.7807566E-12 7.8141748E-12 8.1030285E-12
8.6580485E-12 9.3292611E-12 1.0014639E-11 1.0954885E-11 1.1845243E-11 1.3052217E-11 1.2967442E-11 1.1661577E-11
9.5758438E-12 7.8104252E-12 7.1351748E-12 7.1126737E-12 7.2343980E-12 7.3829861E-12 7.5347583E-12 7.6656300E-12
7.7597340E-12 7.8350000E-12 7.8765823E-12 7.8478174E-12 7.7807566E-12 7.8141748E-12 8.1030285E-12 8.6580485E-12
9.3292611E-12 1.0014639E-11 1.0954885E-11 1.1845243E-11 1.3052217E-11 1.2967442E-11 1.1661577E-11 9.5758438E-12
7.8104252E-12 7.1351748E-12 7.1126737E-12 7.2343980E-12 7.3829861E-12 7.5347583E-12 7.6656300E-12 7.7597340E-12
7.8350000E-12 7.8765823E-12 7.8478174E-12 7.7807566E-12 7.8141748E-12 8.1030285E-12 8.6580485E-12 9.3292611E-12
1.0014639E-11 1.0954885E-11 1.1845243E-11 1.3052217E-11 1.2967442E-11 1.1661577E-11 9.5758438E-12 7.8104252E-12
7.1351748E-12 7.1126737E-12 7.2343980E-12 7.3829861E-12 7.5347583E-12 7.6656300E-12
1.4670400E-16 1.4845194E-16 1.4969004E-16 1.5039305E-16 1.5028102E-16 1.4973209E-16 1.5026519E-16 1.5352456E-16
1.5937435E-16 1.6607707E-16 1.7246348E-16 1.8030028E-16 1.8701680E-16 1.9535543E-16 1.9407493E-16 1.8293547E-16
1.6404270E-16 1.4563494E-16 1.3777645E-16 1.3753474E-16 1.3925336E-16 1.4166861E-16 1.4431868E-16 1.4670400E-16
1.4845194E-16 1.4969004E-16 1.5039305E-16 1.5028102E-16 1.4973209E-16 1.5026519E-16 1.5352456E-16 1.5937435E-16
1.6607707E-16 1.7246348E-16 1.8030028E-16 1.8701680E-16 1.9535543E-16 1.9407493E-16 1.8293547E-16 1.6404270E-16
1.4563494E-16 1.3777645E-16 1.3753474E-16 1.3925336E-16 1.4166861E-16 1.4431868E-16 1.4670400E-16 1.4845194E-16
1.4969004E-16 1.5039305E-16 1.5028102E-16 1.4973209E-16 1.5026519E-16 1.5352456E-16 1.5937435E-16 1.6607707E-16
1.7246348E-16 1.8030028E-16 1.8701680E-16 1.9535543E-16 1.9407493E-16 1.8293547E-16 1.6404270E-16 1.4563494E-16
1.3777645E-16 1.3753474E-16 1.3925336E-16 1.4166861E-16 1.4431868E-16 1.4670400E-16
3.5487000E-13 3.5725470E-13 3.5927767E-13 3.6174416E-13 3.6590718E-13 3.7111213E-13 3.7383858E-13 3.7008274E-13
3.5972269E-13 3.4649588E-13 3.3296046E-13 3.1469997E-13 2.9769566E-13 2.7454122E-13 2.7069758E-13 2.8425650E-13
3.1119822E-13 3.3777830E-13 3.4978063E-13 3.5237724E-13 3.5304730E-13 3.5315192E-13 3.5351372E-13 3.5487000E-13
3.5725470E-13 3.5927767E-13 3.6174416E-13 3.6590718E-13 3.7111213E-13 3.7383858E-13 3.7008274E-13 3.5972269E-13
3.4649588E-13 3.3296046E-13 3.1469997E-13 2.9769566E-13 2.7454122E-13 2.7069758E-13 2.8425650E-13 3.1119822E-13
3.3777830E-13 3.4978063E-13 3.5237724E-13 3.5304730E-13 3.5315192E-13 3.5351372E-13 3.5487000E-13 3.5725470E-13
3.5927767E-13 3.6174416E-13 3.6590718E-13 3.7111213E-13 3.7383858E-13 3.7008274E-13 3.5972269E-13 3.4649588E-13
3.3296046E-13 3.1469997E-13 2.9769566E-13 2.7454122E-13 2.7069758E-13 2.8425650E-13 3.1119822E-13 3.3777830E-13
3.4978063E-13 3.5237724E-13 3.5304730E-13 3.5315192E-13 3.5351372E-13 3.5487000E-13
4.5065100E-17 4.5188662E-17 4.5312424E-17 4.5466088E-17 4.5705899E-17 4.5998424E-17 4.6160301E-17 4.6004914E-17
4.5572423E-17 4.5035212E-17 4.4497491E-17 4.3760097E-17 4.3075285E-17 4.2159348E-17 4.2146912E-17 4.2769709E-17
4.3778982E-17 4.4688397E-17 4.5262162E-17 4.5372587E-17 4.5281166E-17 4.5131644E-17 4.5041686E-17 4.5065100E-17
4.5188662E-17 4.5312424E-17 4.5466088E-17 4.5705899E-17 4.5998424E-17 4.6160301E-17 4.6004914E-17 4.5572423E-17
4.5035212E-17 4.4497491E-17 4.3760097E-17 4.3075285E-17 4.2159348E-17 4.2146912E-17 4.2769709E-17 4.3778982E-17
4.4688397E-17 4.5262162E-17 4.5372587E-17 4.5281166E-17 4.5131644E-17 4.5041686E-17 4.5065100E-17 4.5188662E-17
4.5312424E-17 4.5466088E-17 4.5705899E-17 4.5998424E-17 4.6160301E-17 4.6004914E-17 4.5572423E-17 4.5035212E-17
4.4497491E-17 4.3760097E-17 4.3075285E-17 4.2159348E-17 4.2146912E-17 4.2769709E-17 4.3778982E-17 4.4688397E-17
4.5262162E-17 4.5372587E-17 4.5281166E-17 4.5131644E-17 4.5041686E-17 4.5065100E-17
6.8239300E-10 7.2047271E-10 7.5922901E-10 7.9880871E-10 8.4029218E-10 8.8244201E-10 9.1852370E-10 9.3977602E-10
9.4358217E-10 9.3642017E-10 9.2326712E-10 8.9538815E-10 8.5087584E-10 7.6236343E-10 6.7960463E-10 6.3015099E-10
6.2161061E-10 6.4334177E-10 6.5119063E-10 6.4223399E-10 6.3592993E-10 6.3882588E-10 6.5383493E-10 6.8239300E-10
7.2047271E-10 7.5922901E-10 7.9880871E-10 8.4029218E-10 8.8244201E-10 9.1852370E-10 9.3977602E-10 9.4358217E-10
9.3642017E-10 9.2326712E-10 8.9538815E-10 8.5087584E-10 7.6236343E-10 6.7960463E-10 6.3015099E-10 6.2161061E-10
6.4334177E-10 6.5119063E-10 6.4223399E-10 6.3592993E-10 6.3882588E-10 6.5383493E-10 6.8239300E-10 7.2047271E-10
7.5922901E-10 7.9880871E-10 8.4029218E-10 8.8244201E-10 9.1852370E-10 9.3977602E-10 9.4358217E-10 9.3642017E-10
9.2326712E-10 8.9538815E-10 8.5087584E-10 7.6236343E-10 6.7960463E-10 6.3015099E-10 6.2161061E-10 6.4334177E-10
6.5119063E-10 6.4223399E-10 6.3592993E-10 6.3882588E-10 6.5383493E-10 6.8239300E-10
7.4884200E-01 7.4884200E-01 7.4884200E-01 7.4884200E-01 7.4884200E-01 7.4884200E-01 7.4884200E-01 7.4884200E-01
7.4884200E-01 7.4884200E-01 7.4884200E-01 7.4884200E-01 7.4884200E-01 7.4884200E-01 7.4884200E-01 7.4884200E-01
7.4884200E-01 7.4884200E-01 7.4884200E-01 7.4884200E-01 7.4884200E-01 7.4884200E-01 7.4884200E-01 7.4884200E-01
7.4884200E-01 7.4884200E-01 7.4884200E-01 7.4884200E-01 7.4884200E-01 7.4884200E-01 7.4884200E-01 7.4884200E-01
7.4884200E-01 7.4884200E-01 7.4884200E-01 7.4884200E-01 7.4884200E-01 7.4884200E-01 7.4884200E-01 7.4884200E-01
7.4884200E-01 7.4884200E-01 7.4884200E-01 7.4884200E-01 7.4884200E-01 7.4884200E-01 7.4884200E-01 7.4884200E-01
7.4884200E-01 7.4884200E-01 7.4884200E-01 7.4884200E-01 7.4884200E-01 7.4884200E-01 7.4884200E-01 7.4884200E-01
7.4884200E-01 7.4884200E-01 7.4884200E-01 7.4884200E-01 7.4884200E-01 7.4884200E-01
0.0000000E+00 0.0000000E+00 0.0000000E+00 0.0000000E+00 0.0000000E+00 0.0000000E+00 0.0000000E+00 0.0000000E+00

```
0.0000000E+00 0.0000000E+00 0.0000000E+00 0.0000000E+00 0.0000000E+00 0.0000000E+00 0.0000000E+00 0.0000000E+00
0.0000000E+00 0.0000000E+00 0.0000000E+00 0.0000000E+00 0.0000000E+00 0.0000000E+00 0.0000000E+00 0.0000000E+00
0.0000000E+00 0.0000000E+00 0.0000000E+00 0.0000000E+00 0.0000000E+00 0.0000000E+00 0.0000000E+00 0.0000000E+00
0.0000000E+00 0.0000000E+00 0.0000000E+00 0.0000000E+00 0.0000000E+00 0.0000000E+00 0.0000000E+00 0.0000000E+00
0.0000000E+00 0.0000000E+00 0.0000000E+00 0.0000000E+00 0.0000000E+00 0.0000000E+00 0.0000000E+00 0.0000000E+00
0.0000000E+00 0.0000000E+00 0.0000000E+00 0.0000000E+00 0.0000000E+00 0.0000000E+00 0.0000000E+00 0.0000000E+00
0.0000000E+00 0.0000000E+00 0.0000000E+00 0.0000000E+00 0.0000000E+00 0.0000000E+00 0.0000000E+00 0.0000000E+00
0.0000000E+00 0.0000000E+00 0.0000000E+00 0.0000000E+00 0.0000000E+00 0.0000000E+00
0.0000000E+00 0.0000000E+00 0.0000000E+00 0.0000000E+00 0.0000000E+00 0.0000000E+00 0.0000000E+00 0.0000000E+00
0.0000000E+00 0.0000000E+00 0.0000000E+00 0.0000000E+00 0.0000000E+00 0.0000000E+00 0.0000000E+00 0.0000000E+00
0.0000000E+00 0.0000000E+00 0.0000000E+00 0.0000000E+00 0.0000000E+00 0.0000000E+00 0.0000000E+00 0.0000000E+00
0.0000000E+00 0.0000000E+00 0.0000000E+00 0.0000000E+00 0.0000000E+00 0.0000000E+00 0.0000000E+00 0.0000000E+00
0.0000000E+00 0.0000000E+00 0.0000000E+00 0.0000000E+00 0.0000000E+00 0.0000000E+00 0.0000000E+00 0.0000000E+00
0.0000000E+00 0.0000000E+00 0.0000000E+00 0.0000000E+00 0.0000000E+00 0.0000000E+00 0.0000000E+00 0.0000000E+00
0.0000000E+00 0.0000000E+00 0.0000000E+00 0.0000000E+00 0.0000000E+00 0.0000000E+00 0.0000000E+00 0.0000000E+00
0.0000000E+00 0.0000000E+00 0.0000000E+00 0.0000000E+00 0.0000000E+00 0.0000000E+00 0.0000000E+00 0.0000000E+00
0.0000000E+00 0.0000000E+00 0.0000000E+00 0.0000000E+00 0.0000000E+00 0.0000000E+00
0.0000000E+00 0.0000000E+00 0.0000000E+00 0.0000000E+00 0.0000000E+00 0.0000000E+00 0.0000000E+00 0.0000000E+00
0.0000000E+00 0.0000000E+00 0.0000000E+00 0.0000000E+00 0.0000000E+00 0.0000000E+00 0.0000000E+00 0.0000000E+00
0.0000000E+00 0.0000000E+00 0.0000000E+00 0.0000000E+00 0.0000000E+00 0.0000000E+00 0.0000000E+00 0.0000000E+00
0.0000000E+00 0.0000000E+00 0.0000000E+00 0.0000000E+00 0.0000000E+00 0.0000000E+00 0.0000000E+00 0.0000000E+00
0.0000000E+00 0.0000000E+00 0.0000000E+00 0.0000000E+00 0.0000000E+00 0.0000000E+00 0.0000000E+00 0.0000000E+00
0.0000000E+00 0.0000000E+00 0.0000000E+00 0.0000000E+00 0.0000000E+00 0.0000000E+00 0.0000000E+00 0.0000000E+00
0.0000000E+00 0.0000000E+00 0.0000000E+00 0.0000000E+00 0.0000000E+00 0.0000000E+00 0.0000000E+00 0.0000000E+00
0.0000000E+00 0.0000000E+00 0.0000000E+00 0.0000000E+00 0.0000000E+00 0.0000000E+00 0.0000000E+00 0.0000000E+00
0.0000000E+00 0.0000000E+00 0.0000000E+00 0.0000000E+00 0.0000000E+00 0.0000000E+00
5.3816200E-10 5.4093087E-10 5.4315077E-10 5.4323300E-10 5.3797960E-10 5.2985845E-10 5.2963842E-10 5.4932601E-10
5.9051825E-10 6.4218573E-10 6.9677016E-10 7.7553813E-10 8.5355484E-10 9.6345370E-10 9.6275802E-10 8.5873033E-10
6.9241058E-10 5.5771695E-10 5.0842217E-10 5.0720782E-10 5.1586596E-10 5.2491708E-10 5.3273793E-10 5.3816200E-10
5.4093087E-10 5.4315077E-10 5.4323300E-10 5.3797960E-10 5.2985845E-10 5.2963842E-10 5.4932601E-10 5.9051825E-10
6.4218573E-10 6.9677016E-10 7.7553813E-10 8.5355484E-10 9.6345370E-10 9.6275802E-10 8.5873033E-10 6.9241058E-10
5.5771695E-10 5.0842217E-10 5.0720782E-10 5.1586596E-10 5.2491708E-10 5.3273793E-10 5.3816200E-10 5.4093087E-10
5.4315077E-10 5.4323300E-10 5.3797960E-10 5.2985845E-10 5.2963842E-10 5.4932601E-10 5.9051825E-10 6.4218573E-10
6.9677016E-10 7.7553813E-10 8.5355484E-10 9.6345370E-10 9.6275802E-10 8.5873033E-10 6.9241058E-10 5.5771695E-10
5.0842217E-10 5.0720782E-10 5.1586596E-10 5.2491708E-10 5.3273793E-10 5.3816200E-10
2.4445359E-21 2.4445359E-21 2.4445359E-21 2.4445359E-21 2.4445359E-21 2.4445359E-21 2.4445359E-21 2.4445359E-21
2.4445359E-21 2.4445359E-21 2.4445359E-21 2.4445359E-21 2.4445359E-21 2.4445359E-21 2.4445359E-21 2.4445359E-21
2.4445359E-21 2.4445359E-21 2.4445359E-21 2.4445359E-21 2.4445359E-21 2.4445359E-21 2.4445359E-21 2.4445359E-21
2.4445359E-21 2.4445359E-21 2.4445359E-21 2.4445359E-21 2.4445359E-21 2.4445359E-21 2.4445359E-21 2.4445359E-21
2.4445359E-21 2.4445359E-21 2.4445359E-21 2.4445359E-21 2.4445359E-21 2.4445359E-21 2.4445359E-21 2.4445359E-21
2.4445359E-21 2.4445359E-21 2.4445359E-21 2.4445359E-21 2.4445359E-21 2.4445359E-21 2.4445359E-21 2.4445359E-21
2.4445359E-21 2.4445359E-21 2.4445359E-21 2.4445359E-21 2.4445359E-21 2.4445359E-21 2.4445359E-21 2.4445359E-21
2.4445359E-21 2.4445359E-21 2.4445359E-21 2.4445359E-21 2.4445359E-21 2.4445359E-21 2.4445359E-21 2.4445359E-21
2.4445359E-21 2.4445359E-21 2.4445359E-21 2.4445359E-21 2.4445359E-21 2.4445359E-21
1.0000000E-01 8.2100000E-02 6.7404100E-02 5.5338766E-02 4.5433127E-02 3.7300597E-02 3.0623790E-02 2.5142132E-02
2.0641690E-02 1.6946828E-02 1.3913346E-02 1.0311248E-02 1.3913346E-02 1.6946828E-02 2.0641690E-02 2.5142132E-02
3.0623790E-02 3.7300597E-02 4.5433127E-02 5.5338766E-02 6.7404100E-02 8.2100000E-02 1.0000000E-01 1.0000000E-01
8.2100000E-02 6.7404100E-02 5.5338766E-02 4.5433127E-02 3.7300597E-02 3.0623790E-02 2.5142132E-02 2.0641690E-02
1.6946828E-02 1.3913346E-02 1.0311248E-02 1.3913346E-02 1.6946828E-02 2.0641690E-02 2.5142132E-02 3.0623790E-02
3.7300597E-02 4.5433127E-02 5.5338766E-02 6.7404100E-02 8.2100000E-02 1.0000000E-01 1.0000000E-01 8.2100000E-02
6.7404100E-02 5.5338766E-02 4.5433127E-02 3.7300597E-02 3.0623790E-02 2.5142132E-02 2.0641690E-02 1.6946828E-02
1.3913346E-02 1.0311248E-02 1.3913346E-02 1.6946828E-02 2.0641690E-02 2.5142132E-02 3.0623790E-02 3.7300597E-02
4.5433127E-02 5.5338766E-02 6.7404100E-02 8.2100000E-02 1.0000000E-01
```

HPT1 - Max power - Mass averaged:

```
1            21          29           0      287.03           0
    1.17883E-05    0.00000E+00
    7.29015E-02    0.00000E+00
    1.48014E-01    2.33000E-01
    2.98833E-02    0.00000E+00
    7.87784E-12    0.00000E+00
    2.61288E-08    0.00000E+00
    3.74385E-06    0.00000E+00
    5.41438E-08    0.00000E+00
    6.67006E-09    0.00000E+00
    3.15494E-04    0.00000E+00
    4.99679E-06    0.00000E+00
    6.03887E-12    0.00000E+00
    7.81056E-11    0.00000E+00
    7.87986E-08    0.00000E+00
    3.09774E-10    0.00000E+00
    2.18535E-05    0.00000E+00
    1.74444E-06    0.00000E+00
    2.29168E-13    0.00000E+00
    5.94824E-12    0.00000E+00
    1.22867E-16    0.00000E+00
    3.60300E-13    0.00000E+00
    5.55086E-17    0.00000E+00
    1.15043E-10    0.00000E+00
    7.48842E-01    7.67000E-01
    0.00000E+00    0.00000E+00
    0.00000E+00    0.00000E+00
    0.00000E+00    0.00000E+00
    4.36994E-10    0.00000E+00
    2.44454E-21    0.00000E+00
       1359.795       1570803    175.9363      0.0038           0           1
       1359.712       1570423    176.2318      0.0038           0           1
       1358.812       1566410     179.302      0.0038           0           1
       1349.544       1526507    214.2155 0.003799999           0           1
       1338.676       1484815    253.0134 0.003790001           0           1
       1324.634       1431395     279.816 0.003800001           0           1
       1307.769       1368246    285.5765 0.003799999           0           1
       1298.097       1332669    257.3565 0.003800001           0           1
       1289.669       1303722    232.7334 0.003799997           0           1
       1285.294       1293009    207.5762 0.003790003           0           1
       1280.689       1258006   215.10745     0.00227           0           1
       1271.736       1209131    233.2347     0.00228           0           1
       1253.796       1148566    294.5791     0.00227           0           1
       1247.374       1131973    338.2817     0.00228           0           1
       1236.726       1098380    369.9686     0.00227           0           1
       1218.939       1042952    394.7301     0.00228           0           1
       1194.913      969092.2    405.5363     0.00228           0           1
       1183.045      926285.8    383.9227     0.00227           0           1
       1181.315      917795.9    352.4142     0.00228           0           1
       1195.526      959228.8     300.664     0.00197           0           1
        1202.61      980842.3    271.0783           0           0           1
```

HPT1 - Max power - High temperature streamline:

```
1          80          29           0      287.03           0
    1.17883E-05    0.00000E+00
    7.29015E-02    0.00000E+00
    1.48014E-01    2.33000E-01
    2.98833E-02    0.00000E+00
    7.87784E-12    0.00000E+00
    2.61288E-08    0.00000E+00
    3.74385E-06    0.00000E+00
    5.41438E-08    0.00000E+00
    6.67006E-09    0.00000E+00
    3.15494E-04    0.00000E+00
    4.99679E-06    0.00000E+00
    6.03887E-12    0.00000E+00
    7.81056E-11    0.00000E+00
    7.87986E-08    0.00000E+00
    3.09774E-10    0.00000E+00
    2.18535E-05    0.00000E+00
    1.74444E-06    0.00000E+00
    2.29168E-13    0.00000E+00
    5.94824E-12    0.00000E+00
    1.22867E-16    0.00000E+00
    3.60300E-13    0.00000E+00
    5.55086E-17    0.00000E+00
    1.15043E-10    0.00000E+00
    7.48842E-01    7.67000E-01
    0.00000E+00    0.00000E+00
    0.00000E+00    0.00000E+00
    0.00000E+00    0.00000E+00
    4.36994E-10    0.00000E+00
    2.44454E-21    0.00000E+00
        1361.67        1579350 163.6325233 0.000974026           0           1
    1361.731133    1579629.425 163.2297162 0.000974026           0           1
    1361.859356    1580212.748 162.3276685 0.000974026           0           1
    1362.045129     1581059.69 161.0120533 0.000974026           0           1
      1362.3448    1582430.668 158.8705417 0.000974026           0           1
    1362.716561    1584132.707 156.1941047 0.000974026           0           1
    1363.187816    1586296.968 152.6077004 0.000974026           0           1
    1363.702964    1588664.787 148.6079543 0.000974026           0           1
    1364.254994     1591211.35 144.1493071 0.000974026           0           1
    1364.740035    1593429.721 139.7613897 0.000974026           0           1
    1365.013192      1594685.8  136.381452 0.000974026           0           1
    1364.936523    1594337.736 134.8354564 0.000974026           0           1
    1364.452676    1592293.788 135.5192932 0.000974026           0           1
    1363.734687    1589264.619 137.8009499 0.000974026           0           1
    1362.954266    1585520.713 140.9655827 0.000974026           0           1
    1362.143905    1581204.741 144.7854538 0.000974026           0           1
     1361.31015    1576323.393 149.0393239 0.000974026           0           1
    1360.469281    1571068.214 153.4957755 0.000974026           0           1
    1359.548987    1565302.737 158.1249937 0.000974026           0           1
    1358.541125    1558991.823 162.8804288 0.000974026           0           1
    1357.438706    1552166.183 167.7122939 0.000974026           0           1
    1356.220931     1544789.46 172.5968847 0.000974026           0           1
    1354.876306    1536784.723 177.4999794 0.000974026           0           1
    1353.383465    1528060.375 182.3620107 0.000974026           0           1
    1351.828607    1518645.336 187.0398626 0.000974026           0           1
    1350.198608    1508591.203 191.3673109 0.000974026           0           1
    1348.521538    1497951.842 195.1452903 0.000974026           0           1
    1346.643097    1486807.582 198.2114491 0.000974026           0           1
     1344.40452    1474694.669 200.5048012 0.000974026           0           1
    1341.584896    1460743.398 202.3211892 0.000974026           0           1
    1337.945957    1444059.825 204.1661148 0.000974026           0           1
    1333.002734     1422694.55 207.2876771 0.000974026           0           1
```

1326.192181	1393886.381	213.7535496	0.000974026	0	1
1319.047329	1365927.603	228.3462013	0.000974026	0	1
1320.246711	1373860.776	216.0797396	0.000974026	0	1
1301.253438	1347200.356	214.4186074	0.000974026	0	1
1294.163824	1327025.625	219.0556362	0.000974026	0	1
1289.593153	1311139.441	220.4491074	0.000974026	0	1
1286.663243	1300574.15	220.1306449	0.000974026	0	1
1284.582895	1293575.863	218.4710914	0.000778679	0	1
1282.58151	1249358.725	218.6341176	0.000583333	0	1
1283.826663	1254086.8	219.2939185	0.000583333	0	1
1284.724178	1257542.561	219.5469849	0.000583333	0	1
1285.955472	1262300.125	218.0146573	0.000583333	0	1
1287.513907	1268338.567	214.8767426	0.000583333	0	1
1289.34823	1275488.125	210.4504239	0.000583333	0	1
1291.30807	1283159.944	205.4279798	0.000583333	0	1
1292.910141	1289454.385	201.5639105	0.000583333	0	1
1294.101112	1294101.381	199.6967323	0.000583333	0	1
1294.815722	1296849.155	199.901098	0.000583333	0	1
1294.303468	1294999.942	203.5542228	0.000583333	0	1
1293.404184	1291706.919	208.5842319	0.000583333	0	1
1292.227073	1287430.792	213.9890612	0.000583333	0	1
1290.823817	1282214.178	219.7755159	0.000583333	0	1
1289.183985	1276026.816	225.650816	0.000583333	0	1
1287.383554	1269183.12	231.5872877	0.000583333	0	1
1285.405252	1261622.65	237.5970562	0.000583333	0	1
1283.251739	1253352.085	243.6246136	0.000583333	0	1
1280.934675	1244372.688	249.6141627	0.000583333	0	1
1278.448822	1234636.376	255.5826876	0.000583333	0	1
1275.752764	1224062.804	261.5443532	0.000583333	0	1
1272.774086	1212436.959	267.5323968	0.000583333	0	1
1269.377606	1199319.479	273.7337962	0.000583333	0	1
1265.572569	1184454.479	280.3494671	0.000583333	0	1
1261.28942	1167675.024	287.5356723	0.000583333	0	1
1256.353664	1148599.814	295.4885152	0.000583333	0	1
1250.646129	1127118.716	304.1021445	0.000583333	0	1
1244.318943	1103821.814	313.0604302	0.000583333	0	1
1237.33245	1078615.991	322.4144125	0.000583333	0	1
1229.14201	1049886.253	332.8202322	0.000583333	0	1
1218.730098	1014461.748	346.5393325	0.000583333	0	1
1205.731857	971575.4713	366.4237725	0.000583333	0	1
1192.502914	928452.9769	393.2397397	0.000583333	0	1
1188.169418	912710.0383	416.661042	0.000583333	0	1
1216.456088	999538.5689	366.9117658	0.000583333	0	1
1221.600443	1024556.716	335.9278348	0.000583333	0	1
1217.887545	1020755.464	321.0972363	0.000583333	0	1
1213.432511	1007409.083	315.0504912	0.000583333	0	1
1209.427894	994491.3791	311.2279984	0.000583333	0	1
1205.671597	984280.3104	307.8753852	0	0	1

HPT1 - Max power - Low temperature streamline:

```
1            80          29           0      287.03           0
    1.17883E-05    0.00000E+00
    7.29015E-02    0.00000E+00
    1.48014E-01    2.33000E-01
    2.98833E-02    0.00000E+00
    7.87784E-12    0.00000E+00
    2.61288E-08    0.00000E+00
    3.74385E-06    0.00000E+00
    5.41438E-08    0.00000E+00
    6.67006E-09    0.00000E+00
    3.15494E-04    0.00000E+00
    4.99679E-06    0.00000E+00
    6.03887E-12    0.00000E+00
    7.81056E-11    0.00000E+00
    7.87986E-08    0.00000E+00
    3.09774E-10    0.00000E+00
    2.18535E-05    0.00000E+00
    1.74444E-06    0.00000E+00
    2.29168E-13    0.00000E+00
    5.94824E-12    0.00000E+00
    1.22867E-16    0.00000E+00
    3.60300E-13    0.00000E+00
    5.55086E-17    0.00000E+00
    1.15043E-10    0.00000E+00
    7.48842E-01    7.67000E-01
    0.00000E+00    0.00000E+00
    0.00000E+00    0.00000E+00
    0.00000E+00    0.00000E+00
    4.36994E-10    0.00000E+00
    2.44454E-21    0.00000E+00
    1361.493333    1578546.667  164.839656 0.000974026           0           1
    1361.466192     1578425.56 164.5952474 0.000974026           0           1
    1361.604002    1579053.754 163.5284478 0.000974026           0           1
    1361.804629    1579966.982 162.0800594 0.000974026           0           1
    1362.145143     1581521.66 159.5112592 0.000974026           0           1
    1362.594095    1583581.799 156.0765876 0.000974026           0           1
    1363.232964    1586517.578 150.9349891 0.000974026           0           1
    1364.042053    1590234.226 144.1284106 0.000974026           0           1
    1365.162053     1595407.78 134.1615632 0.000974026           0           1
    1366.795742    1602985.596 118.3095485 0.000974026           0           1
    1369.272409    1614682.489 89.43887755 0.000974026           0           1
    1364.526187     1584822.24 51.07783472 0.000974026           0           1
    1291.527273    1329161.844 315.6673148 0.000974026           0           1
    1277.678082     1299682.65 377.7369451 0.000974026           0           1
    1275.978669    1326068.804 370.1731122 0.000974026           0           1
    1269.402691    1309584.362 387.5991185 0.000974026           0           1
    1257.998873     1285392.64 403.5493714 0.000974026           0           1
    1245.793181    1258396.257 417.5255673 0.000974026           0           1
    1232.620969    1227732.865 429.6271387 0.000974026           0           1
    1218.498533    1193735.771 438.8576732 0.000974026           0           1
    1203.778588    1157823.321 441.8781725 0.000974026           0           1
    1189.737367    1125553.566  434.522286 0.000974026           0           1
    1177.237046    1099213.408 417.5474688 0.000974026           0           1
    1167.504991    1083412.816 388.1184497 0.000974026           0           1
    1163.923057    1089289.441 341.2596273 0.000974026           0           1
    1168.342227    1125630.029 290.5231776 0.000974026           0           1
    1172.833301    1169261.064 253.0616594 0.000974026           0           1
     1173.29684    1204656.195 231.0850281 0.000974026           0           1
    1167.346347    1218667.702 219.5558085 0.000974026           0           1
    1159.752545    1222097.051 209.8811117 0.000974026           0           1
    1153.419329    1226853.325 199.6633722 0.000974026           0           1
    1146.829021    1232944.565 188.3923005 0.000974026           0           1
```

1143.312018	1243698.304	175.4889752	0.000974026	0	1
1140.402407	1258885.435	161.0597535	0.000974026	0	1
1140.036382	1281944.708	145.2191088	0.000974026	0	1
1175.145197	1335021.695	90.38037157	0.000974026	0	1
1211.306202	1369922.242	147.4152696	0.000974026	0	1
1207.12102	1337729.59	165.8133053	0.000974026	0	1
1206.773496	1319203.566	175.0043011	0.000974026	0	1
1208.699917	1307136	180.816468	0.000778679	0	1
1287.330753	1267688.4	212.7221961	0.000583333	0	1
1287.762684	1269355.101	211.6905576	0.000583333	0	1
1288.820598	1273488.41	206.779503	0.000583333	0	1
1290.589866	1280431.457	197.7692586	0.000583333	0	1
1293.468976	1291761.396	182.5206961	0.000583333	0	1
1297.547167	1307914.898	158.9508226	0.000583333	0	1
1303.602496	1332182.473	118.4879717	0.000583333	0	1
1164.931084	870116.5997	253.5501099	0.000583333	0	1
1144.175412	853904.2104	385.1477051	0.000583333	0	1
1131.419472	839969.4267	445.4349092	0.000583333	0	1
1123.69347	834659.5046	481.7317531	0.000583333	0	1
1116.675521	828255.7264	508.2110508	0.000583333	0	1
1109.91928	820438.2077	530.0886496	0.000583333	0	1
1102.738785	810998.8817	545.8099993	0.000583333	0	1
1098.641442	799476.4425	558.8569498	0.000583333	0	1
1094.594253	784471.2937	571.6215983	0.000583333	0	1
1083.994215	761175.8426	585.1416047	0.000583333	0	1
1073.370783	736268.411	594.5327905	0.000583333	0	1
1062.381619	710342.4874	599.7291891	0.000583333	0	1
1051.045407	682847.2009	599.3197894	0.000583333	0	1
1039.160949	654660.4653	595.8591248	0.000583333	0	1
1031.110655	631251.7175	582.3609096	0.000583333	0	1
1026.345079	616296.2965	560.2919372	0.000583333	0	1
1028.250405	616917.7426	525.6422008	0.000583333	0	1
1040.345257	643772.7946	476.6042655	0.000583333	0	1
1058.673726	689551.6292	422.8428595	0.000583333	0	1
1078.47177	746780.4128	375.6378799	0.000583333	0	1
1092.282331	793869.6333	337.067325	0.000583333	0	1
1100.246523	828547.8406	306.7501579	0.000583333	0	1
1104.8363	855583.6909	284.8229632	0.000583333	0	1
1106.83783	876502.0781	269.4715436	0.000583333	0	1
1105.5863	886148.2441	257.312107	0.000583333	0	1
1105.345968	898562.7729	244.0794738	0.000583333	0	1
1105.586062	913599.3989	229.8527779	0.000583333	0	1
1106.31671	929963.5037	214.9652901	0.000583333	0	1
1106.954414	941075.4732	202.9952434	0.000583333	0	1
1175.93931	1076786.092	54.5923099	0.000583333	0	1
1185.101995	1075679.495	120.8449247	0.000583333	0	1
1180.331047	1046363.434	160.4974738	0.000583333	0	1
1174.886129	1023109.349	179.9368539	0	0	1

HPT1 exit to nozzle exit - Max power - Mass Averaged:

```
1            39          29           0      287.03           0
  1.1183140e-05    0.00000E+00
  7.2902410e-02    0.00000E+00
  1.4801330e-01    0.00000E+00
  2.9883340e-02    0.00000E+00
  9.6843060e-12    0.00000E+00
  4.4202050e-08    0.00000E+00
  3.4493320e-06    0.00000E+00
  3.7568700e-08    0.00000E+00
  3.8295280e-08    0.00000E+00
  3.1464130e-04    0.00000E+00
  5.9002840e-06    0.00000E+00
  1.4215190e-11    0.00000E+00
  1.5348320e-10    0.00000E+00
  4.8974110e-07    0.00000E+00
  2.1678720e-09    0.00000E+00
  2.1842190e-05    0.00000E+00
  1.7583280e-06    0.00000E+00
  9.7461800e-14    0.00000E+00
  1.0319860e-11    0.00000E+00
  1.9406000e-16    0.00000E+00
  3.2799880e-13    0.00000E+00
  4.1740790e-17    0.00000E+00
  8.1290550e-10    0.00000E+00
  7.4884160e-01    0.00000E+00
  0.0000000e+00    0.00000E+00
  0.0000000e+00    0.00000E+00
  0.0000000e+00    0.00000E+00
  7.1511560e-10    0.00000E+00
  2.4445390e-21    0.00000E+00
       1202.61       980842.3         260        0.02           0           1
    1184.993301    955524.7629  264.378224        0.02           0           1
     1146.54476       831071.8     283.547        0.02           0           1
    1111.539513    723225.8061  303.839296        0.02           0           1
    1079.720221    630506.8605  324.569528        0.02           0           1
    1050.839058    551500.6221  345.052112        0.02           0           1
    1024.657707    484858.3293  364.601464        0.02           0           1
     1000.94736       429296.8     382.532        0.02           0           1
    979.4887209    383598.4317  398.158136        0.02           0           1
    960.0720028    346611.2013  410.794288        0.02           0           1
    942.4969292    317248.6653  419.754872        0.02           0           1
    926.5727337    294489.9597  424.354304        0.02           0           1
      912.11816       277379.8     423.907        0.02           0           1
     898.961462    265028.4813  417.727376        0.02           0           1
    886.9404038    256611.8781  405.129848        0.02           0           1
    875.9022595    251371.4445  385.428832        0.02           0           1
    865.7038134    248614.2141  357.938744        0.02           0           1
      856.21136       247712.8     321.974        0.02           0           1
    847.3007039    248105.3949  276.849016        0.02           0           1
    838.8571599    249295.7709 247.8614208        0.02           0           1
    830.7755529    250853.2797 239.9685248        0.02           0           1
    822.9602179    252412.8525 232.1420512        0.02           0           1
       815.325         253675     224.382        0.02           0           1
    807.7932547    254405.8125 216.6883712        0.02           0           1
    800.2978473    254436.9597 209.0611648        0.02           0           1
    792.7811535    253665.6909 201.5003808        0.02           0           1
    785.1950591    252054.8349 194.0060192        0.02           0           1
      777.50096       249632.8   186.57808        0.02           0           1
    769.6697622    246493.5741 179.2165632        0.02           0           1
    761.6818819    242796.7245 171.9214688        0.02           0           1
    753.5272454    238767.3981 164.6927968        0.02           0           1
    745.2052892    234696.3213 157.5305472        0.02           0           1
      736.72496       230939.8       145.4        0.02           0           1
    728.1047145    227919.7197    148.9824        0.01           0           1
    723.7504913     226835.616    176.7896        0.01           0           1
    719.3725196    226123.5453    230.0912        0.01           0           1
    714.9757813    225854.6875         315        0.01           0           1
    710.5658524    226104.3213    437.6288        0.01           0           1
    706.1489037     226951.824    604.0904           0           0           1
```

APPENDIX F

MEDIA CONTAINING SUPLEMENTAL DATA

Several of the computational results obtained in this research are time dependent and thus are best presented with an animation. The attached Compact Disc (CD) contains several figures which were referenced in this thesis. The figures were formatted using HTLM which can be viewed form a typical web browser such as Netscape Communicator 4.7 or Internet Explorer 5.0. To view these figures simply insert the CD into a personal computer, launch the web browser, and open the file "appendix_f.html."

An index of the figures is given below for convenience:

4 Validation
4.4 Convergence Criteria Study
4.4.3 Results
Figure F.1 Convergence time evolution for mass fraction of O
Figure F.2 Convergence time evolution for mass fraction of OH
Figure F.3 Convergence time evolution for mass fraction of SO_3

5 Modeling the NASA/DERA Engine Test
5.4 High Fidelity Modeling
5.4.2 High Fidelity Modeling Results
Figure F.4 Static temperature for max power wake model case
Figure F.5 Mass fraction of SO_3 for max power wake model case
Figure F.6 Mass fraction of SO_3 for max power wake model case (full stage view)
Figure F.7 Static temperature for non-uniform max power wake model case
Figure F.8 Mass fraction of SO_3 for non-uniform max power wake model case

Appendix A Princeton VPFR Validation Modeling
"Unsteady Non-Reacting Flow Solution"
Figure F.9 Initial transient
Figure F.10 One vortex shedding cycle

Finally, the files "SMThesis.doc" and "SMThesis.pdf" is contains the text of this thesis in Microsoft Word 97 and Adobe PDF format, respectively.

REFERENCES

[1] Lukachko, S.P. Research on the Science and Politics of the Atmospheric Effects of Aviation Debate. S.M. Thesis. Massachusetts Institute of Technology. 1997.

[2] Penner, J.E., D.H. Lister, D.J. Griggs, D.J. Dokken, and M. McFarland. Aviation and the Global Atmosphere. New York: Cambridge University Press, 1999.

[3] Penner, J.E., D.H. Lister, D.J. Griggs, D.J. Dokken, and M. McFarland. Summary for Policymakers: Aviation and the Global Atmosphere. A special report of IPCC Working Groups I and III: Published for the Intergovernmental Panel on Climate Change.

[4] GAO/RCED-00-57. Aviation and the Environment: Aviation's Effects on the Global Atmosphere are Potentially Significant and Expected to Grow. United States General Accounting Office: Report to the Honorable James L. Oberstar, Ranking Democratic Member, Committee on Transportation and nfrastructure, House of Representative, February, 2000.

[5] http://hyperion.gsfc.nasa.gov/AEAP/1385links.html

[6] http://hyperion.gsfc.nasa.gov/AEAP/1400links.html

[7] Kerrebrock, J.L. Aircraft Engines and Gas Turbines, 2nd Ed.. Cambridge, MA: The MIT Press, 1992. Chapter 4.

[8] http://hyperion.gsfc.nasa.gov/AEAP/aesa.html

[9] http://hyperion.gsfc.nasa.gov/AEAP/1381links.html

[10] Howard, R.P., et al. "Experimental Characterization of Gas Turbine Emissions at Simulated Flight Altitude Conditions." AEDC-TR-96-3. September 1996.

[11] ICAO, International Civil Aviation Organization. ICAO Engine Exhaust Emissions Data Bank, ICAO Doc 9646-AN/943. 1st ed. : 1995.

[12] Lukachko, S.P., I.A. Waitz, R.C. Miake-Lye, R.C. Brown, M.R. Anderson, and W.N. Dawes. "Simulation of Post-Combustor Chemical Evolution in a Gas Turbine Engine." As submitted to Journal of Propulsion and Power. 1998.

[13] Miake-Lye, R.C., M. Martinez-Sanchez, R.C. Brown, C.E. Kolb. "Plume and wake-dynamics, mixing, and chemistry behind a high speed civil transport aircraft." Journal of Aircraft. 30. July-August 1993: pp. 467-479.

[14] Brown, R.C., R.C. Miake-Lye, M.R. Anderson, C.E. Kolb, and T.J. Resch. "Aerosol dynamics in near field aircraft plumes." Journal of GeophysicalResearch. 101(D17). Ioctober 20, 1996: pp.22939-22953.

[15] Schumann, U., P. Konopka, R. Baumann, R.Busen, T.Gerz, H. Schlager, P. Schulte, and H. Volkert. "Estimation of diffusion parameters of aircraft exhaust plumes near the tropopause from nitric oxide and turbulence measurements." Journal of Geophysical Research. 100(D7). July 20, 1995: pp.14147-14162.

[16] Anderson, M.R., R.C. Miake-Lye, R.C. Brown, and C.E. Kolb. "Calculation of exhaust plume structure and emissions of the ER-2 aircraft in the stratosphere." Journal of Geophysical Research. 101. February 20, 1996: pp. 4025-4032.

[17] Quackenbush, T.R., M.E. Teske, and A.J. Bilanin. "Computation of Wake/Exhaust Mixing Downstream of Advanced Transport Aircraft." AIAA-93-2944. Presented at AIAA 24th Fluid Dynamics Conference. Orlando, Florida. July 6-9, 1993.

[18] Miake-Lye, R.C., R.C. Brown, M.R. Anderson, and C.E. Kolb. "Calculations of Condensation and Chemistry in an Aircraft Contrail." In Impact of Emissions from Aircraft and Spacecraft Upon the Atmosphere, Proceedings. U. Schumman and D. Wurzel, eds. Koln, Germany. April 18-20, 1994.

[19] Schumman, U., AERONOX:The impact of NO_x Emissions from Aircraft Upon the Atmosphere at Flight Altitudes 8-15km: Final Report to the Commission of European Communities. Brussels, Belgium: EC-DLR, August 1995.

[20] National Research Council. A Review of NASA's Atmospheric Effects of Stratospheric Aircraft Project. Washington DC: National Academy Press,1999.

[21] http://hyperion.gsfc.nasa.gov/AEAP/97NRA.html

[22] http://hyperion.gsfc.nasa.gov/AEAP/1333links.html

[23] Mueller, M.A., R.A. Yetter, F.L. Dryer. "Kinetic Modeling of the CO/H2O/O2/NO/SO2 System: Implication for High-Pressure Fall-off in the SO2 + O (+M) = SO3 (+M) Reaction." International Journal of Chemical Kinetics 32. January 2000: pp. 317-339.

[24] Glarborg, P., D. Kubel, K. Dam-Johansen, H-M. Chiang and J.W. Bozzelli. "Impact of SO2 and NO on CO oxidation under Post-Flame Conditions." International Journal of Chemical Kinetics 28. March 1996: pp. 773-790.

[25] DeGraaff, D.B., E.P. Zimmitti, F.L. Dryer. A Study of the Mixing Characteristics of the Variable Pressure Flow Reactor: Final Report. Undergraduate Independent Work. Princeton University. 1993.

[26] Held, T.H.The Oxidation of Methanol, Isobutene and Methyl tertiary-Butyl Ether. PhD. Thesis. Princeton University. 1993.

[27] Veermeersch, M.L. A Variable Pressure Flow Reactor for Chemical Kinetic Studies: Hydrogen, Methane, and Butane Oxidation at 1 to 10 Atmospheres and 880 to 1040 K. PhD. Thesis. Princeton University. 1991.

[28] Lukachko, S.P., I.A. Waitz, R.C. Miake-Lye, R.C. Brown, and M.R. Anderson. "Production of Sulfate Aerosol Precursors in the Turbine and Exhaust Nozzle of an Aircraft Engine." Journal or Geophysical Research 103 (D13). July 20, 1998: pp.16159-16174.

[29] Tremmel, H.G., and U. Schumann. "Model Simulations of Fuel Sulfur Conversion Efficiencies in an Aircraft Engine: Dependence on Reaction Rate Constants and Initial Species Mixing Ratios" Aerosp. Sci. Technol 3. 1999: pp. 17-430.

[30] Brown, R.C. et al. "Aircraft Exhaust Sulfur Emissions." Geophyscial Research Letters 23. December 1, 1996: pp. 3603-3606.

[31] Lukachko, S. Personal Communication, 1998-2000.

[32] Waitz, I.A. Personal Communication, 1998-2000.

[33] Wilson, Chris. Personal Communications, June 2000.

[34] Clague, Andrew or Whiteman, Mike. Internal Project Memorandum, DERA and MIT/ARI Proprietary, 1998-2000.

[35] Caleb Dhanasekeran and Albert Demarnge. Personal Communications, January/March 1999.

[36] Mattingly, J.D. *Elements of Gas Turbine Propulsion.* New York: McGraw-Hill, Inc., 1996.

[37] Horlock, J.H. *Axial Flow Turbines :Fluid Mechanics and Thermodynamics.* Malabar, Florida: Krieger Publishing Company, 1985.

[38] Munson, B.R., D.F. Young, and T.H. Okiishi. *Fundamentals of Fluid Mechanics, 2nd Ed.* New York: John Wiley and Sons, Inc., 1994.

[39] Fox and Kline, S.J. “Flow Patterns in Curvilinear Subsonic Diffusers.” *Transactions of the ASME.* Series E, 1962.

[40] Idelchik, I.E. *Handbook of Hydraulic Resistance, 3rd Ed.* Bergell House, 1996.

[41] Runstadler, P.W., F.X. Dolan, and R.C. Dean. *Diffuser Data Book Creare Technical Note TN-186.* New York: Creare, Inc., 1975.

[42] Bury, M.E. *Influence of Reynolds Number and Blade Geometry on Low Pressure Turbine Performance.* S.M. Thesis. Massachusetts Institute of Technology. 1997.

[43] Guenette, G.R. Jr. *A Fully Scaled Short Duration Turbine Experiment.* PhD. Thesis. Massachusetts Institute of Technology. 1985.

[44] O’Sullivan, M.N. *A Computational Study of the Effects of Viscosity on Lobed Mixer Flowfields.* S.M. Thesis. Massachusetts Institute of Technology. 1993.

[45] Dietz, H. “Linux Parallel Processing HOWTO.” *V980105*. January 5, 1998.

[46] Gropp, W., and E. Lusk. *User’s Guide for* `mpich`, *A Portable Implementation of MPI.* Chicago: University of Chicago Argonne National Laboratory, Mathematics and Computer Science Division, 1996. ANL/MCS-TM-ANL-96/6.

[47] Gropp, W., and E. Lusk. *Installation Guide to* `mpich`, *A Portable Implementation of MPI.* Chicago: University of Chicago Argonne National Laboratory, Mathematics and Computer Science Division, 1996. ANL/MCS-TM-ANL-96/5.

[48] Lukachko, S. *CNEWT Primer*. November 1998. Unpublished Work.

[49] Dawes, W.N. *The Solution-Adaptive 3D Navier-Stokes Solver “NEWT”:User’s Manual*. Cambridge, U.K.: Whittle Laboratory, 199x.

[50] Dawes, W.N., *Advanced Numerical Methods: Solution of the Navier-Stokes Equations.* Cambridge, U.K.: Whittle Laboratory, 199x.

[51] Dawes, W.N., *A Computer Program for the Analysis of Three Dimensional Viscous Compressible Flow in Turbomachinery Blade Rows.* Cambridge, U.K.: Whittle Laboratory, 199x.

[52] Dawes, W.N. “The Practical Application of Solution-Adaptation to the Numerical Simulation of Complex Turbomachinery Problems.” *Prog. Aerospace Sci.* Vol. 29. 1992: pp.221-269.

[53] Yetter, R.A., F.L. Dryer, M.A. Mueller, and J. Scire. *A Study of Hot Section Chemical Kinetics for Gas Turbine Emissions Predictions.* Final Technical Research Report for Combustion Technology Branch. NASA-Lewis Research Center, OH, 1998.

[54] Mueller, M.A., R.A. Yetter, and F.L. Dryer. *Experimental Studies and Modeling of the Kinetic Interactions of CO, NOx, and SO2 between* $.5 \leq P \leq 10$ *atm and* $950 \leq T \leq 1070$ *K.* 1999 AEAP Conference.

[55] Hunter, S.C. “Formation of SO3 in Gas Turbines.” *Transactions of the ASME.* 104. January 1982: pp.44-51.

[56] Harris, B.W. “Conversion of Sulfur Dioxide to Sulfur Trioxide in Gas Turbine Exhaust.” *Journal of Engineering for Gas Turbines and Power.* 112. October 1990: pp.585-589.

[57] Fahey, D.W., E.R. Keim, K.A. Boering, C.A. Brock, J.C. Wilson, H.H. Jonsson, S. Anthony, T.F. Hanisco, P.O. Wennberg, R.C. Miake-Lye, R.J. Salawitch, N. Louisnard, E.L. Woodbridge, R.S. Gao, S.G. Donnelly, R.C. Wamsley, L.A. Del Negro, S. Solomon, B.C. Daube, S.C. Wofsy, C.R. Webster, R.D. May, K.K. Kelly, M. Loewenstein, J.R. Podolske, K.R. Chan. “Emission Measurements of the Concorde Supersonic Aircraft in the Lower Stratosphere.” *Science.* 270. October 6, 1995: pp. 70-74.

[58] Brown, R.C. and R.C. Maike-Lye. “Heterogeneous Reactions in Aircraft Gas Turbine Engines.” To be submitted to *Geophysical Research Letters.*

[59] Penner, S.S. *Similarity Analysis for Chemical Reactors and The Scaling of Liquid Fuel Rocket Engines.* Washingon, D.C.: Office of Ordnance Research, 19xx.

[60] Spalding, D.B. “The Art of Partial Modeling”.: *9th International Symposium on Combustion: Colloquium on Modeleing Principles.* pp. 833-843.

[61] Brown, P.N., G. D. Byrne, and A.C. Hindmarsh. “VODE: A Variable-Coefficient ODE Solver.” *SIAM Journal Sci. Stat. Comput.* Vol. 10, No. 5. Spetember 1989: pp. 1038-1051.

[62] Byrne, G.D. and A.M. Dean. “The Numerical Solution of Some Kinetics Models with VODE and Chemkin II.” *Computers Chem.* Vol. 17, No. 3. 1993: pp. 297-302. s

[63] MIT-ARI Intra-Engine Trace Species Chemistry Research Plan. October 1998-March 1999.

[64] Lee, J.J. Historical and Future Trends in Aircraft Performance, Cost, and Emissions. S.M. Thesis. Massachusetts Institute of Technology. 2000.

[65] Kirk, D. Personal Communication, 2000.

[66] *Unstructured Mesh Generation and Visualization Package.* Cambridge, U.K.: Whittle Laboratory. Unpublished Work.

[67] Brown, R., Miake-Lye, R., Zhang, J. Personal Communication, 1998-2000.

[68] Kee, R.J., F.M. Rupley, and J.A. Miller. “Chemkin-II: A Fortran Chemical Kinetics Package for the Analysis of Gas-Phase Chemical Kinetics.” *SAND89-8009.* Sandia National Laboratories. March 1991.

[69] Dawes, W.N. Personal Communication, 1998-2000.

[70] Darmonfal, D. Personal Communication, 1999.

[71] Haimes, B. “VISUAL3 User’s & Programer’s Manual.” Massachusetts Institute of Technology. 1996.